

Probing GPCR-G α interactions:

A functional study by EM and SPR

Thesis submitted to the Board of the Medical Sciences Division in partial fulfillment of the requirements for the Degree of Doctor of Philosophy at the University of Oxford.



Roslin Jane Adamson

Corpus Christi College

Michaelmas Term 2014

Probing GPCR-G α interactions:
A functional study by EM and SPR

Roslin Jane Adamson, Corpus Christi College

Thesis submitted for the degree of Doctor of Philosophy at the University of Oxford,
Michaelmas Term 2014

Abstract

The G protein-coupled receptor (GPCR), neurotensin receptor type 1 (NTS1), is pharmacologically important and activated by the tridecapeptide hormone, neurotensin (NT), initiating a cascade of interactions through G proteins to effect cellular responses. The mechanisms by which these occur have only recently begun to be examined structurally, and standard assays involving downstream effectors or radioactive GTP γ S G protein activation to describe GPCR-G protein interactions do not assay the interactions directly. Two methods have been used here to study the interaction of NTS1 with the signalling partners, G α_s and G α_{i1} . A novel DNA-nanotechnological approach for preparing samples for electron microscopy (EM) has been used to study NTS1 and G α_{i1} , both separately and complexed, on a functionalised 2D DNA lattice, providing the first direct evidence of this interaction. Single particle reconstruction methods were used to determine a structure of NTS1 at a resolution of ~ 15 Å, a structure of G α_{i1} at ~ 15 Å, and the interaction of G α_{i1} with NTS1 has been observed using EM.

A further nanotechnological approach, using the increasingly popular method of reconstitution of membrane proteins in nanodiscs, has been used to study NTS1- $G\alpha_s$ and NTS1- $G\alpha_{i1}$ interactions, using EM and surface plasmon resonance (SPR). The ligand (NT) affinity of detergent-solubilised NTS1 and NTS1 reconstituted into nanodiscs was ~ 1 nM, and for the first time, the affinity of binding of $G\alpha_{i1}$ and $G\alpha_s$ to NTS1 was directly measured and determined as 15 nM and 31 nM, respectively. These results will facilitate cryo-EM studies on GPCRs with interacting partners, using a tethering system that both activates the GPCR and maintains it in a concentrated form within a restricted, two-dimensional plane; and also will aid a wealth of mutational and lipid-dependent studies whereby the effect on coupling and GPCR-protein interactions of specific residues and lipid types can be directly measured. This thesis primarily demonstrates the development and effective application of a biophysical methodology for measuring the coupling kinetics of GPCRs to G proteins; as well as demonstrating that this coupling can be visually evidenced under EM using gold-labelled G proteins.

List of Publications

From this thesis

Roslin J Adamson, Anthony Watts. Surface plasmon resonance detection of GPCR-G α coupling in nanodiscs. In preparation.

Goddard, A.D., Dijkman, P.M., Adamson, R.J., and Watts, A. (2013). Chapter 18 - Lipid-dependent GPCR dimerization. In *Methods in cell biology*, P.M. Conn, ed. (Academic Press), pp. 341-357.

Selmi, D. N., Adamson, R. J., Attrill, H., Goddard, A. D., Gilbert, R. J., Watts, A., and Turberfield, A. J. (2011) DNA-templated protein arrays for single-molecule imaging, *Nano Lett* 11, 657-660.

From previous work

Nishal Parbhoo, Stoyan H. Stoychev, Sylvia Fanucchi, Ikechukwu Achilonu, Roslin J. Adamson, Manuel Fernandes, Samantha Gildenhuis, and Heini W. Dirr (2011) A conserved interdomain interaction is a determinant of folding cooperativity in the GST fold. *Biochemistry* **50** (32) 7067-7075.

David Balchin, Sylvia Fanucchi, Ikechukwu Achilonu, Roslin J. Adamson, Jonathan Burke, Manuel Fernandes, Samantha Gildenhuis, Heini W. Dirr (2010) Stability of the domain interface contributes towards the catalytic function at the H-site of class alpha glutathione transferase A1-1. *Biochimica et Biophysica Acta - Proteins and Proteomics*. **1804** (12), 2228-2233.

Sylvia Fanucchi, Roslin J. Adamson and Heini W. Dirr (2008) Formation of an unfolding intermediate state of soluble chloride intracellular channel protein CLIC1 at acidic pH. *Biochemistry* **47** (44), 11674–11681

Acknowledgements

First and foremost I would like to thank my supervisor, **Anthony Watts**. Tony trusted and believed in me right from the very first Skype interview. He has trusted and believed in me through my entire time here at Oxford, through one of the most personally and scientifically difficult and challenging periods in my life, and despite my not always feeling like I deserved it. Tony's door has always been open to me, and he has always made time to talk, whether it be about the nitty-gritty of radioligand binding assays or giant waterfalls somewhere in Central America. If he was not in Oxford, he was never far from the end of an email. To my relief, he didn't micromanage, but he was always happy to give advice or help, or push things along gently in ways that he knew I would respond well to. Tony has provided immense support, encouragement, optimism, advice, and wisdom; he has always done everything he can to ensure that whatever I needed to advance my research could be accessed, and he made efforts to put me in touch with people who could help. I am immensely grateful to him for everything he has done for me while at Oxford.

Many thanks go to **Andrew Turberfield** and **Robert Gilbert** for their support and help on the DNA lattice side of the project, and the electron microscopy. Andrew gave me unfettered access to his lab and resources, and inspiration for the world of nano-structures and machines. Robert spent time helping me to collect data on the EMs and instructing me in their use, as well as giving much helpful advice on the data-processing side of the EM work.

Daniele Selmi, my friend and mentor, and fellow weightlifting fanatic, taught me just about everything he could about image collection and processing, lattice preparation,

electron microscopes, and the CTF. He patiently put up with my many, many questions and my lack of experience with command-line computer processing, and some of the drinking sessions were legend.

Thomas Sharp, electron microscopist extraordinaire, literally taught me just about everything I know about EM and cryo-EM, and I am forever grateful. He cringed as he watched me crash the vacuum yet again, winced as I wobbled the cryo-holder off to a funny angle as I desperately tried to catch the liquid nitrogen splashing everywhere, and then patted me on the back for a job well done and assured me it got easier with practice. And then told me a funny story to take my mind off it. Thom, you are great and I thank you so much.

I thank **Alan Goddard** for the many, many discussions about NTS1, GPCRs and G proteins, his brilliant ideas for experiments, and his patient explanations of all things molecular biology related. Alan was always happy to look at reports or presentations and could always be relied on for advice. His knowledge of the intricacies of G protein-coupling is immense, and he could almost always figure out why certain data was behaving the way it was.

Patricia Dijkman, my fellow DPhil student and our lab EPR specialist – well, actually, I don't know what I would have done without Patricia in the lab. She has been a huge support, both in terms of science and in terms of life. For discussions, questions, scientific puzzles, maths, physics, statistics, software, instrumentation, literature, Patricia will know, or she will find out. I have never seen anyone with such stamina or such an ability to keep going during soul-destroying periods of results-droughts. Patricia has given support, advice, encouragement, and has a wit on her that would slice through glass. One well-placed comment would have us falling about

with mirth, an essential skill on days when research is not giving much joy. Patricia has always been happy to bounce ideas around and help come up with new ones, and, close to my own heart, she doesn't leave a mess in the lab.

Many thanks also go to **Peter Judge**, who, during many interesting and enjoyable discussions, has encouraged, advised and helped me through difficult theory or unanswerable questions. Peter knows his biophysics backwards, and has a knack for explaining complex concepts in easy terms. He has also helped me with my undergraduate teaching, and has generously helped me to move house several times.

Jo Oates was one of the lab cohort who started around the same time I did, and I thank her for the many helpful discussions and the practical help she gave me in the lab, teaching me my first NTS1 expression and purification, and giving advice on the project.

Garrick Taylor and **Juan Bolivar-Gonzales** have been incredibly supportive and kind, have let me cry on their shoulders, and are always up for a good laugh, as well as sharing their knowledge of the dark arts of membrane proteins.

Thanks to **Dave Staunton** for all his help and advice on the SPR machine and the other biophysics suite instruments, and his help with the data analysis. Thanks also to **Alistair Siebert** for his incredible patience with me on the cryo-EM and the T12. He taught me a lot about the practical and theoretical aspects of EM, and was always quick and efficient about giving me booking slots for the EMs.

Thanks go also to **Pete Fisher**, who is always a friendly face around the lab, and always willing to help with anything I needed fixed, ordered or found, and as a fellow lifter was always keen to discuss training and the latest world championship results.

Mary Gregorio was instrumental in my actually getting to Oxford – she helped me with all the admin needed to get a scholarship from Corpus Christi College that enabled me to take up my Wellcome Trust Scholarship. **Tania Boyt** and **Lindsay Johnson** in the MSDTC office were incredibly helpful with admin type questions to do with funding, and Lindsay was my guardian angel when it came to getting my suspension of status and further funding to cover the extension.

I am exceedingly grateful to the **Wellcome Trust**, whose funding made it possible for me to actually do this degree, to the **Oppenheimer Fund** who helped fill in the gap between the home and overseas rates, and to **Corpus Christi College** for the AE Haigh scholarship that completed the gap, and also for pastoral care. Thanks also go to **Delon Human**, who generously provided me with the airfare for my trip from South Africa to get to Oxford.

I would never have had the confidence or character to even apply to Oxford if it weren't for **Mom and Dad**. My parents have always shown me complete love, support and encouragement and have believed in me despite my insistence on doing things my way, usually the hard way, and definitely not the way they'd do it. Both have been incredibly generous, in all ways possible, and have helped me out of many a rut. I have always known, beyond a shadow of a doubt, if I need help, they'll be there, and I thank them from the bottom of my heart. The same goes for my siblings, **Graeme, Jocelyn** and **Pears**, whose love, care, compassion, warmth, joy, senses of humour, encouragement, support and companionship I have always known I can count on. I thank **Lizzie** too, for her care and love.

And finally, last but not least, my heartfelt love, appreciation and gratitude to my partner, **Anneke**, and her children **Dylan**, **Aidan** and **Lyla-Rose**, who have shown me in so many ways that are simply inexpressible, that love, really, is everything.

Roslin Adamson

Oxford, January 2014

To Anneke

Soul twin

Abbreviations

Ab	antibody
AC	affinity chromatography
APS	ammonium persulphate
BioNT	N-terminally biotinylated neurotensin
BLM	bilayer lipid membrane
BODIPY	4,4-difluoro-4-bora-3a,4a-diaza- <i>s</i> -indacene
bp	base pair
BPL	brain polar lipids
BSA	bovine serum albumin
cAMP	cyclic-3',5'-adenosine monophosphate
CD	circular dichroism
CHAPS	3-[(3-cholamidopropyl) dimethylammonio]-1-propanesulfonate
CHAPSO	3-[(3-cholamidopropyl)dimethylammonio]-2-hydroxyl-1-propanesulfonate
CHS	cholesteryl hemisuccinate
CM	carboxymethylated

cmc	critical micellar concentration
CTF	contrast transfer function
CysNT	N-terminally cysteine-labelled neurotensin
DAG	diacylglycerol
DDAO	dodecyldimethyl- <i>N</i> -amineoxide
DDM	<i>n</i> -dodecyl- β -D-maltoside
DHPC	1,2-dihexanoyl- <i>sn</i> -glycero-3-phosphocholine
DMPC	1,2-dimyristoyl- <i>sn</i> -glycero-3-phosphocholine
DNA	deoxyribonucleic acid
DTT	dithiothreitol
EDC	1-ethyl-3-(3-dimethylaminopropyl) carbodiimide hydrochloride
EDTA	ethylenediamine tetraacetic acid
EM	electron microscopy
FC	flow cell
FRET	Förster resonance energy transfer
FSC	Fourier shell correlation
G α_{i1}	α subunit of the heterotrimeric guanine nucleotide binding protein

$G\alpha_s$	α subunit of the heterotrimeric guanine nucleotide binding protein s
GDP	guanosine diphosphate
GPCR	G protein coupled receptor
G protein	guanine nucleotide binding protein
GTP	guanosine triphosphate
GTP γ S	guanosine 5'-O-[gamma-thio]triphosphate, a non-hydrolysable analogue of GTP
GUVs	giant unilamellar vesicles
HEPES	4-(2-hydroxyethyl)-1-piperazineethanesulfonic acid
HJ	Holliday junction
His ₆	hexahistidine tag
His ₆ - $G\alpha_{i1}$	hexa-his-tagged $G\alpha_{i1}$
His ₆ - $G\alpha_{i1}$ *	hexa-his-tagged Nanogold®-labelled $G\alpha_{i1}$
His ₆ - $G\alpha_s$	hexa-his-tagged $G\alpha_s$
His ₁₀	deca-histidine tag
IMAC	immobilised metal ion affinity chromatography
IP ₃	inositol triphosphate
IPTG	isopropyl β -D-1-thiogalactopyranoside

k_a	association constant
k_d	dissociation constant
K_D	affinity constant
K_{eq}	equilibrium constant
K_m	Michaelis constant
k_{ob}	observed rate constant
LB	Luria-Bertani
LaB ₆	lanthanum hexaboride
LDS	laurel dodecyl sulphate
LUVs	large unilamellar vesicles
MBP	<i>E. coli</i> maltose binding protein
MLVs	multilamellar vesicles
MS	mass spectrometry
MSP	membrane scaffold protein
MWCO	molecular weight cut-off
NHS	N- hydroxysuccinimide
NMR	nuclear magnetic resonance

NT	neurotensin, 13-mer peptide ligand for NTS1 (ELYENKPRRPYIL)
NTS1	neurotensin receptor type 1 (post Ni ²⁺ column TEV protease-cleaved NTS1B)
NTS1B	fusion construct of NTS1 (MBP-TEV-T43-NTS1-TEV-Trx-His ₁₀)
OG	n-octyl-β-D-glucoside
OrGr488-NT	Oregon Green 488-labelled NT
PA	phosphatidic acid
PC	phosphatidylcholine
PCR	polymerase chain reaction
PDB	protein data bank
PDEA	2-(2-pyridinyldithio)ethaneamine
PE	phosphatidylethanolamine
PI	phosphatidylinositol
PKC	protein kinase C
POPC	1-palmitoyl-2-oleoyl- <i>sn</i> -glycero-3-phosphocholine
POPE	1-palmitoyl-2-oleoyl- <i>sn</i> -glycero-3-phosphoethanolamine
POPG	1-palmitoyl-2-oleoyl- <i>sn</i> -glycero-3-phospho-(1'- <i>rac</i> -glycerol)
PPPC	POPC:POPG:POPE:cholesterol mixture

PS	phosphatidylserine
PWR	plasmon waveguide resonance
RU	resonance units
SDS-PAGE	sodium dodecyl sulphate polyacrylamide gel electrophoresis
SNR	signal to noise ratio
SPA	single particle analysis
SPR	surface plasmon resonance
SUVs	small unilamellar vesicles
TAE	tris acetate EDTA buffer
TCEP	tris(2-carboxyethyl)phosphine
TEV	tobacco etch virus
T _m	gel to liquid crystalline phase transition temperature
Trx	<i>E. coli</i> thioredoxin

Table of Contents

Abstract.....	2
List of Publications	4
Acknowledgements	6
Abbreviations	12
List of Figures.....	23
List of Tables	28
Chapter 1 - Introduction	29
1.1. Biological membranes	29
1.1.1. Structure/function	30
1.1.2. Model membrane systems.....	35
1.1.2.1. Detergent-based systems	35
1.1.2.2. Planar lipid systems.....	37
1.1.2.3. Liposomes	38
1.1.2.4. Nanodiscs	39
1.2. G protein-coupled receptors.....	41
1.2.1. Receptors.....	41
1.2.2. G proteins.....	44
1.3. Neurotensin receptors	45
1.4. Biophysical methods.....	46
1.4.1. Electron microscopy	46
1.4.2. Surface plasmon resonance.....	51
1.4.2.1. Introduction	51
1.4.2.2. Coupling methods.....	53
1.5. Aims of the thesis.....	57

Chapter 2 - Materials and Methods	59
2.1. Introduction	59
2.2. Recombinant protein expression and purification	59
2.2.1. Neurotensin receptor type 1	60
2.2.2. TEV NIa protease	66
2.2.3. $G\alpha_s$ and $G\alpha_{i1}$	68
2.2.4. Membrane scaffold protein 1D1	71
2.3. Functional assessments	74
2.3.1. NTS1 activity	74
2.3.1.1. 3H -neurotensin binding assay	74
2.3.1.2. Fluorescence-based affinity assay	75
2.3.2. $G\alpha$ subunit activity	77
2.4. DNA lattice formation.....	78
2.4.1. The lattice.....	78
2.4.2. Oligonucleotide-NT conjugation	80
2.4.3. DNA lattice formation	81
2.4.4. Protein arrays	82
2.5. Reconstitution	83
2.5.1. Lipid preparation.....	83
2.5.2. NTS1 reconstitution into liposomes	84
2.5.2.1. Liposome preparation.....	84
2.5.3. Liposome/lipid concentration determination	87
2.5.4. NTS1 reconstitution into nanodiscs	88
2.6. Ternary complex formation	91
2.7. Electron microscopy.....	92
2.7.1. Nanogold® labelling.....	92
2.7.2. Negative stain.....	92

2.7.3. Cryo-electron microscopy.....	93
2.7.4. Data processing.....	94
2.8. Surface plasmon resonance	94
2.8.1.1. Streptavidin coupling and ligand capture.....	94
2.8.1.2. Thiol coupling of NT.....	95
2.8.1.3. pH scouting for G α subunits, anti-His antibody and ovalbumin	96
2.8.1.4. Amine coupling of G proteins, anti-His and ovalbumin	97
2.8.2. On-chip reconstitution	98
2.8.2.1. Detergent:lipid mixtures.....	98
2.8.2.2. On-chip reconstitution.....	99
2.8.3. FLAG-NTS1-nanodisc-G protein coupling	99
2.8.4. Data analysis	101
Chapter 3 - Characterisation of system components.....	104
3.1. Introduction	104
3.2. Protein purification and determination of protein activity	104
3.2.1. Neurotensin receptor type 1	104
3.2.2. TEV protease	113
3.2.3. G α_s and G α_{i1}	115
3.2.4. Membrane scaffold protein 1D1	121
3.3. Ternary complex formation	123
3.4. DNA lattice formation.....	125
3.4.1. Oligo-neurotensin conjugation.....	125
3.4.2. DNA lattice microscopy	125
3.4.3. 2D electron crystallography	128
3.5. Nanodisc formation	130
3.6. SPR chip preparation.....	139
3.7. Conclusion.....	139

Chapter 4 - Protein-protein interactions: Electron microscopy	140
4.1. Introduction	140
4.2. Electron microscopy	141
4.2.1. DNA-protein arrays	141
4.2.2. Single particle reconstructions	143
4.2.3. NTS1-G protein coupling in detergent	148
4.2.4. NTS1-G protein complex in nanodiscs	150
Chapter 5 - Protein-protein interactions: Surface plasmon resonance	156
5.1. Introduction	156
5.2. NTS1-NT coupling in detergent	157
5.3. NTS1-Gα coupling in detergent	158
5.4. NTS1-Gα coupling in a bilayer	164
5.4.1. On-chip bilayer formation and reconstitution	164
5.5. NTS1-NT binding in nanodiscs	174
5.6. NTS1-Gα coupling in nanodiscs	176
Chapter 6 - Discussion	187
6.1. (Cryo-)electron microscopy of small complexes	187
6.2. Nanostructures in structural and functional studies of protein-protein interactions	193
6.3. Conclusion	202
Chapter 7 - Summary and future work	204
7.1. Summary	204
7.2. Future work	206
References	208
Appendix	242

DNA oligonucleotide sequences.....	242
---	------------

List of Figures

Figure 1.1. Gel and liquid crystalline phases of bilayer lipid membranes.....	34
Figure 1.2. Schematic structure of a bicelle.....	37
Figure 1.3. Schematic structure of an LUV.	40
Figure 1.4. Model of a nanodisc with a GPCR reconstituted into it.	41
Figure 1.5. Effect on receptor activity of different ligands.....	43
Figure 1.6. Crystal structure of the β_2 AR-G _s complex.	43
Figure 1.7. GPCR signalling.	45
Figure 1.8. Typical SPR instrument arrangement.....	52
Figure 1.9. Amine and thiol coupling chemistry.	54
Figure 2.1. Structures of fluorescein and Oregon Green 488	76
Figure 2.2. Structure of BODIPY- GTP γ S.	78
Figure 2.3. Schematic of the DNA lattice structure.....	79
Figure 2.4. Reconstitution of NTS1 into liposomes.	86
Figure 2.5. Schematic diagram illustrating nanodisc formation.....	90
Figure 3.1. Scheme showing the steps from purification to demonstration of GPCR-G protein coupling.	105

Figure 3.2. Active receptor yields during purification process.....	106
Figure 3.3. Trial proteolytic cleavage of NTS1B with His ₆ -TEV protease.....	108
Figure 3.4. SDS-PAGE silver stain and Western blot analysis of purified NTS1.....	109
Figure 3.5. SDS-PAGE Coomassie stain and Western blot analysis of FLAG-NTS1 purification.....	110
Figure 3.6. Receptor-ligand affinity assays.	112
Figure 3.7. TEV protease purification.	114
Figure 3.8. G α_{i1} Ni ²⁺ purification.	115
Figure 3.9. G α_{i1} size exclusion purification.	116
Figure 3.10. G α_s purification.	117
Figure 3.11. His ₆ -G α_{i1} and His ₆ -G α_{i1} * purified by gel filtration.	118
Figure 3.12. Pseudo-first order association kinetics of G α_{i1} -BODIPY-GTP γ S binding.	119
Figure 3.13. One-site global analysis of G α_{i1} -BODIPY-GTP γ S binding.....	120
Figure 3.14. Pseudo-first order association kinetics of G α_s -BODIPY-GTP γ S binding.	121
Figure 3.15. H7-MSP1D1 Ni ²⁺ purification.....	122
Figure 3.16. H7-MSP1D1 TEV protease cleavage.....	123

Figure 3.17. Gel filtration analysis of ternary complex formation.	124
Figure 3.18. DNA-NT conjugate gel purification.....	126
Figure 3.19. Transmission electron micrograph of negatively stained, NT- functionalised large lattice.	127
Figure 3.20. Cryo-EM micrographs and crystal structure of 3.5 turn lattice.....	129
Figure 3.21. Cryo-EM micrograph and crystal structure of the 2.5 turn lattice.	130
Figure 3.22. Gel filtration profile of empty BPL nanodiscs.	132
Figure 3.23. Gel filtration profiles of empty and loaded nanodiscs.....	133
Figure 3.24. Negative stain EM images showing nanodiscs prepared with different lipid mixtures.	134
Figure 3.25. SDS-PAGE gels and blots of purification and enrichment of nanodiscs.	137
Figure 3.26. NT column fractions of NTS1 nanodisc purification.	138
Figure 4.1. Cryo-electron micrographs of NTS1 bound to NT-functionalised large lattice.....	142
Figure 4.2. Single particle reconstruction of NTS1.	144
Figure 4.3. Single particle reconstruction of His ₆ -Gα _{i1}	145
Figure 4.4. DNA-templated His ₆ -Gα _{i1}	147
Figure 4.5. His ₆ -Gα Nanogold® labelling.....	148

Figure 4.6. TEM of His ₆ -Gα _{i1} *-coupled NTS1 ligand-bound to a DNA lattice.	149
Figure 4.7. Co-localisation of His ₆ -Gα _s * and nanodiscs.	152
Figure 4.8. Micrograph of MSP-NTS1-Gα _{i1} -PC:PG nanodiscs bound to DNA template.....	155
Figure 5.1. Single-cycle kinetics sensorgrams of NTS1-NT interactions.	159
Figure 5.2. Single-cycle kinetics sensorgram of His ₆ -Gα _{i1} -NTS1 interactions in detergent.....	160
Figure 5.3. Single-cycle kinetics sensorgram of Gα _s -NTS1 interactions in detergent.	161
Figure 5.4. Multi-cycle NTS1-Gα _{i1} capture and binding kinetics.	162
Figure 5.5. Representative sensorgrams for bilayer deposition on L1 chip.....	165
Figure 5.6. SPR traces and binding data produced during DDM-BPL bilayer scouting.	167
Figure 5.7. SCK of His ₆ -Gα _{i1} binding to NTS1 reconstituted on-chip in DDM-BPL.	168
Figure 5.8. SPR traces and binding data produced during CHAPS-BPL bilayer scouting.	169
Figure 5.9. SPR traces and binding data produced during CHAPS-PPPC bilayer scouting.	170

Figure 5.10. On-chip reconstitution of NTS1.	171
Figure 5.11. SCK of His ₆ -Gα _{i1} binding to NTS1 reconstituted on-chip in CHAPS-BPL.	172
Figure 5.12. Capture and inject kinetics of NTS1 proteoliposomes and His ₆ -Gα _s	173
Figure 5.13. MSP-FLAG-NTS1-PC:PG-NT binding kinetics.....	176
Figure 5.14. FLAG-NTS1-nanodisc-G protein coupling with immobilised Gα subunits.	178
Figure 5.15. FLAG-NTS1-nanodisc-G protein coupling with immobilised anti-His antibody.....	181
Figure 5.16. His ₆ -Gα _s coupling to FLAG-NTS1-PC:PG nanodiscs captured on an L1 chip.....	182
Figure 5.17. Control flow cell.....	182
Figure 6.1. Negative stain micrograph of FLAG-NTS1-PC:PG nanodiscs incubated with bioNT and Nanogold®-labelled streptavidin.	191
Figure 6.2. Schematic depiction of a Gα-coupled GPCR in a nanodisc with streptavidin bound.....	192
Figure 6.3. Schematic depiction of NTS1 nanodisc-Gα coupling in an SPR flow cell.	198
Figure 6.4. Comparison of accessible Lys residues in Gα _s and Gα _{i1}	199

List of Tables

Table 1. Raw data showing kinetic parameters obtained for each of 22 different experiments coupling His ₆ -Gα _{i1} or His ₆ -Gα _s to NTS1-PC:PG nanodiscs for which reasonable fits were obtained.	183
Table 2. Averaged kinetic parameters for Gα coupling to FLAG-NTS1-PC:PG nanodiscs.	185

Chapter 1 - Introduction

1.1. Biological membranes

Biological membranes are essential for life; they form specialised, semi-permeable barriers between cells and their environments, and between organellar contents and the cytoplasmic environment. This allows the passage of water and certain solutes while blocking the passage of other solutes. Contrary to early models of biological membranes as simple sac-like structures functioning only to enclose the contents of the cell, biomembranes are composed of hundreds, if not thousands, of different lipid molecules that form a highly complex matrix for the basic functions of respiration, photosynthesis, transport, motility and signal transduction ^(1, 2). A new research field, referred to, analogously with genomics and proteomics, as *lipidomics*, studies the biological significance of the complexity and diversity of lipids coded for by the genome ⁽³⁾. Lipids have diverse functions, including energy storage and signalling in addition to separating cellular compartments from one another. Until recently, these important functions have been overlooked, with membrane proteins being regarded as the functional units within membranes, and the lipids functioning simply as a passive solvent ⁽⁴⁾. New techniques for visualising and analysing membrane components, such as new mass spectrometry (MS) methods and new single molecule spectroscopy and microscopy techniques have allowed the analysis of dynamics within the membrane ⁽⁵⁻⁷⁾. Förster resonance energy transfer (FRET), and single particle tracking methods have revealed dynamic nanoscale domains known as rafts, sphingolipid–cholesterol–protein assemblies that function in signalling ^(8, 9). It is increasingly apparent that the type and structure of specific lipids and their dynamic association

with membrane proteins is critical in the structure and function of membrane proteins themselves. Within the membrane *milieu* exist up to 30 % of the proteins encoded by the genome of a typical organism ^(10, 11). This exciting, liminal, and complex environment is the subject of intense research, not least because of the multiple challenges of its complexity and the wide-ranging, dynamic nature of molecular interactions that it encompasses, but also because of the high concentration of drug targets found in biological membranes, in the form of membrane receptors and channels. Membrane proteins constitute approximately 60 % of drug targets today, while making up only about 2 % of the crystal structures in the protein data bank (PDB) ^(12, 13). Their roles in critical physiological processes such as signalling, ion regulation and energy transduction mean that mutations or malfunctions in these proteins result in chronic and potentially fatal diseases, such as hypertension, cancer, mental illnesses and “channelopathies” like cystic fibrosis ⁽¹⁴⁾. Understanding how membrane proteins exert their roles and functions, and their interactions with the lipid environment within which they function, is essential to understand the basis and therefore the treatment for these diseases.

1.1.1. Structure/function

The defining factor within the cellular environment is its aqueous nature. Without water, life as we know it simply would not exist. The unique physical properties of water and its broad solvent properties for ions and other polar substances allow for a multiplicity of different functional environments within the cell and its compartments. However, the *lack* of solvent power of water for non-polar substances is as important

and unique a property, since without this property, compartmentalisation of the cell and its contents could not exist. This is the hydrophobic effect ⁽¹⁵⁻¹⁷⁾.

Biomembranes are composed mostly of amphipathic molecules made up of a strongly hydrophilic head group attached via a glycerol or ceramide molecule to, usually, two long hydrocarbon chains ^(17, 18). The head groups are phosphate (phospholipids) or carbohydrate (glycolipids) esters. The amphipathic nature of phospholipids and glycolipids gives rise to the common structure of biomembranes in aqueous solution: the bilayer lipid membrane (BLM), whereby the hydrocarbon tails of the phospho- or glycolipids line up to face each other with the polar head groups exposed to the aqueous solution. This structure naturally arises due to the hydrophobic effect. The attraction of water molecules for each other is much stronger than the attraction of water for hydrocarbon molecules or of hydrocarbon molecules for each other, and thus it is thermodynamically favourable for water to exclude hydrocarbon-water contacts ⁽¹⁷⁾.

The major components of mammalian biological membranes, depending on cell type and organism, are phosphatidylcholine (PC - 10-60 %), phosphatidylethanolamine (PE - 20-30 %), phosphatidylserine (PS - ~10 %), sphingomyelin (5-20 %), phosphatidylinositol (PI - 5-10 %), glycolipids (10-25 %), phosphatidic acid (PA - ~1.5 %) and cholesterol (20-30 %) (reviewed in ^(17, 18)). The structures of phospholipids will be the focus of this discussion.

PS, PI and PA are negatively charged at physiological pH. These negative charges act to attract protons to the membrane surface, rendering the pH at the surface of the membrane and extending 5-15 Å out from the surface up to 2 pH units lower than the pH in bulk cytosol ⁽¹⁹⁻²⁶⁾. This fact has important consequences for integral membrane proteins. The distribution of phospholipids across the membrane is asymmetric, with the extracellular leaflet of typical eukaryotic plasma membranes being made up mainly of PC and sphingomyelin, while the intracellular leaflet is composed predominantly of PE and PS ^(27, 28). This distribution is functionally significant, for example, for apoptosis, which is preceded by a translocation of PS to the extracellular leaflet ⁽²⁹⁾.

PC and PS are based on the PE structure. In PC, the nitrogen is triply methylated. In PS, the ethanolamine is carboxylated. Generally speaking, saturated fatty acids are esterified to carbon 1 of the *sn*-glycerol 3-phosphate, and unsaturated fatty acids to carbon 2 ⁽³⁰⁾, although fully saturated and fully unsaturated molecules are not uncommon. Saturated fatty acids usually exist in the *all-trans* conformation, but *gauche* conformations may be introduced with low energetic cost (about 1 kcal/mol⁻¹), resulting in a “kink” in the chain ⁽³⁰⁾. The carbon-carbon double bonds in unsaturated fatty acids are almost all in the *cis* conformation, giving a permanent “kink” to the chain at the double bond. Double bonds are never spaced immediately next to each other, since this would result in a rigid, planar structure forming, and they appear after carbon 8 in the chain ⁽³⁰⁾, meaning that the chains closer to the head groups are more restricted in their movements than those toward the centre of the bilayer. The existence of double bonds and *gauche* conformations in the fatty acyl chains results in gaps and spaces between the chains and decreases the packing efficiency of the

phospholipids. In biological membranes these gaps are often filled by cholesterol, a rigid, planar steroid, an important precursor to vitamin D₃ and the steroid hormones. Cholesterol is marginally amphiphilic by virtue of its single OH group.

The length of the hydrocarbon chains in biological membranes is of the order of 16-22 carbons. This gives an average thickness of the hydrophobic domain of a membrane of about 30 Å, which means about 21 residues in a typical protein helix, non-tilted, would be required to span the hydrophobic portion of the membrane.

The mobility of the hydrocarbon chains is temperature-dependent in single-component lipid dispersions. Below the gel to liquid crystalline phase transition temperature (T_m), bilayers are in an ordered gel phase. Above this temperature, rotational freedom around the carbon bonds of the acyl chains increases and they take on a disordered liquid state (Figure 1.1). In this state, the area of the phospholipid head groups and fatty acid tails increases ⁽³¹⁾. However, liquid ordered states have been observed, for example, in mixtures of PC, cholesterol and sphingomyelin, where preferential association between cholesterol and sphingomyelin causes the formation of liquid ordered states referred to as rafts ⁽³²⁾. As discussed in Section 1.1., membrane proteins are frequently preferentially located in lipid rafts, which aids trafficking and signalling ⁽³³⁾. Non-bilayer phases are also possible in biomembranes. PE, for example, forms hexagonal (tubular) phases, and increasingly popular is the use of lipidic cubic phase for the growth of membrane protein crystals, since they provide nucleation sites for seeding of crystal growth, as well as allowing lateral diffusion of proteins within the three-dimensional matrix, enabling “feeding” of the

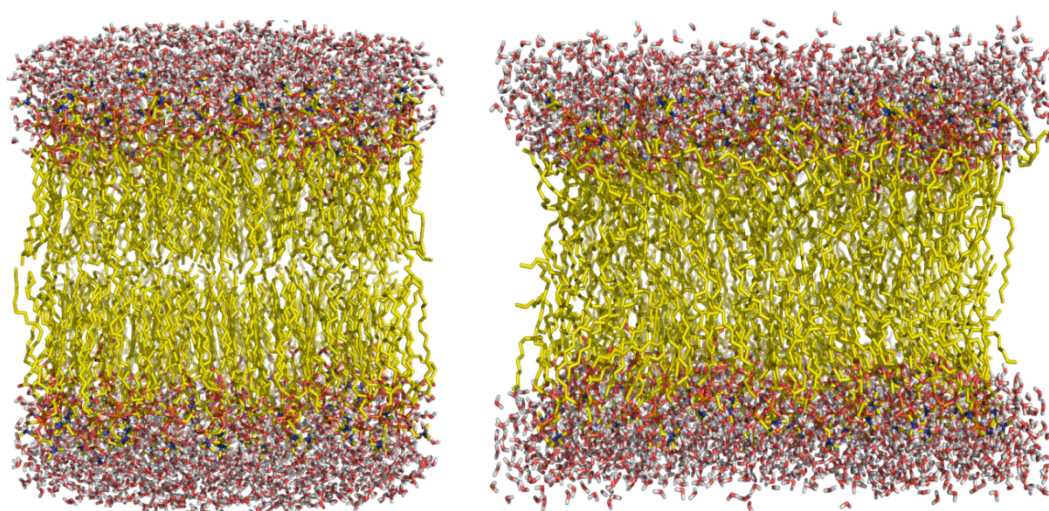


Figure 1.1. Gel and liquid crystalline phases of bilayer lipid membranes.

Ordered gel (left) and disordered liquid crystalline (right) phases of bilayer lipid membranes. In the liquid phase hydrocarbon chains have much greater freedom of movement and are less tightly packed. PDB codes GEL.pdb and FLUID.pdb from ⁽³⁴⁾; visualised using PyMOL™ v. 0.99 (DeLano Scientific, 2006).

nucleation sites ⁽³⁵⁾. Saturated fatty acids have higher phase transition temperatures than unsaturated fatty acids, which are usually in the liquid phase at room temperature. This has implications for the insertion of membrane proteins. If packing is too tight due to the membrane being in the gel phase or too-ordered a liquid ordered phase, proteins will be unable to insert. Thus the proportion of saturated to unsaturated fatty acids within a membrane is very important. It should be noted, though, that in the absence of large temperature fluctuations in physiological systems, changes in the fluidity of membrane structure can and do occur. Gross changes in bilayer structure can be brought about by rather small changes in ionic environment. The presence of divalent cations increases the T_m of negatively charged membranes by charge neutralisation, in accordance with Gouy-Chapman theory, and monovalent

cations lower the T_m ⁽³¹⁾. These are critical features, for example, in nerve excitation and signal transduction, where cation-induced structural changes in biomembranes are essential for function ⁽³¹⁾. The fluidity of BLMs gave rise to the “fluid-mosaic” model of membrane structure ⁽⁴⁾. This model basically depicts membrane proteins as floating in a fluid solvent created by the lipid bilayer. This model is now regarded as an oversimplification, since regions of restricted motion of both proteins and lipids exist in practically all membranes.

1.1.2. Model membrane systems

One of the primary obstacles in the study of membrane proteins is the provision *in vitro* of an appropriate environment to satisfy the complex structural requirements of molecules that normally reside within a fluid *milieu* of amphiphilic lipids. A number of model membrane systems have been developed in order to study the structures and functions of membrane proteins. The major systems in use are micelles, bicelles, planar lipid bilayers, lipid monolayers, liposomes, and more recently, nanodiscs and amphipols.

1.1.2.1. Detergent-based systems

Micelles are small, roughly spherical structures formed from the self-association of detergent monomers above a critical concentration threshold called the critical micellar concentration (cmc) ⁽³⁶⁾. The size and shape of micelles depends on the size, type and stereochemistry of the detergent monomer and the solvent environment ^(37, 38). A number of different detergents can be used for micelle formation, the main

categories of which are: a) ionic detergents; b) non-ionic detergents; and c) zwitterionic detergents ⁽³⁹⁾. Ionic detergents have a head group with either a net cationic or anionic charge attached to a hydrophobic hydrocarbon chain (as in SDS) or steroidal backbone (as in bile acid salts such as sodium cholate). Ionic detergents can be relatively denaturing. Non-ionic detergents such as Triton® X-100 or *n*-dodecyl- β -D-maltoside (DDM) are mild and relatively non-denaturing, although the shorter-chain ones can inactivate membrane proteins ⁽³⁹⁾. They contain uncharged hydrophilic head groups with hydrophobic tails. Zwitterionic detergents such as dodecyltrimethyl-*N*-amineoxide (DDAO) combine the properties of ionic and non-ionic detergents.

The advantage of using micelle-forming detergents as model membrane systems is that the detergents can both solubilise membrane proteins from their lipid environment and then replace that environment to some extent, although loss of activity and lowered half-life are common with membrane proteins stored in detergent solutions. Mixed detergent-lipid micellar systems are also in use for membrane-protein study, and often provide a more stabilising environment than detergent micelles alone (reviewed in ⁽³⁹⁾). Despite their small size and high surface curvature, micelles have been used extensively as biomimetic systems for membrane proteins and peptides, utilising techniques such as high-resolution nuclear magnetic resonance (NMR), Fourier transform infrared spectroscopy and circular dichroism (CD) ⁽⁴⁰⁾.

Bicelles are a form of mixed detergent-lipid micelle, but have a much higher lipid component ⁽⁴¹⁾. Usually short chain lipids such as 1,2-dimyristoyl-*sn*-glycero-3-

phosphocholine (DMPC) are used with detergents such as 1,2-dihexanoyl-*sn*-glycero-3-phosphocholine (DHPC ⁽⁴²⁾) or a zwitterionic bile salt derivative, 3-[(3-cholamidopropyl)dimethylammonio]-2-hydroxyl-1-propanesulfonate (CHAPSO ⁽⁴³⁾). Mixed in empirically determined compositions, the detergent-lipid mixture forms edge-stabilised, bilayered, discoidal structures known as bicelles (Figure 1.2). They are used primarily in NMR studies because of the fact that they can be magnetically aligned ⁽⁴⁴⁾.

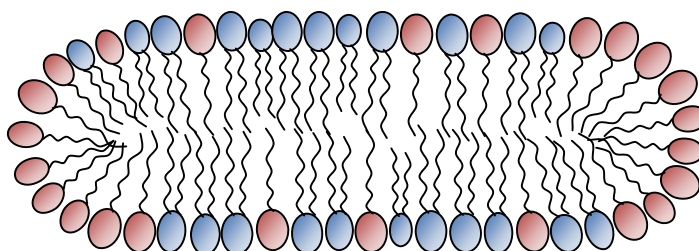


Figure 1.2. Schematic structure of a bicelle.

Cross-section of a bicelle composed of a mixture of phospholipids (blue) and detergent (red). The detergent molecules stabilise the edge of the disc.

1.1.2.2. Planar lipid systems

Planar lipid systems such as bilayers and monolayers aim to model the phospholipid ordering within cellular membranes and to mimic the lateral organisation of cell surfaces ⁽⁴⁵⁾. Phospholipid monolayers deposited at the air-water interface of aqueous solutions (Langmuir monolayers) are used as model membrane systems for studying the interactions of certain peptides and membrane proteins with membranes. Thermodynamic and microscopy techniques such as pressure-area isotherms and fluorescence microscopy can be used to investigate, for example, structural disruption

and phase separation caused by peptides incorporated into the monolayers ⁽⁴⁶⁾. Phospholipid monolayers can also be used in so-called “tip-dip” electrophysiology experiments, whereby a monolayer is spread on the surface of an aqueous bath, and a glass pipette passed repeatedly through the monolayer until the resistance reaches a certain level ^(47, 48). The relevant membrane-insertion-competent protein is then added to the bath and electrophysiological recordings made. The most common use of planar lipid bilayers is as black lipid membranes. These consist of thin lipid films placed across small apertures separating baths containing ionic solutions ⁽⁴⁹⁾. Conductance measurements are then undertaken to study the formation of pores and ion channels in the membrane, their relative permeability and their ion selectivity.

1.1.2.3. Liposomes

Liposomes are bilayer lipid vesicles that enclose an occluded aqueous space separate from the external solution. There are four major classes of liposomes: small unilamellar vesicles (SUVs), large unilamellar vesicles (LUVs), giant unilamellar vesicles (GUVs) and multilamellar vesicles (MLVs). SUVs range in diameter up to about 100 nm, averaging between 30-70 nm, and are generally prepared by sonication of MLVs ⁽⁵⁰⁾. LUVs have hydrodynamic diameters of 100-1000 nm, and can be prepared by a number of methods, including sonication ⁽⁵¹⁾, reverse-phase evaporation ⁽⁵²⁾, extrusion ⁽⁵³⁻⁵⁵⁾ and detergent dialysis ⁽⁵⁶⁾ (Figure 1.3). GUVs can range up to 100 μm , but are generally of the order of up to 10 μm . They are prepared by electroporation ⁽⁵⁷⁾. MLVs consist of multiple concentric bilayers and are formed by hand-shaking of a dried lipid film hydrated with aqueous buffer ⁽⁵¹⁾. The surfaces and properties of liposomes can be modified by the choice of phospholipid, as well as by

the incorporation of proteins such as lectins and glycoproteins, or even synthetic polymers⁽⁵⁸⁾.

A significant amount of research has gone into the formation, structure, properties and applications of liposomes, and a search of the PubMed database at NCBI retrieves 46 203 results of articles with the word “liposome” in their text. This intense interest is driven by the fact that liposomes partially mimic a simple biological cell in that they are a BLM around an enclosed aqueous volume; as such they can be used to study cellular processes such as transport phenomena, and their biological compatibility also means that they are particularly useful as drug delivery systems⁽⁵⁸⁾. Liposomes have been used to deliver chemotherapeutic agents⁽⁵⁹⁾, antiviral drugs⁽⁶⁰⁾, antibacterials⁽⁶¹⁾, and have also been used for gene therapy^(62, 63). They have also been used as cosmetic agents for the delivery of moisturisers or anti-inflammatory agents to the skin⁽⁶⁴⁻⁶⁶⁾. Generally, larger vesicles are preferred for structural and functional studies of membrane-incorporated proteins because of the closer resemblance of the surface curvature of these vesicles to that of biological cells, and because of the larger encapsulated volume inside these vesicles^(67, 68).

1.1.2.4. Nanodiscs

Nanodiscs have in the past few years received much attention within the field of membrane protein research for their distinct advantages over liposomes or planar lipid systems for biophysical studies. A number of different G protein-coupled receptors (GPCRs) have been reconstituted into nanodiscs already, to study the effects of lipids

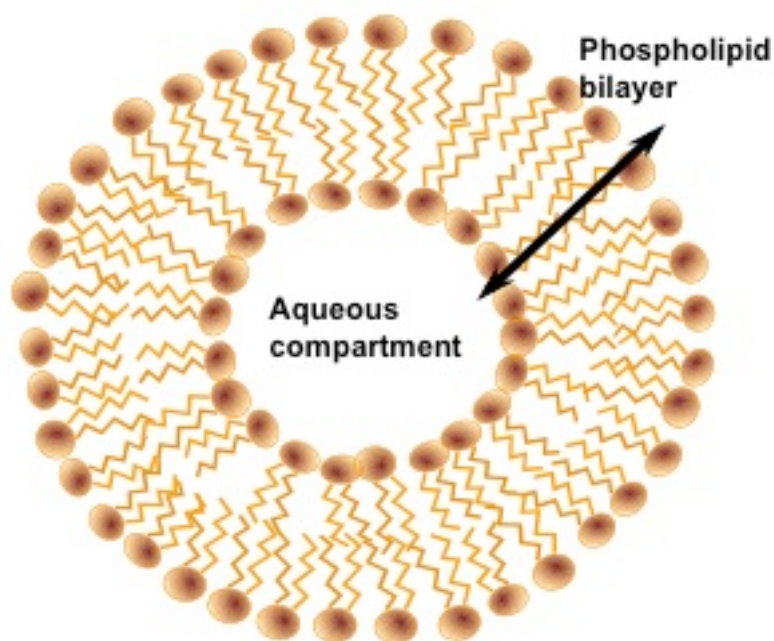


Figure 1.3. Schematic structure of an LUV.

Large unilamellar vesicle showing aqueous compartment enclosed by phospholipid bilayer.

on modulation of function, receptor-dependent G protein activation, ligand activation and dimerisation ⁽⁶⁹⁻⁷⁴⁾. Based on a recombinant construct of Apolipoprotein A-1, a plasma protein responsible for moving cargos of lipid molecules in blood, the so-called membrane scaffold protein (MSP) has been cloned in several variations differing in the length of the polypeptide ⁽⁷⁵⁻⁷⁷⁾. Two MSPs wrap around discs of lipid, within which a membrane protein may be sequestered, to create approximately 10-nm sized soluble lipid particles (Figure 1.4). The target protein is solubilised in detergent, as are the required lipids, mixed with MSP, and Biobeads are added to remove the detergent, at which point nanodiscs spontaneously self-assemble. The discs maintain the target protein in a stable lipid environment, and can be concentrated, dialysed and frozen, as evidenced in a technical report on reconstitution of the β_2 adrenergic

receptor (β_2 AR) into nanodiscs, where the concentration was able to reach the millimolar range ⁽⁶⁹⁾. They can be used in a number of different types of biophysical studies, such as ligand and GTP γ S binding ⁽⁶⁹⁾, in addition to their use in this thesis, as the analytes in a laminar flow protein-protein binding detection system.

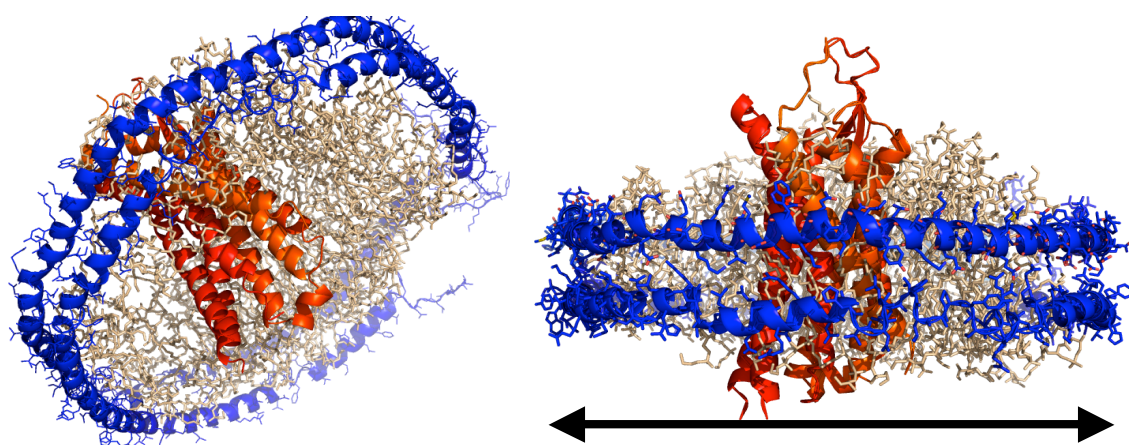


Figure 1.4. Model of a nanodisc with a GPCR reconstituted into it.

The PDB files for the SecYE-ribosome-nanodisc structure, with ribosome and SecYE removed, and the PDB for NTS1 (3J00 and 4GRV, respectively)⁽⁷⁸⁾ were used to create this model of a GPCR reconstituted into a nanodisc. The blue is the membrane scaffold protein, with NTS1 in red. The discs used in this thesis are 10 nm in diameter (arrow).

1.2. G protein-coupled receptors

1.2.1. Receptors

GPCRs comprise the largest superfamily of membrane receptors in the human genome, with over 800 members, and are pharmaceutically significant. Estimates suggest that up to half of all currently available drugs target GPCRs ⁽⁷⁹⁾. GPCRs are responsible for the transmittance of signals from the exterior to the interior of cells via interactions with heterotrimeric guanine nucleotide binding proteins (G proteins) ⁽⁸⁰⁾.

This diverse family of proteins binds a tremendous array of ligands: peptides, biogenic amines, odorants, ions, lipids, nucleotides and photons. They are also relatively diverse in terms of sequence, but all have a core of seven hydrophobic transmembrane (TM) segments, which is one of the main requirements for a protein to be classified as a GPCR ⁽⁸¹⁾. The most recent classification system groups GPCRs into five families: the glutamate (22 members), rhodopsin (672 members), adhesion (33 members), frizzled/taste2 (36 members), and secretin (15 members), thus designating this the GRAFS classification ⁽⁸¹⁾. The high-resolution structures of around 23 unique GPCRs have been resolved, with approximately 70 structures solved in total. Most of these structures have the GPCR bound to antagonists (ligands with 0 % efficacy), inverse agonists (ligands with negative efficacy, or an inverse effect on function) or partial agonists (ligands with only partial efficacy, not reaching 100 %), with only a few bound to agonists (ligands with 100 % efficacy) (Figure 1.5), and so the activated state has not easily been studied. GPCRs are conformationally flexible membrane proteins and as such have resisted several decades of attempts to solve their structures. A breakthrough came in 2000, with the determination of the structure of rhodopsin ⁽⁸²⁾. The next structure was the β_2 -adrenergic receptor (β_2 AR) in 2007 ⁽⁸³⁾, and with the development of methods to stabilise the receptors via alanine scanning to produce thermostabilised mutants, the use of lysozyme and nanobodies to stabilise parts of the structures, such as the loops, and also to create large hydrophilic surface areas for crystal contacts, and with the development of new types of stabilising detergents, a new era of GPCR structure determination has begun ⁽⁸⁴⁻⁹²⁾. Indeed, until just over two years ago, the dream of resolving the structure of a GPCR-G protein complex seemed impossible, yet Brian Kobilka's group succeeded against all odds ⁽⁹³⁾ (Figure 1.6).

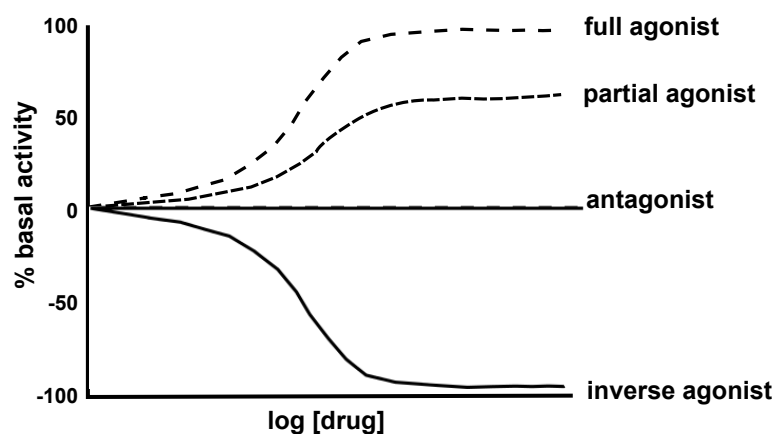


Figure 1.5. Effect on receptor activity of different ligands.

Modelled plot illustrating the effects on receptor activity of agonists, partial agonists, antagonists and inverse agonists.

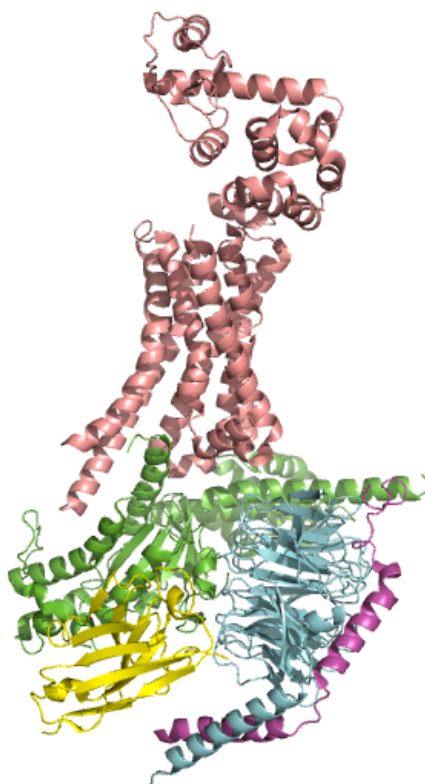


Figure 1.6. Crystal structure of the β_2 AR-G_s complex.

The β_2 AR is shown in pale pink with the T4-lysozyme structure in pale pink above it. G α is shown in green, G β in blue, G γ in pink and the stabilising nanobody in yellow. The α -helical domain of the G α is swung 127° round with respect to the GTPase domain in the receptor-bound structure. (PDB 3SN6).

All of the structures so far bear the same canonical seven-transmembrane (7TM) α -helical structure. Their differences lie in the ligand-binding pockets and in the loops. The loops are not resolved in many of the structures, due to their flexibility.

1.2.2. G proteins

Guanine nucleotide binding proteins (G proteins) are a family of heterotrimeric proteins that interact with GPCRs, regulatory proteins and cellular effector proteins to transduce messages from the outside of a cell to the interior and to the nucleus in order to effect cellular response to a stimulation mediated by GPCRs in the cell membrane. There are 21 $G\alpha$, 6 $G\beta$ and 12 $G\gamma$ members. They are GTPases, which catalyse the hydrolysis of guanine triphosphate (GTP) to guanine diphosphate (GDP) upon activation by a GPCR. G proteins signal through second messengers such as inositol triphosphate (IP_3), Ca^{2+} , diacylglycerol (DAG) and cyclic adenosine monophosphate (cAMP) (Figure 1.7). G_s proteins are stimulatory, G_i proteins are inhibitory. The G protein α subunit consists of two domains: a GTPase domain and an α -helical domain, with three switch regions that are either rigid (GTP) or collapsed (GDP) when the nucleotide is bound. $G\alpha$ binds to a cleft that opens in the GPCR upon activation via its C-terminal α -helix ($\alpha 5$), and the α -helical domain swings around 127° relative to the GTPase domain, as seen in Figure 1.6.

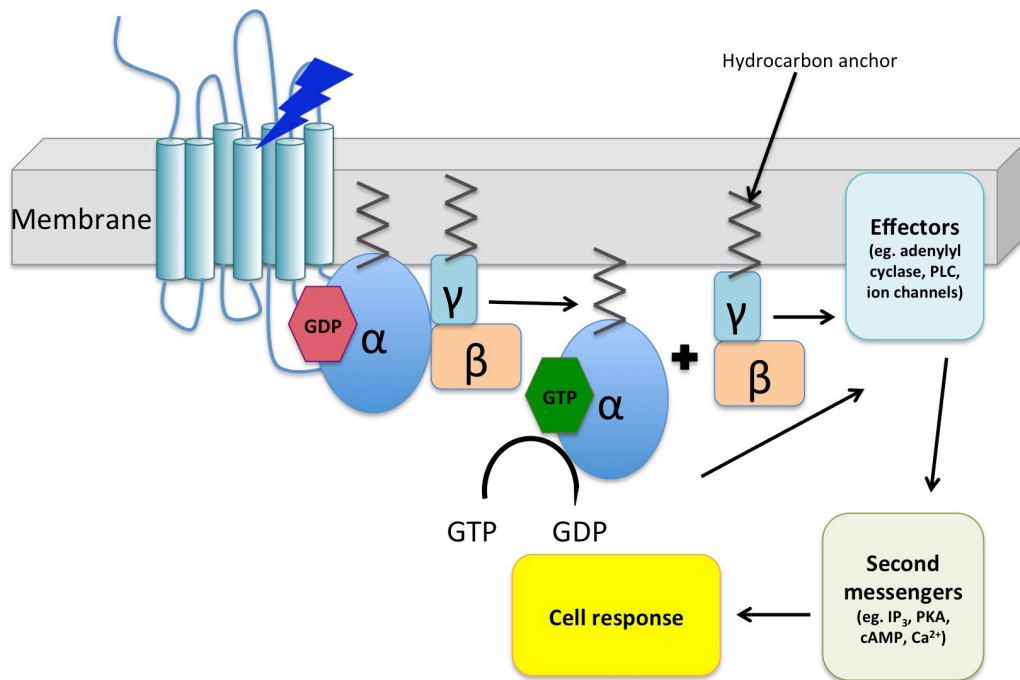


Figure 1.7. GPCR signalling.

A GPCR (light blue) binds its ligand (blue lightning), which activates the receptor. The receptor undergoes a conformational change that allows it to bind heterotrimeric G proteins (labelled α , β and γ), whose α and γ subunits are anchored to the lipid bilayer by palmitate or myristate. $G\alpha$ binds GTP, causing dissociation from $G\beta\gamma$. $G\alpha$ and $G\beta\gamma$ bind effector proteins such as adenylyl cyclase and phospholipase C (PLC), which signal via second messengers such as protein kinase A (PKA), cyclic AMP or inositol triphosphate (IP_3), ultimately to cause cellular response.

1.3. Neurotensin receptors

Neurotensin receptor type 1 (NTS1) is one of three neurotensin receptors, designated NTS1, NTS2 and NTS3. The first two are GPCRs and bind neurotensin (NT), a 13 amino acid peptide (ELYENKPRRPYIL) that acts as a neurotransmitter in the brain and as a local hormone in peripheral organs, with high affinity ($K_D \sim 1$ nM)⁽⁹⁴⁾. NTS3/sortilin is structurally dissimilar and mediates lipoprotein lipase degradation⁽⁹⁵⁾. NTS1 mediates the effects of analgesia, dopaminergic modulation, appetite

regulation, digestive function regulation, and acts as a growth factor on cells. NT induces a conformational change that enables the α subunit of a G protein to bind the receptor, initiating a cascade of signalling events within the cell via various effectors ^(80, 94). Coupling to $G\alpha_{i1}$, for example, inhibits adenylate cyclase activity, leading to decreased levels of cyclic-3',5'-adenosine monophosphate (cAMP) in the cell, which decreases protein kinase A activity ^(96, 97). The receptor is implicated in diseases involving schizophrenia, psychosis, drug addiction, colon and breast cancer, and Parkinson's disease (reviewed in ^(94, 98)). The receptor binds to G_i and G_s at its C-terminal domain and to G_q at its third intracellular loop ⁽⁹⁹⁾. Few studies of the interactions of NTS1 with G proteins have been reported, and the crystal structure was only recently solved after two decades of work ⁽¹⁰⁰⁾. Studies on the structure and function of NTS1, and the mechanism by which it signals, are crucial to elucidate the molecular basis of the diseases in which it is implicated.

1.4. Biophysical methods

1.4.1. Electron microscopy

Electron microscopy (EM) and cryogenic EM (cryo-EM) are fast becoming prime methods of choice for the determination of sub-nanometer resolution structures of large complexes, viruses and cellular machinery. Cryo-EM has, however, recently experienced an upsurge in interest in determining the structures of smaller proteins and complexes, due to advancement of instrument sensitivity and quality, and in the sophistication of software used for processing data collected under low-dose ($\sim 20 \text{ e}^-/\text{\AA}^2$), high resolution conditions ⁽¹⁰¹⁻¹¹⁰⁾. The high-resolution structural

investigation of large macromolecular complexes such as transcription machinery and ribosomes, as well as large structures such as viruses has been hindered by the fact that these complexes seldom can be purified as complexes, and even if purification is successful, they will not crystallise, eliminating X-ray crystallography as a tool. EM has, however, suffered from low resolution, not because EM is inherently unable to record high-resolution information, given that the theoretical resolution of EM is less than atomic bond length, but because of the fact that biological molecules are highly radiation-sensitive ⁽¹¹¹⁻¹¹³⁾. Without the protective shield of multiplication of molecules that 3D crystals offer, biological samples in the high vacuum and accelerated voltage beam of the EM simply explode without negative staining with heavy metals or cryogenic preservation by vitrification. Vitrification preserves the sample in a native, frozen-hydrated state, but the low-dose conditions ($20 \text{ e}^-/\text{\AA}^2$) decrease the contrast significantly, in samples that inherently do not have much density difference to ice. Preparing homogeneous samples can also be problematic, and EM structures suffer from blurring of resolution due to heterogeneity of conformations. Lens defects within the EM, such as chromatic and spherical aberration and astigmatism have in large part been greatly improved by advancements in instrumentation, and detectors currently becoming the norm are direct electron detectors with motion-correcting software that correct for beam-induced motion in the sample. With these improvements, EM is becoming a tool that can potentially be used to solve the structures of smaller complexes and asymmetric molecules that are resistant to crystallisation. These include membrane proteins and membrane protein complexes. Smaller structures have not been able to be aligned due to low signal to noise ratios (SNR), but with better detectors smaller and smaller structures of

membrane proteins in their native states, without mutations and fusions, are likely to be solved.

The practical resolution limit for biological cryo-electron microscopy derives from the limitations of the sample more than any instrument-based limitation. A new crop of highly sophisticated spherical- and chromatic-aberration-corrected EMs with Zernike phase plates, electron-counting direct detectors and the ability to correct for beam-induced motion mean that the limit for large, macromolecular complexes on the order of one megadalton, with high symmetry has been brought close to atomic resolution ⁽¹¹⁴⁻¹¹⁷⁾, and sub-nanometer resolution is achievable for smaller complexes and asymmetric molecules ⁽¹¹⁸⁻¹²⁰⁾. Until very recently, it was generally acknowledged that reconstructions of proteins smaller than about 200 kDa would not achieve resolutions higher than 20 Å, and that it was not possible to study proteins smaller than 100 kDa. This is because of the primary source of resolution limitation encountered in the electron microscope under cryogenic conditions: radiation damage. Richard Henderson stated almost 20 years ago that the structures of particles smaller than 100 kDa should be able to be determined to atomic resolution, given that the electron wavelength is smaller than the atomic bond length, and phase and amplitude information is present in electron micrographs ⁽¹¹¹⁾. However, the low electron-dose conditions required to prevent radiation damage to friable biological samples maintained in a frozen hydrated state under the beam result in low contrast, thus low signal to noise (SNR) and low resolution. The smaller the particle, the lower the density difference in relation to their surround, and thus the lower the SNR; this is compounded by the fact that smaller particles have fewer recognisable structural

features such that even if they can be imaged, determining their orientation parameters (three Euler angles and 2 in-plane shifts) in order to align them may prove impossible. With technical improvements to microscopes and detectors, obtaining sub-nanometer resolution structures of large and/or symmetric particles or complexes has become more routine. It is highly desirable to solve the structures of smaller complexes (100-500 kDa) or flexible proteins that cannot be crystallised, which are more likely to be membrane protein complexes or complexes involved in critical cell functions, but their size or hydrophobic nature means they do not readily lend themselves to crystal structure determination. Researchers in cryo-EM are taking up the challenge of smaller as well as small asymmetric complexes, many of which are membrane proteins playing critical roles in communication between the exterior and interior of cells ^(108, 121, 122).

There are several routes to improving the sample itself that can be explored to address some of the problems associated with imaging and processing data from small molecules in order to improve resolution. The first, and which has been elegantly addressed by the group of Yifan Cheng, is to make the molecule bigger ⁽¹²³⁾. As a means of increasing the size of the target protein, and at the same time incorporate a fiducial marker into the molecule, Wu and co-workers developed monoclonal fragments antigen binding (Fabs), 50-kDa antibody fragments composed of one constant and one variable domain from the heavy and light chains, against HIV-1 integrase (64 kDa dimer) and human proprotein convertase subtilisin/kexin type 9 (PCSK9) (70 kDa), as well as two membrane proteins, an *E. coli* homologue of the mammalian vesicular glutamate transporter (EcoliVGLUT3) (50 kDa) and an ATP

binding cassette (ABC) transporter (130 kDa). The Fabs form rigid and stable complexes with their target proteins. This prevents heterogeneity in the complex, and provides a marker of known size and shape for projection alignment. In this way, and using a small aperture to increase contrast, and with a direct detector camera, the group was able to solve the structure of the HIV-1 integrase to close to nanometer resolution. Sample heterogeneity is, in fact, another of the sample-related barriers to higher resolution in cryo-EM. Heterogeneity averaged over thousands of particles blurs the resolution.

In this thesis, self-assembling functionalised DNA lattices were used to create protein arrays for analysis by transmission electron microscopy (TEM). The use of this lattice offers a number of advantages for data collection and processing over standard cryo-EM. Functionalising the lattices with groups via which proteins may be tethered, such as tris-NTA or the NTS1 peptide ligand, NT, causes thousands of protein particles (~10 000 per micrograph) to be confined in well-ordered arrays within each field of view, allowing much greater numbers of particles to be picked and boxed during image processing than if samples were simply pipetted onto the EM grid. However, there is no aggregation because each particle has its own tether, spatially separate from others. Normally, hundreds if not thousands of images have to be recorded to obtain enough particles for processing. The functional groups are on relatively long linkers, thus allowing the particles to sample orientational space broadly, ensuring that Fourier space is fully sampled for complete reconstruction of the molecule density. The particles are also confined to the plane of the lattice, which greatly reduces variations in defocus arising from particles being scattered throughout the

volume formed by ~50-nm thick ice. For particles that are tethered to the lattice via their ligand, conformational heterogeneity is eliminated, since they are all in the active conformation. Since single particle reconstructions derive from an averaging of all the particles imaged and processed, heterogeneity decreases accuracy of alignment and resolution, and is one of the current stumbling blocks to achieving higher resolution with cryo-EM single particle analysis (SPA) ^(103, 124, 125). For these reasons it has been proposed that the use of these lattices may enable the solution of structures of much smaller, asymmetric particles, at higher resolution, than has previously been possible (Daniele N. Selmi, DPhil thesis, University of Oxford, 2010).

1.4.2. Surface plasmon resonance

1.4.2.1. Introduction

Surface plasmon resonance (SPR) is a biophysical method that measures the association and dissociation kinetics and binding affinities of a binding pair through the use of a laminar flow system within a microfluidic flow cell coated with one of a pair of binding partners, while the other is injected through the cell in solution. SPR is based on the principle that, under conditions of total internal reflection, a surface plasma wave will be propagated at the interface of a metal and a dielectric medium ⁽¹²⁶⁾: a glass prism covered with a thin gold film (high refractive index) and the aqueous medium in the flow cell (low refractive index). Any perturbation of the wave by changes in mass or refractive index at the surface will result in an optical signal corresponding to the angular dependence of the reflectance of totally internally reflected light (Figure 1.8) ^(126, 127). This enables the real-time, label-free kinetics of an interaction to be measured. Dips in the intensity of the reflectance are output as

changes in response units (RU) in the form of a sensorgram. The system is exquisitely sensitive, and thus even very small changes in refractive index due to buffer composition, the presence of protein, or temperature changes generate a signal, although these can usually be corrected for by using a reference flow cell ⁽¹²⁸⁾.

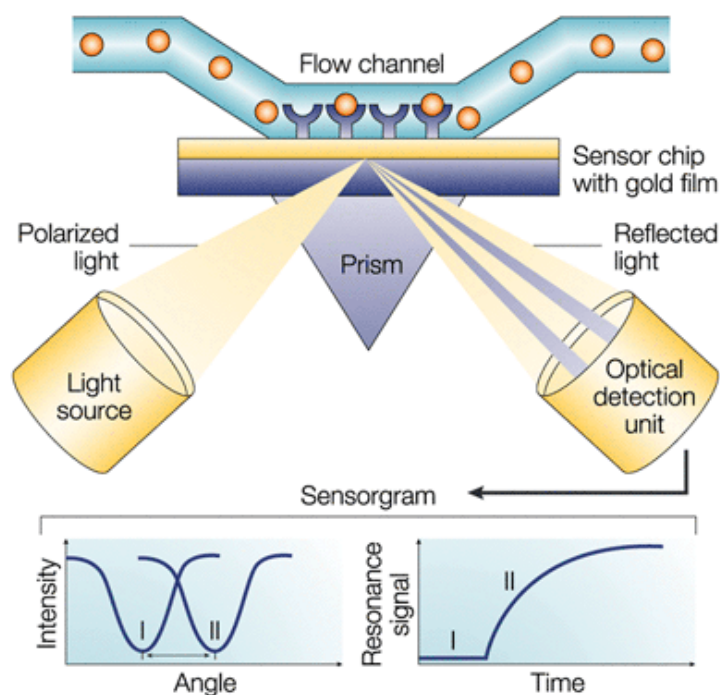


Figure 1.8. Typical SPR instrument arrangement.

A change in refractive index at the surface or close to the surface of the sensor chip is detected by the instrument as a change in the angle of the reflected light. The change in angle (shift from I to II) is dependent upon the mass of molecules bound to the surface, and is monitored as resonance signal versus time. Image from ⁽¹²⁹⁾.

In practice one binding partner (the analyte) is injected through the flow cell (20-60 nl) to the floor of which the second binding partner (the ligand) has been immobilised. Specialised sensor surfaces in the form of chips have been developed which are coated with a 200-300 nm layer of carboxymethylated (CM) dextran, and this increases the available volume to which a ligand can be immobilised. The surface can be activated and covalently modified using a variety of different chemistries. The most commonly used chemistries are amine-coupling and thiol-coupling, although hydrophobic capture, where lipids or other hydrophobic ligands are captured on a CM surface that additionally has alkyl chains attached to it, is increasingly popular with the growing interest in using SPR for the study of membrane proteins. Pre-prepared chips functionally modified with Ni-NTA, monolayers or streptavidin are also available.

1.4.2.2. Coupling methods

There are various means by which ligands can be coupled to the surfaces of sensor chips, the most common of which, and which were used in this thesis, are amine and thiol coupling (Figure 1.9). Hydrophobic capture is also used frequently with chips modified to contain hydrophobic groups on their surfaces, and was used for nanodisc, liposome and lipid capture in this thesis. Amine coupling is relatively non-specific. Carboxyl groups on the chip surface are activated using a 1:1 mixture of N-hydroxysuccinimide (NHS) and 1-ethyl-3-(3-dimethylaminopropyl) carbodiimide hydrochloride (EDC). This forms reactive succinimide esters, which spontaneously react with primary amine groups or other nucleophilic groups on the ligand when it is passed over the surface and covalently link it to the dextran. The ligand is diluted in

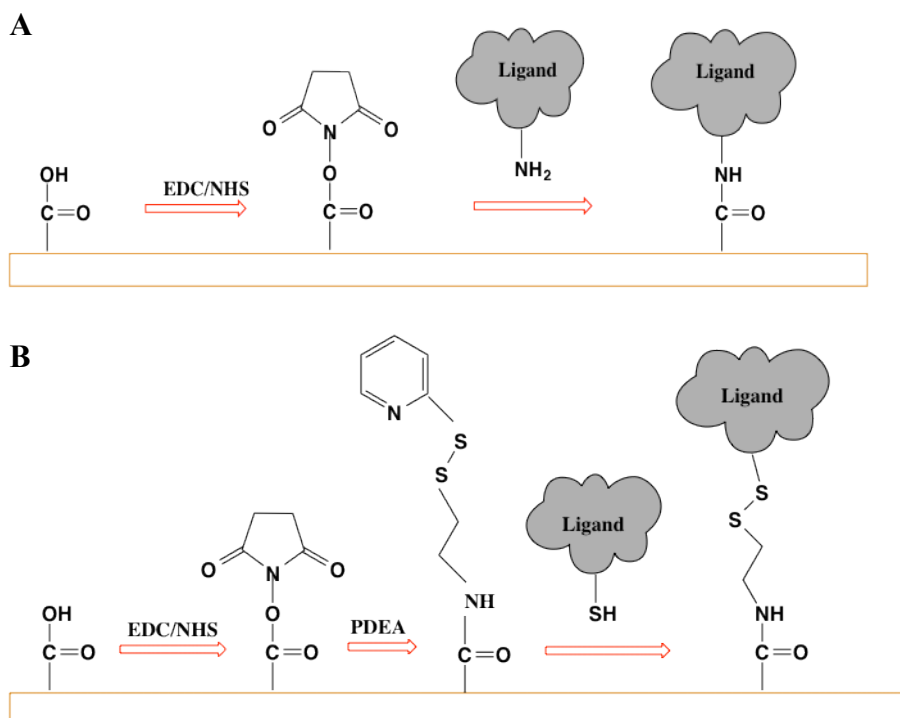


Figure 1.9. Amine and thiol coupling chemistry.

Cartoons showing amine coupling (**A**) and thiol coupling (**B**) chemistry. In both cases the carboxylated sensor chip surface is activated with 1:1 mixtures of NHS/EDC to form succinimide esters. In the case of amine coupling, primary amines or other nucleophilic groups on the ligand react spontaneously with the esters to covalently link it to the dextran. In the case of thiol coupling, reactive disulphides are introduced to the surface by substitution of the carboxyl groups with PDEA, which reacts with thiol groups on the ligand to immobilise it to the chip. Images modified from Biacore Sensor Surfaces Handbook, prepared using ChemBioDraw 13.

the lowest pH buffer possible that does not denature it, in order to ensure the most efficient pre-concentration at the surface. This is usually approximately 1-2 pH units below its isoelectric point if it is a protein ligand and is determined empirically. The efficiency of pre-concentration, the amount of time ligand is injected over the surface and the concentration of the ligand determine how much will be immobilised on the surface. Ethanolamine is injected after ligand immobilisation to block the remainder of the reactive sites. Because of its low specificity, amine coupling can result in

heterogeneous binding because of the occlusion of some binding sites. Thiol coupling is more specific and ligand can be coupled in a defined orientation due to there being fewer potential reactive sites. The surface is activated with EDC/NHS and reactive disulphide groups are introduced by substituting carboxyl groups with 2-(2-pyridinyldithio)ethaneamine (PDEA). The ligand is immobilized via its thiol groups by thiol-disulphide exchange, and remaining reactive groups are blocked with ethanolamine. On-chip reconstitution using mixed lipid-detergent micelles, or liposome or nanodisc capture can readily be achieved by hydrophobic adsorption to the hydrophobic L1 or HPA sensor chips (GE Healthcare). The sample is simply injected over the surface for 10-20 minutes at a slow flow rate (2-5 $\mu\text{l}/\text{min}$) and then washed until the baseline stabilises. Modified lipids containing biotin or thiol groups are also relatively easily captured on standard CM5 chips using amine-coupled streptavidin for capture or thiol-coupling.

The applicability of SPR to biological systems is limited only by the imagination of the researcher. While the size of analytes used to be a limiting factor in the study of small molecules, new instruments, which are more sensitive and can detect binding events on the order of a few RU, are now available. The sensitivity of the instruments means that care must be taken to avoid collecting artefactual data that looks “real”. A reference flow cell is always used to subtract the effects of differences in refractive index between the running buffer and the sample buffer. Dialysis is the preferred method of preparing samples for SPR. The CM dextran surface responds to changes in pH, temperature or even ionic concentration by swelling or shrinking, altering the volume of the flow cell and changing the response detected. An unmodified or simply

activated and blocked reference flow cell could be the source of artefactual results for this reason, and thus it is generally recommended to immobilise to the surface of the reference flow cell an unresponsive, non-binding molecule of approximately the same size as the ligand being used in the sample cell. An unmodified CM surface is also electrostatically active, and will non-specifically bind positively charged proteins, causing noise in the response. An additional factor to be aware of is the phenomenon of mass transport⁽¹³⁰⁾. The diffusion-controlled movement of ligand to the surface of the flow cell may not be able to keep up with the binding events happening right at the surface of the flow cell if a high level of ligand has been immobilised. Diffusion to the surface then becomes the rate-limiting step, and the association rate measured will not be a true reflection of the actual rate. An addendum to this is that with a high level of ligand binding the potential for re-binding after dissociation is increased, such that the measured off rate will not be a true reflection of the actual dissociation rate. This is a caveat to not immobilise more ligand than will result in an R_{\max} , or maximal response, or more than 100 RU. The final factor to be aware of is the temptation to “model-surf”. The standard model to which most biological data fits is the 1:1 model. Additional models are provided in the evaluation software of the instrument, which, as they increase in complexity, add more parameters to their algorithms, thus making a better and better fit, which may not be biologically relevant to the system under study at all.

SPR has been used to study the interactions between proteins and membranes as well as membrane proteins and proteins or ligands in bilayers or detergent⁽¹³¹⁻¹⁴⁰⁾. Some SPR studies on GPCRs, including NTS1, have elucidated the kinetic parameters of the

interactions between the receptors and their ligands, or have demonstrated that GPCRs can be reconstituted or captured in membranes on SPR chips ^(136, 141-158). The only studies available that investigate directly the interactions of GPCRs with G proteins in a lipid bilayer using a biosensor are those done by Alves *et al.* using plasmon waveguide resonance (PWR), a variant of SPR, to study interactions between the δ -opioid receptor and G proteins, either $G\alpha$ subunits or $G\alpha\beta\gamma$, and the influence of ligands on the interactions ^(127, 159-161). The affinity constants ranged from 10-500 nM depending on the G protein used, the type of ligand (agonist/antagonist), or even the presence of ligand ^(127, 160).

The work presented in this thesis is the first time a study of GPCR-G protein coupling in nanodiscs has been demonstrated using SPR. Additionally, the work presents for the first time EM evidence of GPCR-G protein coupling using gold-labelled $G\alpha$ proteins.

1.5. Aims of the thesis

The aim of this study was to investigate the interactions of NTS1 with G proteins to obtain structural and kinetic information about this important first intracellular step in the GPCR-G protein signalling cascade.

The means by which this was to be accomplished were:

- to demonstrate NTS1-NT binding and NTS1-G α coupling by electron microscopy (EM) using a novel self-assembling DNA lattice;
- to demonstrate NTS1-NT binding and NTS1-G α coupling using surface plasmon resonance (SPR) ; and
- to demonstrate reconstitution of active NTS1 into nanodiscs and functional G α coupling using negative stain EM and SPR

By these means, further knowledge and understanding of GPCR structure and function should be generated.

Chapter 2 - Materials and Methods

2.1. Introduction

This chapter deals with the preparation and characterisation of all of the protein and lipid components of the experimental work undertaken in the thesis, as well as the methods used to apply the purified and characterised components within structure- and function-based experiments. The expression and purification of all the proteins used is described, and the assays used to assess their activity. The formation of liposomes, nanodiscs and the DNA lattice is described, along with reconstitution of NTS1, G protein coupling experiments and EM experiments.

2.2. Recombinant protein expression and purification

Gel analysis of purification stages was performed at 200 V for ~40 min using 12 % NuPAGE® Bis-Tris precast gels (Invitrogen) with SeeBlue Plus2 Prestained Standard markers (Invitrogen) or Novex® Sharp Unstained Protein Standard (Life Technologies™). NuPAGE® MES SDS Running Buffer (Invitrogen) was used for electrophoresis. PageBlue Protein Staining Solution (Thermo Scientific), based on Coomassie Brilliant Blue G-250, was used for staining gels. For Western blots, gels were electrophoresed for one hr at 100 mA using a BioRad Trans-Blot® SD semi-dry transfer cell and nitrocellulose membranes pre-wetted in methanol-containing transfer buffer. A chromogenic anti-mouse Novex® Western Breeze™ Immunodetection Kit was used for detection (Invitrogen). Anti-MBP (1:7000), anti-His (1:3000), anti-FLAG M2 (1:10 000) (Sigma-Aldrich) or anti-NTR1 (1:200) (R-20; #sc-7598; Santa

Cruz Biotechnology) antibodies were used for Western blots. An alkaline phosphatase-conjugated mouse anti-goat antibody (#sc-2355; Santa Cruz Biotechnology) was used as the secondary antibody for anti-NTR1. Silver Plus (BioRad) silver stain kit was used for silver stained gels. Protein purification systems used were either an ÄKTA basic UPC 900 with P-900 pump or an ÄKTA Pure (GE Healthcare), both maintained in a cold cabinet at 4 °C. Purified water (18.2 MΩ) was used in the preparation of all buffers and media and for rinsing glassware and gels. Data were fitted using Prism 5 (GraphPad), apart from surface plasmon resonance data, which were fitted using BiaEvaluation T100 or T200 software (GE Healthcare).

2.2.1. Neurotensin receptor type 1

The NTS1B fusion construct has been described previously ^(162, 163). The construct consists of an N-terminal *E. coli* maltose binding protein (MBP) with periplasmic targeting sequence, followed by a short linker (GSNNNNNNNNNN), after which a tobacco etch virus (TEV) NIa protease cleavage site (ENLYFQS, with cleavage after Q) has been inserted. The 1-42 residue N-terminally truncated rat NTS1 sequence (T43NTS1) is inserted between the latter site and another TEV protease cleavage site, followed by the sequence for *E. coli* thioredoxin, and a C-terminal deca-histidine tag (MBP-TEV-T43NTS1-TEV-Trx-His₁₀). FLAG-NTS1B contains the coding sequence for the FLAG peptide (DYKDDDDK) between the first TEV cleavage site and T43 NTS1 (MBP-TEV-FLAG-T43NTS1-TEV-Trx-His₁₀). The tag sequence (5' GATT ATAAAGATGATGATGATAAA 3') was inserted using QuikChange II Site-Directed Mutagenesis Kit (Stratagene) with the following primers: 5'

GTACTTCCAGTCTGATTATAAAGATGATGATGATAAAGGATCCACCTCGG
 3' (forward primer) and CCGAGGTGGATCCTTTATCATCATCATCTTT-
 ATAATCAGACTGGAAGTAC (reverse primer) where blue indicates the FLAG
 sequence. A fusion construct of NTS1-G α_{i1} (the α subunit of guanine nucleotide
 binding protein i1) was provided by Reinhard Grisshammer (National Institutes of
 Health, USA) in the form of MBP-T43NTS1-G α_{i1} . A TEV cleavage site between
 MBP and NTS1 and a hexa-His-tag after the signal peptide sequence on MBP were
 added by Alan Goddard (Lincoln University, UK) to form H6-MBP-TEV-T43NTS1-
 G α_{i1} , hereafter termed NTS1-G α_{i1} . Competent DH5 α^{TM} cells (Calbiochem) were
 transformed with the polymerase chain reaction (PCR) products with a 75 second heat
 shock, one hr outgrowth, and overnight growth at 37 °C on sterile Luria-Bertani-agar
 (LB-agar) plates containing 100 $\mu\text{g/ml}$ ampicillin. Cultures for small-scale DNA
 purification (5 ml) were grown overnight from single colonies in sterile LB medium
 (1 g tryptone, 0.5 g yeast extract, 1 g NaCl per 100 ml H₂O) containing 100 $\mu\text{g/ml}$
 ampicillin. Plasmid DNA was purified from cultures using QIAprep Spin Miniprep
 Kit (Qiagen), based on the alkaline lysis method of DNA purification ^(164, 165).
 Competent BL21(DE3) cells (Calbiochem) were transformed with 100-500 ng
 NTS1B, FLAG-NTS1B or NTS1-G α_{i1} plasmid DNA with a 75 s heat shock, one hr
 outgrowth, and overnight growth at 37 °C on sterile Luria-Bertani-agar (LB-agar)
 plates containing 100 $\mu\text{g/ml}$ ampicillin.

Single BL21(DE3) colonies harbouring the relevant plasmids were used to inoculate
 5 ml aliquots of sterile LB medium containing 100 $\mu\text{g/ml}$ ampicillin. Cultures were

grown overnight at 37 °C with shaking at 200 rpm. Overnight cultures were used to inoculate sterile 2xYT medium (16 g tryptone, 10 g yeast extract and 5 g NaCl per litre) in 10 L batches made up of 500 ml aliquots containing 100 µg/ml ampicillin and 0.2 % (w/v) glucose. These large-scale cultures were grown for approximately 2 hrs (37 °C; 200 rpm) until the OD₆₀₀ reached ~0.3, whereupon the temperature was reduced to 26 °C for a further 1-2 hrs until the OD₆₀₀ reached ~0.6. NTS1B (101 kDa), FLAG-NTS1B (102 kDa) or NTS1-Gα_{i1} (130 kDa) was expressed with 0.25 mM IPTG induction for up to 16 hrs. Cells were harvested for 10 minutes in a Beckman Coulter™ Avanti J-25I centrifuge using a JLA 9.1 rotor (8000 g, 4 °C), snap frozen in liquid nitrogen and stored at -80 °C for up to 2 months.

Frozen cell pellets (~80 g) were crushed and then thawed in 160 ml 2x solubilisation buffer (100 mM Tris-HCl pH 7.4, 60 % (v/v) glycerol, 400 mM NaCl) at 4 °C while stirring, as described ⁽¹⁶⁶⁾. A hand blender was used to homogenise the thawed pellet. Protease inhibitors were added as follows: leupeptin and pepstatin A to a final concentration of 2 µg/ml, and aprotinin to 3 µg/ml. Hen egg white lysozyme (Sigma-Aldrich) was added to 1 mg/ml, and 1 mg deoxyribonuclease I (DNase) from bovine pancreas (Sigma-Aldrich) per 20 g pellet. MgCl₂ was added to a final concentration of 5 mM. The mixture was left to stir for approximately 30 min. Cell lysis and solubilisation of membrane components was effected by addition of the detergents dodecyl-β-D-maltoside (DDM; Melford), 3-[(3-cholamidopropyl) dimethylammonio]-1-propanesulfonate (CHAPS; Melford) and cholesteryl hemisuccinate (CHS; Sigma-Aldrich) to final concentrations of 1%, 0.5% and 0.1% (w/v),

respectively, and the final volume topped up to 320 ml with chilled water, for a further 4-6 hrs. Unsolubilised material was pelleted for 75 min (65000 g; 4 °C) in a JA 25.5 rotor using a Beckman Coulter™ Avanti J-25I centrifuge. The supernatant was filtered through a 0.45 µm syringe filter and either used for purification immediately or snap frozen in liquid nitrogen and stored at -80 °C for up to 2 weeks.

Based on the protocol in ⁽¹⁶⁷⁾, NTS1B was purified by immobilised metal ion affinity chromatography (IMAC) at 4 °C using a HisTrap HP column (GE Healthcare) and by affinity chromatography (AC) using biotinylated neurotensin (NT) immobilized on Tetralink™ tetrameric avidin resin (Promega). Solubilised cell supernatant was brought to 50 mM imidazole using 2 M stock at pH 7.4, and fresh protease inhibitors (leupeptin and pepstatin A: 2 µg/ml, and aprotinin: 3 µg/ml) were added. The sample was loaded onto a 5 ml HisTrap column equilibrated in NiA buffer (50 mM Tris-HCl pH 7.4, 15 % (v/v) glycerol, 200 mM NaCl, 0.5 % (w/v) CHAPS, 0.1 % (w/v) DDM, 0.1 % (w/v) CHS, 50 mM imidazole, 2 µg/ml leupeptin and pepstatin A, and 3 µg/ml aprotinin) at 3 ml/min. The column was washed with 150-200 ml NiA buffer at 5 ml/min and then eluted in approximately fourteen 2 ml fractions using 67% NiC buffer (50 mM Tris-HCl pH 7.4, 15 % (v/v) glycerol, 200 mM NaCl, 0.5 % (w/v) CHAPS, 0.1 % (w/v) DDM, 0.1 % (w/v) CHS, 500 mM imidazole, 2 µg/ml leupeptin and pepstatin A, and 3 µg/ml aprotinin). Samples for gel analysis were collected from each fraction (20 µl), mixed and boiled at 100 °C for 5 min with 10 µl NuPAGE® laurel dodecyl sulphate (LDS) Sample Buffer (4X) (hereafter termed Sample Buffer), and 15-20 µl run on SDS-PAGE gels as described in Section 2.1. Peak fractions were pooled, concentrated using Vivaspin (Sartorius) 100 000 MWCO centrifugal

concentration tubes, and the imidazole concentration diluted below 70 mM to prevent precipitation, using TEV cleavage buffer (50 mM Tris-HCl pH 7.4, 30 % (v/v) glycerol, 0.5 % (w/v) CHAPS, 0.1 % (w/v) DDM, 0.1 % (w/v) CHS, 1 mM ethylenediamine tetraacetic acid (EDTA), 1 mM dithiothreitol (DTT)). NTS1 (T43NTS1 cleaved from NTS1B) (43.3 kDa), FLAG-NTS1 (44.3 kDa) or NTS1-G α_{i1} (84.5 kDa) were obtained by overnight TEV protease cleavage of the fusion protein followed by affinity purification of the receptor using TetraLink™ Tetrameric Avidin Resin (Promega) modified with N-terminally biotinylated neurotensin (bioNT) (NT resin). For TEV cleavage, AcTEV™ Protease (Invitrogen) was used initially, but this rapidly became economically non-viable, and TEV protease thereafter was heterologously expressed and purified in the laboratory (Section 2.1.3.). Tests using OD₂₈₀ values of 1:5-1:100 TEV:NTS1B Ni²⁺ column eluate (equivalent to approximately a 1:1-1:16 mol:mol ratio) in a final reaction volume of 100 μ l were performed to determine appropriate amounts of TEV protease for complete cleavage. Concentrated and diluted HisTrap column eluate was incubated overnight with TEV protease (1:1-1.5:1 mol ratio) at 4 °C on a rotator at 4 rpm. Three ml Ni²⁺ Sepharose High Performance affinity medium (GE Healthcare) were added in the morning for one hr to remove the His-tagged thioredoxin or MBP fusion partner and the His-tagged TEV protease. The reaction was poured through an empty gravity flow column and the flow-through collected for affinity purification. Affinity chromatography of the receptor using neurotensin to capture NTS1 from solution (hereafter termed NT purification) ensures that essentially all the receptor molecules eluted from the NT column are in the active state. One-two ml NT resin was equilibrated in NT70 buffer (50 mM Tris-HCl pH 7.4, 70 mM NaCl, 15% (v/v) glycerol, 1 mM EDTA, 0.5%

(w/v) CHAPS, 0.1% (w/v) DDM, 0.1% (w/v) CHS). The TEV protease cleavage reaction was incubated in batch with the resin rotating at 4 °C at 4 rpm for 1-2 hrs. Receptor constructs were eluted over ~30 1 ml fractions using high salt NT1 buffer (50 mM Tris-HCl pH 7.4, 1 M NaCl, 10% (v/v) glycerol, 1 mM EDTA, 0.1% (w/v) DDM, 0.1% (w/v) CHS). The flow-through could be reloaded on the re-equilibrated column and eluted up to three more times to obtain more cleaved receptor. Samples for gel analysis were collected from each fraction as above. Fractions were pooled and concentrated using Vivaspinn (Sartorius) 100 000 MWCO centrifugal concentration tubes, and the final sample diluted ten times to 100 mM NaCl using NT0 buffer (50 mM Tris-HCl pH 7.4, 10% (v/v) glycerol, 1 mM EDTA, 0.1% (w/v) DDM, 0.1% (w/v) CHS). Protein was snap frozen in liquid nitrogen in 100-500 μ l aliquots and stored at -80 °C. The column was extensively cleaned using A3 buffer (50 mM Tris-HCl pH 7.4, 1 mM EDTA, 2M NaCl), and stored in B3 buffer (50 mM Tris-HCl pH 7.4, 1 mM EDTA, 3 mM NaN₃).

Protein concentration determined spectroscopically from the A_{280} was calculated using molar extinction coefficients (ϵ) of 139 000 M⁻¹ cm⁻¹ for NTS1B and 57 000 M⁻¹ cm⁻¹ for NTS1, 58 000 M⁻¹ cm⁻¹ for FLAG-NTS1, or 83 000 M⁻¹ cm⁻¹ for NTS1-G α_{i1} (<http://web.expasy.org/protparam>). In combination with the activity calculated from the [³H]-NT binding assay, specific activity was calculated. Receptor concentration was also estimated using SDS-PAGE gels by comparing band intensity of the receptor against concentrations of bovine serum albumin (BSA) ranging from 0.5 mg/ml to 0.01 mg/ml. The receptor, however, understains in Coomassie Brilliant Blue by approximately four times, as noted when comparing the intensity of the MBP

band and the NTS1 band on gels analysing TEV cleavage efficiency. Gels for Western blots were electrophoresed for one hr at 100 mA using a BioRad Trans-Blot® SD semi-dry transfer cell and a nitrocellulose membrane and then blotted according to the instructions for Novex® Western Breeze™ Immunodetection Kit (Invitrogen).

2.2.2. TEV NIa protease

TEV NIa protease cleaves with high specificity at its substrate ENLYFQS between QS, leaving only a single S residue at the N-terminus of the downstream fusion partner. The TeV-His₆ construct was kindly donated by Dr Huanting Liu and Prof. Jim Naismith (University of St. Andrews). Overnight cultures (5 ml aliquots LB with 50 µg/ml kanamycin) of *E. coli* BL21(DE3) cells harbouring the pETNIP plasmid with the His₆-TEV protease sequence were grown at 37 °C and 200 rpm from single colonies plated on LB agar containing 50 µg/ml kanamycin. These cultures were used to inoculate fresh, sterile 2xYT medium containing 50 µg/ml kanamycin (5 ml/500 ml). The cultures were grown to an OD₆₀₀ of 0.25 (37 °C, 120 rpm). The temperature was lowered to 20 °C and growth allowed to continue until the OD₆₀₀ reached 0.6. TEV NIa protease expression was induced with 0.4 mM IPTG and expression allowed for 16-20 hrs. Cells were harvested by centrifugation in a JLA 9.1 rotor (7000 g, 10 min, 4 °C), snap frozen in liquid nitrogen and stored at -80 °C until further use.

TEV protease was purified as described ^(168 63, 102-11), but Tris-HCl buffer was used instead of phosphate buffer. The cells were thawed at 4 °C with stirring in 10 ml

sample buffer (50 mM Tris pH 7.4, 0.3 M NaCl, leupeptin and pepstatin A at a final concentration of 2 µg/ml, and aprotinin at 3 µg/ml) per litre of culture. Hen egg white lysozyme (Sigma-Aldrich) was added to 1 mg/ml, and 1 mg DNase from bovine pancreas (Sigma-Aldrich) per 20 g pellet. MgCl₂ was added to a final concentration of 5 mM. After stirring for 30 min at 4 °C, cells were lysed three times in a French press at 1000 psi. Cell debris was removed by centrifugation (20 000 g, 20 min; 70 000 g, 30 min; 4 °C). The supernatant was filtered through a 0.45 µm syringe filter, imidazole added to 30 mM, and loaded at 2 ml/min onto a 5 ml HisTrap HP column equilibrated in sample buffer. The column was washed with 120-150 ml wash buffer (50 mM Tris-HCl pH 7.4, 0.3 M NaCl, 30 mM imidazole, 2 µg/ml leupeptin and pepstatin A, 3 µg/ml aprotinin). The column was then further washed stepwise with approximately 20 ml each of wash buffer containing 100 mM, 150 mM and 200 mM imidazole respectively. TEV protease was eluted over 30-35 2 ml fractions with elution buffer (50 mM Tris-HCl pH 7.4, 0.3 M NaCl, 350 mM imidazole, 2 µg/ml leupeptin and pepstatin A, 3 µg/ml aprotinin). Gel samples were collected (20 µl with 10 µl NuPAGE® LDS Sample Buffer (4X)) and fractions analysed by SDS-PAGE. The least contaminated fractions were pooled and concentrated using Vivaspin 10 000 MWCO centrifugal concentrator tubes (Sartorius). Imidazole was diluted to below 60 mM using sample buffer, concentration was checked spectroscopically using a molar extinction coefficient of $33\ 500\ \text{M}^{-1}\ \text{cm}^{-1}$ ($M_r\ 30\ 000$) (<http://web.expasy.org/protparam>) and the final sample was snap frozen in sample buffer with a final glycerol concentration of 25 %.

2.2.3. $G\alpha_s$ and $G\alpha_{i1}$

Heterotrimeric guanine nucleotide-binding proteins (G proteins) mediate the first step in the signalling pathway from receptors at the cell membrane through the interior of the cell to the nucleus, where changes in transcription and translation are then carried out. The GPCR undergoes a conformational change when it binds ligand and thereafter is able to activate G proteins. The α - and $\beta\gamma$ -subunits dissociate and signal through separate pathways, and then reassociate. The α -subunit binds to the GPCR at intracellular loop 3 (ICL3) or the C-terminus via residues toward its C-terminus. Binding to the GPCR catalyses exchange of GDP for GTP, and hydrolysis of GTP releases the α -subunit from the GPCR to reassociate with the $\beta\gamma$ -subunits. In this study, only the α -subunits of G_{i1} and G_s were used, both in order to simplify the system under study, and because these can be expressed functionally in *E.coli*. The expressed proteins do not carry any post-translational modifications, such as the palmitoylation or myristoylation usually present on G_{i1} and G_s α -subunits. The pET15 plasmids for the His₆- $G\alpha_{i1}$ and His₆- $G\alpha_s$ were kindly donated by Renaud Wagner (University of Strasbourg, France), and a deletion error in the start codon corrected by Alan Goddard (University of Lincoln, UK) using QuikChange II Site-Directed Mutagenesis Kit (Stratagene) and the following primers: forward primer: CACATCACCATCACCATCACA TAGTATG; reverse primer: CCATGGTATATCTCCTTCTTAAAGTTAAAC. The frameshift correction inserts an Ala after the initial Met.

Competent *E. coli* DH5 α [™] cells were transformed with the PCR product from the frameshift correction in the same manner as described above for FLAG-NTS1 (Section 2.1.1.). Plasmid DNA was purified from the cells as described in Section 2.1.1., and used to transform BL21(DE3) cells, which were spread on sterile LB-agar plates containing 100 μ g/ml ampicillin. Starter cultures (5 ml) were grown overnight from single colonies in enriched medium (20 g tryptone, 10 g yeast extract, 5 g NaCl, and 2 ml glycerol per litre, with 50 mM potassium KH₂PO₄, pH 7.2) containing 100 μ g/ml ampicillin. One aliquot was used to prepare glycerol stocks (15 % glycerol), which were snap-frozen in liquid nitrogen and stored at -80 °C. The remaining starter cultures were pooled and 5 ml aliquots used to inoculate twenty 500 ml aliquots of sterile enriched medium containing 100 μ g/ml ampicillin. The cells were grown until the OD₆₀₀ reached 0.5–0.7 (30 °C; 200 rpm). IPTG was added to a final concentration of 100 μ M and His₆-G α _{i1} (41.5 kDa) or His₆-G α _s (45.6 kDa) were expressed for 16 hrs at 26 °C, as described ⁽¹⁶⁹⁾. The cells were harvested by centrifugation in a Beckman JLA 9.1 rotor (9 000 g, 10 min, 4 °C), snap-frozen in liquid nitrogen and stored at -80 °C.

His₆-G α _{i1} or His₆-G α _s were purified by IMAC at 4 °C using a 5 ml HisTrap HP column (GE Healthcare) as described ⁽¹⁶⁹⁾, with minor modifications. The cell pellet from 5-10 L fermentation (usually 7-10 g/L) was crushed and thawed in 40 ml/10 g Equilibration buffer (50 mM Tris-HCl, pH 8.0, 20 mM β -mercaptoethanol, and the protease inhibitors leupeptin and pepstatin A (2 μ g/ml) and aprotinin (3 μ g/ml)). Lysozyme was added to 0.2 mg/ml and the mixture stirred for 30 min at 4 °C. MgSO₄

was added to 5 mM with 2 mg DNase per 40 ml. The cells were stirred for a further 30 min 4 °C, then sonicated on ice at 40 % amplitude with a 6 mm tip for three one min rounds of 10 s on, 0.2 s off, using a Vibra-cell™ sonicator (Sonics). Insoluble material was pelleted in a Beckman JA 25.5 rotor (70 000 g, 30 min, 4 °C). The supernatant was collected and filtered through a 0.45 µm filter.

The charged HisTrap column was equilibrated with six column volumes Equilibration buffer. The supernatant was loaded on the column at 3 ml/min, then washed with 100-150 ml Wash buffer (50 mM Tris-HCl pH 8.0, 20 mM β-mercaptoethanol, 0.5 M NaCl, 10 mM imidazole, 2 µg/ml leupeptin and pepstatin A, 3 µg/ml aprotinin). Gα_{i1} was eluted using a linear gradient of 10-150 mM imidazole over 12 ml, using Elution buffer 1 (50 mM Tris-HCl pH 8.0, 20 mM β-mercaptoethanol, 100 mM NaCl, 10 mM imidazole, protease inhibitors as above) and Elution buffer 2 (50 mM Tris-HCl pH 8.0, 20 mM β-mercaptoethanol, 100 mM NaCl, 150 mM imidazole, protease inhibitors). Gα_s was eluted using a step gradient of 20, 25 and 30 % Elution buffer 2, with an initial wash step at 10 % Elution buffer 2. The column was washed with Elution buffer 3 (50 mM Tris-HCl pH 8.0, 20 mM β-mercaptoethanol, 100 mM NaCl, 500 mM imidazole, protease inhibitors) to ensure complete elution. Gel samples were collected (20 µl with 10 µl NuPAGE® LDS Sample Buffer (4X)) and fractions analysed by SDS-PAGE. The least contaminated fractions were pooled and concentrated using Vivaspın 10 000 MWCO centrifugal concentrator tubes (Sartorius). Gα subunits were extensively dialysed into 50 mM Tris-HCl pH 7.4, 100 mM NaCl, 5 mM MgCl₂. Samples to be used for amine coupling in surface plasmon

resonance (SPR) were dialysed into three changes of 40 mM sodium phosphate buffer, pH 7.4. Spectroscopic concentration determination used $\epsilon = 31\,910\text{ M}^{-1}\text{ cm}^{-1}$ ($\text{G}\alpha_{\text{i1}}$) and $43\,000\text{ M}^{-1}\text{ cm}^{-1}$ ($\text{G}\alpha_{\text{s}}$). In this thesis, His₆- $\text{G}\alpha_{\text{i1}}$ and $\text{G}\alpha_{\text{i1}}$, and His₆- $\text{G}\alpha_{\text{s}}$ and $\text{G}\alpha_{\text{s}}$ will be referred to interchangeably.

2.2.4. Membrane scaffold protein 1D1

The expression plasmid for membrane scaffold protein 1D1 (pMSP1D1, Addgene plasmid 20061) ⁽⁷⁶⁾ is a derivative of pET28a. It codes for a deletion mutant ($\Delta 1-11$) of human apolipoprotein A-1, one of a set of plasma proteins composed of amphipathic helices that are able to form complexes with lipids for soluble lipid and cholesterol transport through the blood. The first N-terminal helix has little role in lipid binding and has been found to be unnecessary for lipoprotein particle formation ^(76, 170). An N-terminal hepta-histidine (H7) sequence followed by a TEV protease recognition site have been engineered into the sequence (H7-MSP1D1). The plasmid is supplied in DH5 α cells, which were streaked on sterile LB-agar plates containing 50 $\mu\text{g/ml}$ kanamycin. Single colonies were picked for small scale DNA purification. Cultures (5 ml) were grown overnight in sterile LB medium containing 50 $\mu\text{g/ml}$ kanamycin. Plasmid DNA was purified from cultures using QIAprep Spin Miniprep Kit (Qiagen). Competent BL21(DE3) cells (Calbiochem) were transformed with 100-500 ng H7-MSP1D1 plasmid DNA with a 75 s heat shock, one hr outgrowth, and overnight growth at 37 °C on sterile Luria-Bertani-agar (LB-agar) plates containing 50 $\mu\text{g/ml}$ kanamycin.

H7-MSP1D1 was expressed and purified as described ⁽¹⁷¹⁾, with minor adjustments. Starter cultures (5 ml) of *E. coli* BL21(DE3) cells harbouring the H7-MSP1D1 plasmid were grown either overnight or for 3-4 hrs (37 °C, 200 rpm) until the OD₆₀₀ reached 0.4–0.6 in sterile LB medium containing 50 µg/ml kanamycin. If grown in the day, the cultures were stored overnight at 4 °C for use the next day. Starter cultures were used to inoculate sterile terrific broth (TB) medium (12 g tryptone, 24 g yeast extract, 4 ml glycerol per litre, including 100 ml 0.17 M KH₂PO₄ and 0.72 M K₂HPO₄, sterilised separately) in 5-10 L batches made up of 500 ml aliquots containing 50 µg/ml kanamycin. After 3-4 hrs (37 °C, 200 rpm), once the OD₆₀₀ reached ~1.6 and ceased increasing, the culture was induced with 1 mM IPTG. Fermentation was stopped 3 hrs after induction. The cells were harvested by centrifugation in a JLA 9.1 rotor (8000 g, 10 min), snap frozen in liquid nitrogen and stored at -80 °C until further use.

The cell pellet collected from 5 L fermentation (40–60 g) was crushed and resuspended in 100 ml of 20 mM phosphate buffer, pH 7.4, with stirring at 4 °C. Leupeptin and pepstatin A were added to a final concentration of 2 µg/ml, and aprotinin to 3 µg/ml. After the cells were completely thawed, Triton X-100 (Sigma) was added to a final concentration of 1% (v/v). DNase (5 mg) and 5 mM MgCl₂ were added and stirring allowed to continue for 30-60 min. The cells were lysed by sonication in 40 ml aliquots on ice at 40 % amplitude, with 3 one-min rounds of 10 s on, 2 s off pulses. Cell debris was removed by centrifugation in a JA 25.5 rotor

(30000 g, 30 min, 4 °C). The supernatant was filtered through a 0.45 µm filter syringe and brought to 20 mM imidazole using a 2 M stock at pH 7.4.

A 5 ml HisTrap FastFlow (FF) (GE Healthcare) Ni²⁺ column, equilibrated in 40 mM phosphate buffer, pH 7.4, was used to purify H7-MSP1D1. The supernatant was loaded on the column at 3 ml/min at 4 °C. The column was then washed with approximately 250 ml of each of the following: Wash buffer 1 (40 mM Tris-HCl, 0.3 M NaCl, 1% (v/v) Triton X-100, pH 8.0), Wash buffer 2 (40 mM Tris-HCl, 0.3 M NaCl, 50 mM sodium cholate, 20 mM imidazole, pH 8.0) and Wash buffer 3 (40 mM Tris-HCl, 0.3 M NaCl, 50 mM imidazole, pH 8.0). The scaffold protein was eluted with 40 mM Tris-HCl, 0.3 M NaCl, 0.4 M imidazole and collected over 25 2 ml fractions. Samples of each fraction (20 µl) mixed with 10 µl Sample Buffer and boiled for 5 min at 100 °C were electrophoresed at 200 V for 40 min, and stained with PageBlue Protein Staining Solution (Thermo Scientific). Uncontaminated fractions were pooled, concentration determined spectroscopically using a molar extinction coefficient of 21 430 M⁻¹ cm⁻¹ and molecular mass of 24 793 (<http://web.expasy.org/protparam>), then concentrated to approximately 5 mg/ml using Vivaspin 10 000 MWCO centrifugal concentrator tubes (Sartorius), and extensively dialysed against MSP Dialysis buffer (20 mM Tris-HCl, 0.1 M NaCl, 0.5 mM EDTA, pH 7.4) at 4 °C. The protein was snap-frozen in liquid nitrogen for storage in 2 ml aliquots at -80 °C.

For scaffold protein with no His tag, H7-MSP1D1 was incubated with TEV protease overnight at 4 °C at a 1:10 TEV:H7-MSP1D1 molar ratio. The cleavage reaction was passed over a 5 ml HisTrap HP Ni²⁺ column equilibrated in 40 mM phosphate buffer, pH 7.4, to remove the cleaved tag and the His-tagged TEV protease. The flow-through was collected, concentrated using Vivaspin 10 000 MWCO centrifugal concentrator tubes (Sartorius), dialysed against MSP Dialysis buffer (20 mM Tris-HCl, 0.1 M NaCl, 0.5 mM EDTA, pH 7.4) at 4 °C, and snap-frozen in liquid nitrogen for storage in 2 ml aliquots at -80 °C. The molar extinction coefficient and molecular mass used were 18 450 M⁻¹ cm⁻¹ and 22 000 (<http://web.expasy.org/protparam>).

2.3. Functional assessments

2.3.1. NTS1 activity

2.3.1.1. ³H-neurotensin binding assay

Receptor activity was assessed using a ³H-NT saturation binding assay^(172, 173). Dilute receptor in Storage buffer (50 mM Tris-HCl pH 7.4, 100 mM NaCl, 10% glycerol, 1 mM EDTA, 0.1% DDM, 0.1% CHS) was incubated on ice for 1 hr with 8.3 nM ³H-NT (Perkin Elmer) in a final volume of 60 µl Assay buffer (50 mM Tris-HCl, pH 7.4, 0.5% CHAPS, 0.1% CHS, 0.1% DDM, 1mM EDTA, 0.1mg/ml BSA), then separated from unbound ³H-NT in an Eppendorf benchtop centrifuge (1 000 g; 3 min) using P30 spin columns (BioRad) equilibrated in Assay buffer. Binding was quantified by scintillation counting using a Wallac 1409 DSA Liquid Scintillation Counter (Perkin Elmer), assuming one binding site per ligand and a saturation of 89.2 % of binding

sites ⁽¹⁶⁶⁾. Non-specific binding was assayed in the presence of 6.7 μ M unlabelled NT₈₋₁₃.

For affinity assays, ~1 nM NTS1 was incubated on ice for three hrs with concentrations of ³H-NT ranging from 0.1-12 nM in triplicate in a final volume of 70 μ l standard Assay buffer (50 mM Tris-HCl, pH 7.4, 0.5% CHAPS, 0.1% CHS, 0.1% DDM, 1mM EDTA, 0.1mg/ml BSA). Non-specific binding was assessed in the presence of 10 μ M unlabelled NT₈₋₁₃. Receptor was separated from unbound ³H-NT in an Eppendorf benchtop centrifuge (1 000 g; 3 min) using P30 spin columns (BioRad) equilibrated in Assay buffer. Binding was quantified by scintillation counting using a Wallac 1409 DSA Liquid Scintillation Counter (Perkin Elmer). Data were analysed using a one site (total and non-specific binding) model in Prism 5 (GraphPad).

2.3.1.2. Fluorescence-based affinity assay

In an effort to develop a less unwieldy, cheaper and safer activity assay than the radioactive ³H-NT binding assay, the affinity of Oregon Green 488-labelled NT (OrGr488-NT) for the receptor was tested. A fluorescence-based activity assay could utilise fluorescence intensity or fluorescence polarisation for quantifying binding. Oregon Green 488 (2',7'-difluorofluorescein) is a fluorinated analogue of fluorescein (Figure 2.1) ⁽¹⁷⁴⁾, which is more photostable and less pH-sensitive in the physiological range than fluorescein. To prevent the so-called “propeller effect”, whereby a label is able to spin around the bond to which it is attached when attached via a long linker,

negating any polarisation effects gained by slowed rotational tumbling upon binding of a small ligand to a large receptor, NT was synthesised with Oregon Green 488 at position five (Alta Bioscience, Birmingham), with no linker, as follows: Oregon Green 488 – KPRRPYIL. In this way, the receptor should still be able to bind the ligand easily at the last six residues, but the Oregon-Green 488 should be bound closely enough that it cannot spin around.

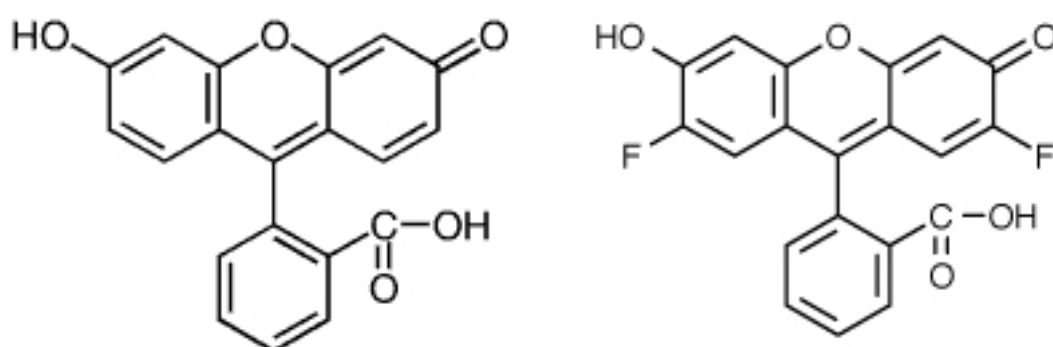


Figure 2.1. Structures of fluorescein and Oregon Green 488

Oregon Green 488 differs from fluorescein only in the fluorination at the 2 and 7 positions of the phenyl ring. This increases the photostability of the compound, reduces quenching effects and decreases pH sensitivity in the physiological range.

In a final volume of 70 μ l standard Assay buffer in triplicate, \sim 1 nM NTS1B or NTS1 was incubated on ice for three hrs with concentrations of OrGr488-NT ranging from 0.1-12 nM or 0.3 to 15 nM. Non-specific binding was assessed in the presence of 10 μ M unlabelled NT₈₋₁₃. Standard curves to check the linearity of fluorescence over the concentration ranges used were constructed in triplicate using Assay buffer instead of receptor. NTS1B was separated from unbound ligand in an Eppendorf benchtop centrifuge (1 000 g; 3 min) using P30 spin columns (BioRad) equilibrated in Assay

buffer. Samples were transferred to 384-well black, flat- and glass-bottomed, low-flange plates, with non-binding surfaces (Corning). Fluorescence intensity was measured with excitation at 488 nm using a Pherastar fluorescence plate-reader (BMG) with the gain adjusted to 90 % on the 15 nM standard sample. Data were collected at 520 nm and fitted using a one-site (total and non-specific binding) model in Prism 5 (GraphPad), or linear regression for the standard curves.

2.3.2. G α subunit activity

Fluorescence polarisation (FP) could potentially be a useful, higher throughput alternative to the ^3H -NT radioligand binding assay used for NTS1 activity assays, and might also prove useful as an assay of G protein C-terminal peptide binding to the receptor. To test the potential usefulness of this assay type, the binding kinetics and affinity of His₆-G α_{i1} and guanosine 5'-O-(3-thiotriphosphate) BODIPY® FL thioester (BODIPY-GTP γ S) (M_r 894.28) (Molecular Probes®), and the kinetics of BODIPY-GTP γ S binding to His₆-G α_s were assayed using fluorescence polarisation. BODIPY-GTP γ S is a non-hydrolysable analogue of guanosine 5'-triphosphate (GTP) labelled at the γ thiol of GTP γ S with the fluorescent BODIPY molecule (Figure 2.2). BODIPY fluorescence is 90 % quenched relative to the free dye, but fluorescence intensity is recovered upon binding to G proteins. For a timecourse assay, 25 nM BODIPY-GTP γ S was injected into 250 nM His₆-G α_{i1} or His₆-G α_s in a final volume of 50 μl , and the fluorescence polarisation followed at 520 nm using a Pherastar fluorescence plate-reader (BMG), with the gain adjusted to 90 % on a 25 nM standard sample. Saturation binding experiments were used to determine the affinity constant, K_D , of

BODIPY-GTP γ S for His₆-G α_{i1} . Serial dilutions of 0-2 μ M His₆-G α_{i1} were incubated with 25 nM BODIPY-GTP γ S for one hr and endpoint polarisation recorded at 520 nm. Both assay types used 500 μ M unlabelled GTP γ S to assess non-specific binding.

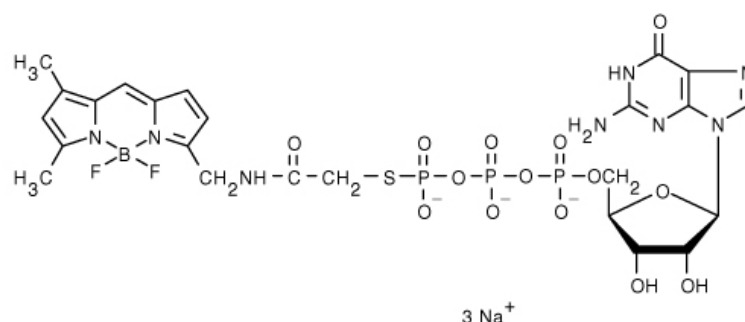


Figure 2.2. Structure of BODIPY- GTP γ S.

A thioester bond is formed between the γ thiol of GTP γ S and the BODIPY molecule. The BODIPY fluorescence is 90 % quenched relative to the free dye, but is recovered upon binding to G proteins, thus binding may be followed by monitoring increasing fluorescence emission during a timecourse or endpoint experiment.

2.4. DNA lattice formation

2.4.1. The lattice

The lattices assemble from four oligonucleotides that hybridise to their complementary sequences on adjoining strands to form the four arms of an immobile, χ -stacked Holliday junction (HJ) ⁽¹⁷⁵⁾ (Figure 2.3). The oligonucleotides are designed with 6-bp “sticky ends” that are complementary to those on one other strand. Pairs of double-stranded arms stack co-axially in the presence of Mg²⁺ and the sticky ends hybridise to assemble the junctions into an extended *p3*-symmetrised DNA crystal with 2.5 or 3.5 DNA helical turns between adjacent junctions. The half-integral

number of turns means that helices weave alternately above and below one another, such that the interweaving of three sets of parallel helices form a so-called Kagome lattice ^(175, 176). So-called “small lattice” (26 bp, 2.5 turns) sequences were designed by Jonathan Malo ⁽¹⁷⁵⁾ using the programme SEQUIN ⁽¹⁷⁷⁾; large lattice (37 bp, 3.5 turns) sequences were designed by Daniele Selmi (formerly Clarendon Laboratories, Physics Department, University of Oxford) using the programme NANEV ⁽¹⁷⁸⁾. Oligonucleotide 4 (Green) of each set of four was functionalised with either a 5′ thiol modifier on a C₆ linker to which reduced N-terminally cysteine-labelled NT (CysNT) was conjugated by oxidation ⁽¹⁷⁹⁾, or tris-nitrilotriacetic acid (NTA) ⁽¹⁸⁰⁾, such that three binding sites were available in each hexagon (Figure 2.3). The large lattice was designed for this project in order to create enough space for the NTS1-G protein complex to bind.

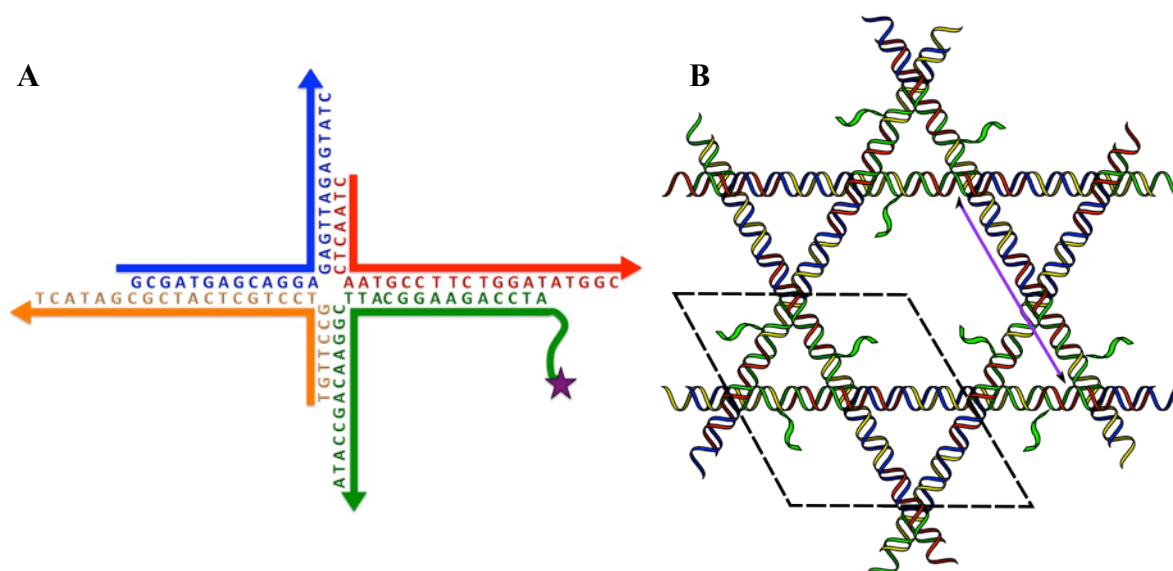


Figure 2.3. Schematic of the DNA lattice structure.

A: Schematic showing the four oligonucleotides of the large (3.5 turn) lattice, their sticky ends, and the 5′ thiol group synthesised on the Green strand (purple star). **B:** Schematic showing a portion of the 2.5 turn DNA lattice crystal with linker strands shown. One unit cell is outlined in dotted lines. The lattice constant (purple arrow) is approximately 14 nm for the small lattice and 18 nm for the large lattice. (B modified from an image by Thomas H. Sharp, University of Oxford).

2.4.2. Oligonucleotide-NT conjugation

Oligonucleotides were purchased from Integrated DNA Technologies, Inc. Oligo 4 (Green) of the small or large lattices (small Green: 5' TCC AGA AGG CAT TCG GAA CA *GCCATA* 3'; large Green: 5' GTA AGG TCC AGA AGG CAT TCG GAA CAT GAC A *GCCATA* 3'; Appendix A1) was synthesised with a 5' thiol modifier on a C₆ linker. Conjugation was performed as described ⁽¹⁷⁹⁾. Oligo 4 (200 µM) was reduced in 10 mM tris(2-carboxyethyl)phosphine (TCEP) (Sigma-Aldrich) at room temperature (RT) for 2 hrs. N-terminally cysteine-modified NT (CysNT; Alta Bioscience, UK) was reduced in 20 mM TCEP for 20 min at 50 °C. TCEP was removed from both samples by centrifugation (1 000 g; 4 min) using Bio-Gel P-6 (BioRad) columns equilibrated in TAE buffer (40 mM Tris-acetate pH 8.3, 1 mM EDTA). Reduced oligo 4 (~130 µM) and reduced CysNT (~7 mM) were incubated together in the presence of 2.4 mM copper (II) nitrate for 2-3 hrs at RT.

Conjugated oligos were purified from unconjugated CysNT by preparative native PAGE on a 15 % gel prepared from 29:1 acrylamide/bis-acrylamide 30 % solution (Sigma-Aldrich) and TAE buffer, pH 8.3. Acrylamide/bis-acrylamide solution was prepared at 15 % in a total volume of 10 ml TAE buffer pH 8.3. Ammonium persulphate (APS; 100 µl of 10 % solution; Sigma-Aldrich) and 10 µl *N,N,N',N'*-Tetramethylethylene-diamine (TEMED; Sigma-Aldrich) were added to polymerise the gel in a Biorad Miniprotean III kit with 0.75 mm spaces. Gel samples were with a 5x loading buffer containing 50 % glycerol (v/v) and 0.01 % (w/v) bromophenol blue and xylene cyanol. Gels were run for 2 hrs at 200 V at 4 °C. Gels were stained with 2 µl Sybr Gold (Molecular Probes, Invitrogen) in a small volume of water and imaged

using a Pharos FX Plus Molecular Imager (Bio-Rad Laboratories Inc, USA). The appropriate band was cut out from the gel, crushed and mixed with 60-80 μ l TAE buffer, and incubated at RT overnight. To remove the gel fragments, the suspension was placed in Ultrafree MC columns (Millipore, USA) and centrifuged (1 000 g, 3 min) to obtain the final purified conjugate product. The concentration of the conjugate was determined based on the absorbance of single-stranded DNA at 260 nm. Absorbance readings were taken with a Varian Cary 1E spectrophotometer (Varian Ltd., UK) and the concentrations calculated using the extinction coefficients provided by the manufacturer.

For tris-NTA conjugation, oligo 4 was purchased with three sequential 5' Uni-LinkTM amino modifiers (Clontech, supplied by Integrated DNA Technologies) and modified and purified as described in ⁽¹⁸⁰⁾.

2.4.3. DNA lattice formation

DNA lattices were prepared as described ⁽¹⁷⁹⁾. Stoichiometric ratios of each of the four oligonucleotides were mixed at 3 μ M each in TAE buffer pH 8.3 (NT-functionalised DNA lattice) or 20 mM Tris-HCl pH 8.8 (Tris-NTA-functionalised lattice), in the presence of 30 mM MgCl₂. The reaction mixture was cooled from 96 °C to 4 °C over 72 hrs, and stored at 4 °C.

2.4.4. Protein arrays

His₆-Gα_{i1} was linked by its His-tag to the tris-NTA lattice via a Ni²⁺-mediated interaction. NTS1 and Ni-NTA-Nanogold®-labelled (Nanoprobes) NTS1B (NTS1B*) were linked to the NT-functionalised lattice via the ligand ($K_D \sim 1$ nM). The arrays were prepared as follows:

His₆-Gα_{i1} or NTS1: DNA lattice solution (2 μl; 3 μM) was incubated with 2 μl protein solution (~0.05 mg/ml) in buffer (His₆-Gα_{i1}: 10 mM Tris-HCl pH 8.3, 25 mM NiCl₂, 500 mM NaCl; NTS1: 50 mM Tris-HCl pH 7.4, 0.1 % DDM (w/v), 0.01 % CHS (w/v), 1 mM EDTA) for 30-60 min on ice.

NTS1-Gα_{i1} complex: DNA lattice solution (2 μl; 3 μM) was incubated with 2 μl NTS1 (~0.05 mg/ml) in 50 mM Tris-HCl pH 7.4, 0.1 % DDM (w/v), 0.01 % CHS (w/v), 1 mM EDTA for 30 min on ice. His₆-Gα_{i1} or His₆-Gα_{i1}* (2 μl; ~0.05 mg/ml) was then added and the complex incubated for a further 30-60 minutes.

Controls: The following controls were performed: use of unmodified DNA lattice, omission of Ni²⁺ from conjugation buffer for His₆-Gα_{i1} binding to tris-NTA-modified lattice, addition of 10-fold excess of NT to conjugation reaction for binding of NTS1 to NT-modified lattice. No specific binding was seen in control samples – protein either aggregated around the edges of the electron microscope grid holes or was washed off. His₆-Gα_{i1} did not bind to the NT-modified lattice in the absence of NTS1.

2.5. Reconstitution

2.5.1. Lipid preparation

Glassware used in the preparation of lipids was cleaned thoroughly in phosphate-free detergent, rinsed in distilled water (dH₂O), twice in deionised water (DI water) and twice in methanol to remove excess water. All lipids were purchased from Avanti® Polar Lipids as powder or 25 mg/ml chloroform stocks. Lipids were stored at -20 °C and brought to room temperature prior to opening the containers. For liposomes, BPL (Avanti) or 3:1:1 POPC:POPG:POPE with 25 mol % cholesterol (PPPC) were solubilised in 1:1 chloroform:methanol or simply measured out (chloroform stocks) using glass Hamilton syringes and dried under a stream of nitrogen. For nanodiscs, 3:1:1 POPC:POPG:POPE with 25 mol % cholesterol; 1:1 POPC:POPG (PC:PG); 3:1 POPC:POPE (PC:PE) or 1.07:1.5:1 BPL:POPC:POPG (BPL:PC:PG) lipid mixtures were used. Residual solvent was removed under vacuum overnight. For liposomes, the lipids were resuspended at 5 mg/ml in 100 mM Tris (final 50 mM), pH 7.4, 200 mM NaCl (final 100 mM), 2 mM EDTA (final 1 mM) and bath sonicated for 2 min. DDM, CHAPS or OG were added to the lipid to the required detergent:lipid ratios (see below) and volumes made up with deionised water. For nanodiscs, at least 8-10 µmol per batch of discs was made up to 50 mM in 100 mM sodium cholate (M_r 430.55) in 50 mM Tris-HCl pH 7.4, 100 mM NaCl, 1 mM EDTA. Solutions were freeze-thawed with liquid nitrogen three times (nanodiscs) or eleven times (liposomes). Liposome preparations were extruded through 0.1 µm polycarbonate membranes above the phase transition temperature (T_m) using 1 ml syringes in an Avanti® Mini-Extruder. Liposomes or detergent-solubilised lipids were stored overnight at 4 °C, or snap-frozen in liquid nitrogen and stored at -80 °C.

2.5.2. NTS1 reconstitution into liposomes

Reconstitution of NTS1 into liposomes was performed using Biobeads SM-2 (BioRad) as described ^(181, 182), with minor changes. Biobeads were chosen over the dialysis method of reconstitution because it is possible to control the amount of detergent removed with each step, due to relatively well-characterised Biobead-to-detergent ratios ⁽¹⁸³⁾; because of the relative rapidity of the method compared to dialysis; and also because of the short half-life of NTS1 in detergent (Peter Harding, DPhil thesis, University of Oxford). Hydrophobic adsorption takes hrs rather than days, resulting in a larger proportion of functionally reconstituted receptors. However, lipid adsorption to the beads can be up to 30 %, so this possibility needs to be accounted for. Size homogeneity of proteoliposomes formed using Biobeads is far greater than for the dialysis method.

2.5.2.1. Liposome preparation

Saturating the liposomes with detergent prior to reconstitution improves membrane protein incorporation into vesicles from solution ^(184, 185). For each detergent and lipid mixture, there is an effective detergent:lipid molar ratio (R_{eff}) at which the lipids are saturated but not completely solubilised by the detergent, obtained by: $R_{\text{eff}} = ([\text{detergent}] - [\text{cmc}]) / [L]$, where cmc is the critical micellar concentration (cmc) of the detergent, and L is lipid. The saturation (R_{sat}) and solubilisation (R_{sol}) points are obtained by plotting turbidity at 500 nm against detergent concentration in specific lipid mixtures and obtaining the values from $[\text{detergent}] = R_{\text{eff}}[L] - [\text{cmc}]$. A table listing these parameters for several of the most common detergents is available in ⁽¹⁸⁶⁾.

For DDM R_{sat} is 1 (mol/mol), and R_{sol} 1.6 (mol/mol), and these values were used for liposome and lipid preparation.

DDM (196 mM) was added to 500 μl liposomes to a final concentration of 5.5 mM (Figure 2.4). The solution was allowed to incubate at RT with stirring for three hrs to ensure complete equilibration of the detergent with the lipids. Following saturation and prior to addition of the protein solution, the lipid-detergent mixture was bath sonicated for approximately 10 minutes. NTS1 (8 μM) in storage buffer (50 mM Tris-HCl pH 7.4, 100 mM NaCl, 0.1 % DDM (w/v), 0.01 % CHS (w/v), 1 mM EDTA, 10 % (v/v) glycerol) was incubated with 20 μM NT on ice for one hr. Receptor was added to the lipid-detergent solution to a final [NTS1] of 1.8 μM and the reaction mixture was incubated with gentle mixing (one hr, 4 °C) before the addition of 150 mg/ml washed Biobeads.

Biobeads were thoroughly washed several times with methanol and then water. Prior to use, they were washed in detergent-free buffer several times and all of the buffer aspirated. The solution was incubated above the phase transition temperature of the lipids for 1-2 hrs, and then aspirated into fresh Biobeads and incubated with rotation overnight at 4 °C. Proteoliposomes were pelleted at 100 000 g for 3 hrs in a TLA 100.2 rotor using an Optima XL100K benchtop ultracentrifuge at 4 °C. Proteoliposomes were resuspended in 50 mM Tris-HCl pH 7.4, 100 mM NaCl, 1 mM EDTA.

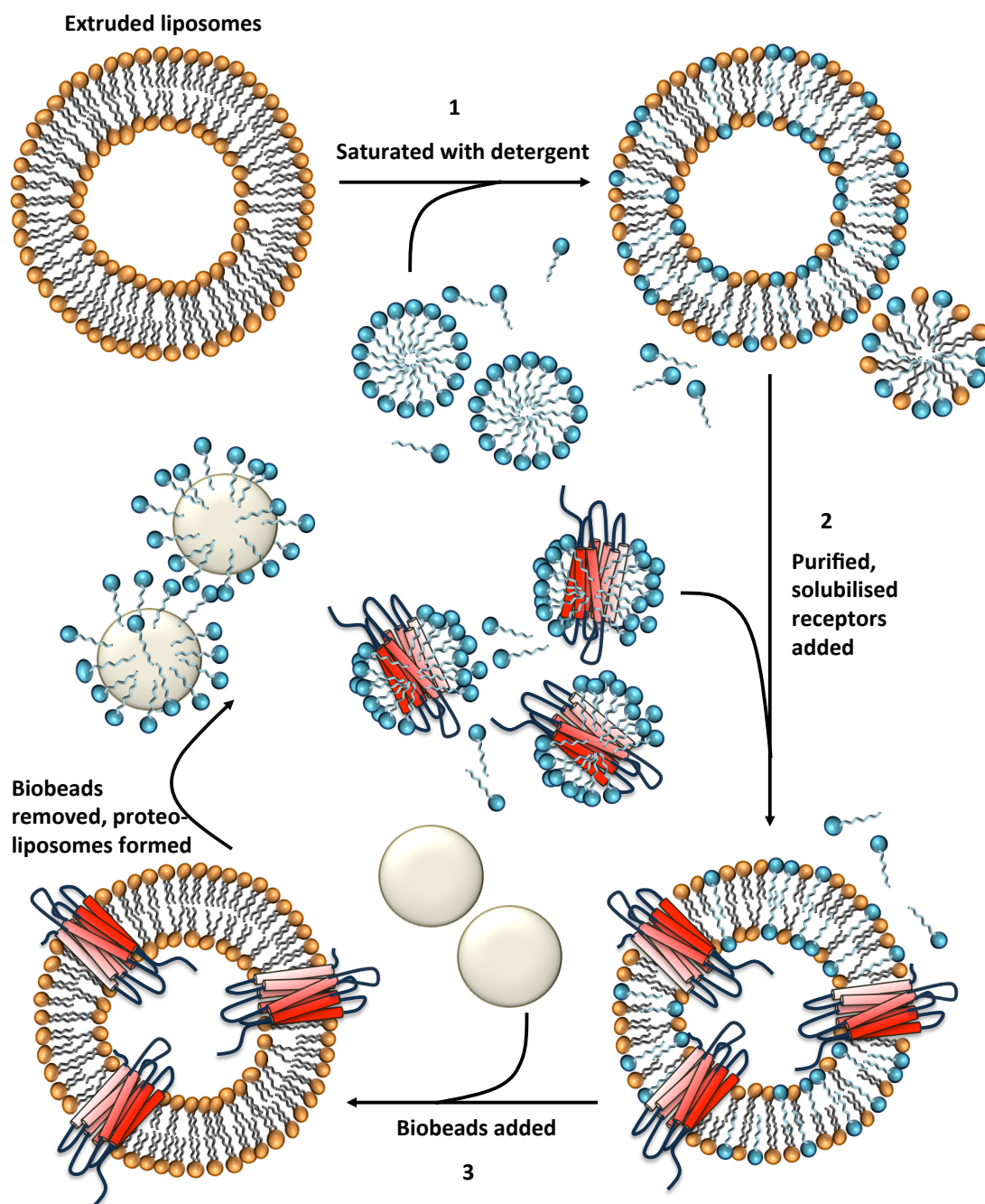


Figure 2.4. Reconstitution of NTS1 into liposomes.

Schematic representation of reconstitution of NTS1 into liposomes. (1) Extruded liposomes are destabilised with a detergent concentration giving the appropriate R_{eff} value. (2) Purified, detergent-solubilised protein is added to the required concentration for the desired lipid:protein ratio, and the mixture incubated for one hr at 4 °C. (3) Detergent is removed with Biobeads at a 10:1 Biobead to detergent ratio (w/w), allowing spontaneous proteoliposome formation. Figure originally prepared for (181).

Samples (20 μ l) mixed with 10 μ l Sample Buffer and boiled for 5 min at 100 °C were electrophoresed (15 μ l per well) at 200 V for 40 min, and stained with Silver Plus (BioRad) silver stain kit according to the manufacturer's directions.

2.5.3. Liposome/lipid concentration determination

Various methods for the determination of lipid concentration are in use. The method used here was based on that of Chen et al. ⁽¹⁸⁷⁾ and is a total phosphorus assay. Although it cannot directly account for cholesterol, which does not have a phosphate headgroup, the cholesterol concentration can be calculated from the molar ratio once the phosphorus concentration is known. The phosphorus assay is a colorimetric assay for inorganic phosphate, which involves acid hydrolysis of phospholipids followed by conversion of inorganic phosphate to phospho-molybdic acid with the addition of ammonium molybdate. This compound is then reduced while heating by ascorbic acid to form a blue-coloured complex whose absorbance is read at 820 nm. The more phosphorus present, the deeper blue the colour development. A standard curve was constructed from triplicate samples of 0.0-0.228 μ mol phosphorus made up from 0.65 mM stock phosphorus solution (Sigma-Aldrich 661-9). The standard samples and triplicate samples of prepared liposomes, nanodiscs or lipid stocks were acid-hydrolysed by addition of 0.45 ml 8.9 N H₂SO₄ to each tube with heating in an aluminium block at 200-215 °C for 25 min. The tubes were removed from the heating block and allowed to cool for five minutes before 150 μ l H₂O₂ was added to each tube. Heating was continued above 200 °C for a further 30 min. DI water (3.9 ml) was added to each tube, followed by 0.5 ml 2.5 % (w/v) ammonium molybdate (VI) tetrahydrate solution. All tubes were vortexed five times, 0.5 ml 10 % (w/v) ascorbic

acid added, and vortexed five times each again. Tubes were covered with glass playing marbles to prevent evaporation and heated at 100 °C for 7 min. Once cooled to room temperature (20 °C) the absorbance at 820 nm of all standards and samples was determined. The 0.0 μ mol phosphorus standard was used for blank-correction and triplicate averages plotted as a function of phosphorus amount. The phosphorus concentration, and thus the phospholipid concentration of the samples were determined from the equation of a regression line fitted to the data.

2.5.4. NTS1 reconstitution into nanodiscs

The use of nanodiscs ⁽⁷⁵⁻⁷⁷⁾ for reconstitution of membrane proteins has become an increasingly popular and useful alternative to liposomes, not least because they are homogenously-sized, soluble while still maintaining the protein in a membrane environment, relatively rapid to prepare, the protein is accessible from both sides of the membrane, and they lend themselves to a number of biophysical techniques for which liposomes are not suitable, such as microscale thermophoresis or as analytes in SPR. Preparation of NTS1-loaded and empty nanodiscs followed the protocol developed by Sligar's group ⁽¹⁷¹⁾ with some modifications based on the lipid types used and empirically determined optimal H7-MSP1D1:lipid:NTS1 ratios, with reference to ^(69, 74, 188) (Figure 2.5). The following guidelines were adhered to for successful nanodisc formation: the final [lipid] must be ≥ 4 mM, final [sodium cholate] must be 12-40 mM, final [glycerol], must be less than 3 %. Scaffold protein:lipid ratios of 1:50 to 1:60 were most effective. Empty nanodiscs were reconstituted with 5 additional lipid molecules per MSP, and were prepared simultaneously with loaded nanodiscs. Ratios of 80:1 and 50:1 MSP:FLAG-NTS1 or

NTS1 were effective. NTS1 or FLAG-NTS1 (2-5 nmol at ~0.2-0.5 mg/ml (M_r 43 303, $\epsilon = 57\,000\text{ M}^{-1}\text{ cm}^{-1}$ or 44 298, 58 500 $\text{M}^{-1}\text{ cm}^{-1}$)), or NTS1 buffer alone (for empty nanodiscs) was added to sodium cholate-solubilised lipid mixtures described in Section 2.4.1. above. H7-MSP1D1 or TEV-cleaved MSP1D1 (4-10 mg, or 0.16 – 0.25 μmol at 4.5 mg/ml (M_r 24 793, $\epsilon = 21\,430\text{ M}^{-1}\text{ cm}^{-1}$)) was added in a final volume of 2.5-3.5 ml, with final concentrations of receptor at approximately 1 μM , MSP at 1.6-3.5 mg/ml (70-170 μM) and lipid at 7 mM. The solution was incubated for one hr with rotation at 4-6 rpm at 4 °C. Washed Biobeads (0.8-1.0 g/ml) were added to the solution and rotation continued overnight at 4 °C. The solution was aspirated off the Biobeads in the morning and fresh, washed Biobeads (0.5 g/ml) were added for further incubation for one hr. The nanodiscs preparations were aspirated off the Biobeads again and concentrated in pre-washed centrifugal concentration tubes, Vivaspin 6, 10 000 MWCO followed by centrifugation in a Beckman Avanti™ 30 benchtop centrifuge (10 000 g, 4 °C, 10 min).

The supernatant was aspirated off any pellet that had formed and filtered through a Nanosep® MF low-volume 0.2 μm centrifugal filter (PALL Corporation) and loaded on a calibrated Superdex 200 10/300 GL column (GE Healthcare) equilibrated in 50 mM Tris HCl pH 7.4, 100 mM NaCl, 5 mM MgCl_2 . The gel filtration (GF) column was run at 0.4 – 0.5 ml/min for 30 ml and 0.5 ml fractions were collected.

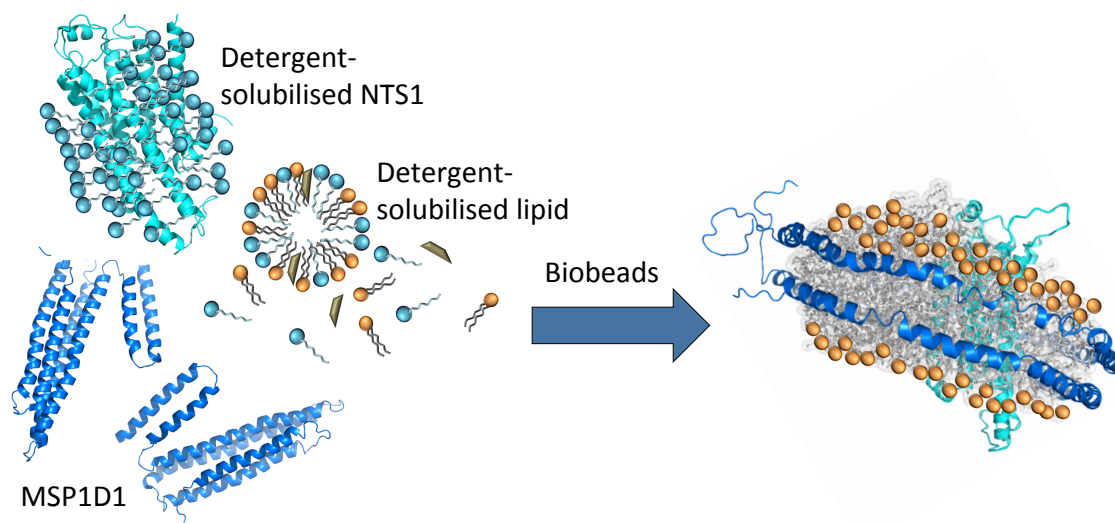


Figure 2.5. Schematic diagram illustrating nanodisc formation.

A lipid film is solubilised in 100 mM sodium cholate to a final concentration of 50 mM lipid. Detergent-solubilised, purified NTS1 (cyan ribbon structure surrounded by blue detergent molecules) is added to the lipid-detergent mixture at the target concentration (lipid molecules are orange with gold rectangles representing cholesterol). Membrane scaffold protein is added to the reaction mixture at the target MSP:lipid and MSP:NTS1 ratio, and the sample incubated with rotation at 4 °C for one hr. Biobeads (1g/ml) are added to remove the detergent overnight, and nanodiscs spontaneously form.

SDS-PAGE gels and Western blots of the fractions were run as described above. Peak fractions containing NTS1 as well as MSP were pooled and concentrated in Vivaspinn 6 100 000 MWCO centrifugal concentrator tubes (Sartorius). FLAG-NTS1 nanodiscs were enriched by purification using anti-FLAG M2 resin (Sigma-Aldrich) according to the manufacturer's instructions with minor modifications. Briefly, the resin (1 ml) was transferred to an empty column and washed with 10 column volumes 50 mM Tris-HCl, with 150 mM NaCl, pH 7.4 (TBS). Three column volumes glycine-HCl pH 3.5 were passed over the column, followed by a further 10 column-volume wash in TBS. FLAG-NTS1 nanodiscs in 50 mM Tris-HCl pH 7.4, 100 mM NaCl, 1 mM

EDTA were incubated on the resin with rotation at 4 °C for 1-2 hrs. The column was washed with 10 column volumes TBS and the nanodiscs eluted with 10 sequential column volumes of FLAG peptide at 100 µg/ml in TBS. Nanodiscs were extensively dialysed at 4 °C in three changes of 50 mM tris-HCl, 100 mM NaCl, 5 mM MgCl₂. Samples were stored for gel electrophoresis. Gels for silver stain were stained with Silver Plus (BioRad) silver stain kit according to the manufacturer's directions.

2.6. Ternary complex formation

Gel filtration and NT affinity column purification were used to purify the NT-NTS1- $G\alpha_s$ or $G\alpha_{i1}$ complex. Purified NTS1 and NTS1B (0.1 µM) were bound to 100 µl NT resin equilibrated in NT70 buffer for one hr at 4 °C. His₆- $G\alpha_{i1}$ (10 times molar excess) was added for 30 min incubation. The resin was washed with 10 column volumes NT70, and the protein eluted with two 200 µl NT1 washes, followed by a 200 µl wash reloaded four times. For gel filtration, 1 µM NTS1 was incubated with 10 µM NT for one hr on ice, followed by addition of three times molar excess His₆- $G\alpha_s$ for 30 min. The sample was loaded on a Superdex 200 10/30 GL column (GE Healthcare) equilibrated in 50 mM Tris-HCl pH 7.4, 10 % (v/v) glycerol, 100 mM NaCl, 0.1 % (w/v) DDM, 0.1 % (w/v) CHS, 5 mM MgCl₂ and run at 4 ml/min. The same procedure was followed for NTS1 nanodiscs incubated with His₆- $G\alpha_s$, but detergent was omitted from the gel filtration buffer.

2.7. Electron microscopy

2.7.1. Nanogold® labelling

His₆-Gα_{i1} was labelled by incubation with 10x molar excess of Ni-NTA-Nanogold® (Nanoprobes) (30 min; 25 °C) according to the manufacturer's instructions. Free Nanogold® was removed by gel filtration chromatography (XK 16/100, Superdex 200) in 50 mM Tris-HCl pH 7.4, 100 mM NaCl, 5 mM MgCl₂, and labelling efficiency was quantified by absorbance spectroscopy (A_{280} : $\epsilon_{\text{gold}} = 4.12 \times 10^5 \text{ M}^{-1} \text{ cm}^{-1}$; $\epsilon_{\text{protein}} = 31\,910 \text{ M}^{-1} \text{ cm}^{-1}$; A_{420} : $\epsilon_{\text{gold}} = 1.56 \times 10^5 \text{ M}^{-1} \text{ cm}^{-1}$).

2.7.2. Negative stain

NTS1 (2 µl of 0.05 mg/ml) was incubated with NT-functionalised DNA lattice (the concentration of each DNA strand was 2.1-3 µM) (1 hr; 4 °C). The negative control contained 10-fold molar excess NT. For G protein coupling, NTS1 (2 µl of 0.05 mg/ml) was incubated with NT-functionalised DNA lattice (30 min; 4 °C). Ni-NTA-Nanogold®-labelled His₆-Gα_{i1} (His₆-Gα_{i1}*) (2 µl of 0.08 mg/ml) was added and the sample incubated for a further 30 min. Samples were adsorbed onto glow-discharged holey carbon grids for 1 min and negatively stained with 8 µl 2 % (w/v) uranyl acetate (lattice alone) or methylamine vanadate (NanoVan (Nanoprobes)) (lattice with protein) for 10-30 s. The negative control contained no NTS1. No specific protein binding was observed in the controls. The protein either aggregated at the edges of the holes or washed off. For nanodiscs, loaded or empty discs (8 µl, 200-300 nM); or loaded or empty discs incubated with 5 – 10 µM NT for one hr followed by 30 min incubation with 1 µM His₆-Gα_s* were adsorbed onto glow-discharged continuous

carbon grids for 1 min. Sample was rapidly wicked and immediately negatively stained with 8 μ l 0.5-2 % (w/v) uranyl acetate or methylamine vanadate (NanoVan (Nanoprobes)) for 10-30 s. NTS1- $G\alpha_i$ -nanodiscs (6 μ l, 300 nM) were incubated with 2 μ l DNA lattice, adsorbed onto glow-discharged holey carbon grids for 1 min and negatively stained with 8 μ l 0.5-2 % (w/v) uranyl acetate or Nanovan for 10-30 s. Images were recorded on film using a JEOL 2000FX transmission electron microscope (TEM) operating at 200 kV (nominal magnification 50,000 \times) or on a Tecnai G² series T12 TEM (FEI) with BioTWIN lens and lanthanum hexaboride (LaB₆) gun, operating at 80-120 kV and fitted with an Eagle 4k x 4k CCD camera (FEI).

2.7.3. Cryo-electron microscopy

Solutions of either DNA template alone or with protein (2-3 μ l) was adsorbed onto a holey carbon grid for \sim 1 min, washed briefly by inverting the grid on a drop of deionized water to remove excess salt and detergent, and flash-frozen in liquid ethane, using a Vitrobot Mark IV (FEI) operating at 100 % humidity. Grids were stored in liquid nitrogen and transferred using a cryoholder (Gatan). Images were recorded using an FEI Tecnai F30 field emission transmission electron microscope operating at 200 or 300kV (nominal magnification 59 000 \times , defocus \sim 3.5-6.5 μ m) fitted with an Eagle 4k x 4k CCD camera, or on film and scanned with an Epson F-3200 scanner (1.32 \AA /pixel). The spherical aberration (C_s) of the microscope was 2 mm and the camera pixel size was 15 μ m.

2.7.4. Data processing

Images were scanned with an Epson F-3200 scanner (1.32 Å/pixel). The initial models for SPA were generated by filtering the crystal structure of the active β_2 adrenoreceptor with the nanobody removed (PDB 3P0G ⁽⁸⁷⁾) or the inactive β_2 adrenoreceptor with the T4-lysozyme removed (PDB 2RH1 ⁽⁸³⁾) in each case to 40 Å.

Single-particle images (13 331) were manually selected using BOXER ⁽¹⁸⁹⁾ (64×64 pixel box), corrected for the contrast transfer function using CTFFIND2 ⁽¹⁹⁰⁾, aligned by centre of mass and classified into groups containing typically 25-50 members using multivariate statistical analysis. Images were not masked before orientation.

Reconstructions were refined by iterative projection-matching alignment using SPIDER ⁽¹⁹¹⁾. After padding the boxes to 100×100 pixels, angular bin sizes were reduced from 10° to 3° over 8 iterations until rotation and shift parameters, Fourier shell correlation (FSC) and map features converged. The 95% of particles with the best correlations with previous density map reprojections were used in the final reconstruction. The final map was low-pass filtered to its respective resolution.

2.8. Surface plasmon resonance

2.8.1.1. Streptavidin coupling and ligand capture

Streptavidin was amine-coupled to CM5 chips as follows: 50 mM NaOH was injected over the chip for 60 s at 8 µl/min. A 1:1 mix of NHS and EDC was injected over the

surface at 5 $\mu\text{l}/\text{min}$ for 420 s. Streptavidin (Sigma-Aldrich) at 100 $\mu\text{g}/\text{ml}$ was injected over the surface at 5 $\mu\text{l}/\text{min}$ for 840 s. The surface was then blocked with a 420 s injection of 1 M ethanolamine hydrochloride, pH 8.5. Streptavidin was coupled to the L1 chip in the same manner. Running buffer was 10 mM 4-(2-hydroxyethyl)-1-piperazineethanesulfonic acid (HEPES), 150mM NaCl, 1 mM ethylenediamine tetraacetic acid (EDTA), 0.05% P20. BioNT was captured by the streptavidin by a 600 s injection of 0.01 mg/ml bioNT. NTS1 serially diluted from 2.5-40 nM or 3.125-50 nM was injected over this surface at 30-50 $\mu\text{l}/\text{min}$ in 50 mM Tris pH 7.4, 100 mM NaCl, containing 0.1 % DDM, 0.01 % CHS, using the Biacore T100 single cycle kinetics assay, with a contact time of 120 s and dissociation time of 60 s. Prior to G protein coupling, the surface was saturated with NTS1 for 10 min. $G\alpha_{i1}$ (0.25-4.0 μM) was injected over the bound NTS1 for 180-300 s association and 600-1200 s dissociation on both the CM5 and L1 chips, but the L1 chip running buffer contained no detergent. The sample compartment was maintained at 8 $^{\circ}\text{C}$ and the flow cells at 25 $^{\circ}\text{C}$.

2.8.1.2. Thiol coupling of NT

CysNT was thiol-coupled to the surface of the L1 chip using the GE Healthcare ligand thiol-coupling protocol. Briefly, the surface was activated with a 2 min injection of EDC/NHS (10 $\mu\text{l}/\text{min}$). Reactive disulphide groups were introduced to the surface with a 4 min injection of 80 mM PDEA in 0.1 M sodium borate, pH 8.5. CysNT (10 $\mu\text{g}/\text{ml}$) in 100 mM sodium acetate, pH 4.3 was then injected for 7 min. Unreacted

groups were then blocked with a 5 min injection of freshly prepared 50 mM L-cysteine in 100 mM sodium acetate, pH 4.3 with 1 M NaCl.

2.8.1.3. pH scouting for G α subunits, anti-His antibody and ovalbumin

The most effective pH for pre-concentration of the ligand to be immobilised on the surface was empirically determined by so-called pH scouting. Negatively charged groups/molecules are repelled from the carboxylated surface of the chip, thus lowering coupling efficiency. The ideal conditions for pre-concentrating the ligand close to the chip surface so that enough ligand is available for efficient immobilisation require the ligand to be far enough below its isoelectric point (*pI*) that it is positively charged, but not so far that it is irreversibly denatured. pH scouting involves injecting the ligand across the unactivated surface at different pH values below the *pI* and checking the response level during injection and after washing begins. The ideal response is a high signal during injection, which goes immediately back to the baseline when washing begins. If the signal does not return to the baseline it implies the protein has denatured, aggregated and adhered to the surface.

His₆-G α_s in 40 mM sodium phosphate buffer pH 7.4 was diluted to 20 μ g/ml in 10 mM sodium acetate buffer pH 4.3, 5.0 and 5.5. The calculated *pI* for His₆-G α_s is 5.95 (<http://web.expasy.org/protparam>) ⁽¹⁹²⁾. A CM5 chip was primed in 10 mM HEPES pH 7.4, 150 mM NaCl, 3 mM EDTA, 0.05 % (v/v) P20 (HBS-EP) or 10 mM HEPES pH 7.4, 150 mM NaCl (HBS-N), then conditioned with two 60 s injections of 50 mM NaOH at 30 μ l/min, followed by 120 s injection at 10 μ l/min of G protein at the

relevant pH. His₆-Gα_{i1} (pI = 6.1) was tested in the same manner at pH 4.5, 5.0 and 5.5. Antibodies and ovalbumin were tested at pH 4.0, 4.5, 5.0 and 5.5. The sample compartment was maintained at 8 °C and the flow cells at 25 °C.

2.8.1.4. Amine coupling of G proteins, anti-His and ovalbumin

His₆-Gα_s (M_r 46 877, ε = 43 360 M⁻¹ cm⁻¹) or His₆-Gα_{i1} (M_r 41 574, ε = 36 000 M⁻¹ cm⁻¹; <http://web.expasy.org/protparam>) ⁽¹⁹²⁾ (10-20 µg/ml extensively dialysed into 40 mM sodium phosphate buffer) were coupled to a CM5 S Series Sensor Chip (Biacore, GE Healthcare). The chip was primed in 10 mM HBS-EP or 10 mM HBS-N and the normalise procedure run before starting. This procedure normalises the basal signals of the flow cells relative to one another when the signal is expected to be very small. The flow rate was set to 10 µl/min. NaOH (50 mM) was injected over selected flow cells for 2x 60 s. A 1:1 EDC/NHS mixture prepared just prior to use was injected over the surface for 420 s. His₆-Gα_s (~10-20 µg/ml) diluted into 10 mM sodium acetate buffer pH 5.5, or His₆-Gα_{i1} in 10 mM sodium acetate buffer pH 5.0 was injected over the activated surface for 840-1 000 s. Ethanolamine was injected for 420 s to block unbound activated sites. The reference cell (flow cell 1 (FC1)) was activated and blocked with no ligand, or a non-binding reference protein such as ovalbumin (using the same protocol, but at pH 4, after scouting for the optimal pH) was coupled.

2.8.2. On-chip reconstitution

2.8.2.1. *Detergent:lipid mixtures*

Lipid preparation for testing the deposition of a bilayer on an L1 SPR chip involved either preparing a 6.6 mM stock solution of BPL or PPPC in 50 mM Tris-HCl pH 7.4, 100 mM NaCl, 1 mM EDTA, as described in Section 2.5.1. for liposomes, but without extrusion, or from lipid films in 500-1 000 μ l aliquots in individual 4 ml glass tubes once optimal lipid concentrations had been determined and further detergent concentrations were still to be tested. For DDM, initially lipid-detergent mixed micelle solutions were prepared using BPL concentrations from 0.5 to 6 mM with DDM concentrations ranging from 0.33 to 7.35 mM, giving a range of R_{eff} values from 0.8 to 1.4, thus covering the R_{sol} to R_{sat} range for DDM of 1 to 1.6. Further trials used BPL concentrations of 2.5 and 5.0 mM with DDM concentrations ranging from 0.05 mM up to 19.5 mM, below and far above the cmc for DDM. Samples were incubated for 3 hrs after resuspension of the vacuum-dried lipid and three cycles of freeze-thawing.

For solubilisation using CHAPS, 3.3 or 6.9 mM BPL or 4 mM PPPC were mixed with 0.5-20 mM CHAPS in 1 mM increments and tested for bilayer deposition on the SPR chip.

2.8.2.2. *On-chip reconstitution*

The method of Karlsson and Löfås ⁽¹⁴³⁾ was followed for bilayer scouting (i.e. searching for ideal bilayer formation conditions) on the L1 chip. The surface was conditioned with three 60 s injections of 20 mM CHAPS or 50 mM OG prior to use. Detergent:lipid mixtures were injected over the surface at 5 µl/min for 480-600 s, followed by a 120 s wait period before washing with 50 mM Tris pH 7.4, 100 mM NaCl, 1 mM EDTA containing no detergents. The surface was regenerated with a 60 s injection of 20 mM CHAPS, 50 mM OG or 1:1 solution of isopropanol:50 mM NaOH.

On-chip reconstitution of NTS1 was accomplished by use of the DUAL-INJECT function available on the Biacore T100 instrument. This function allows for immediately successive injections of sample, without a wash step between them, the default setting. After CysNT immobilisation, detergent-solubilised NTS1 was captured via the ligand with an 8 min injection at 5 µl/min, followed immediately by injection of mixed lipid-detergent micelles for ~20 min. The surface was then washed for 10-30 min at 50 µl/min with detergent-free buffer. The sample compartment was maintained at 8 °C and the flow cells at 25 °C.

2.8.3. FLAG-NTS1-nanodisc-G protein coupling

Single cycle kinetics were used for all experiments since no adequate regeneration conditions could be found to reproducibly clean bound analyte from the chip surface.

G α subunits were coupled to the chip surface as described above and then washed extensively for up to an hr at 50 μ l/min to stabilise the baseline. Stock empty and (FLAG-)NTS1-loaded nanodiscs were incubated with 10 μ M NT₈₋₁₃ for one hr on ice, and then were serially diluted between 25 and 400 nM or 41.25 and 660 nM and injected for 90-180 s over the prepared G α surface in increasing concentrations at 30-50 μ l/min.

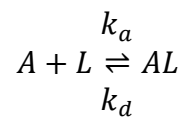
An anti-His antibody (Sigma-Aldrich) was amine-coupled to the CM5 chip surface as above but at pH 4.0. The His-tagged G α subunits were captured with a 10 min injection at 10 μ l/min. Nanodiscs formed using cleaved MSP1D1, with no His-tag, were serially diluted and injected across the chip surface as above.

Nanodiscs (empty and loaded, in reference and sample cells respectively) were captured on the hydrophobic surface of an L1 chip (Biacore, GE Healthcare) with a 10-min injection 1 μ M at 5 μ l/min. Serial dilutions of G α subunits were injected across the flow cells at 30-50 μ l/min. The running buffer was 50 mM Tris-HCl pH 7.4, 100 mM NaCl, 5 mM MgCl₂. The sample compartment was maintained at 8 °C and the flow cells at 25 °C.

2.8.4. Data analysis

The simplest and most commonly used binding model for fitting Biacore data is the Langmuir 1:1 model, which describes the binding of one ligand molecule with one analyte molecule. The assumption is that the sites are equivalent and independent of each other. The rate expression is as follows:

Equation 1



where A is the analyte, B is the ligand, k_a is the association rate and k_d is the dissociation rate. Association and analyte-ligand complex formation follow second order kinetics in theory, but because of the laminar flow system of the SPR instrument, the concentration of analyte is kept constant by continuous flow, resulting in pseudo first order kinetics. The net rate expression is:

Equation 2

$$\frac{d[AL]}{dt} = k_a \cdot [A_{free}][L_{free}] - k_d \cdot [AL]$$

But $L_{free} = L_{tot} - AL$, so

Equation 3

$$\frac{d[AL]}{dt} = k_a \cdot [A_{free}][L_{tot} - AL] - k_d \cdot [AL]$$

Where L_{free} is unbound ligand and L_{tot} is the total amount of ligand. In SPR terms the equation is:

Equation 4

$$\frac{d[R]}{dt} = k_a \cdot [C][R_{max} - R] - k_d \cdot [R]$$

Where R is the response signal, measured in response units (RU), C is the concentration of analyte and R_{max} is the maximal signal. The dissociation rate equation is:

Equation 5

$$\frac{d[R]}{dt} = -k_d \cdot [R]$$

The integrated rate equations, for association and dissociation, respectively are:

Equation 6

$$R(t) = R_{eq} - R_{eq} \cdot e^{-k_{obs} \cdot t}$$

Equation 7

$$R(t) = R_0 \cdot e^{-k_d \cdot t}$$

Where $k_{obs} = k_a \cdot C + k_d$

Dissociation follows a simple exponential decay, and is time-dependent. The built-in software on the Biacore T100 and T200 instruments (GE Healthcare) includes correction factors for drift and mass transport. The latter occurs when the ligand density is so high that analyte binding occurs faster than diffusion can replenish the analyte close to the surface of the chip. For kinetics, it is advisable to avoid immobilising very high levels of ligand for this reason. Additionally, after dissociation, analyte can rebind to the surface, creating unnecessary complexity in the response. More complex models are based upon the 1:1 binding model, but include

terms for additional parameters. The heterogeneous binding model used extensively in this thesis includes a term for a second ligand binding site.

Chapter 3 - Characterisation of system components

3.1. Introduction

The biological system under structural and kinetic study in this thesis, the formation of a ternary complex of signalling partners, requires the relevant partners to be available in a pure and native-like form, in amounts that can be usefully employed for various assays, and that each of the partners is active and functional. This chapter will cover the purifications, labelling protocols and functional assays that were used to ensure the individual binding partners and accessories were functional (Figure 3.1). Much effort went into ensuring that this was the case not only in detergent, which was used for proof of principle throughout the thesis, but also in bilayer lipid membranes, as the ultimate aim of the thesis was to investigate the function and structure of the ternary complex in the most native-like environment possible.

3.2. Protein purification and determination of protein activity

3.2.1. Neurotensin receptor type 1

NTS1 is one of only a few GPCRs that can be expressed heterologously, in an active form, in bacterial cells ^(166, 193-202). Expression is low - 800-1 000 receptors per cell ^(173, 200), but the two-step purification method described in Section 2.1.1 yielded adequate amounts of pure NTS1 for numerous experiments at a time (approximately 0.2-0.4 mg active receptor per 60 g cell pellet, as measured using ³H-NT binding assays), despite significant losses occurring through each stage of the purification process (Figure 3.2). Up to 0.4 mg NTS1B was lost through concentrator membranes, even though the

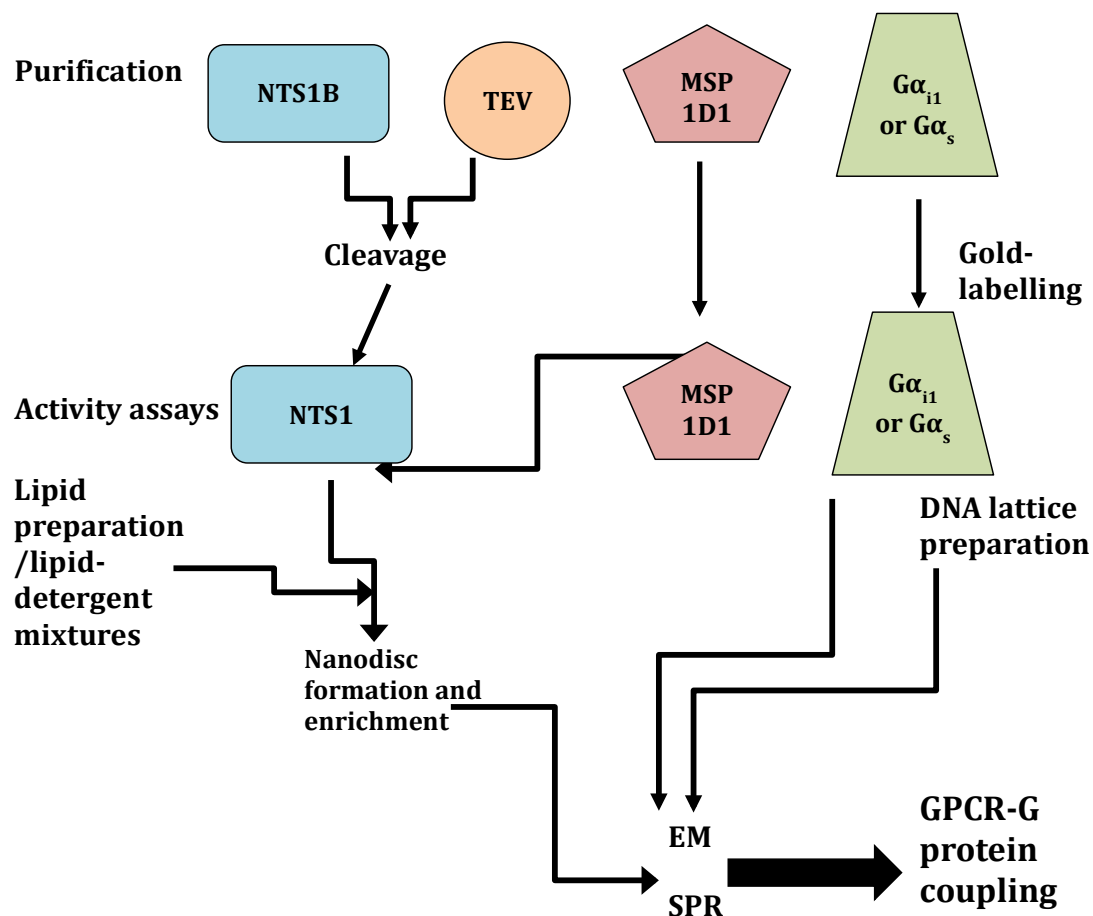


Figure 3.1. Scheme showing the steps from purification to demonstration of GPCR-G protein coupling.

The five necessary proteins, NTS1B, TEV protease, MSP1D1 and the two $G\alpha$ subunits were purified, and NTS1B was cleaved using TEV. The activity of the receptor and G proteins was assayed, and lipids and lipid-detergent mixtures were prepared. The DNA lattice was prepared, and EM on NTS1 alone, $G\alpha$ alone, and the coupled receptor and gold-labelled G protein together were visualised. NTS1-G protein coupling was also visualised in nanodiscs. NTS1 nanodiscs were used as the analyte in SPR studies to demonstrate NTS1-G protein coupling.

NTS1B-micelle size is estimated at much higher than the 100 000 Da membrane cut-off. NTS1B cleavage yielded small amounts (~0.1 mg) of active NTS1.

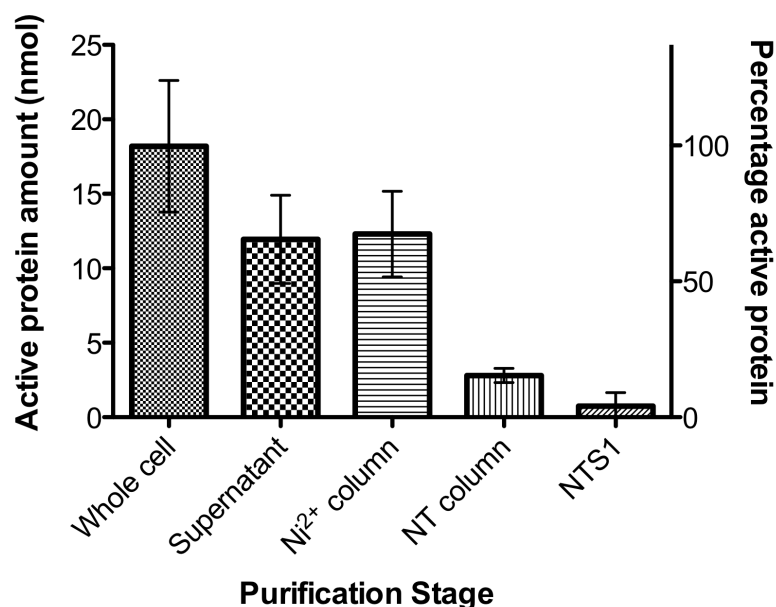


Figure 3.2. Active receptor yields during purification process.

The amount of active protein (left axis) and percent of active protein (right axis) of the initial amount of NTS1B in a 60 g cell pellet, purified as described in the Materials and Methods, for each stage of the process. Number of samples (n) is as follows: Whole cell: n=5; Supernatant: n=8; Ni²⁺: n=7; NT column eluate: n=4; NTS1: n=4. NT column eluate here refers specifically to NTS1B, although cleaved NTS1 is also purified using NT affinity chromatography (AC). Overconcentration of cleaved receptor lowered activity.

Absorbance spectra of NTS1B and NTS1 showed 4-10 times higher protein content than that indicated by ³H-NT binding assays. This, however, appeared to be a function of how much the sample had been concentrated. After elution from the NT column, the receptor is in 1 M NaCl, which is diluted ten times followed by centrifugal concentration of the sample. Concentration of the sample in this manner dramatically overconcentrates DDM in the buffer, both as a natural result of the protein itself being concentrated, being surrounded by a set number of detergent

molecules, and also because DDM has a large micelle size (70 kDa), and thus does not travel freely through the concentrator membrane, despite the MWCO being 100 000. Highly concentrated samples contained up to 7 % DDM (personal communication with Joanne Oates and Patricia Dijkman, University of Oxford; determined using an assay for glycosidic detergents). Thereafter, NTS1 eluted from the NT column was concentrated before dilution to minimise the amount of detergent concentrated, and also to minimise protein losses through the membrane and by loss of activity. Protein eluted from the NT column was taken to be active and the OD₂₈₀ used to determine concentration.

The fusion partners on the NTS1B construct are useful for soluble and relatively stable expression of NTS1, but were regarded for this thesis as potentially detrimental to the G protein coupling activity of the receptor, and the desire was to work with the most native-like receptor that could be obtained. Thus the fusion tags were cleaved using TEV protease and NTS1 almost exclusively worked with throughout the project. TEV protease cleavage of NTS1B after elution from the Ni²⁺ column was tested with varying mol ratios of protease (Figure 3.3). Cleavage of NTS1B is generally inefficient, probably due to the detergent micelle ⁽²⁰³⁾ and general inaccessibility of the cleavage sites, requiring 1:1-1:4 mol:mol ratios of protease to receptor for complete cleavage, about fourfold what is usually recommended by manufacturers (AcTEV™ Protease product description (Invitrogen)). Purchasing the vast quantities of AcTEV™ Protease (Invitrogen)

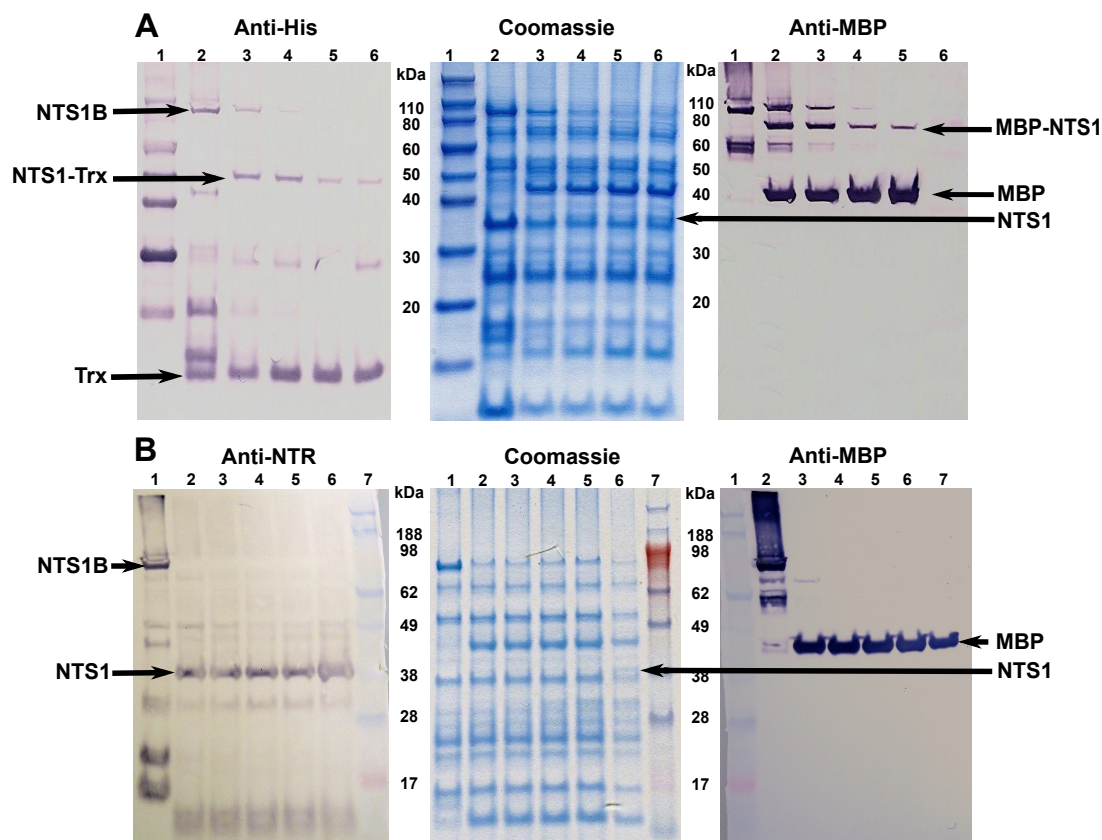


Figure 3.3. Trial proteolytic cleavage of NTS1B with His₆-TEV protease.

IMAC-purified NTS1B was incubated with increasing amounts of AcTEV Protease (Invitrogen) (A) or His₆-TEV protease (B) at 4 °C overnight. OD₂₈₀ ratios of 1:100 to 1:2.5 of TEV protease to NTS1B were tested. A ratio of 1:12 to 1:5 was determined to give adequate cleavage (lanes 6 or 7 in A and B), translating to approximately a 1:1-1:4 mol:mol ratio. Comparison of the Western blots in A and B show the cleavage efficiency of expressed and purified TEV to be greater than that of the purchased protease. It is also clear from the Coomassie-stained gels, by comparing the MBP bands and NTS1 bands, that NTS1 does not stain nearly as well as NTS1B or MBP. MW markers are in Coomassie A Lane 1, Coomassie B Lane 7; Anti-NTR A Lane 1, Anti-NTR Lane 7; Anti-MBP A Lane 6, Anti-MBP Lane 1. In A, Lanes 2, 2 and 1 respectively contain uncleaved NTS1B, and the subsequent 4 lanes 1:16, 1:13, 1:9, 1:4 and 1:1 mol:mol TEV:NTS1B. In B, Lanes 1, 1 and 2 respectively contain uncleaved NTS1B, and the subsequent 5 lanes 1:20, 1:16, 1:13, 1:9, 1:4 and 1:1 mol:mol TEV:NTS1B.

required was not economically viable, but expressing and purifying His₆-TEV protease in-house made cleavage a routine part of the protocol (see Figure 3.4 and Figure 3.5). Thereafter 1-2 mg pure and active NTS1 was obtained for each batch of 60 g cell pellet.

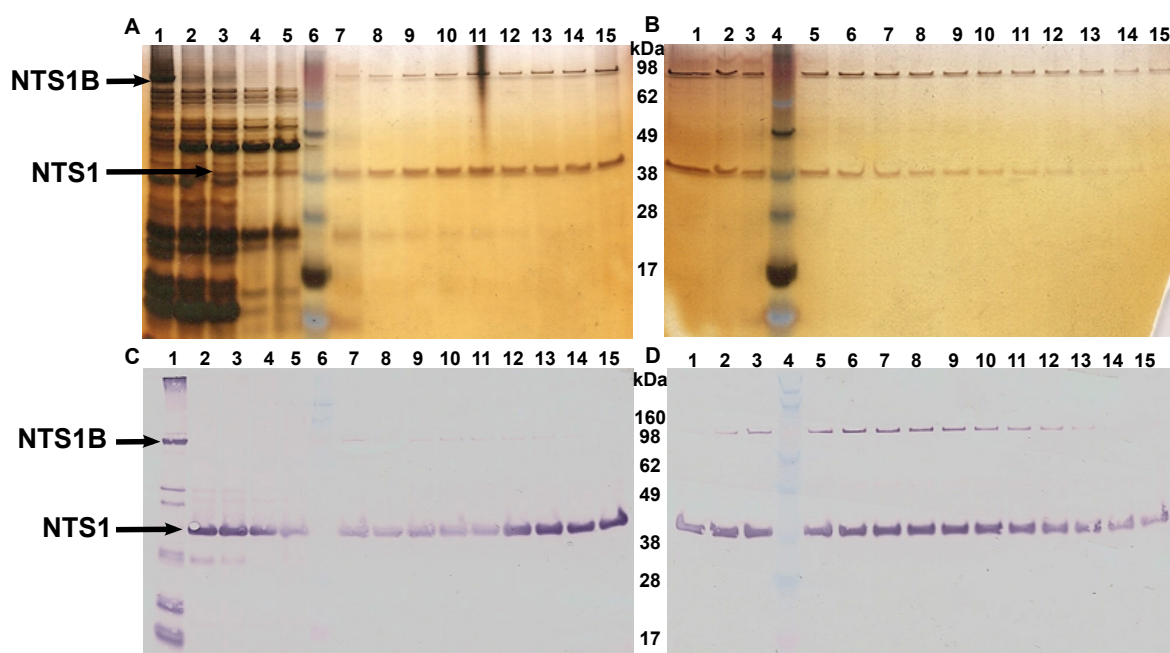


Figure 3.4. SDS-PAGE silver stain and Western blot analysis of purified NTS1.

Comparison of silver stained (A and B) and anti-NTS1 blots (C and D) of NTS1 fractions from the NT AC column shows that NTS1 stains poorly compared to NTS1B. Lanes (A and C): 1 - NTS1B prior to TEV cleavage; 2 and 3 - NTS1 post-TEV prior to addition of nickel and amylose beads; 4 - NTS1 after nickel and amylose beads – the beads remove His-tagged TEV, thioredoxin and uncleaved NTS1B; 5 – flow-through from NT AC column; 6 – molecular mass markers; 7 to 15 – fractions 1 to 9 off NT AC column. Lanes (B and D): 1 to 3 and 4 to 15 – fractions 10, 11, 12, 13, 15, 17, 19, 21, 23, 25, 27, 28, 30 and 32 collected from NT AC column; lane 4 – molecular mass markers.

NTS1B and FLAG-NTS1B were purified and cleaved to yield 1-2 mg NTS1 or FLAG-NTS1 per batch of 60 g cells (Figure 3.4 and Figure 3.5). It became apparent from parallel SDS-PAGE gels blotted and probed with antibodies, Coomassie-stained or silver-stained, that the staining capacity of cleaved NTS1 or FLAG-NTS1 is low, and that concentration estimates relying on comparison with known concentrations of bovine serum albumin (BSA) for example, on SDS-PAGE gels, is not accurate.

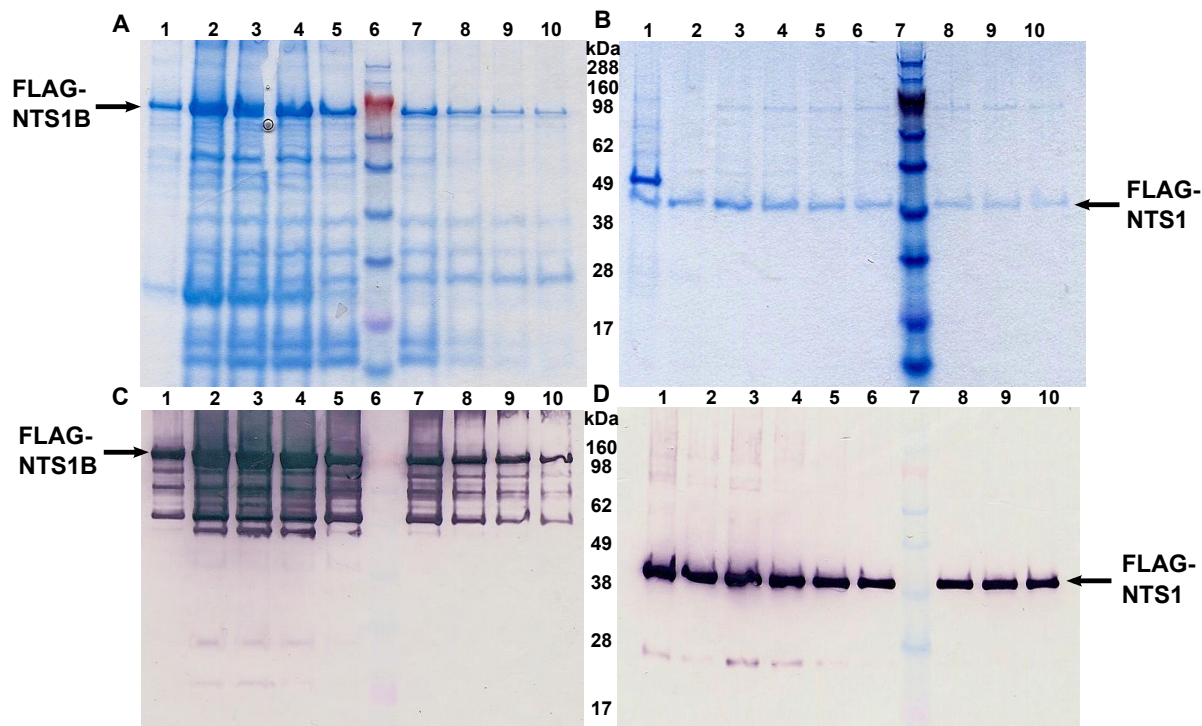


Figure 3.5. SDS-PAGE Coomassie stain and Western blot analysis of FLAG-NTS1 purification.

Comparison of Coomassie Brilliant Blue stained gels (A and B) and anti-FLAG blots (C and D) of FLAG-NTS1 fractions from the Ni²⁺ (A and C) and NT (B and D) AC columns. A) and C): Lanes 1-10: FLAG-NTS1B elution from Ni²⁺ column (fractions 3-12). B) and D): Lane 1 – NT column flow-through; lanes 2-10 – fractions 1-8 from NT column. Molecular mass markers are lanes 6 (A and C) and 7 (B and D), with sizes as indicated in kDa.

Because of error introduced by overconcentration of receptor, counting efficiency of the scintillation counter, pipetting of radioactive, methanol-solubilised ³H-NT, and the loss of ligand-bound receptor on the spin columns used for the activity assay, an effort was made to develop a rapid, high-throughput activity assay for NTS1 that was not radioactive, and did not use spin columns. Fluorescence polarisation was considered as a possibility. It was calculated that a radioactive binding stability assay checking the effect, in triplicate, over time on NTS1, of a variety of glycerol and detergent

concentrations and types, at two different temperatures, would require ~3 000 spin columns. Fluorescence polarisation negates the need for spin columns, since no signal arises from unbound fluorescent ligand, and multi-well plates can be used in a platereader for rapid signal readout, as opposed to the five minutes per sample that the radioligand assay requires in the scintillation counter, to say nothing of the number of glass vials and the volume of scintillation fluid required for an undertaking such as this. The affinity of OrGr488-NT for the receptor was compared with that of ^3H -NT using the traditional format of the assay, with spin columns, and a fluorescence intensity readout as opposed to fluorescence polarisation (Figure 3.6). This was to ensure that the fluorescent molecule covalently attached to the ligand did not affect the binding affinity.

Unfortunately, fluorescence polarisation activity assays using OrGr488NT as the “hot” ligand were not successful and will need further optimisation. However, assays using OrGr488NT in the standard manner, with spin columns, were comparatively effective in determining activity.

It would be useful to determine the specific activity of NTS1. This requires knowing accurately the concentration and the activity of the receptor. Radioligand binding assays showed marked losses of activity (and protein) through the 4-5 steps of the purification process (Figure 3.2), and markedly under-estimated concentrated NTS1 protein concentration. Due to its cumbersome nature, radioactivity and inaccuracy, and upon the assumption that all protein bound to the NT column is active, and all

protein that binds the NT-functionalised NT lattice is active by definition, and after many ^3H -NT assays had been performed, it was decided to use the OD_{280} for assessing protein concentrations.

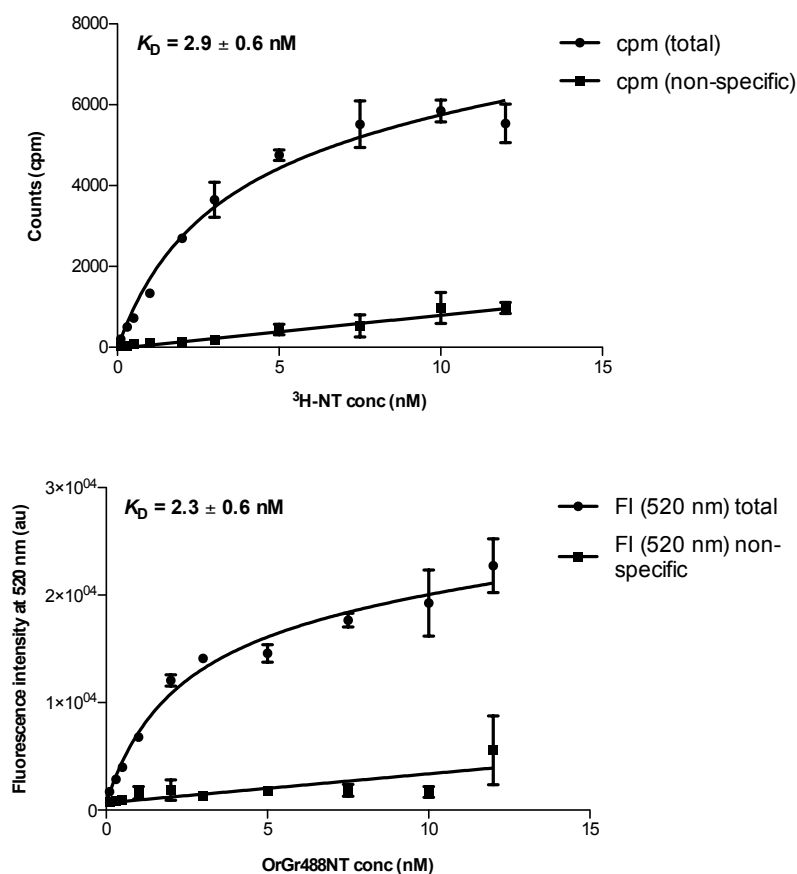


Figure 3.6. Receptor-ligand affinity assays.

Affinity assays using ^3H -NT (upper plot) or Oregon Green 488-labelled NT (lower plot) to assess whether the fluorescent label affected the affinity of the ligand for the receptor. There is no significant difference in the affinities, as indicated on the graphs. A one-site total and nonspecific binding model was used to fit the data in Prism 5 (GraphPad).

3.2.2. TEV protease

TEV protease is a highly specific and non-promiscuous protease. Approximately 2 mg of TEV protease per litre of culture was purified, far short of the 10-65 mg per litre of culture obtained by researchers using improved constructs and mutants ^(204, 205), but sufficient, given the poor yields of NTS1. The protease purifies as two bands on an SDS-PAGE gel (Figure 3.7), due to autocatalysis, but both of which are active. Each batch of TEV protease was tested on a small scale with NTS1B to determine its activity. An OD₂₈₀ ratio of approximately 1:5-1:12 (His₆-TEV:NTS1B) (1:1-1:4 mol:mol) was adequate to obtain complete cleavage of one batch of Ni²⁺-purified NTS1B.

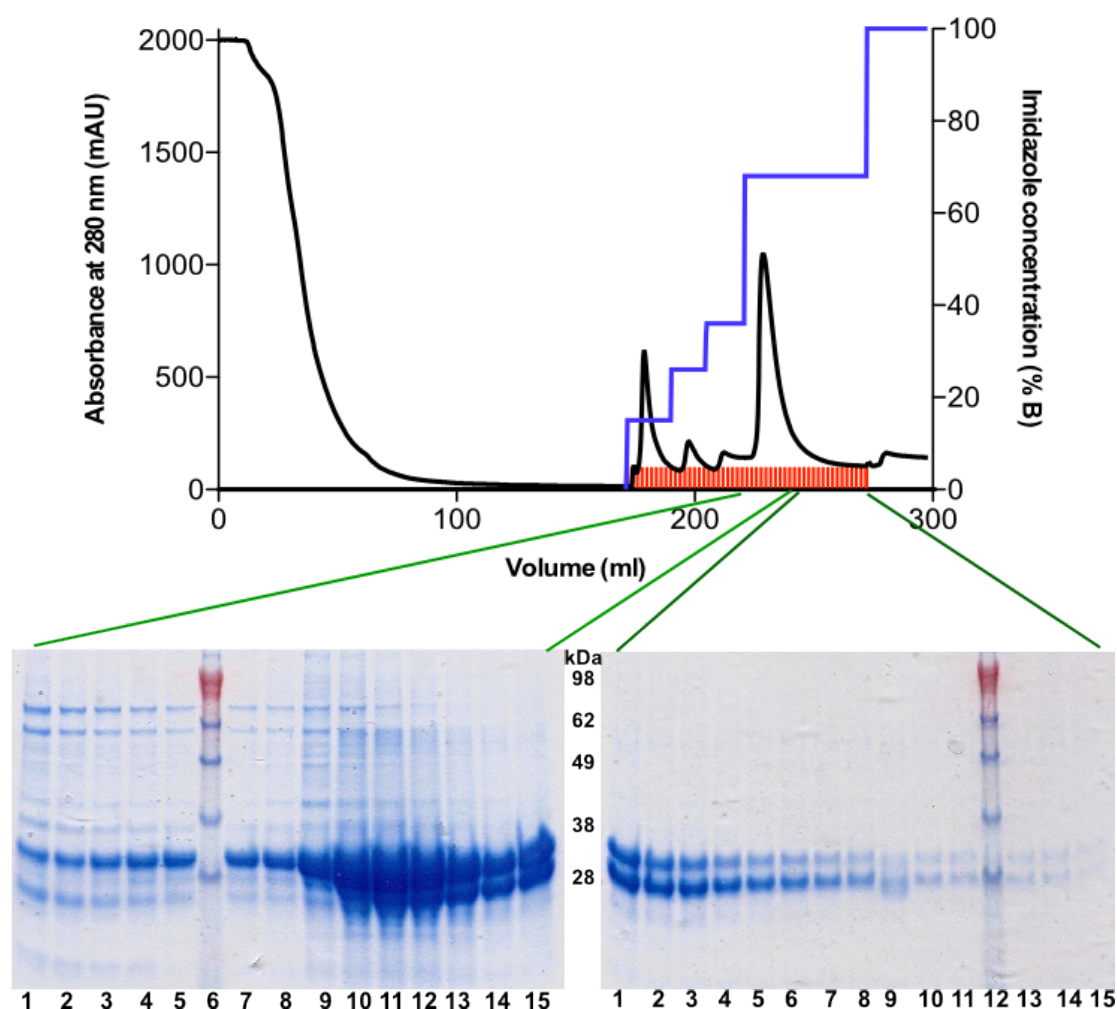


Figure 3.7. TEV protease purification.

Ni^{2+} column elution profile and SDS-PAGE gels of TEV protease IMAC purification. The column was washed until the OD_{280} returned to the baseline, and TEV protease was eluted stepwise, thus eluting contaminating endogenous *E. coli* proteins first. Steps of 18-35 % B buffer (60-130 mM imidazole) were used to remove these contaminants before eluting TEV at 65 % B (325 mM imidazole). Green lines indicate the parts of the elution profile from which the fraction samples were taken. Red bars indicate fractions. The protease purifies as two bands, both of which are active.

3.2.3. $G\alpha_s$ and $G\alpha_{i1}$

Approximately 15 mg of His₆- $G\alpha_{i1}$ and 3.5 mg His₆- $G\alpha_s$ was obtained per litre of culture. His₆- $G\alpha_{i1}$ eluted from the HisTrap FF column (Figure 3.8) was concentrated using Vivaspin 10 000 MWCO centrifugal tubes (Sartorius) and loaded on a Superdex 200 16/100 XK (GE Healthcare) gel filtration column.

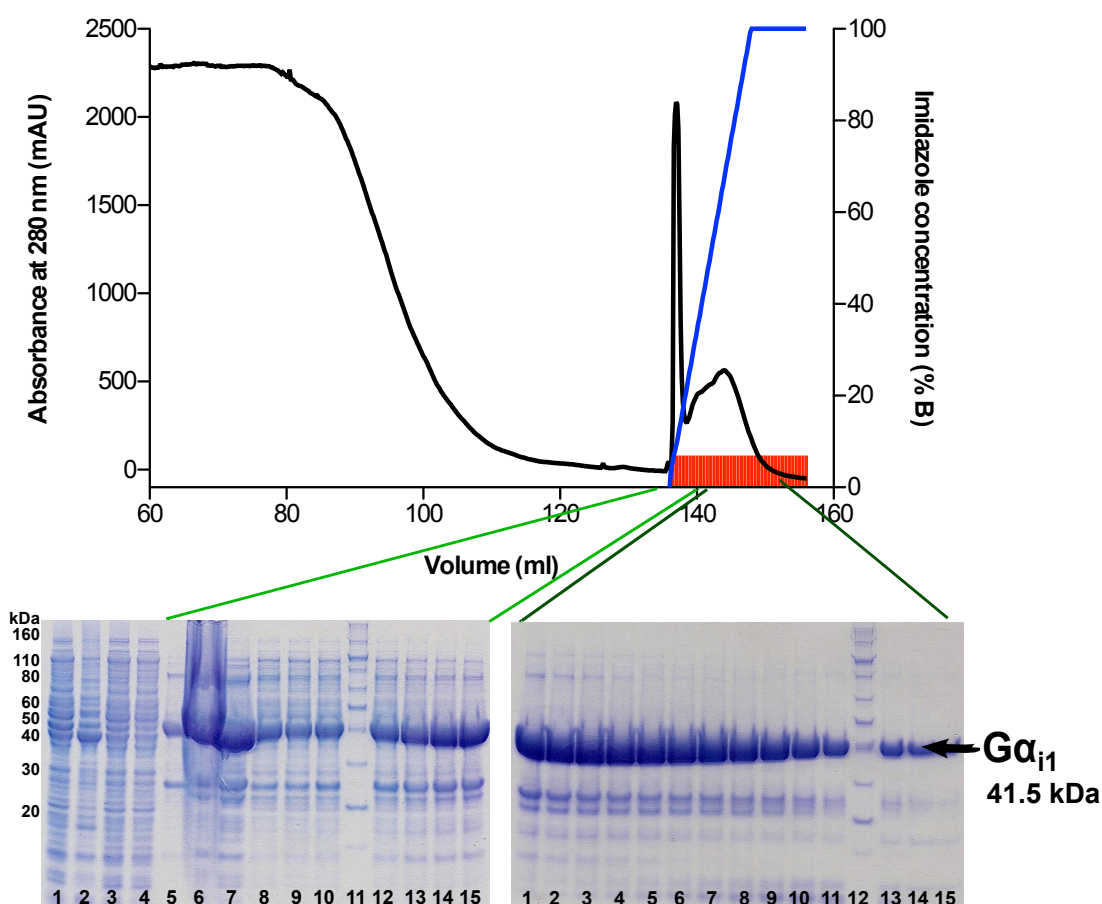


Figure 3.8. $G\alpha_{i1}$ Ni^{2+} purification.

Coomassie Brilliant Blue-stained gels showing purification fractions of His₆- $G\alpha_{i1}$ (red bars). A linear imidazole gradient (blue line) was used to elute the protein over 30 fractions. The green lines indicate which part of the elution profile the gel fractions were from. Lanes 1-4 of the left gel show samples from whole cells (lysed), pellet after centrifugation, supernatant after centrifugation and flow-through from loading the supernatant on the Ni^{2+} column, respectively. Lane 5 is MW markers, as is lane 12 in the right hand gel.

Size exclusion removed most of the contaminating proteins eluted with His₆-Gα_{i1} from the Ni²⁺ column (Figure 3.9). This strategy was unsuccessful with His₆-Gα_s, as was the use of Q Sepahrose ion exchange resin (data not shown). Ultimately, a series of small steps in the imidazole concentration gradient were used to elute less contaminated His₆-Gα_s from the Ni²⁺ column (Figure 3.10).

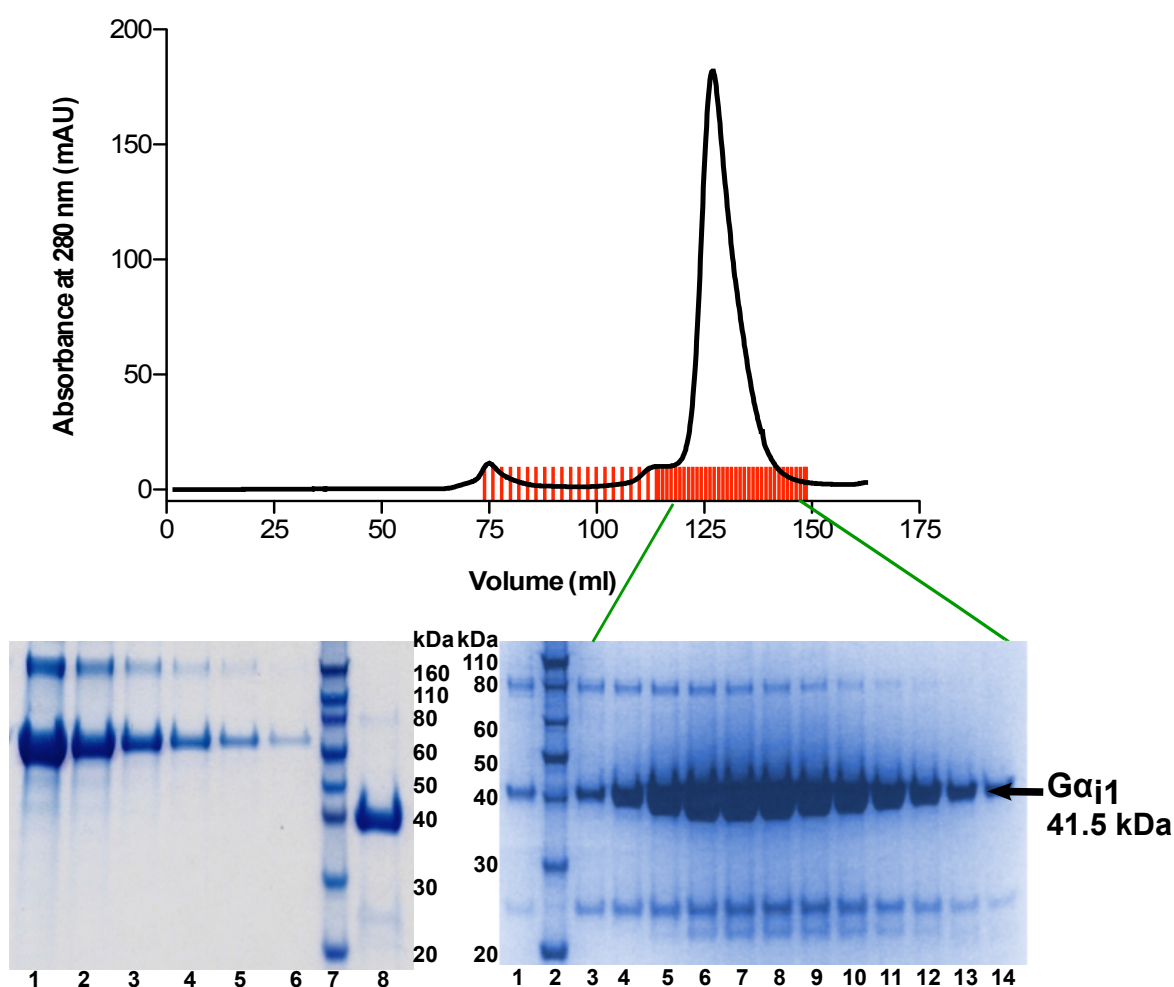


Figure 3.9. Gα_{i1} size exclusion purification.

His₆-Gα_{i1} was further purified using size exclusion chromatography on a Superdex 200 16/100 XK column. After pooling and concentrating the GF eluate, the relative protein concentration was checked against BSA (left gel). Lanes for left gel: 1 – BSA 1.0 mg/ml; 2 – BSA 0.5 mg/ml; 3 – BSA 0.2 mg/ml; 4 – BSA 0.1 mg/ml; 5 – BSA 0.05 mg/ml; 6 – BSA 0.02 mg/ml; 7 – MW markers; 8 – His₆-Gα_{i1}.

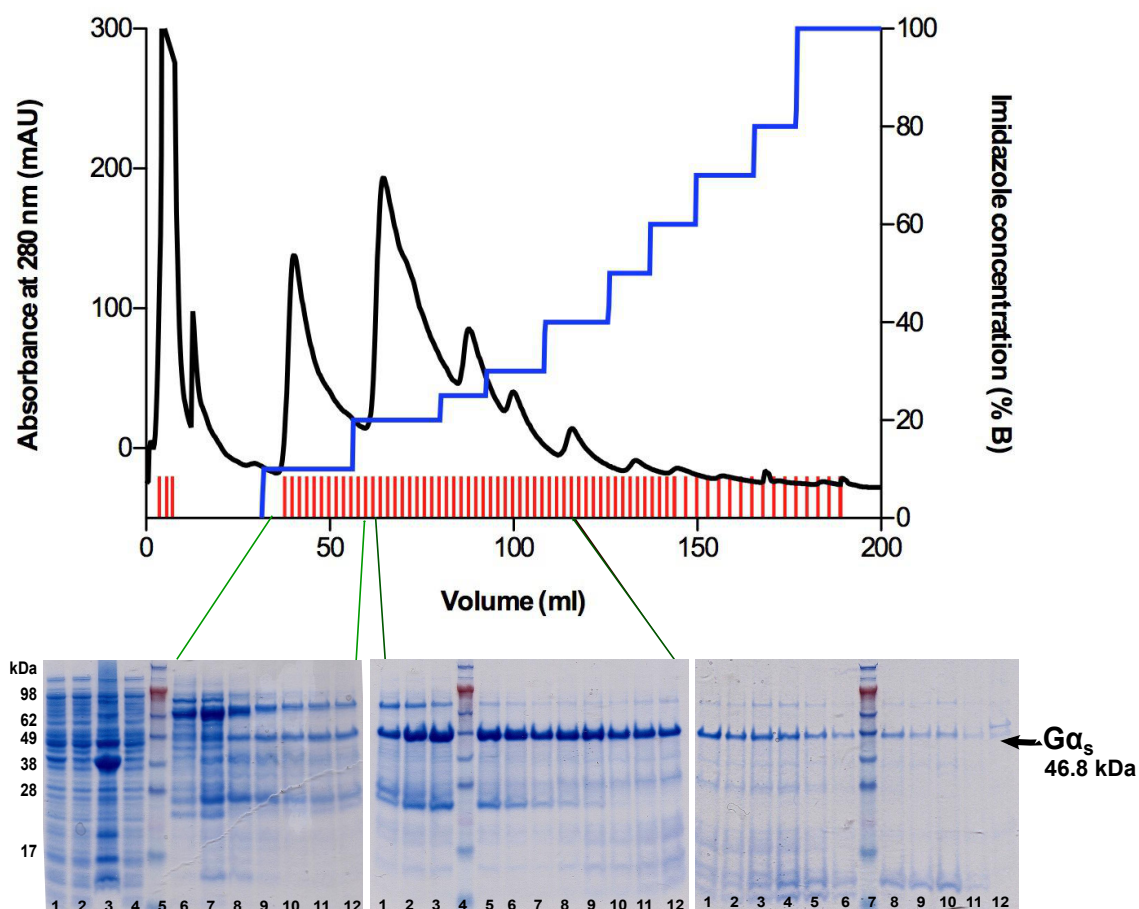


Figure 3.10. $G\alpha_s$ purification.

$\text{His}_6\text{-}G\alpha_s$ was loaded on a 5 ml His|Trap FF column (GE Healthcare) and washed with 180 ml wash buffer. The protein was eluted in small steps of an imidazole concentration gradient (blue line), with the least contaminated fractions eluting between 20-30 % B (centre gel). The green lines indicate which part of the elution profile the gel fractions were from. Red bars indicate fractions. Lanes 1-4 of the left gel show samples from whole cells (lysed), supernatant after centrifugation, pellet after centrifugation, and flow-through from loading the supernatant on the Ni^{2+} column, respectively.

The $G\alpha$ subunits were labelled at their His tags with Ni-NTA Nanogold® (Nanoprobes) and subsequently separated from unlabelled fractions using size exclusion chromatography (SEC) (Figure 3.11).

Nanogold®-labelling efficiency of His₆-Gα_{i1} was 42 % and 59 % for two sets of pooled fractions, respectively, as determined spectroscopically. Of the 0.06 mg His₆-Gα_{i1} used for Nanogold® labelling, approximately 0.03 mg of labelled protein was retrieved after gel filtration to remove unbound gold. Three attempts to label Gα_s with Ni-NTA-Nanogold® gave labelling efficiencies between 4 and 10 %.

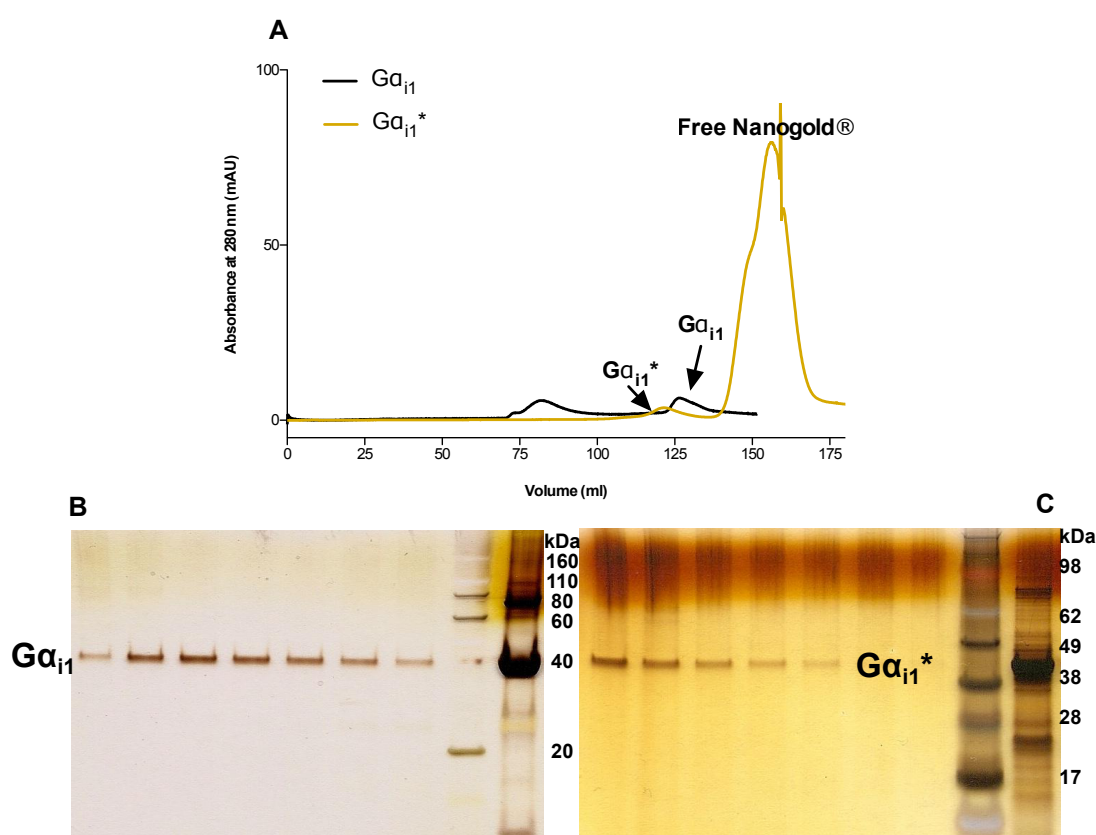


Figure 3.11. His₆-Gα_{i1} and His₆-Gα_{i1}* purified by gel filtration.

One fraction of His₆-Gα_{i1} nickel column eluate or aliquot of Nanogold®-labelled His₆-Gα_{i1}* was applied to a Superdex 200 16/100 XK column. Unlabelled protein (black trace) started eluting after 122 ml and peaked at 127 ml. Gold-labelled protein (gold trace) began eluting after 105 ml and peaked at 122 ml (**B**). The fractions were detectable on silver-stained gels (**B** and **C**). **A**) GF elution profiles of His₆-Gα_{i1} and His₆-Gα_{i1}*. **B**) GF fractions of His₆-Gα_{i1}. **C**) GF fractions of His₆-Gα_{i1}*. (**B** and **C**) Lanes 1-7: GF fractions; (**B**) lane 8: Novex® Sharp unstained protein standard, (**C**) lane 8: SeeBlue Plus 2 prestained protein standard; (**B** and **C**) lane 9: His₆-Gα_{i1} or His₆-Gα_{i1}* prior to gel filtration. Stain: Silver Stain Plus (BioRad).

G α subunit activity was assayed using BODIPY®-GTP γ S by following the fluorescence polarisation of the molecule as it bound the G proteins. A one-phase exponential association curve yielded an observed rate constant, k_{ob} , of $0.24 \text{ min}^{-1} \pm 0.29 \times 10^{-3}$ for His₆-G α_{i1} (Figure 3.12). Saturation binding experiments were used to determine the affinity constant, K_D , of BODIPY-GTP γ S for His₆-G α_{i1} (Figure 3.13).

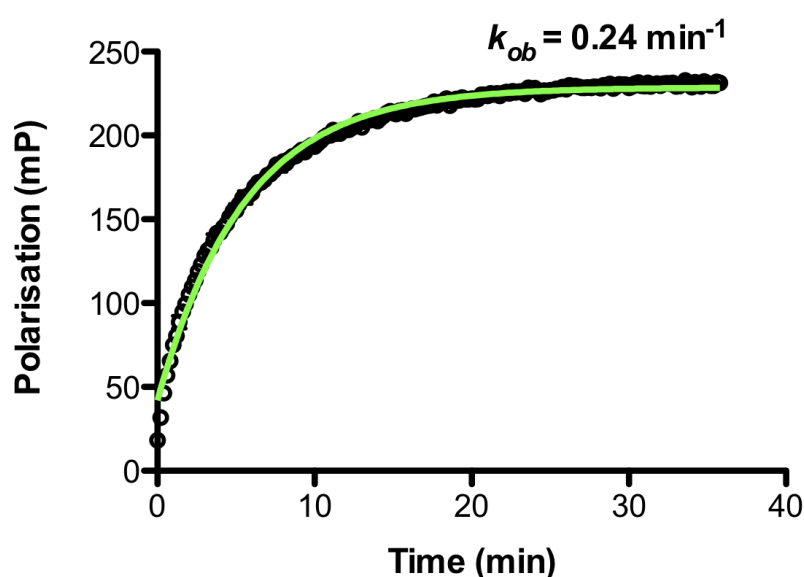


Figure 3.12. Pseudo-first order association kinetics of G α_{i1} -BODIPY-GTP γ S binding.

BODIPY-GTP γ S was injected into wells containing G α_{i1} and the time course of association followed. The data was analysed using a one-phase exponential association equation. The observed rate constant was calculated from the fit: $k_{ob} = 0.24 \pm 2.9 \times 10^{-3} \text{ min}^{-1}$ (SE) (n=6) – errors are too small to be seen. Calculation of the association rate constant, k_a , requires the dissociation rate constant, k_d , to be known.

Serial dilutions of 0-2 μM His₆-G α_{i1} were incubated with 25 nM BODIPY-GTP γ S for one hr and endpoint polarisation recorded at 520 nm. Both assay types used excess unlabelled GTP γ S for non-specific binding. One-site global analysis of the data yielded a K_D of $192 \pm 14 \text{ nM}$ (SE), similar to the $150 \pm 50 \text{ nM}$ determined by

(206)

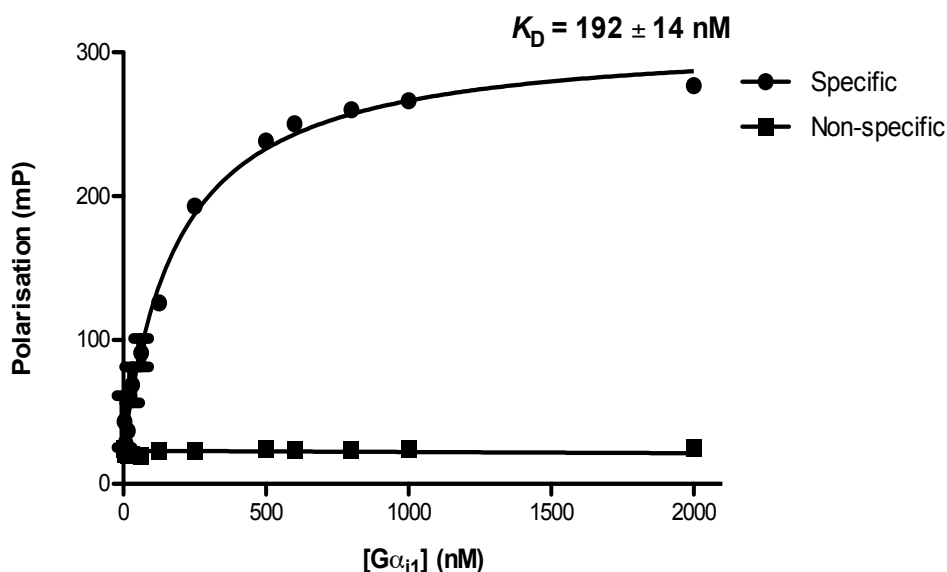


Figure 3.13. One-site global analysis of $G\alpha_{i1}$ -BODIPY-GTP γ S binding.

Fluorescence polarisation saturation binding experiment to determine affinity of $G\alpha_{i1}$ for BODIPY-GTP γ S. The plot is derived from two sets of triplicate data for each curve (i.e. $n=6$). A one-site global fit to the data yielded an affinity constant $K_D = 192 \pm 14$ nM (SE). Errors are too small to be seen.

Injection of 25 nM BODIPY-GTP γ S into wells containing 250 nM $G\alpha_s$ yielded an observed rate constant, k_{ob} , of 1.0 ± 0.2 min $^{-1}$ when the fluorescence data was fitted with a one-phase exponential association curve: $Y = Y_{max} \cdot (1 - e^{-kt})$ (Figure 3.14). This is four times faster than the k_{ob} for $G\alpha_{i1}$, and the fluorescence intensity plateaued and then began to drop off again after eight minutes, whereas $G\alpha_{i1}$ continued to bind BODIPY-GTP γ S for a further ~30 minutes. While the affinity constant of BODIPY-GTP γ S for $G\alpha_s$ was not determined here, the more rapid association and dissociation potentially implies a lower K_D than that for $G\alpha_{i1}$, supported by ⁽²⁰⁶⁾, who determined a K_D of 70 nM for the interaction. These assays showed conclusively that the $G\alpha$ subunits were active.

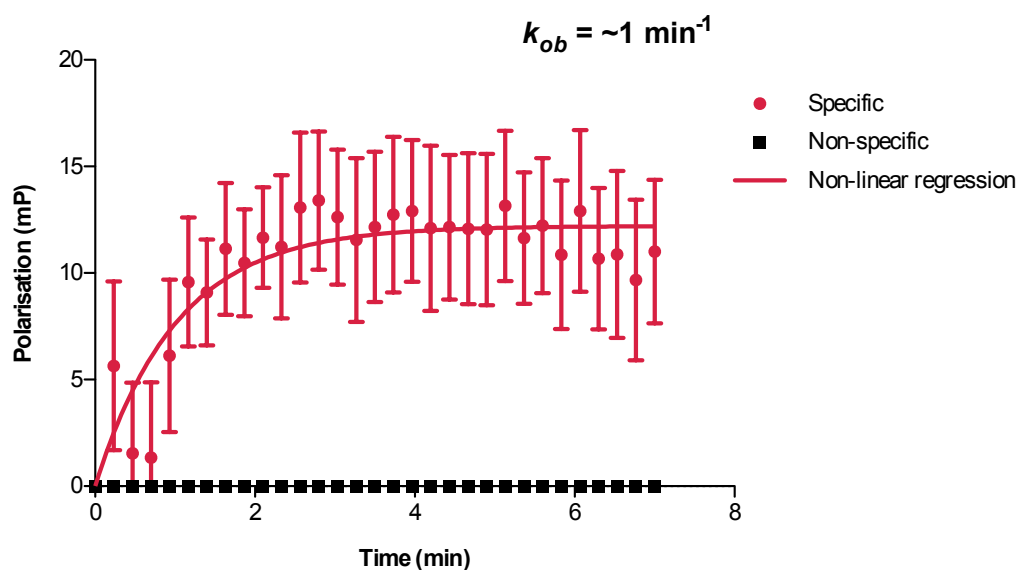


Figure 3.14. Pseudo-first order association kinetics of $G\alpha_s$ -BODIPY-GTP γ S binding.

BODIPY-GTP γ S was injected into wells containing $G\alpha_s$ and the time course of association followed. The data was analysed using a one-phase exponential association equation. The observed rate constant was calculated from the fit: $k_{ob} = 1 \pm 0.2 \text{ min}^{-1}$ (SE). It was unclear why the errors were so large on a triplicate data set, but the assay indicated the protein was active, which was the primary aim.

3.2.4. Membrane scaffold protein 1D1

Approximately 11 mg H7-MSP1D1 was obtained per litre of culture. The protein was relatively easy to express, with induction complete within three hrs, and purification was straightforward (Figure 3.15). For SPR experiments using an anti-His antibody for ligand capture, the His-tag had to be cleaved off the scaffold protein. A 1:10 mol:mol TEV:H7-MSP1D1 ratio was sufficient for complete cleavage, and the His-tag and His₆-TEV were removed from the reaction mixture by capture on a HisTrap FF column (GE Healthcare) (Figure 3.16).

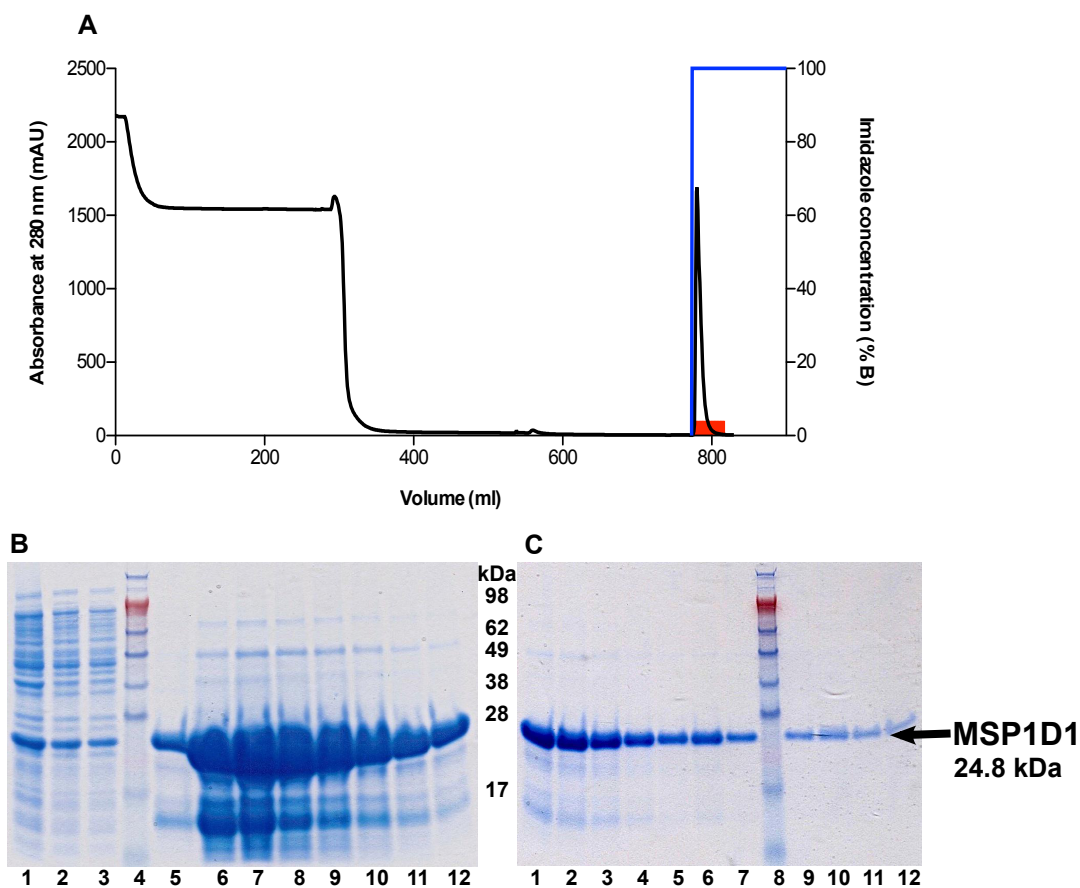


Figure 3.15. H7-MSP1D1 Ni^{2+} purification.

MSP1D1 was purified by IMAC. The supernatant from solubilised cells was loaded on a 5 ml Ni^{2+} affinity column, washed extensively with three separate wash buffers and eluted in a single step with 400 mM imidazole. The protein eluted in a sharp peak (A). SDS-PAGE gels (B and C) showed highly concentrated and relatively uncontaminated scaffold protein. Lanes 1-3 in B show samples of lysed whole cell (lane 1), supernatant loaded on the column (lane 2) and supernatant flow-through from the Ni^{2+} column (lane 3), suggesting that more protein could be obtained by reloading the flow-through. Lanes 4 and 8 in B and C, respectively, are MW markers.

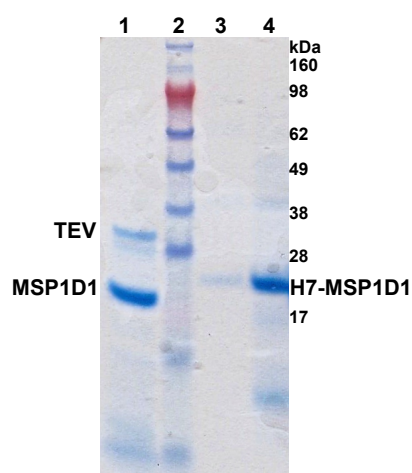


Figure 3.16. H7-MSP1D1 TEV protease cleavage

SDS-PAGE gel showing H7-MSP1D1 before and after TEV cleavage. Heptahistidine MSP1D1 was cleaved overnight at 4 °C with a 1:10 mol:mol ratio of TEV:H7-MSP1D1. The His-tag and His₆-TEV were removed using a Ni²⁺ affinity column. Lane 1: the reaction mixture prior to loading on the Ni²⁺ column; Lane 2: MW markers; Lanes 3 and 4: uncleaved H7-MSP1D1. Stained with Coomassie Brilliant Blue.

3.3. Ternary complex formation

Two methods were used to try to purify the ternary complex of ligand-bound NTS1 coupled to a G α subunit, primarily to ensure that the sample placed on the EM grid was homogeneously in the ternary complex, but also as another means to show evidence for the interaction. The first was to bind NTS1 to an NT column and then incubate it with G protein, wash the column, elute the NTS1 as usual, and run gels of the elution. The second was to incubate the ligand, receptor and G protein together and then perform size exclusion chromatography on the sample. Gel filtration showed no evidence of complex formation in detergent-solubilised or nanodisc samples (Figure 3.17). Silver-stained gels of fractions eluted from the NT column did not

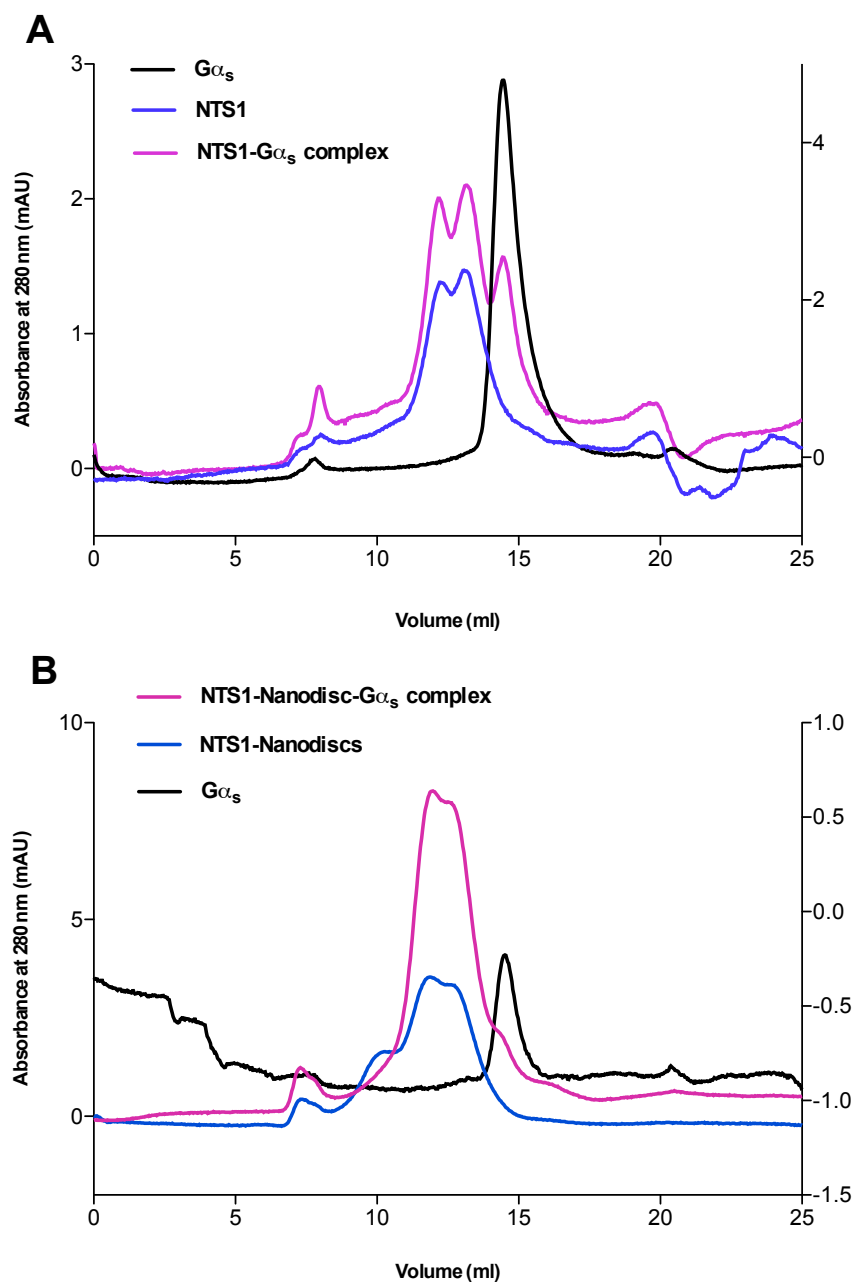


Figure 3.17. Gel filtration analysis of ternary complex formation.

NTS1 (**A**) or NTS1-nanodiscs (**B**) were incubated with NT and with His₆- $G\alpha_s$ and then loaded onto a Superdex 10/300 GL column and the trace monitored against traces of the receptor or G protein alone to determine if the ternary complex had formed. No complex formation could be detected in either trace. The shoulder on the nanodisc trace in B is most likely aggregate or contaminant.

show any evidence of complex formation. According to Holger Stark (personal communication, Max-Planck-Institute for Biophysical Chemistry, Göttingen), the majority of macromolecular complexes dissociate during gel filtration or chromatography, and are more ideally purified by a mild fixation process coupled with sucrose gradient ultracentrifugation ⁽²⁰⁷⁾.

3.4. DNA lattice formation

3.4.1. Oligo-neurotensin conjugation

DNA lattices were prepared as described ⁽¹⁷⁵⁾ with cooling from 90 °C to 4 °C over 72 hrs. One oligonucleotide was functionalised with either a 5' thiol modifier on a C₆ linker to which reduced Cys-NT was conjugated by oxidation, or tris-nitrilotriacetic acid (tris-NTA) ⁽¹⁸⁰⁾. Unconjugated material was removed by preparative gel electrophoresis (Figure 3.18).

3.4.2. DNA lattice microscopy

Uranyl acetate-stained DNA lattice was readily visible under EM, both across the holes and on the carbon areas of holey carbon grids (Figure 3.19). The periodicity was striking and occurred over large areas of the grid. The lattice could stretch almost unbroken across micrometres of grid area. The 3.5 turn lattice was more fragile than the 2.5 turn lattice, and more frequently had tears or holes in it. For cryo-EM the

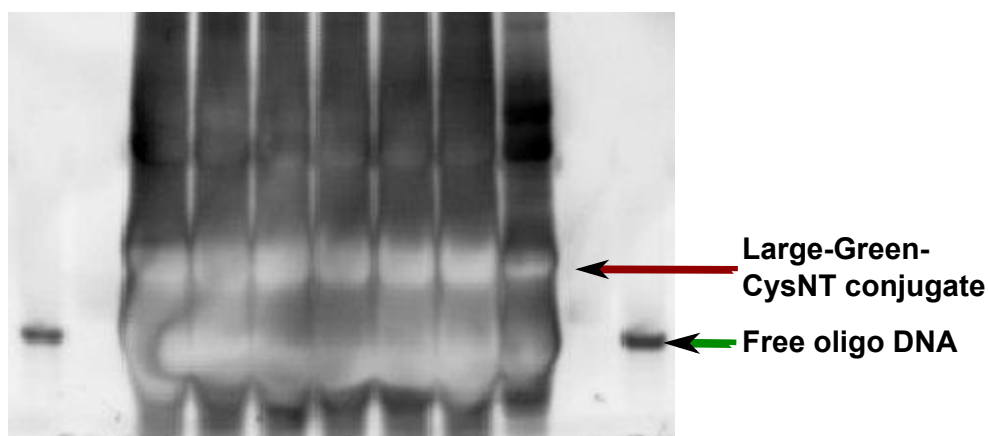


Figure 3.18. DNA-NT conjugate gel purification.

PAGE separation of NT-conjugated Large Green from free oligonucleotide. The seven central lanes contain the conjugate with free oligonucleotide. The outer lanes, with one black band in each, contain free oligonucleotide, and act as markers. The red arrow indicates the NT-Large-Green conjugate, the green arrow indicates unconjugated DNA. The conjugate band was cut from the gel, crushed and incubated with TAE buffer to extract the conjugate. The white bands indicate saturation of the scanner. Diluted DNA appears as black bands as seen in the free oligo lanes running down the sides of the gel.

sample had to be pipetted vigorously prior to adsorption onto the grid, and also when applying the sample to the grid, in order to prevent folding and doubling over of the lattice; however, this treatment did not damage the lattice much – it is relatively robust. Layered lattice resulted in twinned and imperfect diffraction patterns when images were Fourier transformed, and the images could not be used for structure resolution.

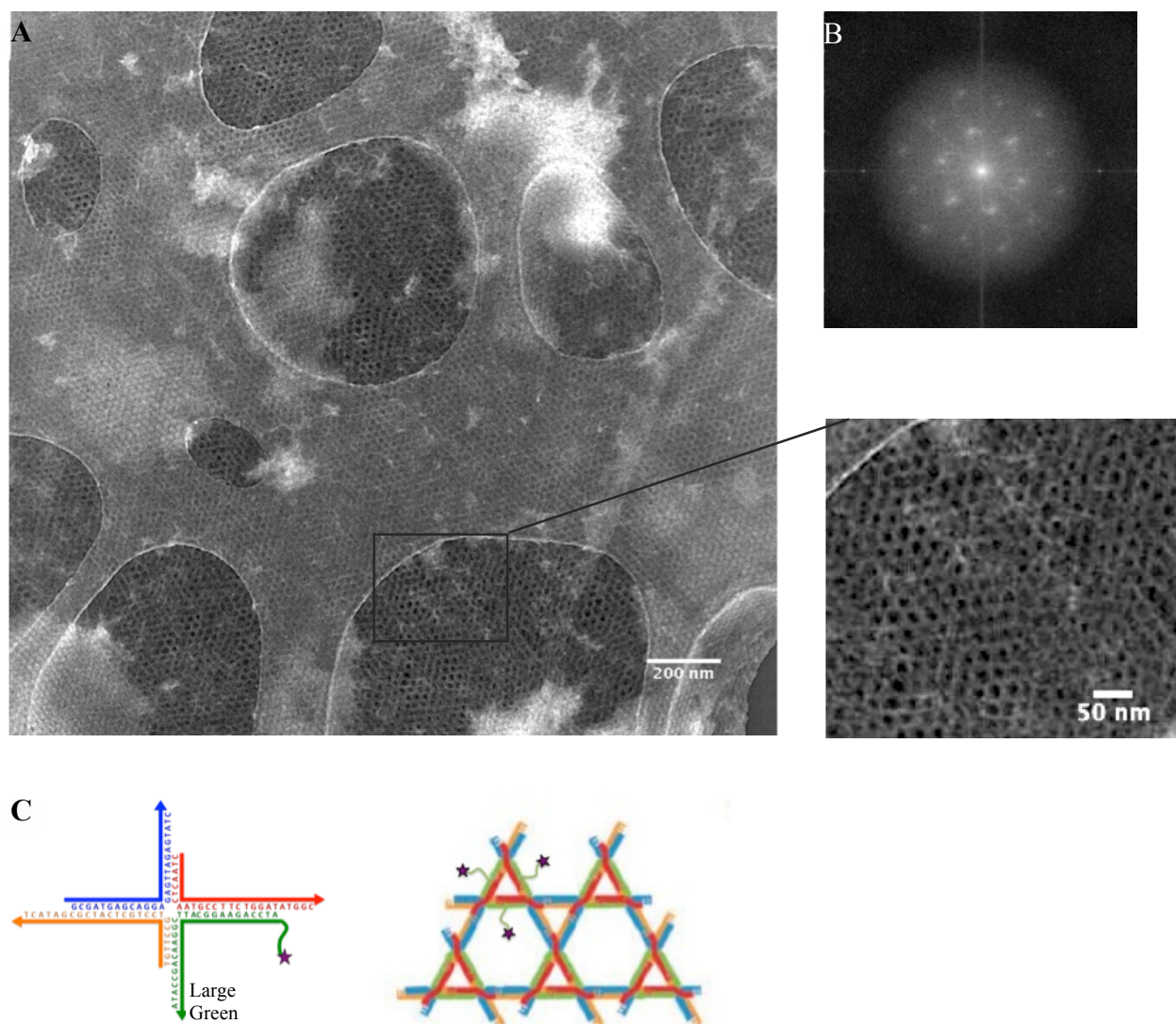


Figure 3.19. Transmission electron micrograph of negatively stained, NT-functionalised large lattice.

A: NT-functionalised DNA lattice negatively stained with 2 % (w/v) uranyl acetate. The lattice extends across the holes of a holey carbon grid, with the periodicity of the lattice structure formed clearly apparent. A magnified image (right) shows the DNA strands light against the negative stain, and the hexagonal, periodic structure of the lattice. **B:** The periodicity is observed in a Fourier transform of the micrograph. **C:** Schematic diagram of the lattice structure showing the Holliday junction formed by the oligonucleotides with one strand (Large Green) thiol-modified (left) and the Kagome lattice structure formed upon annealing (right). The lattice constant is 18 nm. (Schematic from ⁽²⁰⁸⁾).

3.4.3. 2D electron crystallography

Single particle reconstructions rely on the molecule of interest sampling as much of the Euler or orientational space as possible. Crystal structures, however, require all particles to repeat in a highly ordered, symmetric manner. The periodic, $p3$ -symmetrised structure of the DNA lattice forms a 2D crystal that can be imaged and processed to solve its structure using standard 2D electron crystallography methods. Images were taken at three tilt angles: 0° , 30° and 45° and processed using 2dx⁽²⁰⁹⁾. Inbuilt scripts were used for automatic spot selection and unbending, and the contrast transfer function (CTF) was corrected for each image. A low-resolution structure (~ 40 Å) of negatively stained 3.5 turn lattice (Figure 3.20) and a higher resolution cryo structure (~ 15 Å) for the 2.5 turn lattice were solved (Figure 3.21), the latter by Thomas H. Sharp (Physics Department, University of Oxford).

These images and structures show that the lattice forms easily visible and highly periodic 2D crystals reproducibly and over large areas of the EM grids, where its presence can be used to rapidly find small protein particles on the grid when it has been incubated with the lattice.

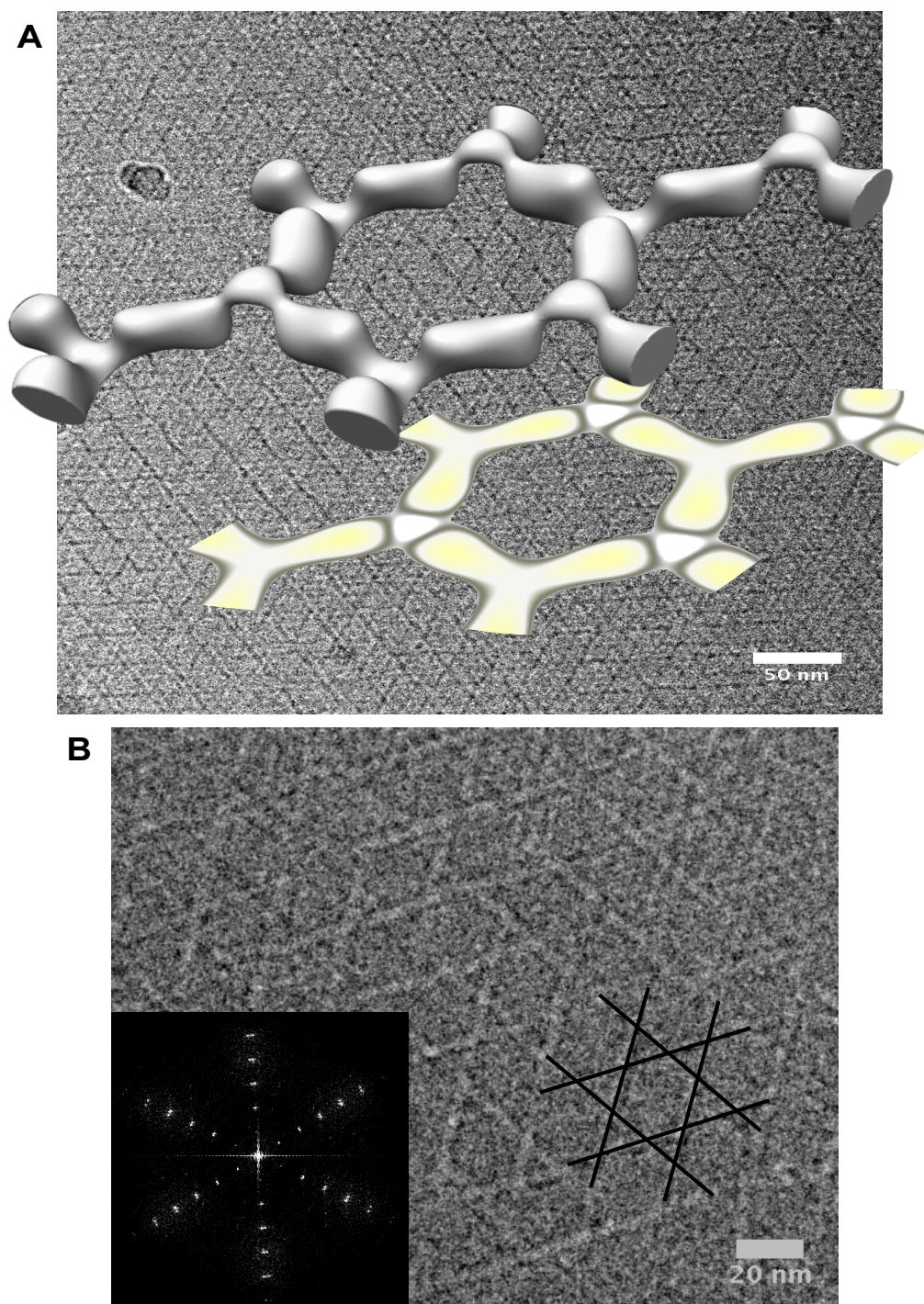


Figure 3.20. Cryo-EM micrographs and crystal structure of 3.5 turn lattice.

A: Low resolution (40 Å) crystal structure of the 3.5 turn lattice solved by 2D electron crystallography with a 2D projection of the same structure (yellow) on a background of a cryo-EM micrograph of the lattice. The “over-under” structure of the corners of the hexagon, where the triangles form, show the three-way-weave structure of the Kagome lattice. The scale bar refers to the background micrograph. A series of images of lattice negatively stained with Nanovan™ (Nanoprobes) and recorded at tilt angles of 0, 30 and 45° were processed using 2dx⁽²⁰⁹⁾ to solve the 3D structure. **B:** Magnified section of the micrograph in **A**, with contrast inverted. The black lines trace the kagome lattice structure, and a Fourier transform shows the perfect periodicity of the lattice.

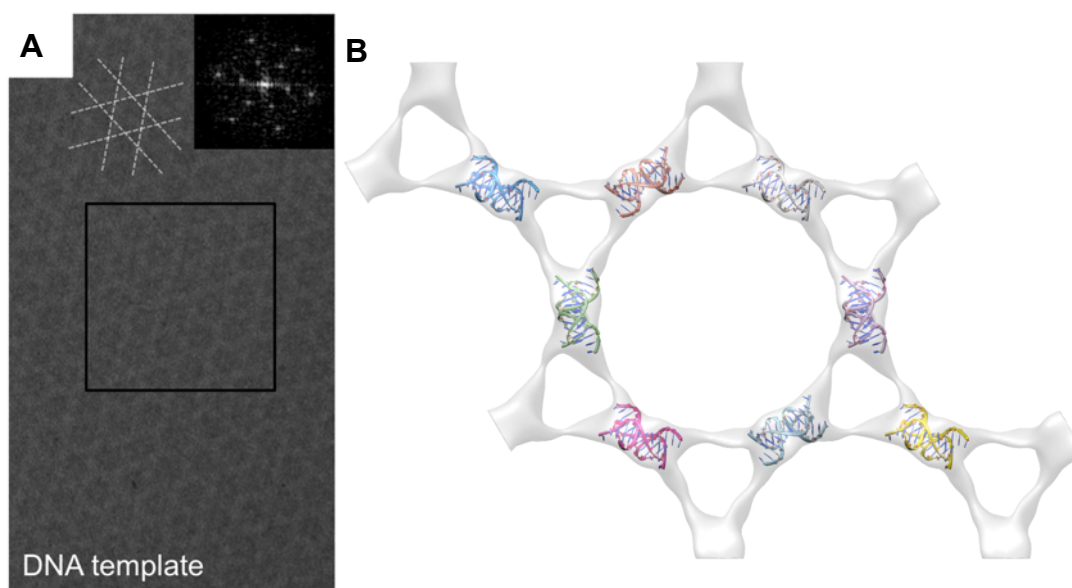


Figure 3.21. Cryo-EM micrograph and crystal structure of the 2.5 turn lattice.

A: Cryo-EM micrograph of the 2.5 turn lattice **B:** cryo structure of the 2.5 turn lattice at ~15 Å resolution showing Holliday junctions fitted into the crossover points of the three-way weave of the lattice. (A: image from ⁽¹⁷⁹⁾; B: data collected, processed and image prepared by Thomas H. Sharp).

3.5. Nanodisc formation

NTS1 was reconstituted into nanodiscs as a means to form soluble particles of membrane-bound receptor that could be accessed from both sides, dialysed, concentrated, and were big enough to be seen on an EM grid. The optimal lipid types and ratios of lipid:MSP:(FLAG-)NTS1 were empirically determined over several test batches of nanodiscs using literature from the Sligar group for reference ^(69, 75, 76, 171), and knowledge of NTS1 lipid and handling requirements. The first indication of how well the reconstitution had worked was the size of the pellet after centrifuging the

sample prior to gel filtration. This was determined after EM visualisation of several batches and comparisons of the GF elution peaks. A large pellet indicated that the lipid:protein ratios were wrong and much of the sample had gone into aggregates; no pellet suggested that either the whole sample had reconstituted perfectly, or not all of the detergent had been removed by Biobeads, and reconstitution had failed; a small pellet generally suggested that most of the sample had successfully reconstituted. Depending on the lipid type and ratio to protein, in most cases the pellet constituted an acceptable loss.

The second indication of successful reconstitution was the size of the aggregate peak in the void volume (at about 8 ml) of the gel filtration column compared to the sample peak (Figure 3.22 and Figure 3.23 - usually at approximately 12 ml). A smaller aggregate peak is desirable, and in most cases was one third to a half the height of the nanodisc peak. However, despite this, the BPL nanodiscs whose gel filtration profile is shown in Figure 3.22, were relatively homogeneously formed, despite their small GF peak (see Figure 3.23D). Figure 3.23 shows representative gel filtration profiles of empty and loaded PC:PG nanodiscs, in this case empty discs prepared with H7-cleaved MSP (noHisMSP-EMPTY-PC:PG) and FLAG-NTS1-loaded discs prepared with H7-MSP (MSP-FLAG-NTS1-PC:PG). Stokes radii/diameters were calculated from the calibrated column values, and molecular masses extrapolated accordingly. Diameters for the loaded PC:PG or PC:PE discs were 10-10.4 nm, and slightly smaller for the PPPC discs at 9.4-9.6 nm. Empty discs tended to be 0.5-0.7 nm smaller than the respective loaded discs. The diameters correspond to molecular masses of approximately 200 ± 15 kDa for the loaded PC:PG discs, with empty discs 10-20 kDa

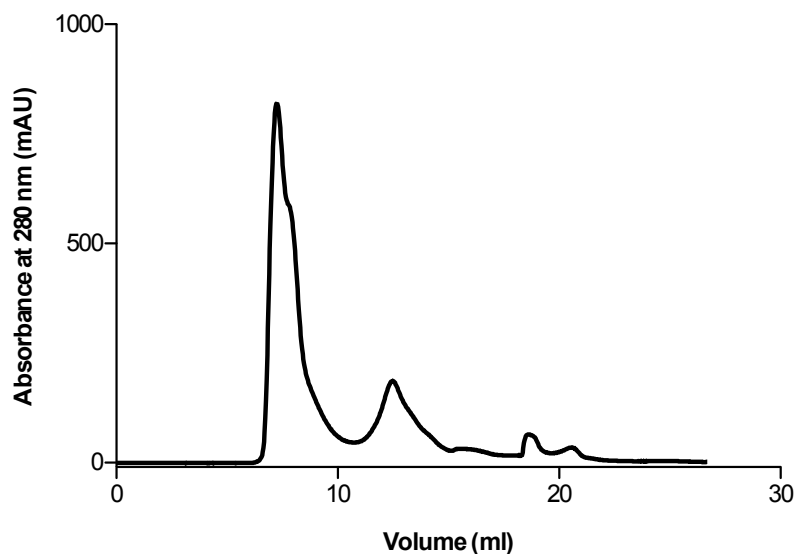


Figure 3.22. Gel filtration profile of empty BPL nanodiscs.

Empty nanodiscs were formed using a 1:70 ratio of MSP:BPL. The pellet after centrifuging before gel filtration was large, and the aggregate peak in the void volume (at ~ 8 ml in this figure), is much larger than the peak for formed nanodiscs (~12 ml).

less. PPC discs were 160-180 kDa, with empty discs up to 15 kDa lighter. The Stokes radius, of course, assumes a spherical particle, thus overestimating the mass of a disc-shaped object, so the number of lipid molecules calculated from the area of the disc is likely to be lower than that calculated for the molecular mass. This is, in fact, the case.

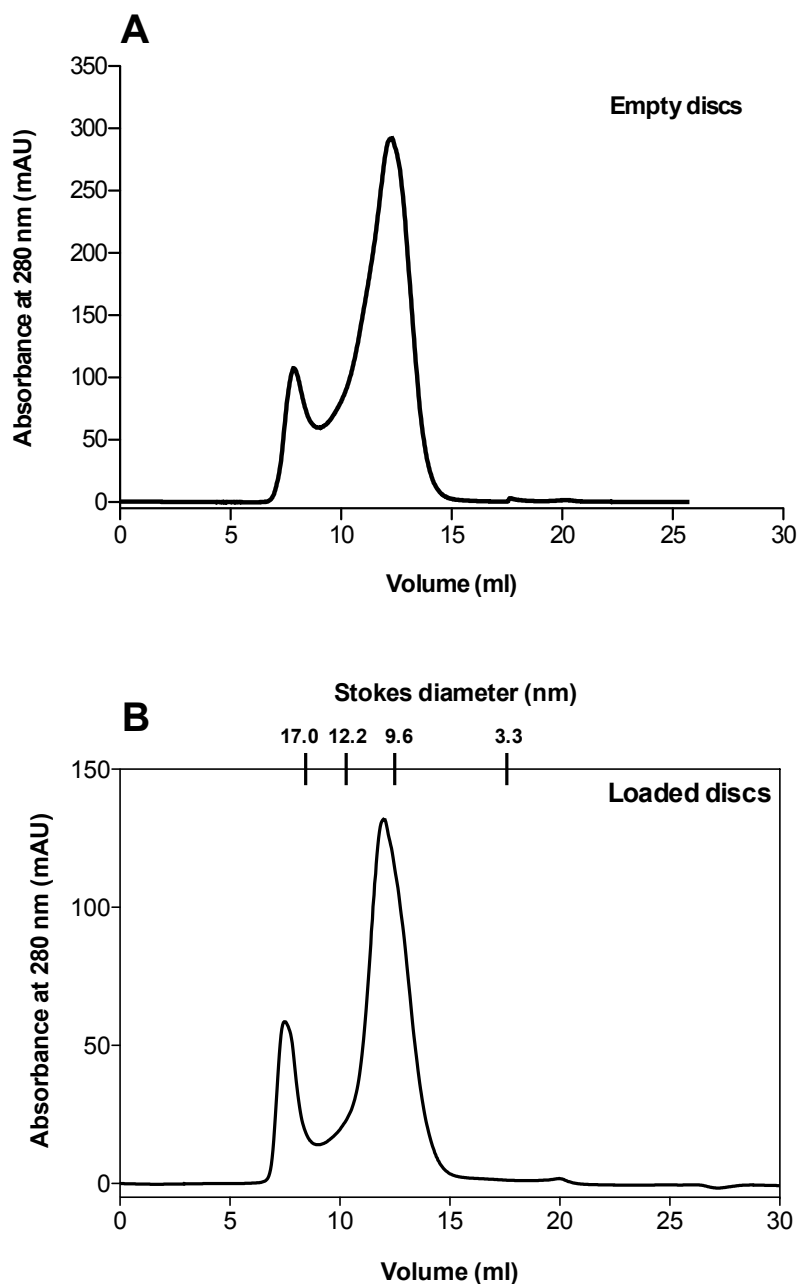


Figure 3.23. Gel filtration profiles of empty and loaded nanodiscs.

Representative gel filtration profiles of empty (A) and FLAG-NTS1-loaded (B) PC:PG nanodiscs. For these particular samples the empty discs were formed from His-tag-cleaved MSP, and the MSP used for the loaded discs had not been cleaved. The Stokes diameter for the FLAG-NTS1 loaded discs was calculated from values for the calibrated gel filtration column, giving a diameter of 10.3 nm, while the size for empty discs was 9.4 nm. The void volume of the column was approximately 8 ml, and the nanodisc peak was usually near 12 ml.

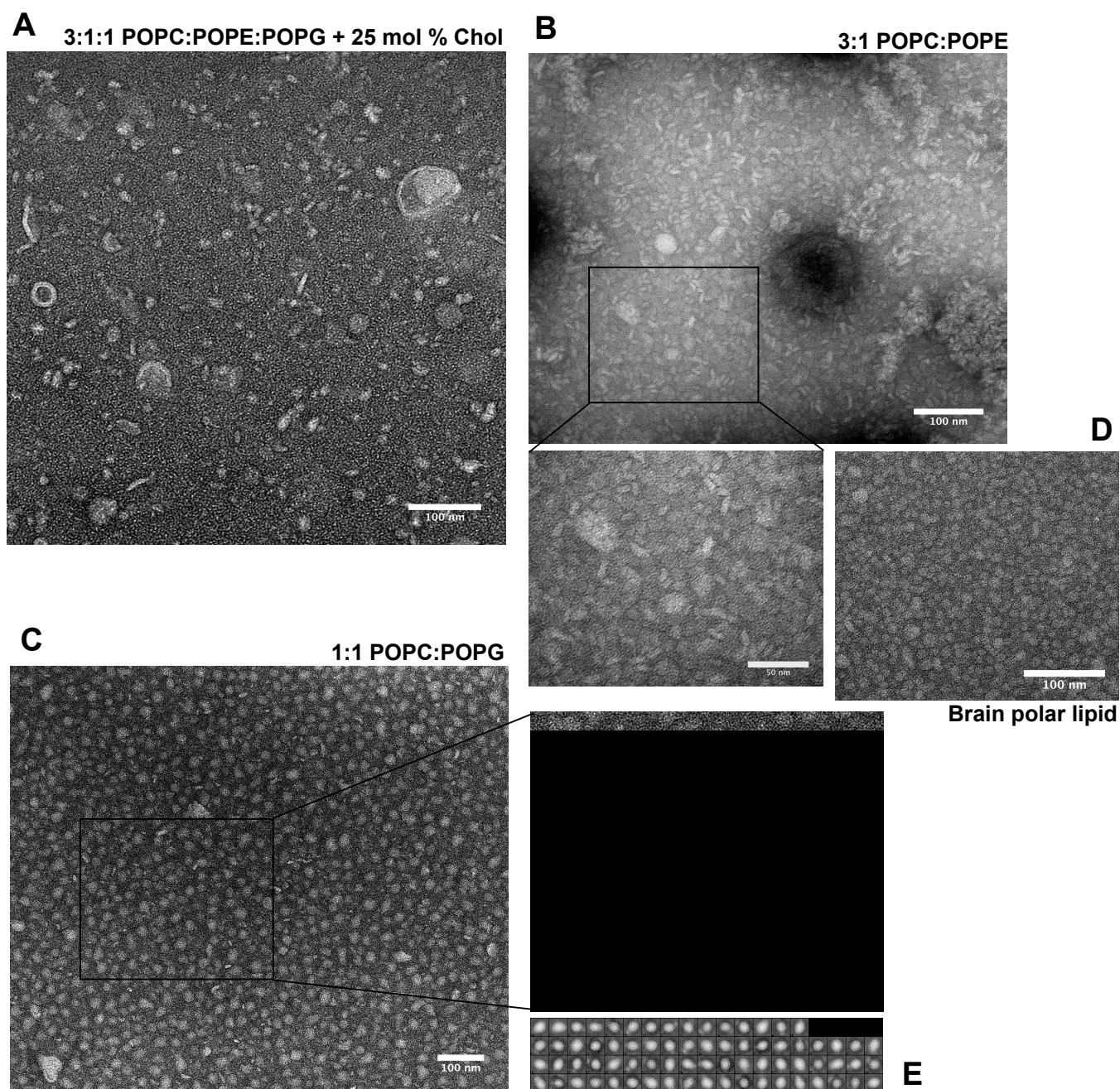


Figure 3.24. Negative stain EM images showing nanodiscs prepared with different lipid mixtures.

Nanodiscs were prepared with 3:1:1 POPC:POPG:POPE with 25 mol % cholesterol (A), 3:1 ratio of POPC:POPE (B), a 1:1 ratio of POPC:POPG (C) or BPL (D) (the latter prepared by Patricia Dijkman, University of Oxford, imaged by RJA). PC:PG and BPL form homogeneous populations, while PC:PE discs form, but appear to include large aggregates of discs and possibly free MSP (B), although this may be a staining artefact. Stain was 2 % uranyl acetate. E: reference-free class averages of 10-12 nm PC:PG discs (prepared using EMAN2)⁽¹⁸⁹⁾. Box size is 18.5 nm.

Taking the PC:PG discs as an example, and using lipid areas of 0.56 nm^2 for POPG and 0.66 nm^2 for POPC ⁽²¹⁰⁾, subtracting 1 nm from the radius of the disc for the diameter of an α -helix (the MSP), and subtracting the area of NTS1 based on a radius of approximately 2 nm, it can be calculated that there are approximately 62 lipid molecules per leaflet (or 70 for empty discs). This, incidentally, is the number of lipid molecules put into the reaction mixture in most cases, where a 1:60 MSP:lipid ratio was used, and also correlates very well with data from the Sligar laboratory indicating a typical lipid number of 62 lipid molecules per leaflet for POPC only discs, where a slightly larger lipid area for POPC was used ^(75, 76). In effect, NTS1 would be surrounded by a layer of just over three lipid molecules in the nanodisc. Calculating the number of lipid molecules from the molecular mass would give almost 20 lipid molecules more per nanodisc.

Coomassie-stained and anti-FLAG western blot gels were used to check that peak fractions from the GF column contained both H7-MSP1D1 and FLAG-NTS1 (Figure 3.25). Fractions within the sample peak that contained both were pooled prior to enrichment using an anti-FLAG resin. As can be seen from the gels in Figure 3.25, a fairly significant amount of FLAG-NTS1 was lost in the aggregate peak. It is hoped that further optimisation of lipid types and lipid:protein ratios in terms of the charge on the lipids and the amounts of lipid included in the reaction, will decrease the amount of receptor lost in the formation of nanodiscs. After enrichment, the final nanodisc sample was pure, and approximately 1-2 ml of $\sim 1 \text{ }\mu\text{M}$ could be obtained (Figure 3.25, C and D).

In most cases, disc formation was checked using negative stain EM (Figure 3.24). Once acceptable working ratios had been determined, nanodisc formation was relatively straightforward and reproducible. A 3:1:1 mixture of POPC:POPE:POPG with 25 mol % cholesterol produced nanodiscs with large size disparity (Figure 3.24A), but this mixture was initially tried because NTS1 is known to be highly active in this particular lipid mixture (Peter Harding, PhD thesis, University of Oxford). A 1:1 mixture of POPC:POPG was very successful and reproducible for nanodisc formation, and NTS1 reconstituted in these nanodiscs was able to bind to an NT column or to NT on an SPR chip, albeit in small quantities. A 3:1 mixture of POPC:POPE produced heterogeneous nanodiscs interspersed with aggregates (Figure 3.24B), but it is possible these aggregates came about as a result of the uranyl acetate (UAc) used for staining, given that it is acidic and POPE is basic. A 1.07:1.5:1 mixture of BPL:POPC:POPG previously used for the μ opioid receptor⁽²¹¹⁾ gave a gel filtration profile similar to PC:PG alone, apart from a much larger aggregate peak, but EM images were not collected, so size heterogeneity could not be assessed. BPL formed relatively homogeneous populations of empty nanodiscs (prepared by Patricia Dijkman, University of Oxford, EM images by RJA), but loaded BPL discs have not yet been tested. PC:PG nanodiscs were the most homogeneously-sized samples, but did not appear to display much NT-binding activity. Whether this is a steric or lipid-dependent effect is as yet unclear but the discs did not bind the NT column in large amounts, although small quantities could be enriched this way (Figure 3.26), and binding to NT immobilised to an SPR chip gave the correct affinity value, but the signal was unexpectedly small (see Section 5.5).

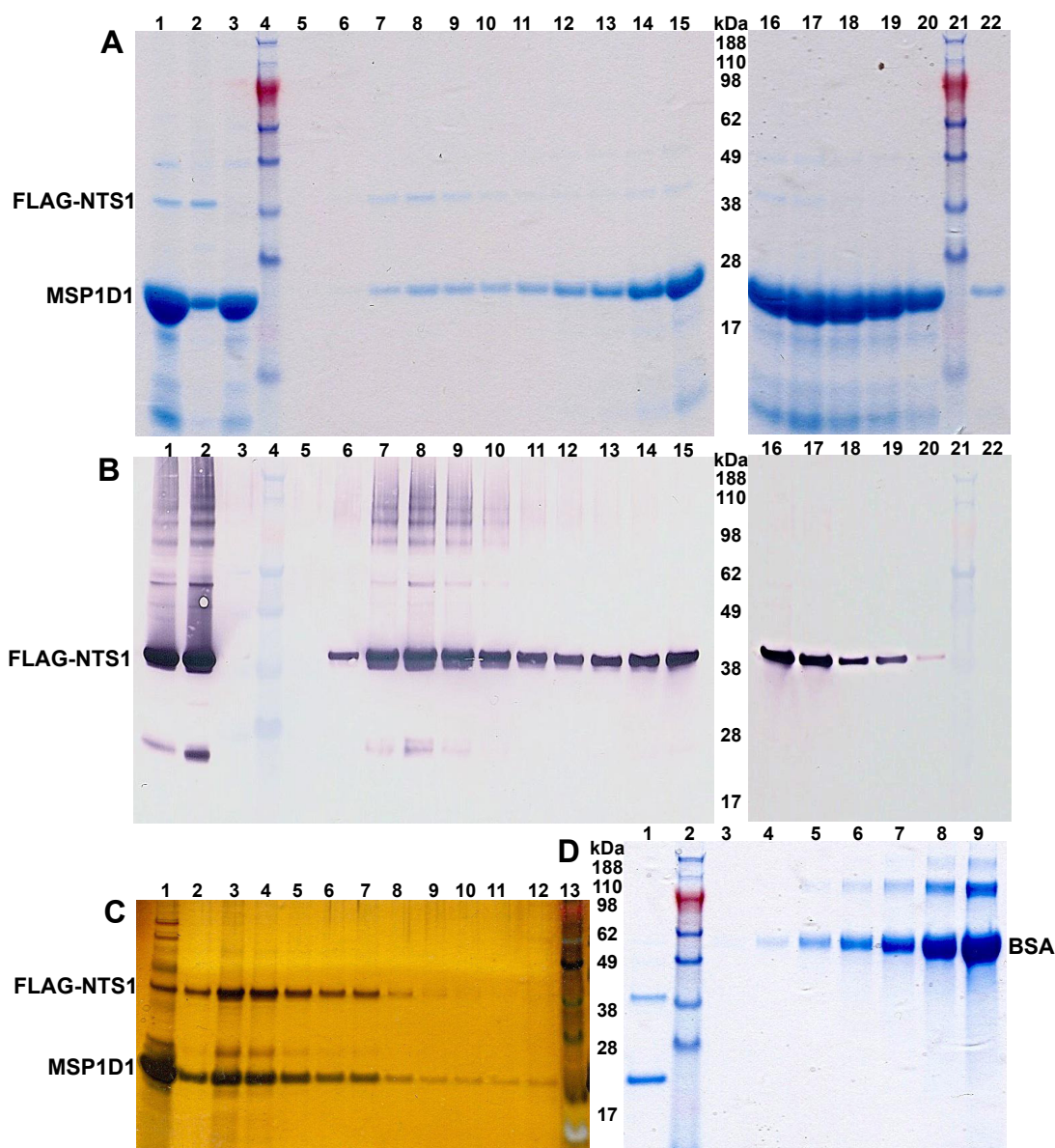


Figure 3.25. SDS-PAGE gels and blots of purification and enrichment of nanodiscs.

Nanodiscs were purified by gel filtration (**A** and **B**), and FLAG-NTS1-loaded discs enriched using an anti-FLAG column (**C**). The Coomassie-stained gels in (**A**) show the same samples as the western blots in (**B**). Lanes 1-3 show the sample that was loaded on the GF column, the pellet obtained from centrifuging the nanodisc sample prior to gel filtration, and the pellet obtained from a sample of empty nanodiscs, respectively. Lanes 6-12 are fractions from the aggregate peak in the void volume, and lanes 13-22 are fractions from the nanodisc peak approximately 11-13 ml. Lanes 4 and 21 are MW markers. **C**: fractions eluted from the anti-FLAG column used to enrich loaded nanodiscs. Lane 1 is the sample loaded on the column, lane 13 is MW markers. **D**: lane 1 shows a sample of enriched FLAG-NTS1-PC:PG nanodiscs after pooling, concentration and dialysis. Lanes 3-9 are 0.01, 0.02, 0.05, 0.1, 0.2, 0.5 and 1 mg/ml BSA for concentration comparison.

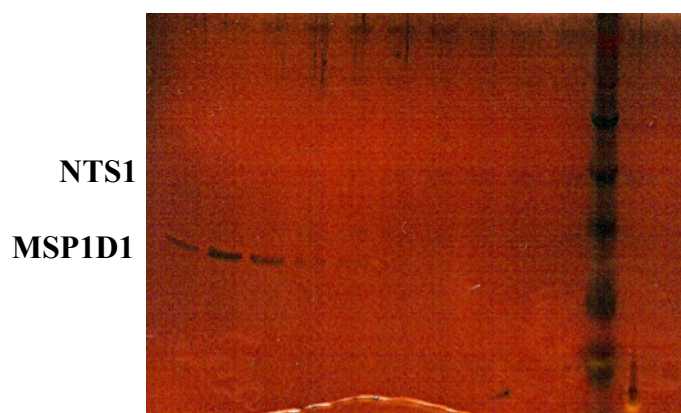


Figure 3.26. NT column fractions of NTS1 nanodisc purification.

NTS1-loaded nanodiscs were able to be purified using an NT column, albeit in small quantities. This demonstrated that the receptor was active in nanodiscs. NTS1, characteristically understained, is just visible in this silver-stained gel, while the scaffold protein is clear in the first few fractions.

In summary, this section shows that NTS1 can be reproducibly reconstituted in populations of homogenously-sized nanodiscs in a functional form. The nanodiscs can be concentrated, dialysed and flash-frozen (as were the nanodiscs shown in Figure 3.24), and have several other advantages over liposomes including that they are small and soluble but still constitute a lipid environment for the receptor. They are also large enough to be seen easily under the EM. NTS1 reconstituted in nanodiscs made it possible to carry out some novel experiments with G protein coupling, to be discussed in the next sections, that otherwise may not have been possible.

3.6. SPR chip preparation

pH scouting was undertaken to ensure that proteins coupled to the SPR chip surface were not denatured during the coupling process, and to ascertain the optimal conditions for coupling. It was thus determined that the optimal pH values for His₆-Gα_{i1} and His₆-Gα_s coupling were 5.0 and 5.5 respectively. The optimal coupling pH for ovalbumin was pH 4.0, as was the pH for the anti-His antibody, as shown by the binding profiles of these proteins when injected across an unmodified chip surface. If the signal is large and rapidly returns completely to baseline when washing begins, the protein is not aggregated by is highly pre-concentrated, a desirable combination.

3.7. Conclusion

This chapter has described the purification and preparation of the components of the signalling system to be used to detect GPCR-G protein coupling. The various proteins, NTS1, MSP1D1, TEV protease, and the Gα subunits, were purified and their activity assayed where appropriate. DNA lattices were formed and their structures solved. Nanodiscs were formed and their preparation optimised for homogeneous disc formation, and imaged under negative stain EM.

Chapter 4 - Protein-protein interactions: Electron microscopy

4.1. Introduction

Electron microscopy was used in this thesis to study NTS1 on its own and in complex with $G\alpha$ subunits. While low-resolution structures of NTS1 in its active and inactive conformations have been solved using SPA (PhD thesis, Daniele N. Selmi, University of Oxford), and the former repeated here from a smaller, independent data set, the lower size limit for SPA is regarded by most in the cryo-EM community as ~ 400 kDa. NTS1 is one-tenth of that size. We have proposed that the use of a functionalised DNA lattice improves the resolution attainable in the microscope by various means (discussed in Chapter 2), and are working toward obtaining a cryo-structure of the ternary complex of ligand-bound NTS1 coupled to $G\alpha$.

To that end, Chapter 4 describes initial studies on the coupling of NTS1 to $G\alpha_{i1}$ and $G\alpha_s$ using negative stain and gold-labelled proteins, showing that receptor-G protein interactions can be visualised by EM ⁽¹⁷⁹⁾. This is of striking significance since it opens the way potentially for the structural study, using EM, of these interactions using frozen hydrated samples in their native state, the ultimate aim of this work. Indeed, not long after our arrays were published, a negative stain structure of the detergent-solubilised β_2 -adrenergic receptor in complex with heterotrimeric G_s was

published ⁽²¹²⁾. Solving the structures of signalling complexes in their native states, without thermostabilising mutations or other, potentially interfering modifications, is critical for our further understanding of the mechanisms of action of these signalling pathways. In this thesis, NTS1-G α coupling was studied in detergent and in nanodiscs using Nanogold®-labelled G proteins with some limited cryo-EM performed on unlabelled protein, providing some understanding of the best conditions for the study of the system and the limitations of the technique.

4.2. Electron microscopy

4.2.1. DNA-protein arrays

His₆-G α_{i1} was linked by its His-tag to the tris-NTA lattice via a Ni²⁺-mediated interaction (K_D in the nanomolar range), whilst NTS1 was linked to the NT-functionalised lattice via the ligand ($K_D \sim 1$ nM). DNA lattices and protein arrays were always observed under negative stain before cryo-imaging, in order to confirm that lattice and/or protein arrays had formed, and in order to perform the necessary controls described above. Cryo-EM images of NTS1 bound to the DNA lattice via NT formed dense arrays that were neither overlapping or aggregated (Figure 4.1). When NTS1 was ligand-bound to the lattice, no arrays were observed in the presence of excess NT (not shown). The DNA lattice allows for large fields of view of non-aggregated, concentrated protein particles to be imaged, such that up to 10 000 particles per field of view can be boxed for single particle processing. In the case of

the NT-functionalised lattice, due to attachment necessitating GPCR activation, all of the bound particles are in the active conformation, reducing heterogeneity. The peptide ligand is covalently attached to the lattice, so any receptor that binds the lattice must by definition be in the active state.

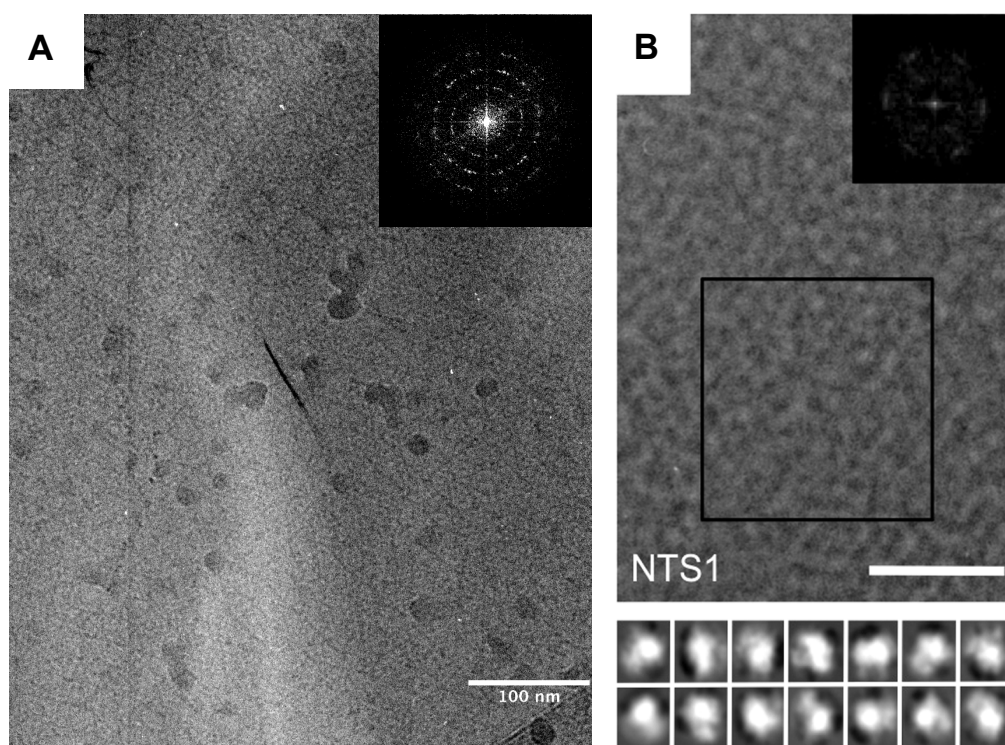


Figure 4.1. Cryo-electron micrographs of NTS1 bound to NT-functionalised large lattice.

DNA-templated array of NTS1 bound to the template via the ligand, NT, and observed under cryo-EM. **A:** wide field of view, showing a Fourier transform of the entire area in the top right corner. The high-density of the protein array is readily apparent, with particles (light against darker background) filling the entire field of view. The dark circles are ice crystals. **B:** magnified section (bar is 50 nm) with representative reference-free class averages below. The class averages of NTS1 have a diffuse boundary that is attributed to the detergent micelle. The Fourier transforms indicate the presence of the DNA lattice beneath the protein. B is from ⁽¹⁷⁹⁾.

4.2.2. Single particle reconstructions

Using a small test data set of particles (~13 000) independent electron density maps of NTS1 were reconstructed from refinements against two different starting models: crystal structures of active and inactive conformations of the β_2 adrenoreceptor: PDB 3P0G (nanobody removed) and 2RH1 (T4-lysozyme removed), respectively. These were both filtered to 40 Å prior to refinement to remove model-bias, a common cause of both over-refinement and false-positives (Figure 4.2). Alignment of the final density map refined against the active (3P0G) starting model with the 3P0G crystal structure gave a cross Fourier shell correlation (FSC) of 15 Å, significantly higher than the initial model (which was filtered to 40 Å). These reconstructions resemble those processed by Daniele Selmi (Department of Physics, University of Oxford, personal communication) from the same data set, as well as the more refined, higher resolution structures solved by Daniele Selmi (PhD thesis, University of Oxford, unpublished results). The cross-correlation between the separate maps refined against 3P0G solved by the author and Daniele Selmi was 0.94 as determined using UCSF Chimera ⁽²¹³⁾. The similarity of structures processed from independent data sets by different people supports our proposal that use of the DNA lattice for sample preparation and data collection improves the quality of sample, data, and the structures that can be solved from the data.

In the absence of a crystal structure with which to compare the NTS1 reconstruction at the time (2011), a low resolution negative stain $G\alpha$ structure was solved using the same method as that used for the NTS1 density map, in order to show that the method was feasible for proteins under 100 kDa (Figure 4.3). $G\alpha_{i1}$ was tagged to the Ni-NTA

functionalised lattice via the His-tag and a dataset of ~30 000 particles collected, boxed and processed. The resolution of the resulting structure was low (15.5 Å) but was sufficient to distinguish between GTP and GDP bound conformations, and in fact, for a small particle structure solved using SPA, the resolution is unusually good. When $G\alpha_{i1}$ is GTP-bound, its Switch II region in the GTP-binding domain is structured, but after hydrolysis of the GTP to GDP, this region becomes unstructured and flaps open to the “top” of the molecule. This feature made it possible to determine from the reconstruction that the $G\alpha_{i1}$ bound to the template was GDP-bound.

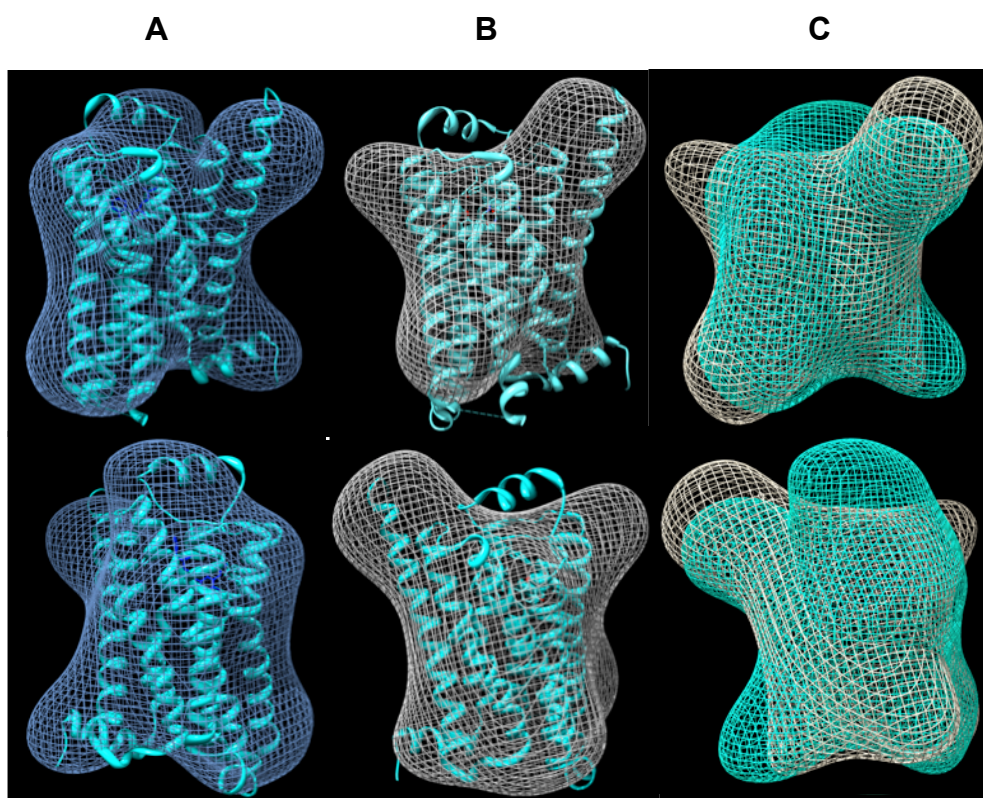


Figure 4.2. Single particle reconstruction of NTS1.

A) Alignment of reconstructed NTS1 electron density (mesh representation) with the crystal structure of the active β_2 adrenoceptor, 3P0G (cyan), nanobody removed. Opposite faces of the structure are shown. An iterative projection-matching refinement scheme was used in a refinement of the complete 13 331-particle data set against this crystal structure filtered to 40 Å. The cross FSC between the resulting electron density map and the crystal structure was ~15 Å. **B)** Alignment of reconstructed NTS1 electron density with 3P0G (cyan), nanobody removed. This map was refined against the inactive β_2 adrenoceptor structure, 2RH1, T4-lysozyme removed, filtered to 40 Å. The cross FSC between this map and the crystal structure was lower. **C)** Alignment of A and B density maps. The cross-correlation between the two as determined in UCSF Chimera was 0.91⁽²¹³⁾.

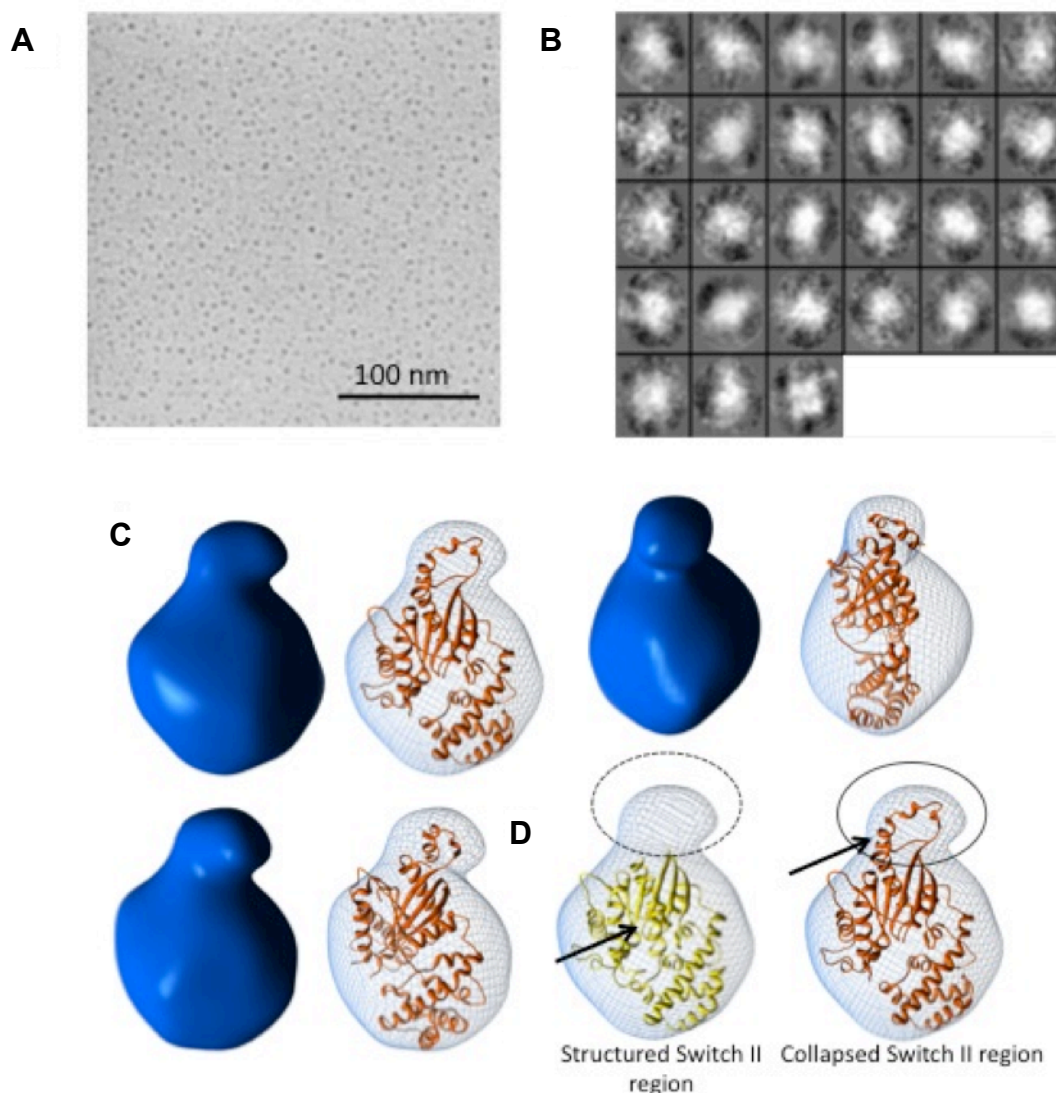


Figure 4.3. Single particle reconstruction of His₆-Gα_{i1}.

A: DNA-templated array of positively-stained (NanoVan) Gα_{i1} bound to the template through a His₆ affinity tag and observed under TEM. Fourier transforms (FT) (not shown) of selected areas of the micrograph show faint periodicity to first order, providing evidence for the underlying template. **B:** Representative class average images corresponding to distinct orientations of His₆-Gα_{i1}. **C:** Top, Distribution of out-of-plane Euler angles (ϕ, θ) describing inferred particle orientations – complete coverage of Euler space is observed. **C:** Reconstructed electron density of Nanovan-stained His₆-Gα_{i1} alone (blue surface) in 3 different orientations (side view and rotated $\sim 45^\circ$ (bottom) and 90° (right) about the vertical axis). For each orientation, the computationally aligned crystal structure of Gα_{i1} (GDP complex; PDB 1AS3) is also shown aligned to a mesh representation of the density map. Note the excellent agreement between the density map and crystal structure at this limited resolution (in one orientation (right) the density map appears slightly thicker than the crystal structure; this is likely due to positive staining by Nanovan). **D:** Comparison between the density map of His₆-Gα_{i1} (mesh), the crystal structure of Gα_{i1} (GTP complex (PDB 1AS0) – yellow) and Gα_{i1} GDP complex (PDB 1AS3) – orange, as in D). The crystal structure of Gα_{i1} (GDP complex) fits the entire density map. In contrast, the smaller lobe, which corresponds to the collapsed Switch II region in the crystal structure, is not fit by Gα_{i1} (GTP complex). This indicates that His₆-Gα_{i1} in our sample is in complex with GDP, as opposed to GTP. (Reconstruction and images prepared by D.N.S.).

Cryo-electron micrographs of His₆-Gα_{i1} bound via its His-tag to the tris-NTA-functionalised lattice were used to prepare higher resolution class averages from a much larger data set (38 990 particles) than those from the negative stain data set (Figure 4.4) ⁽¹⁷⁹⁾. The particles and class averages from these micrographs were less diffuse than those obtained for NTS1 images, and this is attributed to the presence of detergent in the NTS1 samples. The crystal structure of GDP-bound Gα_{i1} (PDB 1AS3; ⁽²¹⁴⁾) was filtered to 2.0 nm and projected to sample particle orientations broadly and randomly (represented by a broad distribution of the out-of-plane Euler angles (ϕ, θ)). Multivariate statistical analysis was used to group particles into class averages, and projection-matching alignment against projections of the crystal structure was used to determine the orientations of the class averages. Projections of the crystal structure in 10° increments across $0^\circ < \theta < 180^\circ$ were compared to best-matching class averages (Figure 4.4B). The two-domain structure of His₆-Gα_{i1} is apparent in a number of these projections. Imaging and data-processing for the G protein were carried out by Daniele N. Selmi (Department of Physics, University of Oxford).

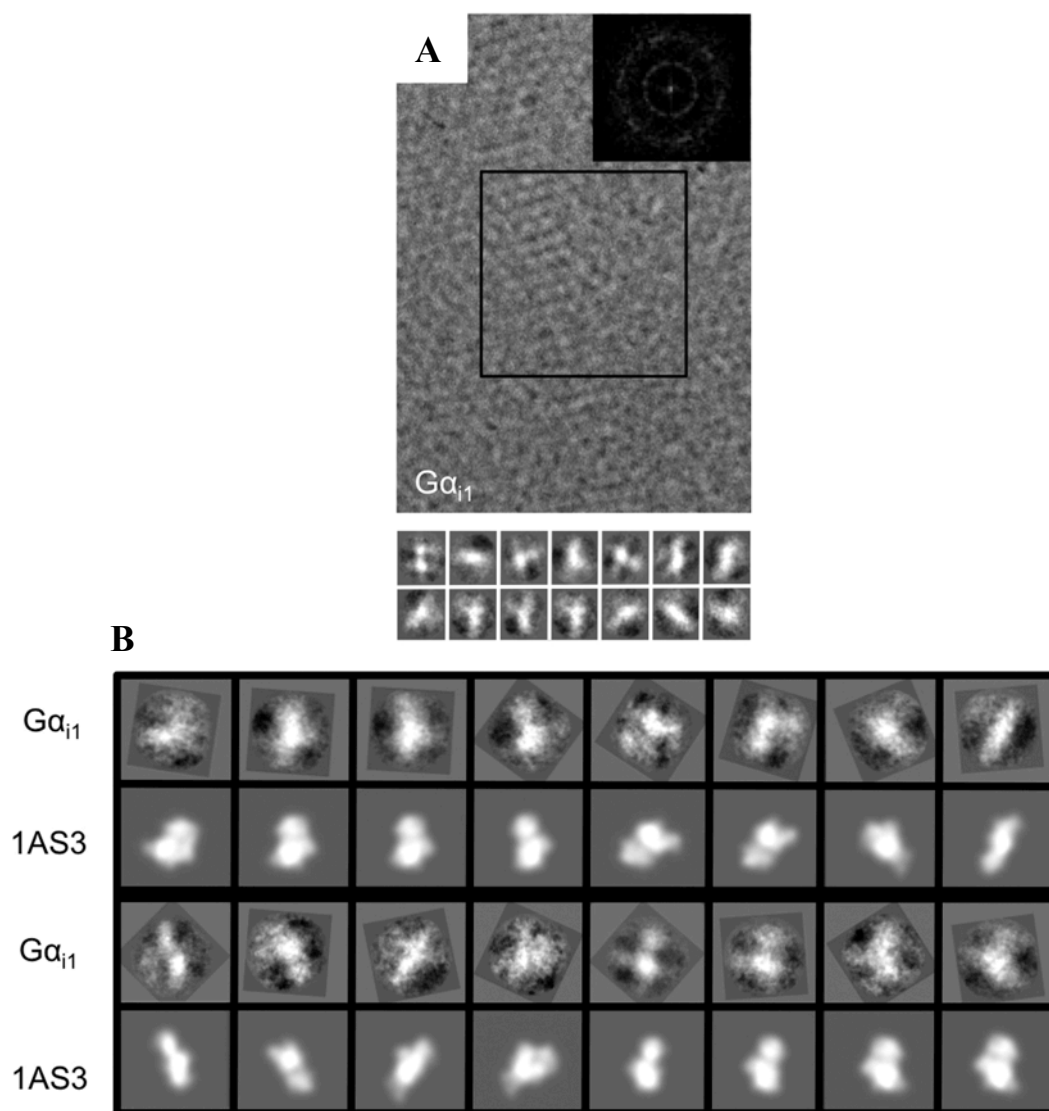


Figure 4.4. DNA-templated His₆-Gα_{i1}.

A: Cryo-EM micrograph of His₆-Gα_{i1} bound to the tris-NTA-functionalised DNA template via its His₆ tag (image width 150 nm). Representative class averages are shown below the image (box width 8 nm). Fourier transform of the indicated area shows the periodicity of the lattice beneath the protein array. **B:** Projections of the crystal structure of Gα_{i1} (PDB 1AS3; ⁽²¹⁴⁾) filtered to 2.0 nm and broadly sampling configuration space, compared with best-matching class averages, matched by eye.

4.2.3. NTS1-G protein coupling in detergent

His₆-Gα_{i1} and His₆-Gα_s were Nanogold®-labelled at their His tags using a Ni²⁺-mediated interaction (Figure 4.5.). His₆-Gα_{i1} labelling was ~60 % efficient, but His₆-Gα_s labelling efficiency could not be increased above ~10 %. Gold-labelled samples had much higher contrast than unlabelled samples, and were easily visible in the EM.

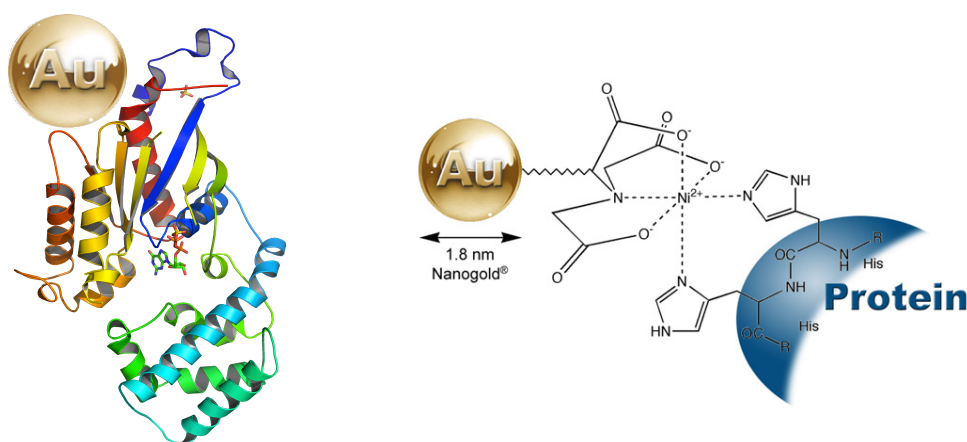


Figure 4.5. His₆-Gα Nanogold® labelling.

Schematic showing the N-terminal labelling of His₆-Gα subunits with Nanogold®. The crystal structure of Gα_{i1} was used, and the approximate relative sizes of the molecules are shown (Nanogold is 1.8 nm). (PDB file 1BOF⁽²¹⁵⁾). The chelating chemistry is shown (from: <http://www.nanoprobe.com/instructions/Inf2080.html>). The distance from the gold particle to the protein is estimated to be ~1.5 nm.

Dense arrays were observed when DNA-templated NTS1, bound to the template via its ligand, was incubated with His₆-Gα_{i1}* (Figure 4.6). The gold particles were clearly visible and of the expected size (2-5 nm for stained Nanogold®). Ordered “lines” of gold particles could be observed, giving evidence for specific binding to the receptor on the ordered lattice below. Fourier transforms of selected areas of the micrographs showed the periodic, hexagonal spot pattern of the underlying lattice, in some cases

blurred or distorted due to overlapping or astigmatism, but nevertheless easily recognisable. No gold was seen when the reaction mixture was incubated with excess NT, but the lattice was clearly visible. Incubation of the sample with excess guanosine diphosphate (GDP), interestingly, appeared to diminish binding, such that only patches of gold particles were seen on the grids. Incubation of the sample with no NTS1, only lattice and His₆-Gα_{i1}* resulted in disordered aggregates clumped around the edges of the holes of the grid or bare lattice (Figure 4.6D).

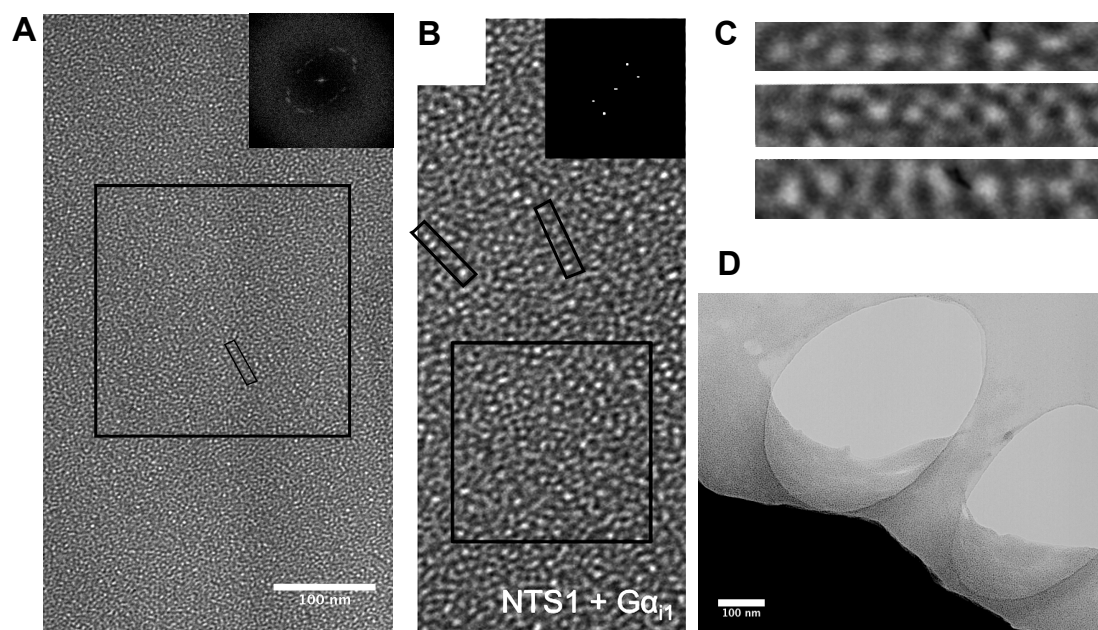


Figure 4.6. TEM of His₆-Gα_{i1}*-coupled NTS1 ligand-bound to a DNA lattice.

A and B: Micrograph of DNA-templated array of negatively stained (Nanovan™) NTS1 bound to the template via the ligand, NT, and coupled to His₆-Gα_{i1}*, at low (A) and higher (B) magnification. The gold-labelled particles are clearly visible, providing direct evidence of His₆-Gα_{i1}* coupling to NTS1. Protein particles are densely arrayed across the entire micrograph area, with no aggregation. The underlying DNA lattice is not visible due to the density of the gold particles, but there is evidence for the order imposed by the lattice in lines of stained gold particles (small boxed areas in A and B, magnified in C), confirmed by interactive Fourier transforms (FT) of the boxed segments (upper right of A and B). **D:** Control sample where NTS1 was omitted from the reaction mixture. Bare lattice (not shown) or gold particles aggregated around the grid holes were found, but no protein arrays. B is from ⁽¹⁷⁹⁾, the width of the micrograph is 100 nm.

Incubation with excess GTP γ S (~120 μ M) when the GTP γ S was added at the same time as the other components, resulted in more homogeneous arrays than without GTP γ S, but when the G protein was incubated with GTP γ S alone prior to addition to the lattice/NTS1 mixture, gold arrays were patchy, with some aggregates clumped around the edges of the holes. According to Yao et al. ⁽²¹⁶⁾, the cellular concentration of GDP is greater than 10 μ M, and at these and higher concentrations the GPCR-G protein complex dissociates. Traut ⁽²¹⁷⁾, gives intracellular concentrations of GDP and GTP as ~50 μ M and ~500 μ M, respectively, the latter of which can rise to the millimolar range in rapidly dividing cells ⁽²¹⁸⁾.

This work, published in *Nano Letters*, was the first direct visualisation, to our knowledge, of NTS1-G protein coupling using purified proteins ⁽¹⁷⁹⁾.

4.2.4. NTS1-G protein complex in nanodiscs

Cryo-EM on small (<100 kDa), asymmetrical particles is still a controversial area, partly because of the difficulty in visualising such small particles in vitreous ice under low dose conditions in the microscope, and because there is not enough information in the signal from such small particles to accurately align them during processing. Partly as a means to overcome the issue of size, as well as to solve the problem of detergent (which is not ideal for vitreous ice formation) and to study NTS1 in a lipid environment, the receptor was reconstituted in nanodiscs. To ascertain if G α couples to NTS1 reconstituted in nanodiscs, especially prior to doing cryo-EM, where it would be very difficult to tell if G α was coupled to the receptor or not, the loaded

nanodiscs were incubated with Nanogold®-labelled $G\alpha_s$ for negative stain analysis (0.5 % UAc to reduce stain interference) (Figure 4.7A-D). The microscope was focussed at high magnification in order to see the gold particles and to distinguish them from stain, and several images were taken of the same field of view from close to focus to a defocus of $\sim 1 \mu\text{m}$. Particles that appear over a range of defoci are gold, as opposed to stain, which resembles gold further from focus but is not visible in the low defocus images. Three images at different defoci were overlaid in ImageJ (<http://rsb.info.nih.gov/ij/index.html>) such that both Nanogold® and nanodiscs were easily apparent. As a result of the low labelling efficiency of His₆- $G\alpha_s$ (5-10 %), the micrographs were sparsely populated with gold particles, and additionally, the light stain lowered the contrast. However, almost all the gold located on the grids was specifically co-localised to nanodiscs, which was not the case in the control (not shown), where empty nanodiscs were used to check gold-labelling specificity, and gold was seen randomly in the field of view. From the data obtained, unfortunately hampered by low gold-labelling efficiency, it appears that one gold particle binds per nanodisc. A schematic representation of a GPCR coupled to a $G\alpha$ subunit in a nanodisc, using the crystal structure of the β_2 -adrenergic receptor coupled to G_s ⁽⁹³⁾ modified to remove the fusion partners and the $\beta\gamma$ subunits (using Swiss-PDB Viewer ⁽²¹⁹⁾), along with the nanodisc from the cryo-EM structure of the ribosome-SecYE complex ⁽⁷⁸⁾, and with a Nanogold® particle included to show the location of the gold relative to the other components, is shown in Figure 4.7. The schematic indicates that because of the large displacement of the α -helical domain of the $G\alpha_s$ relative to the Ras-like GTPase domain when the G protein couples to the receptor, the $G\alpha_s$

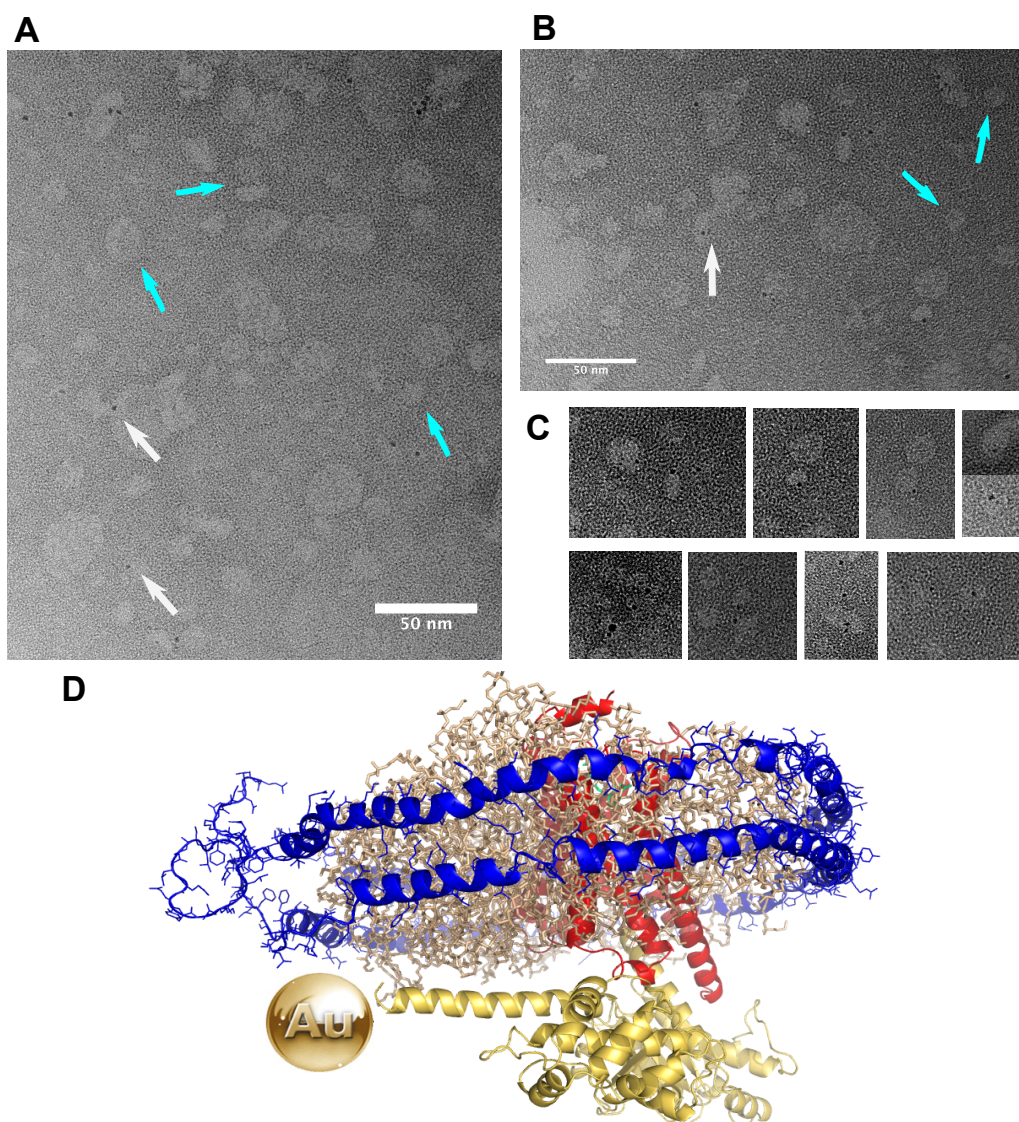


Figure 4.7. Co-localisation of His₆-Gα_s* and nanodiscs.

TEMs showing specific co-localisation of His₆-Gα_s* with FLAG-NTS1:PC:PG nanodiscs. This preparation of nanodiscs was unusually size-disperse, but gold particles (His₆-Gα_s*) (small black dots, some of which are indicated by white arrows) can easily be seen co-localised with the NTS1-containing nanodiscs (large lighter “blobs”, indicated by blue arrows). **A** and **B**: Micrographs showing colocalisation of nanodiscs and gold-labelled G protein, with nanodiscs and Nanogold® particles shown respectively with blue and white arrows. **C**: Magnified views of some of the nanodiscs with gold G protein from A and B. **D**: A model of the β₂AR with G protein bound showing the possible position of the Nanogold® label. Nanodiscs were incubated with 5 μM NT₈₋₁₃ for 30-60 min before His₆-Gα_s* was added for a further 30 min. Sample was adsorbed to the grid for 60-90 s, briefly wicked with filter paper, rinsed by being turned upside down in a 30 μl drop of buffer, then stained for 30-60 s 0.5 % UAc. Three images at defoci of -100, -500 and -900 nm were overlaid to show Nanogold® and nanodiscs.

N-terminus where the Nanogold® chelates to the His-tag, is swung out to the edge of the nanodisc.

This would be an even more prominent effect in the nanodisc used in this thesis, due to the smaller radius of discs formed by MSP1D1. No matter where in the disc the receptor inserted, the Nanogold® would be forced to the edge because of the N-terminus placing. An interesting observation therefore is that the gold particles in many of the nanodiscs shown in Figure 4.7 appear to be to the edge of the discs. This could simply be a function of the orientation of the discs on the carbon film of the grid, but a close look at Figure 3.24 and the class averages of the nanodiscs shows that they tend to adsorb to the carbon flat, rather than on edge. This could imply further evidence for specific coupling of the G protein to NTS1 in the nanodisc.

In summary, Nanogold®-labelled G α subunits have been successfully used, to the author's knowledge, for the first time, to visualise NTS1- or GPCR-G protein coupling under EM. More efficient gold labelling will make it possible to distinguish the frequency of one or two G α subunits binding to one nanodiscs. This is also solid evidence for the formation of the ternary complex (assuming most NTS1 is ligand-bound) with NTS1 in nanodiscs, and implies that similarly prepared samples, without Nanogold®, will in all likelihood be G protein bound when frozen for cryo-EM.

One further piece of evidence for the formation of the ternary complex in the nanodiscs was the use of the NTS1-Ga_{i1} fusion construct reconstituted in nanodiscs. Numerous experiments incubating FLAG-NTS1-PC:PG nanodiscs with NT-functionalised DNA lattice appeared not to show any specific binding of the nanodiscs to the lattice, and SPR studies indicated that the receptor was somehow less accessible to ligand in the nanodisc (Section 5.5). NTS1-Ga_{i1} fusion protein in nanodiscs, however, did appear to bind to the lattice (Figure 4.8), and was present in the vast majority of micrographs where lattice was present, unlike the nanodiscs containing only NTS1. It may be that the NTS1-Gα fusion construct is in a higher affinity pre-coupled state, and as such is able to bind the ligand attached to the lattice more easily.

This section has shown, and will be further discussed in Chapter 6, that purified NTS1 couples to both Ga_{i1} and Ga_s in detergent and in a membrane environment, and that tools such as cryo-EM and negative stain TEM can be used to follow and study this coupling, and that the use of a novel nanotechnological DNA template to which to tether proteins for viewing in the EM has the potential for the solution of the structures of small, frozen-hydrated native complexes in their membrane environment.

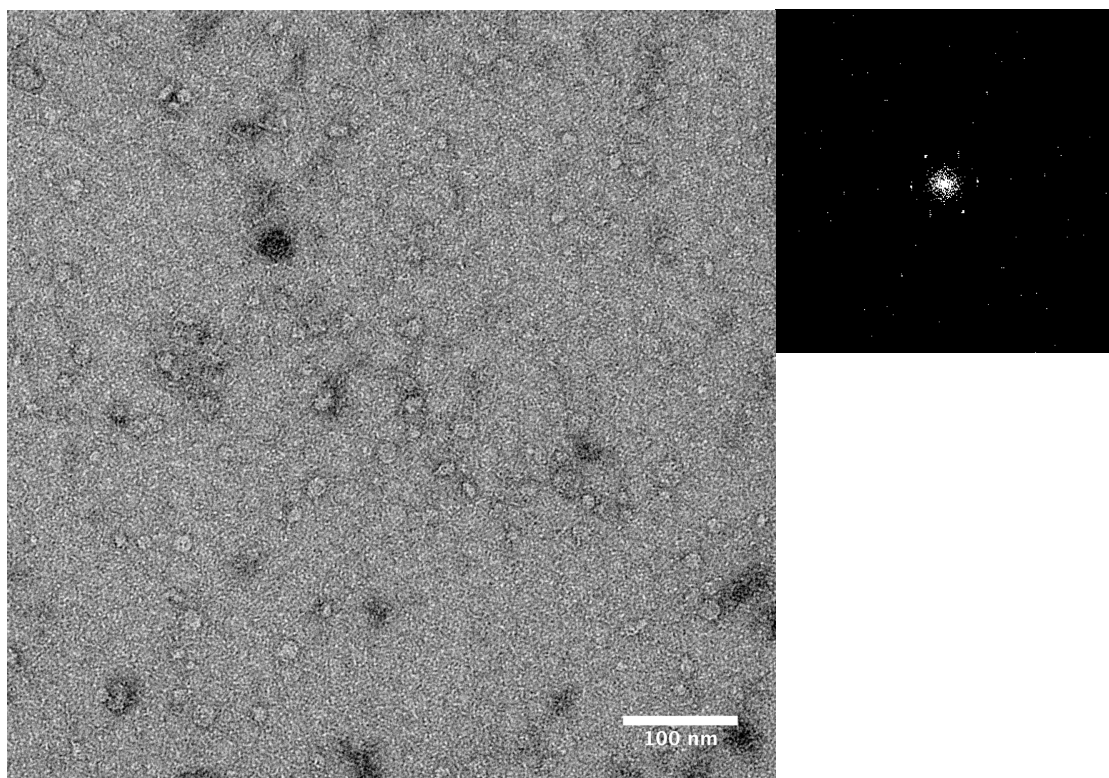


Figure 4.8. Micrograph of MSP-NTS1-G α_{ii} -PC:PG nanodiscs bound to DNA template.

The NTS1-G α_{ii} fusion construct was reconstituted in PC:PG nanodiscs, incubated with NT-functionalised DNA lattice, then stained weakly with 0.5 % UAc and imaged under TEM. The nanodiscs co-localised with the lattice in most micrographs, and appear to be arrayed along the lines of the lattice, as opposed to randomly scattered. The Fourier transform shows the presence of the lattice despite the low contrast.

Chapter 5 - Protein-protein interactions: Surface plasmon resonance

5.1. Introduction

SPR is a sensitive, flexible, label-free technique which is increasingly being used for the study of more complex interactions than previously possible for membranes, such as peptide-membrane⁽¹³⁴⁾ and protein-membrane interactions⁽¹⁴⁰⁾, as reviewed in⁽¹³⁵⁾. The interactions of membrane proteins with their ligands, recently reviewed in⁽²²⁰⁾ and the interactions of membrane proteins with soluble binding or signalling partners are a major area of interest and are growing because of the importance of these proteins, particularly GPCRs, as drug targets^(132, 141, 142, 146, 161, 221). A large number of SPR experiments were performed here whilst exploring the best conditions to investigate the kinetics of the interactions between NTS1 and G α subunits, something that had never been done before with SPR, and which was finally achieved through the novel use of NTS1 reconstituted in nanodiscs and used as the analyte in the experiments. Experiments leading up to this included NTS1-NT binding in detergent; NTS1-G α coupling in detergent; testing of multiple lipid types and detergents in various ratios to determine optimal bilayer reconstitution conditions; on-chip reconstitution of NTS1 in a bilayer, followed by NTS1-G α coupling; and capture of NTS1 reconstituted in proteoliposomes on the chip, followed by NTS1-G α coupling. The sensitivity of the SPR instrument to changes in refractive index and mass on the chip surface meant that most of these experiments were confounded by artefactual

responses arising from residual glycerol in the samples and detergent, as well as drift of lipid surfaces off the chip and negative signals, in addition to the inherent complexities of the biological system under study. The only other work that has been reported on GPCR-G protein interactions in a bilayer using SPR or SPR-like methods (PWR) are on rhodopsin and transducin interactions ⁽²²²⁾ and the δ -opioid receptor with various heterotrimeric G proteins ^(127, 160, 223).

5.2. NTS1-NT coupling in detergent

In much the same way as the functionalised DNA lattice was used, it was ensured in initial experiments where NTS1 was the ligand and the $G\alpha$ subunit the analyte, that all NTS1 molecules on the surface of the SPR chip were active by tethering them to the surface via neurotensin, thus ensuring a more homogeneous ligand population for the $G\alpha$ subunits as they were injected across the surface, and also simplifying data analysis. Thus, CM5 chips (Biacore) were used initially to determine NTS1 binding affinity for NT and thereafter were saturated with NTS1 to prepare a binding surface for His₆- $G\alpha_{i1}$. As has been previously determined in our lab, detergent-solubilised NTS1 bound readily to bioNT captured on amine-coupled streptavidin (Figure 5.1) ^(151, 153). In this thesis, the mean K_D from three experiments using a global fitting procedure with 1:1 Langmuir model was 0.87 ± 0.1 nM (SE), similar to values typically obtained by radioligand binding assays ^(172, 200, 224), ligand binding assays in this thesis, and by SPR ⁽¹⁵³⁾.

5.3. NTS1-G α_{i1} coupling in detergent

The NT-functionalised chip surface created in the manner described above was subsequently saturated with NTS1 and used as the ligand surface for G α_{i1} coupling, by injecting serial dilutions of His₆-G α_{i1} in detergent from 31.25 - 500 nM across the surface. However, these experiments yielded no useable signal. When the interaction was reversed by amine coupling G α_{i1} to the chip surface and injecting NTS1 across it, a signal was obtained but was difficult to interpret due to a strong signal from the buffer the receptor was in, and probably from differences in detergent and/or glycerol concentrations in the NTS1 sample, compared to the buffer. Programmed and manual solvent correction curves, where essentially a standard curve of detergent and/or glycerol concentrations is injected and subtracted from the signal, failed to extract the contribution of the protein buffer from the noise, and the data could not be improved.

To simplify the system further, CysNT was directly thiol-coupled to the surface of a CM5 chip, given that the amine-coupled streptavidin could have been causing steric hindrance to G protein coupling to NTS1 by forcing it into a position where the binding site was occluded; or potentially the additional distance from the chip surface was attenuating the already-small signal too much for it to be detected. This configuration of the system yielded a signal, potentially for the first time that this interaction has been recorded using SPR. Double-referenced single cycle kinetics of His₆-G α_{i1} binding to NTS1 in detergent with a nominal fit to a 1:1 binding model yielded an affinity of 300 nM for the receptor (Figure 5.2).

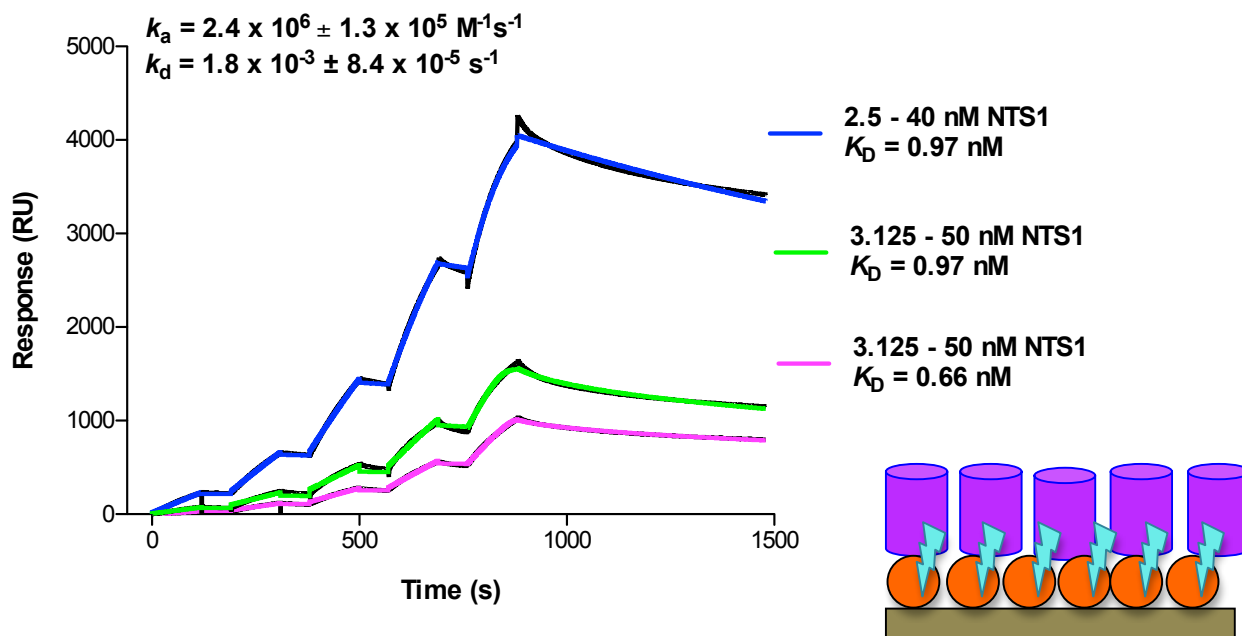


Figure 5.1. Single-cycle kinetics sensorgrams of NTS1-NT interactions.

Analysis of detergent-solubilised NTS1-NT binding kinetics. Representative single cycle kinetics assays showing binding signal (black lines) and fits to the data (blue, green and pink lines). Serial dilutions of 40 nM (top trace), and 50 nM (middle and bottom traces) NTS1 were injected at 30 $\mu\text{l}/\text{min}$ over CM5 chip surfaces prepared with immobilised streptavidin and biotinylated NT (bioNT). NT capture levels were 1200, 300 and 150 RU for the top, middle and bottom traces, respectively. Data was double-referenced. The reference flow cell contained scrambled bioNT captured with amine-coupled streptavidin. Affinity and rate constants obtained are as indicated on the graph, and are the mean and SE of 3 data sets. The mean K_D was 0.87 ± 0.1 nM (SE). The cartoon shows the layering on the chip, with streptavidin (orange) amine-coupled to the chip surface (brown), biotinylated NT (cyan) captured by the streptavidin and NTS1 (purple) bound to the ligand.

Using the same method to measure the binding kinetics of His₆-G α_s generated a much larger signal for lower concentrations injected, despite an unusual, apparently bivalent

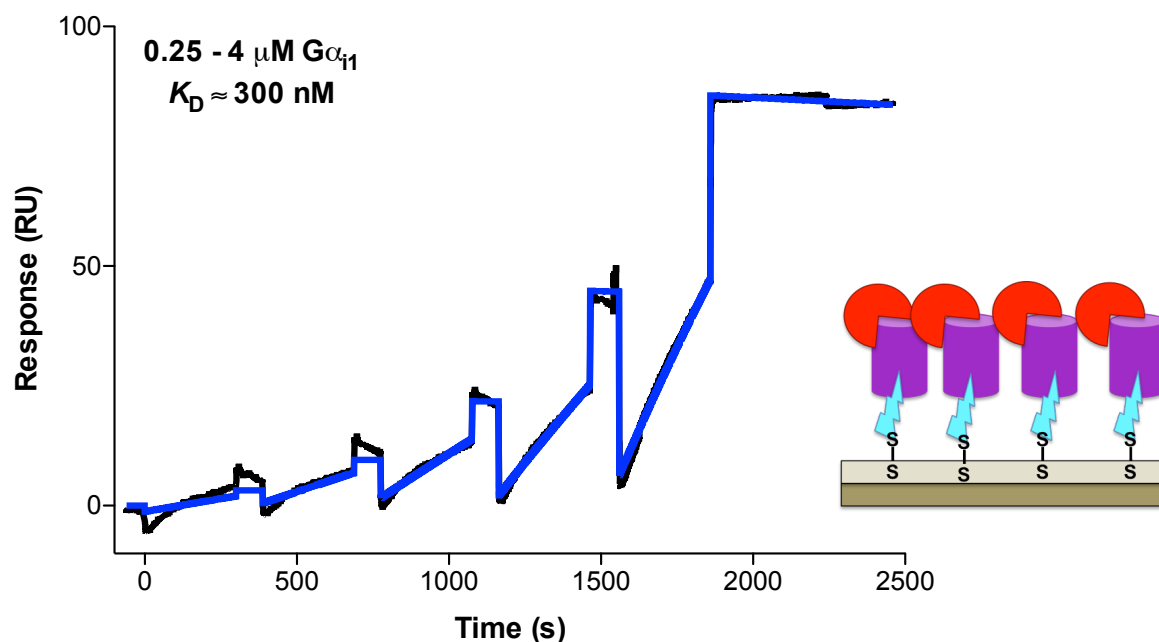


Figure 5.2. Single-cycle kinetics sensorgram of His₆-Gα_{i1}-NTS1 interactions in detergent.

Analysis of detergent-solubilised His₆-Gα_{i1}-NTS1 binding kinetics (with significant bulk effects). Single cycle kinetics assay showing binding signal (black line) and 1:1 binding model fit to the data (blue line). Serial dilutions of 4 μM His₆-Gα_{i1} (0.25 – 4 μM) were injected at 30 μl/min over a CM5 chip surface prepared with NTS1 captured on thiol-immobilised CysNT. NT and NTS1 capture levels were 500 and 1000 RU respectively. The theoretical R_{max} is approximately tenfold higher than that actually achieved, indicating that not all of the ligand is active or accessible. Data was double-referenced. The reference flow cell contained CysNT but no NTS1. A 1:1 binding model could be fitted, yielding a nominal K_D of 300 nM, but the bulk effects were incompatible with ideal analysis. The cartoon shows the layering on the chip: thiol-immobilised CysNT (cyan), used to capture NTS1 (purple), to which His₆-Gα_{i1} (red) was coupled.

binding trace, which could be somewhat attenuated by lowering the concentration of G protein injected. This implied that the affinity of His₆-Gα_s for NTS1 is greater than that of His₆-Gα_{i1}. Rough 1:1 binding fits could be applied to the data, yielding K_D values from 20-50 nM (Figure 5.3).

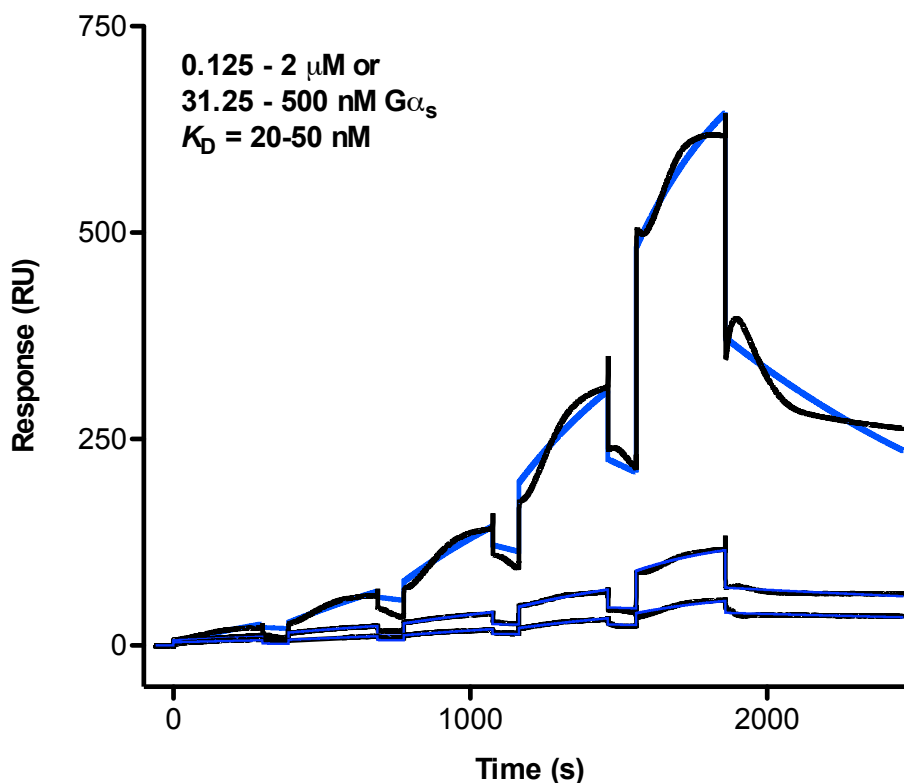


Figure 5.3. Single-cycle kinetics sensorgram of $G\alpha_s$ -NTS1 interactions in detergent.

Analysis of detergent-solubilised $G\alpha_s$ -NTS1 binding kinetics. Single cycle kinetics assay showing binding signal (black lines) and 1:1 binding models fit to the data (blue lines). Serial dilutions of 2 μM $G\alpha_s$ (0.125 – 2 μM) (top trace) or 500 nM (31.25 – 500 nM) (lower traces) were injected at 50 $\mu\text{l}/\text{min}$ over a CM5 chip surface prepared with NTS1 captured on thiol-immobilised CysNT. Data was double-referenced. The reference flow cell contained CysNT but no NTS1. The apparently “bivalent” association phase was corrected to a significant extent by lowering the NTS1 capture levels and decreasing the concentration of His₆- $G\alpha_s$ injected. A 1:1 binding model could be fitted, yielding a nominal K_D of 20-50 nM. The chip set-up is the same as that in Figure 5.2.

Aside from significant bulk effects confounding the G protein binding signal in detergent, a major factor in the unwieldiness of this system was constant drift of NTS1 off the chip surface, such that the baseline could not be fixed. The usual solutions for drifting baseline are computational, in that the drift is corrected for in the fit, but this is only a solution for a small amount of drift; extensive washing until all loosely bound ligand is removed; or covalent coupling. Although the k_d for NT from NTS1 is low (around $1 \times 10^{-3} \text{ s}^{-1}$), it would never stop dissociating, unlike a covalently

coupled ligand. Indeed, the half-life of NTS1 in detergent is such that washing it for several hrs would likely inactivate most of it. Covalent coupling, with its harsh conditions, would simply inactivate NTS1. Thus, so-called multi-cycle capture kinetics were used to minimise drift (Figure 5.4). For each cycle, a new batch of NTS1 was injected over and captured on the NT surface, followed by an injection of a single concentration of G protein. Small binding signals were obtained this way, but again the data could not be adequately processed due to bulk effects and drift. Washing the chip for longer after the NTS1 capture did not lessen the drift significantly.

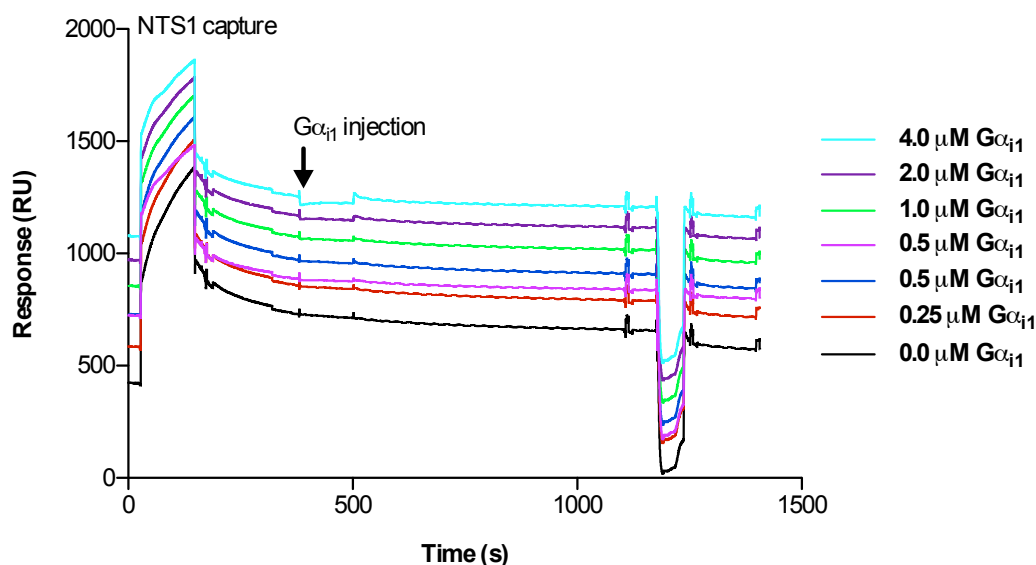


Figure 5.4. Multi-cycle NTS1-G α_{i1} capture and binding kinetics.

NTS1 was captured on a CM5 chip modified with thiol-coupled CysNT. The surface was washed for 5 minutes, and His₆-G α_{i1} was then injected for 120 s at the concentrations shown. A ten-minute dissociation period was followed by regeneration with 10 mM glycine pH 2.2 with 2 M NaCl, followed by another round of capture and binding.

Other methods of attaching NTS1 to the chip were explored, including the use of amine-coupled anti-MBP antibody (Ab) (to capture NTS1B), anti-FLAG and anti-NTS1 antibody. The affinities of antibodies for their epitopes are usually much higher than ligand-binding affinities, and capture using antibodies is common in the SPR literature, providing a more stable surface. Nevertheless, the anti-MBP Ab did not capture NTS1B, either because the amine-coupling inactivated the protein, which is unlikely given that antibodies are extremely robust under SPR coupling conditions, and pH scouting had been performed prior to coupling; or because the binding site for the epitope was occluded by coupling. No G protein coupling signal was obtained from the small amount of NTS1 that the anti-NTS1 and anti-FLAG Abs captured.

This section has demonstrated some of the complexities inherent in working with conformationally flexible and relatively unstable membrane proteins and investigating their interactions with signalling partners in detergent at the surface of a chip, but it is also apparent that seemingly small or simple changes such as changing the method of attachment of the ligand (for example from streptavidin-captured bioNT to thiol-coupled CysNT) can have profound effects on the data obtained from the system. The data here show a 10-fold difference in the apparent affinities of His₆-G α_{i1} and His₆-G α_s for NTS1 (300 nM *vs* 20-50 nM), and the affinities are in the nM range. Similar affinities and differences in affinities were observed for G_{i1} and G_s for the δ -opioid receptor by Alves et al. ⁽¹²⁷⁾ (300 nM for G_{i1} and 10 nM for G_s). The work here also provides proof of principle for the system, making viable the larger task of obtaining kinetic data for coupling interactions in a bilayer.

5.4. NTS1-G α coupling in a bilayer

5.4.1. On-chip bilayer formation and reconstitution

There are a number of ways to assemble a lipid bilayer on an SPR chip, including the use of thiolated or biotinylated lipids for tethering to the thiol-activated or streptavidin-coated surface, fusing captured liposomes on the alkylated carboxymethyl surface of an L1 chip, or building a bilayer from detergent-solubilised lipids. Karlsson and Löfås ⁽¹⁴³⁾ used the latter method to reconstitute rhodopsin on the surface of an L1 chip in a two-step process using the DUAL-INJECT function of the Biacore instrument. Rhodopsin in detergent was covalently amine-coupled to the chip surface, followed immediately by an injection of mixed micelles of POPC solubilised in octyl β -D-glucopyranoside (OG). The lipid molecules were captured by the hydrophobic alkyl groups of the L1 chip, and detergent-free buffer was then used to dilute the detergent below its cmc and wash it away, leaving the GPCR reconstituted in a bilayer. The sensorgrams recording the lipid deposition have an idiosyncratic shape, as shown and explained in Figure 5.5, which indicates whether a bilayer or liposomes have been captured on the chip. Very specific lipid:detergent ratios must be used in order for the lipid to be captured on the chip and the detergent to wash away, but these are dependent on the lipid type and detergent cmc, and must be empirically determined. The authors identify three types of lipid mixtures: clear, detergent-rich mixtures which do not allow POPC to attach and simply wash off; turbid, lipid rich mixtures that attach slowly and do not leave enough lipid on the surface; and clear, balanced mixtures with rapid association kinetics which deposit about 5 000 RU of lipid on the chip, which is indicative of a bilayer.

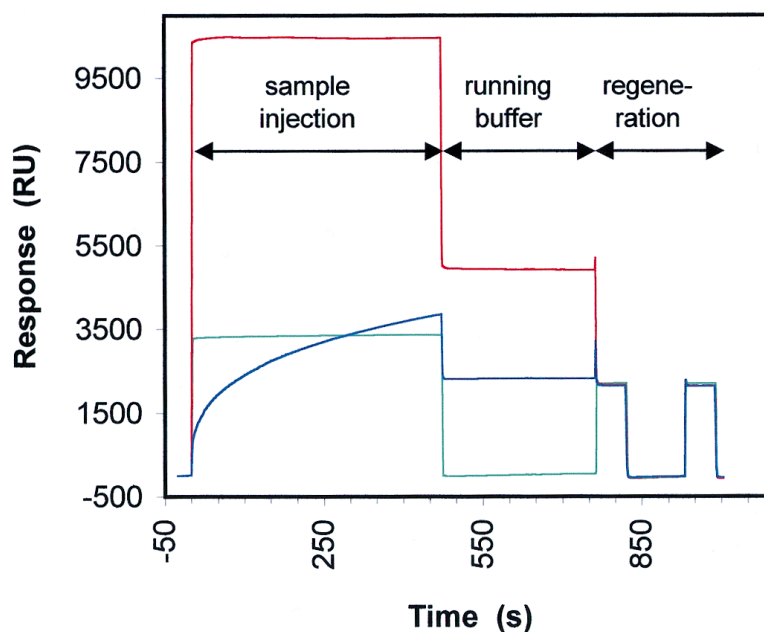


Figure 5.5. Representative sensorgrams for bilayer deposition on L1 chip.

Attachment of mixed micelles to an L1 chip surface, and detergent elution. Mixtures of different ratios of lipid:detergent were tested for their ability to deposit a bilayer on the chip surface. Samples were injected for 8 min then the FC immediately washed for 2 min, followed by regeneration with detergent only. Three types of samples were identified: clear, detergent-rich samples, which attached rapidly and washed off immediately after washing started (green); turbid, lipid-rich samples which attached slowly and deposited only about 2 000 RU of lipid (blue); and clear, balanced samples that attached rapidly and deposited ~5 000 RU of lipid (red). Figure from ⁽¹⁴³⁾.

The same principle was used here to reconstitute NTS1 in a lipid bilayer on an L1 chip surface. Since NTS1 is not active in POPC alone, or in OG, various lipids, detergents, and ratios of the two were tested for their capacity for bilayer deposition. A range of detergent:lipid ratios and detergent concentrations below, near, or above the critical micellar concentration (cmc) were used. The ideal response is strong and rapid with a high response from lipid deposition on the surface after washing begins (~5000 RU for a lipid bilayer) ⁽¹³¹⁻¹³³⁾.

Lipids and detergents tested included DDM, CHAPS, BPL, and a 3:1:1 mixture of POPC:POPG:POPE with 25 mol % cholesterol (PPPC). No mixture with any of a large range of DDM concentrations resulted in deposition of the required level of lipid on the chip (Figure 5.6). The cmc of DDM (~0.15 mM) may be too low to achieve ratios of lipid to detergent that are able to deposit the lipid on the surface. Additionally, the behaviour of BPL on the chip indicated that it is significantly negatively charged, since doubling the NaCl concentration in the sample, thus shielding the charge, effectively almost doubled the deposition level of BPL-detergent mixtures. Phosphatidic acid (PA), phosphatidylserine (PS) and phosphatidylinositol (PI) make up ~25 % of BPL. Only the samples with very low concentrations of DDM (slightly above, at and below the cmc) deposited the required amount of material on the chip, but during extensive washing and in subsequent efforts to detect G α binding, there was significant drift in the baseline as the surface appeared to wash off, and injection signals for the protein were negative (Figure 5.7).

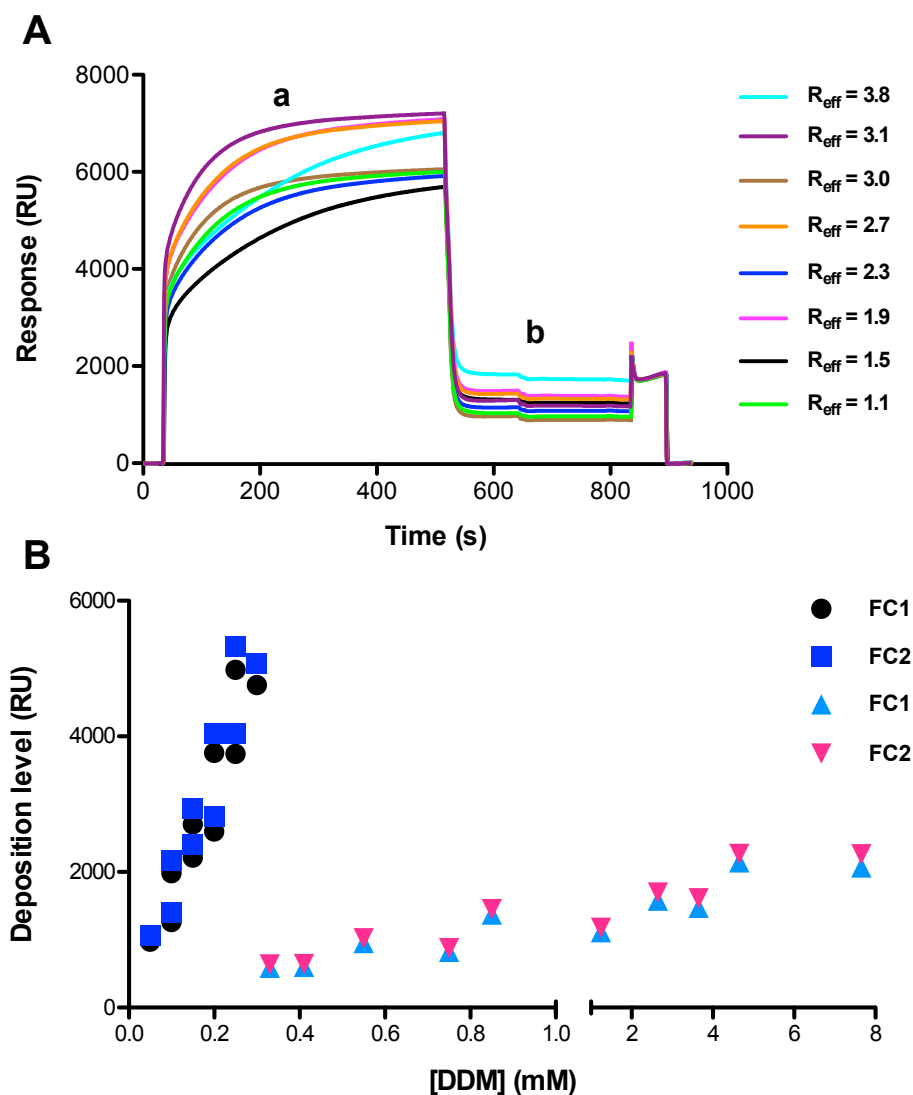


Figure 5.6. SPR traces and binding data produced during DDM-BPL bilayer scouting.

A: Representative sensorgrams and **B:** lipid deposition levels on L1 chip of mixed lipid-detergent micelles made up using varying concentrations of DDM and BPL. R_{eff} values, determined according to $([\text{detergent}] - \text{cmc})/[\text{lipid}]^{(143)}$, ranged from 1.1–3.8. DDM concentrations in the traces in A were 3.9 – 15.6 mM. The sensorgrams indicate slow association kinetics (a), implying the presence of intact liposomes, but low deposition levels (b) suggest the slow association signal may originate from the large DDM micelle (~70 kDa). The resulting surfaces were unstable and tended to drift significantly with extended washing. FC = flow cell. Two flow cells were simultaneously tested.

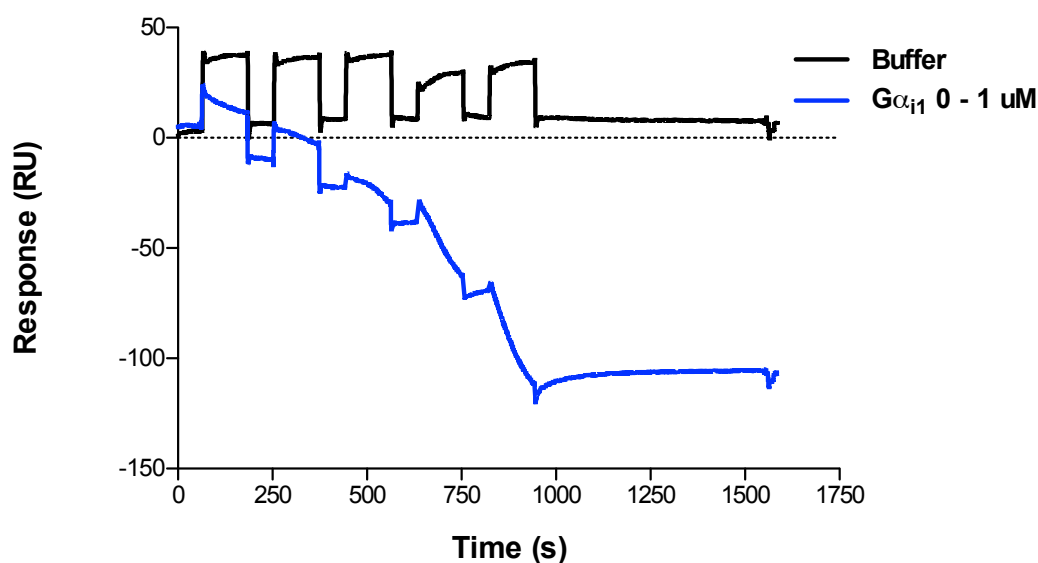


Figure 5.7. SCK of His₆-Gα_{i1} binding to NTS1 reconstituted on-chip in DDM-BPL.

Streptavidin (1000 RU) was amine-coupled to the surface of an L1 chip. BioNT (100 RU) was captured in the sample cell, scrambled bioNT (75 RU) was captured in the reference cell. NTS1 (700 RU) was captured during a 10-minute injection, and was immediately reconstituted in BPL using mixed DDM-BPL micelles followed by detergent-free washes. Lipid was also laid down in the reference cell. Rapid drift of the lipid off the surface coupled with some apparent refractive index interference from the G protein sample itself resulted in a drifting, negative signal that could not be analysed. The data are single-referenced to illustrate the effects.

BPL and PPPC were tested with CHAPS (Figure 5.8 and Figure 5.9). Deposition levels were uniformly low except for the sample with no CHAPS. Subsequent tests with 0.5 mM CHAPS, 6.9 mM BPL ($R_{\text{eff}} = -0.4$) initially appeared successful, and NTS1 was reconstituted apparently in a BPL bilayer on the chip surface (Figure 5.10). Attempts to perform G protein binding analysis with this surface were unsuccessful and gave an unstable surface with drifting baseline, despite 2.5 hrs of surface washing prior to coupling where the signal had stabilised (Figure 5.11). Reconstitution of the receptor on the chip using 6 mM PPPC with 0.5 mM CHAPS

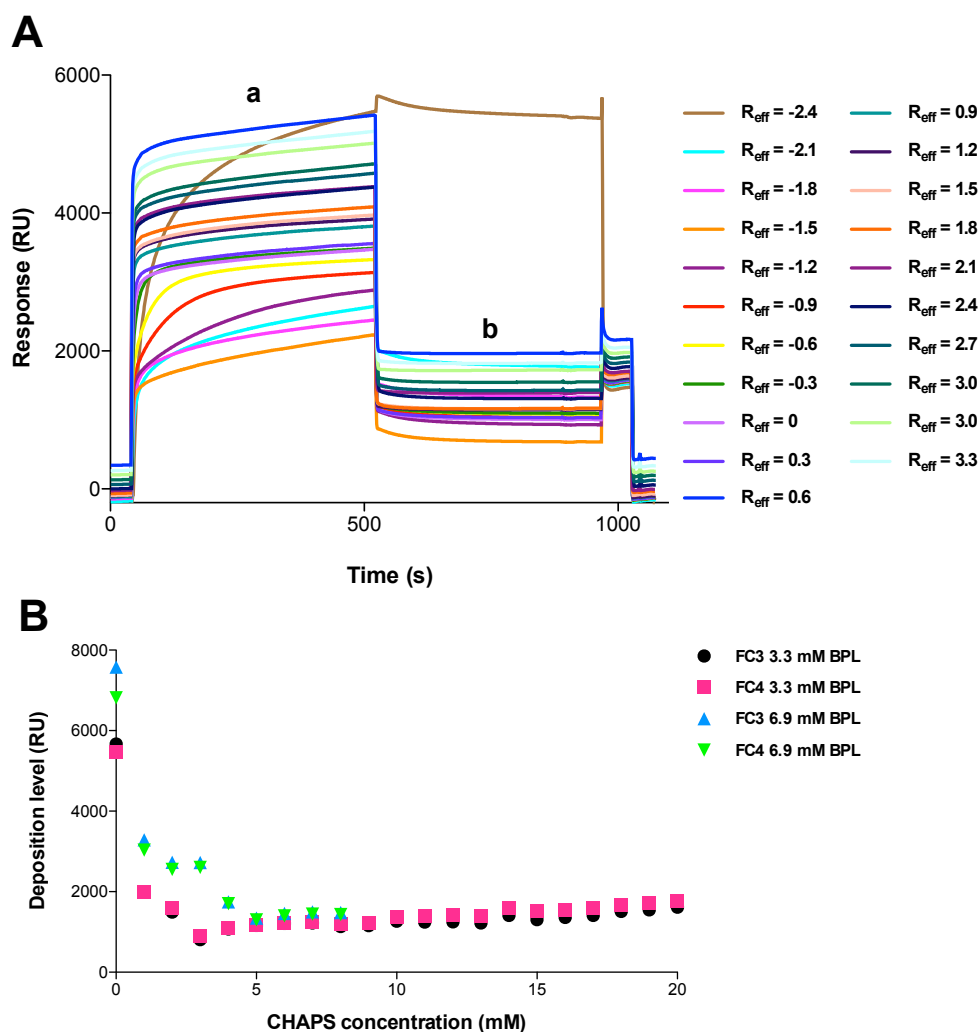


Figure 5.8. SPR traces and binding data produced during CHAPS-BPL bilayer scouting.

Representative sensorgrams (top) and lipid deposition levels (bottom) of mixed lipid-detergent micelles made up using varying concentrations of CHAPS and BPL. R_{eff} values, determined according to $([\text{detergent}] - \text{cmc})/[\text{lipid}]$ ⁽¹⁴³⁾, ranged from -2.4 – 3.3, using a cmc of 8 mM for CHAPS. CHAPS concentrations were 0 - 20 mM. The sensorgrams indicate rapid association kinetics (A), but low deposition levels (B), with the exception of the 0 mM CHAPS sample (gold sensorgram, high deposition), which also shows slow association kinetics, indicating intact liposomes in the sample. Using a higher lipid concentration (6.9 mM, bottom plot) did not increase deposition levels. Two flow cells (FC) were tested for each lipid concentration.

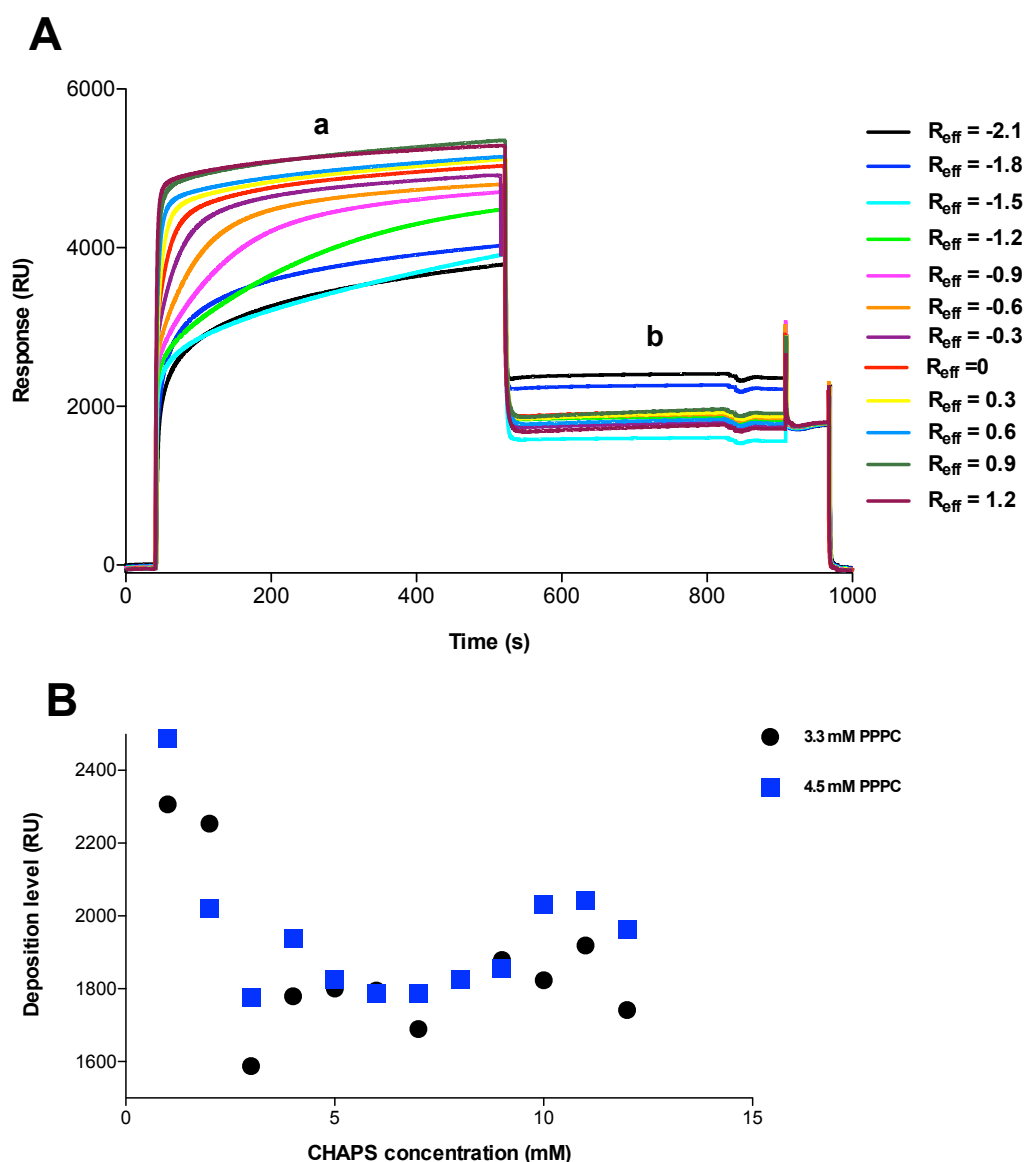


Figure 5.9. SPR traces and binding data produced during CHAPS-PPPC bilayer scouting.

A: Representative sensorgrams and **B:** lipid deposition levels of mixed lipid-detergent micelles made up using varying concentrations of CHAPS and PPPC. R_{eff} values, determined according to $([\text{detergent}] - \text{cmc})/[\text{lipid}]$ ⁽¹⁴³⁾, ranged from -2.1 – 1.2, using a cmc of 8 mM for CHAPS. CHAPS concentrations were 1 - 12 mM. The sensorgrams indicate rapid association kinetics (a), but low deposition levels (b), The sensorgrams indicate both slow and fast association kinetics, depending on CHAPS concentration, but deposition levels were low. The resulting surfaces were unstable and tended to drift significantly with extended washing. Increasing the lipid concentration to 4.5 mM did not increase deposition levels (B).

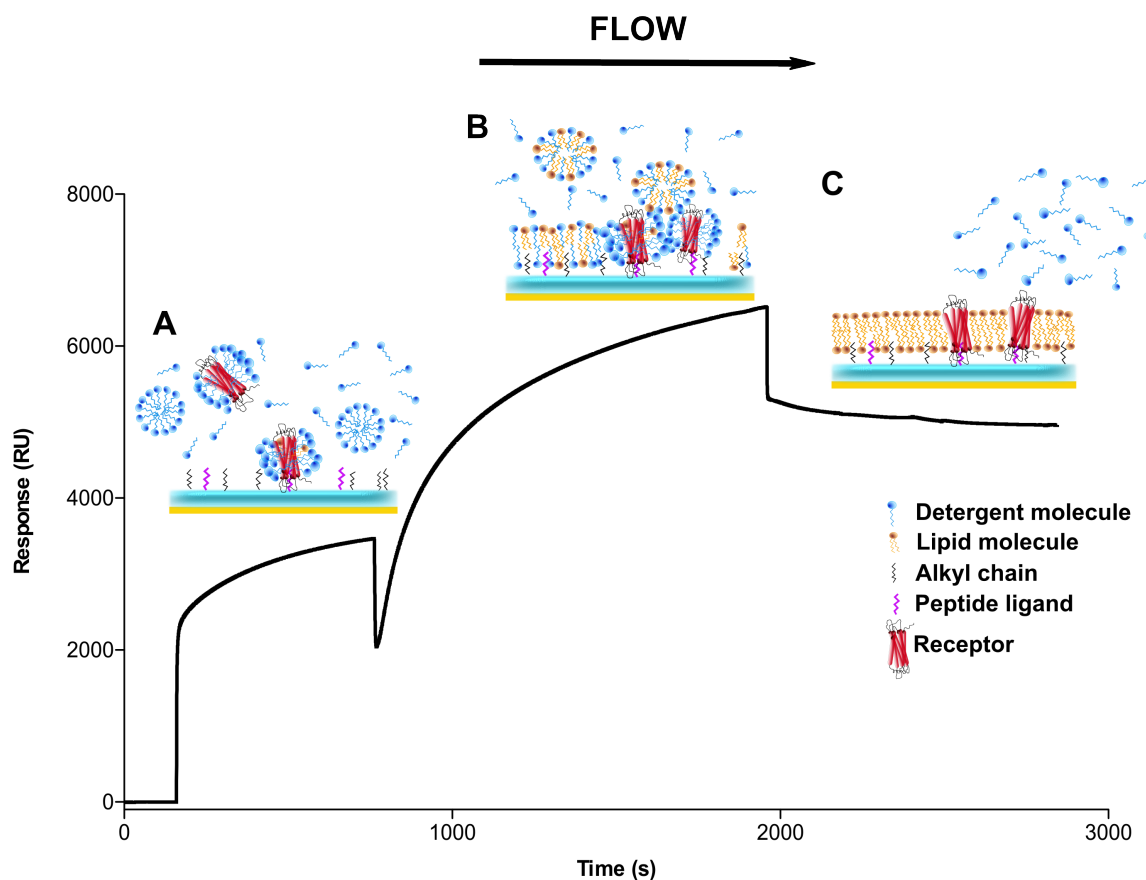


Figure 5.10. On-chip reconstitution of NTS1.

NTS1 was reconstituted in a BPL bilayer on the surface of an S Series L1 SPR chip (GE Healthcare), whose carboxymethylated hydrogel layer is modified to contain hydrophobic alkyl chains, to which liposomes or lipids can adhere. **A:** Capture of detergent-solubilised NTS1 by thiol-coupled CysNT on the surface of the chip for 8 minutes at 5 $\mu\text{l}/\text{min}$, immediately followed by **B:** injection of CHAPS-solubilised BPL for ~20 minutes (6.9 mM BPL, 0.5 mM CHAPS). **C:** detergent-free buffer dilutes the detergent below its cmc and the monomers wash off the chip, leaving the receptor embedded in a lipid bilayer. In theory the prepared surface can then be used for G protein coupling experiments.

gave similar results, and His₆-G α_{11} binding produced a negative signal similar to the results obtained in Figure 5.7, although the NT was thiol-coupled in this case.

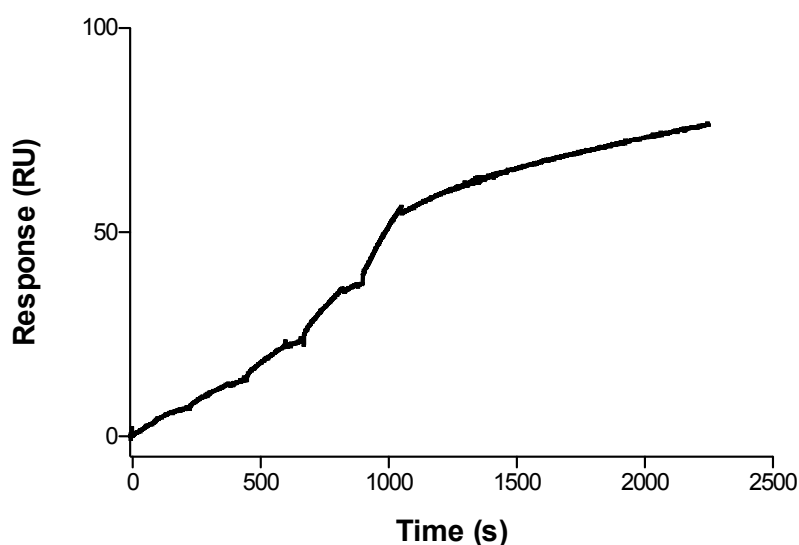


Figure 5.11. SCK of His₆-Gα₁₁ binding to NTS1 reconstituted on-chip in CHAPS-BPL.

NTS1 was reconstituted on-chip as described in the text and in Figure 5.10, then 62.5, 125, 250, 500 and 1 000 nM His₆-Gα₁₁ was injected across the reference and sample flow cells, with a series of 0 nM samples injected for reference. Data was double referenced and plotted, but drift from both flow cells, with faster drift from the reference cell, resulted in an increasingly positive signal. Thus, while it can be seen that binding is occurring, the data cannot be fitted with any model.

Thus, it can be seen from this section that NTS1 can be reconstituted on an SPR chip, but that the mixture of detergents and lipids used, and the ratio of the two, is critical for the bilayer to be stable upon the chip surface and for the receptor to be able to bind G protein functionally. A further experiment, utilising NTS1 reconstituted in BPL liposomes and captured on the L1 chip, demonstrated the careful balance needed for on-chip reconstitution vs. reconstitution and capture, since the liposomes captured very easily, but the signal obtained was very rough (Figure 5.12). It does not follow an exponential curve and clearly some non-specific interactions are occurring. The proteoliposomes were captured on the L1 chip at a slow flow rate, washed extensively

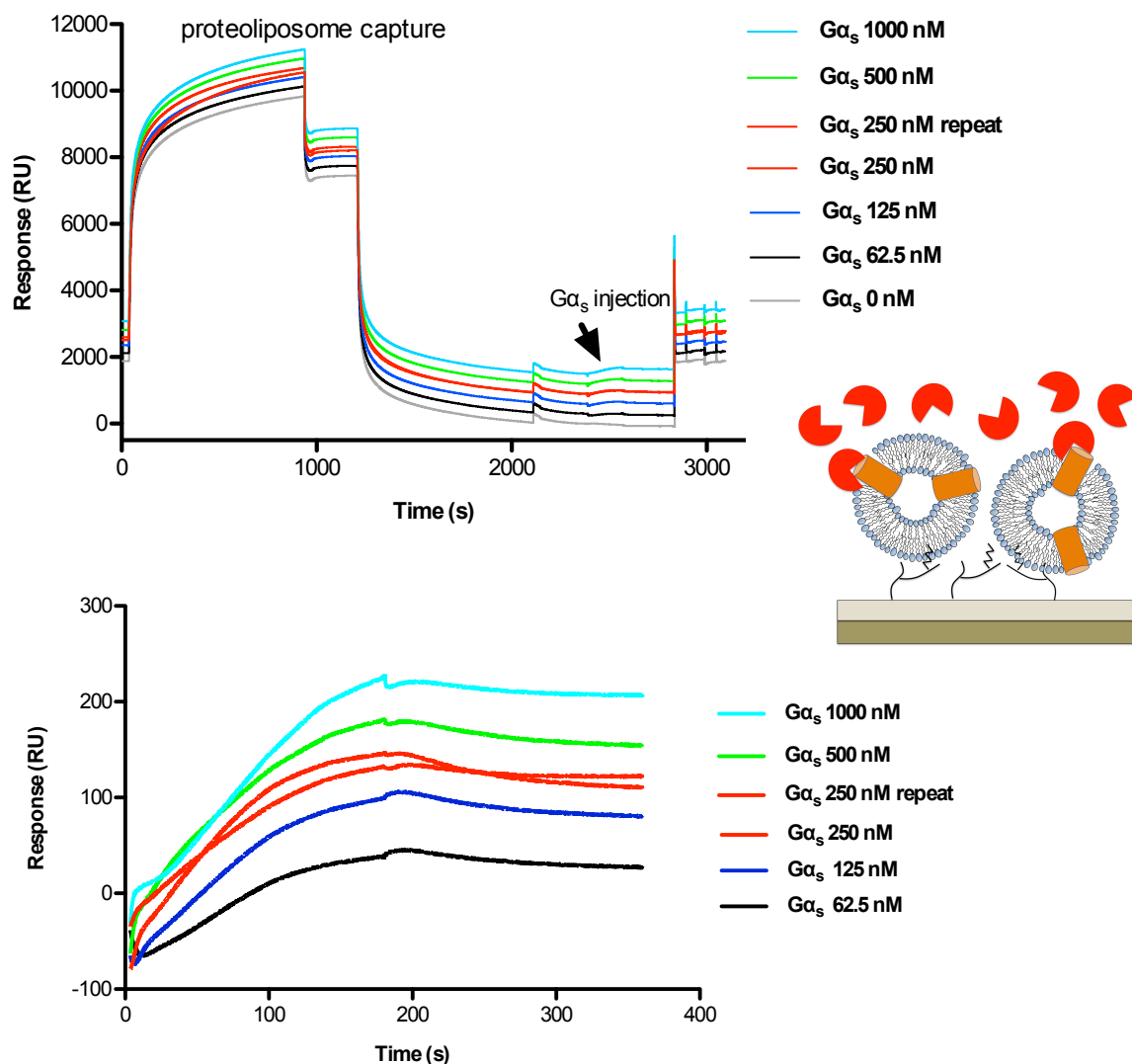


Figure 5.12. Capture and inject kinetics of NTS1 proteoliposomes and His₆-Gα_s.

Proteoliposomes containing NTS1 were injected at 5 $\mu\text{l}/\text{min}$ across an L1 chip and captured. After extensive washing His₆-Gα_s was injected. The traces could not be fitted with a binding model, but the apparent reproducibility of the 250 nM sample implies specific binding. The lower plot is a magnification of the His₆-Gα_s injection. Plots have been nudged for clarity. The cartoon shows the receptor (orange) reconstituted into liposomes captured on hydrophobic alkyl chains on the chip. The G protein (red) is injected over the surface. Not all receptors would be equally accessible in this scheme.

until the baseline stabilised, and concentrations of $G\alpha_s$ ranging from 62.5 – 1 000 nM were injected across the surface. Binding was detected, although the signal could not be fitted. Empty liposomes were used in the reference cell.

This section illustrates both the flexibility of SPR for obtaining binding data, in terms of the types and means by which ligands can be attached to the surface of the chip, but also illustrates that when working with a complex system, this very flexibility means that potentially a large number of conditions may have to be tested in order to obtain useable data. Of all of the bilayer systems constructed on the chip, the most stable bilayer was deposited in mixed PPPC:OG micelles. However, no binding signal was obtained, since NTS1 is not active in OG ⁽²²⁵⁾. This section has shown NTS1- $G\alpha$ coupling in a lipid environment on an SPR chip while bound to its ligand. The data is qualitative, not quantitative, but it is the first time that this interaction has been demonstrated in this way, and these experiments made it clear that further optimisation would most certainly yield quantitative data.

5.5. NTS1-NT binding in nanodiscs

The study of membrane proteins in general and GPCRs in particular, because of their conformational flexibility and relative instability, is complicated by the necessity for the presence of either detergents or lipids (or amphipols) to maintain the stability and activity of the protein. These molecules do not lend themselves readily to most biophysical techniques, and tend, as was shown in the previous section, to interfere

with the signal, or substantially increase noise in relation to signal. This is a problem whose solution has been most elegantly approached by the Sligar group, in the form of nanodiscs, 10-15 nm sized lipid discs wrapped around by a so-called membrane scaffold protein, a recombinant form of Apolipoprotein-A-1, a naturally occurring plasma protein that transports lipid particles through the blood ^(75-77, 226, 227). These particles perfectly encircle a membrane protein within a lipid environment where both sides of the protein are accessible to the aqueous solution around it, while at the same time making it soluble. They are thus a good vehicle for examining the interactions of the membrane protein with ligand or other proteins. They are also particularly suitable for SPR, given the sensitivity of the instrument to bulk effects, and the fact that they are large, thus amplifying the signal that is obtained from binding to surface-immobilised ligand, even if only a small amount of binding occurs. NTS1 reconstituted in nanodiscs was used to study the interactions of NTS1 with the peptide ligand, NT, and with His₆-Gα_{i1} and His₆-Gα_s. All nanodisc samples were dialysed into SPR running buffer to minimise bulk effects. MSP-FLAG-NTS1-PC:PG binding to thiol-coupled NT on a CM5 chip produced a very small signal, unexpectedly low for the concentrations used (Figure 5.13). Nevertheless, global 1:1 binding analysis yielded a K_D of 1.3 ± 0.6 nM for two experiments, thus reproducing the same K_D that has been published for NTS1 in lipid and detergent ^(153, 172, 225), as well as shown in this thesis. The K_D value calculated from the association and dissociation rates (k_d/k_a) was the same as that determined by the fit. The χ^2 value was 0.1, well below the maximum of 5 % of the R_{\max} that indicates a close fit. The low level of binding suggests that NTS1 is either not very active in POPC:POPG, or is somehow sterically hindered in the nanodisc from accessing the ligand on the chip surface. A radioligand binding assay performed on NTS1-nanodiscs also showed low levels of activity.

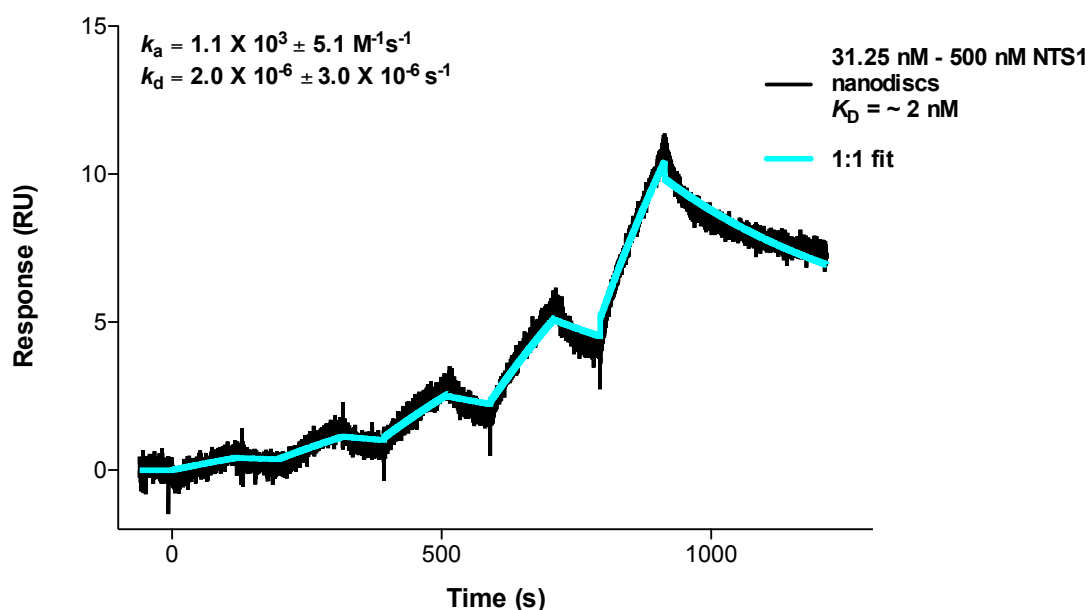


Figure 5.13. MSP-FLAG-NTS1-PC:PG-NT binding kinetics.

Single cycle kinetics sensorgram of FLAG-NTS1-loaded nanodiscs binding to bioNT captured on amine-coupled streptavidin on a CM5 chip. The K_D is similar to those determined elsewhere in this thesis and in the literature, but much higher concentrations of nanodiscs were needed than for NT coupling in detergent, and the response is very weak. This may imply a steric hindrance to binding in nanodiscs on the chip, or potentially suggests that NTS1 is not very active in PC:PG. The results from one experiment are shown above. A 1:1 Langmuir model was used. The χ^2 value was 0.1. The mean from two experiments was $1.3 \pm 0.6 \text{ nM}$ (SE).

5.6. NTS1-G α coupling in nanodiscs

Having established that H7-MSP-FLAG-NTS1-PC:PG could be used as the analyte in SPR experiments and could bind NT, the nanodiscs were then used as the analyte in G protein-coupling experiments. G α subunits were amine-coupled or tagged to antibodies on the surface of CM5 chips, and NTS1 nanodiscs injected over them in single cycles of multiple analyte concentrations. Thus, the kinetic interactions of

NTS1 in a bilayer, specifically NTS1 in nanodiscs, with G α subunits was recorded using SPR, and the data were clean enough to be analysed. Standard 1:1 binding models were applied initially to the data, but bivalency in the curves indicated a model with more parameters. Thus the heterogeneous analyte model was applied to the data. This is commonly used when amine coupling has been the method of surface immobilisation of the ligand, due to the non-specific nature of coupling, and the high likelihood of binding sites being occluded. Regeneration conditions for dissociating the receptor from G protein once coupled, without denaturing the ligand, had proved impossible to establish. Simply washing the surface for long enough to dissociate the receptor was unrealistic, given that with dissociation rates on the order of $10^{-4} - 10^{-6} \text{ s}^{-1}$ in some experiments (Figure 5.14), the time it would take for 50 % dissociation to occur would range from several hrs to a week. Thus numerous single cycle kinetics experiments were performed using varying levels of immobilised ligand and varying ranges of injected analyte concentrations. As mentioned, different means of attaching the binding partner to the surface were employed, in order to ensure that the data was, in fact, not simply artefactual, and to determine if the system could be simplified enough to fit a 1:1 model to the results. Thus, G α subunits were amine coupled to sample flow cells with the reference flow cell either simply activated and blocked, or with ovalbumin amine coupled to the reference surface; or the subunits were captured via an anti His Ab amine coupled to the surface (Figure 5.15); or the nanodiscs themselves were captured by hydrophobic capture on L1 chips (Figure 5.16). It is standard practice in the SPR field to employ different methods of coupling or to reverse the order of attachment of ligand and analyte to show the robustness and reproducibility of the data. Double referencing is also standard. A buffer blank, which in the case of all NTS1-nanodisc-G α coupling

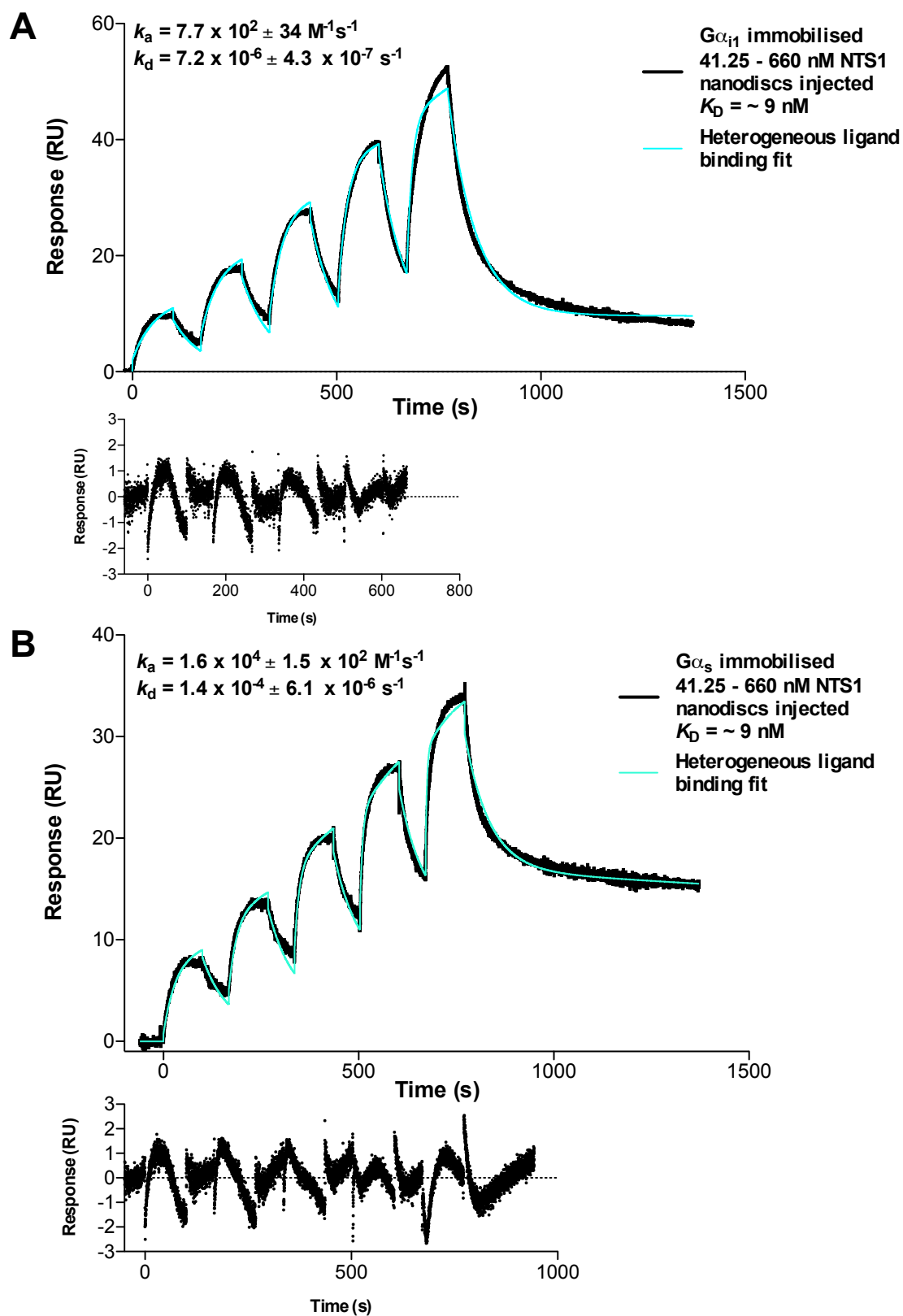


Figure 5.14. (previous page) FLAG-NTS1-nanodisc-G protein coupling with immobilised G α subunits.

Representative plots showing single cycle kinetics traces of **A**: His₆-G α_{i1} and **B**: His₆-G α_s coupling to FLAG-NTS1 in PC:PG nanodiscs, with residuals shown beneath each plot. G protein subunits (13 000 RU His₆-G α_{i1} and 10 000 RU His₆-G α_s) were amine-coupled to the surface of a CM5 sensor chip. Serial dilutions of FLAG-NTS1-PC:PG nanodiscs were injected over the surfaces in 90 s periods at the concentrations indicated, with empty nanodiscs injected as a reference. The data fitted best to a heterogeneous ligand binding model, probably as a result of the non-specific amine coupling of the G protein subunits. The low affinity data has not been included in the plots on the assumption that the low affinity parameters would arise from occluded or otherwise inaccessible sites due to amine coupling. The global fitting has weighted the lower parts of the curves, thus not closely fitting the curves of higher concentrations of G proteins. Using lower concentrations eliminates this problem. The residuals are contained within a relatively tight band, and indicate a reasonable, if not ideal fit.

experiments performed here, was empty nanodiscs, as well as the sample are injected over both the reference and sample cells. The blank is subtracted from sample in both cells, and then the reference cell is subtracted from the sample cell. This helps to correct for both refractive index changes and differences between sample and buffer, and also helps to correct for potential volume differences in the reference cell vs the sample cell, since the sample will generally take up more space on the hydrogel than simply activating and blocking the reference surface, thus increasing the potential for bulk refractive index differences between the two. A non-binding reference molecule is often immobilised to the reference cell surface to account for this. A control surface was also run where nothing was immobilised on the surface, and loaded and empty nanodiscs were injected across it simultaneously to experimental surfaces. Figure 5.17 shows that there is no non-specific binding to the flow cell itself after blank subtraction. In the case of the anti-His tagging, single referencing was used due to binding of G proteins to the anti-green fluorescent protein used in the reference cell, but the data is not significantly different from that obtained by double referencing (Table 1 and Table 2).

All initial NTS1 coupling experiments had taken place using His₆-Gα_{i1}, which produced little or no signal with apparent low affinity for the receptor. The data shown in Figure 5.3 indicated that His₆-Gα_s probably had much greater potential as a reliable binding partner for the experiments. The signal was bigger and more reproducible. After reconstitution into nanodiscs, His₆-Gα_{i1} still appeared to give a lower signal and less reliability in reproducibility of experiments. The kinetic parameters between experiments varied more than those for His₆-Gα_s and the coupled surface frequently gave a very small signal or drifting surface, even if coupled at the same level or higher than His₆-Gα_s. In fact, for the same concentration of protein, approximately double the amount of His₆-Gα_{i1} was always immobilised. This implied that there were more accessible Lys residues on the surface, and potentially, that if this was the case, the binding site for the receptor was more frequently occluded by amine immobilisation.

For the anti-His tagging, around 15 000 RU of anti-His Ab was immobilised, and 700-1 000 RU Gα captured (representative plot in Figure 5.15). In this specific case, the amount of His₆-Gα_{i1} captured was approximately half that of His₆-Gα_s, and the signal obtained was approximately half too. Unlike the amine coupled surface data, a 1:1 model could be fitted to this data as well as a heterogeneous ligand binding model. The K_D was higher than that for His₆-Gα_s, and in other experiments this appeared to be a trend, but upon averaging and analysis of the data, it is apparent that the affinity of His₆-Gα_{i1} for NTS1 is higher than that of His₆-Gα_s (Table 2).

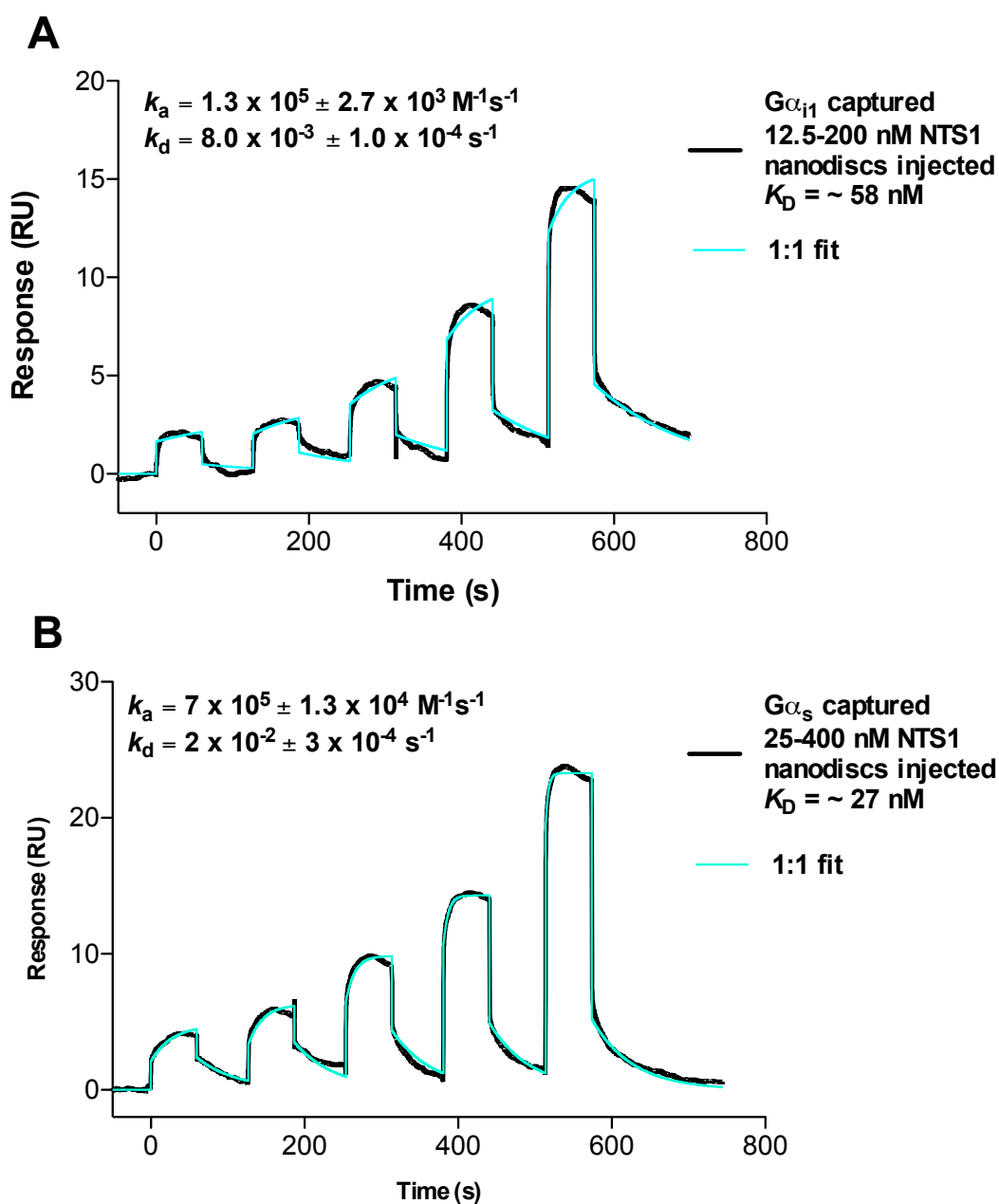


Figure 5.15. FLAG-NTS1-nanodisc-G protein coupling with immobilised anti-His antibody.

Anti-His antibody (15 000 RU) was amine-coupled to a CM5 chip and either His₆-Gα_{i1} (A) or His₆-Gα_s (B) was captured via their His tags. Serial dilutions of 200 nM (12.5, 25, 50, 100, 200 nM) or 400 nM (25, 50, 100, 200, 400 nM) FLAG-NTS1-PC:PG nanodiscs prepared with H7-cleaved MSP were then injected across the prepared surface, with empty PC:PG H7-cleaved discs as the reference. The data are single-referenced and Langmuir 1:1 binding models were globally fitted to the curves to obtain the kinetic parameters shown in the plots.

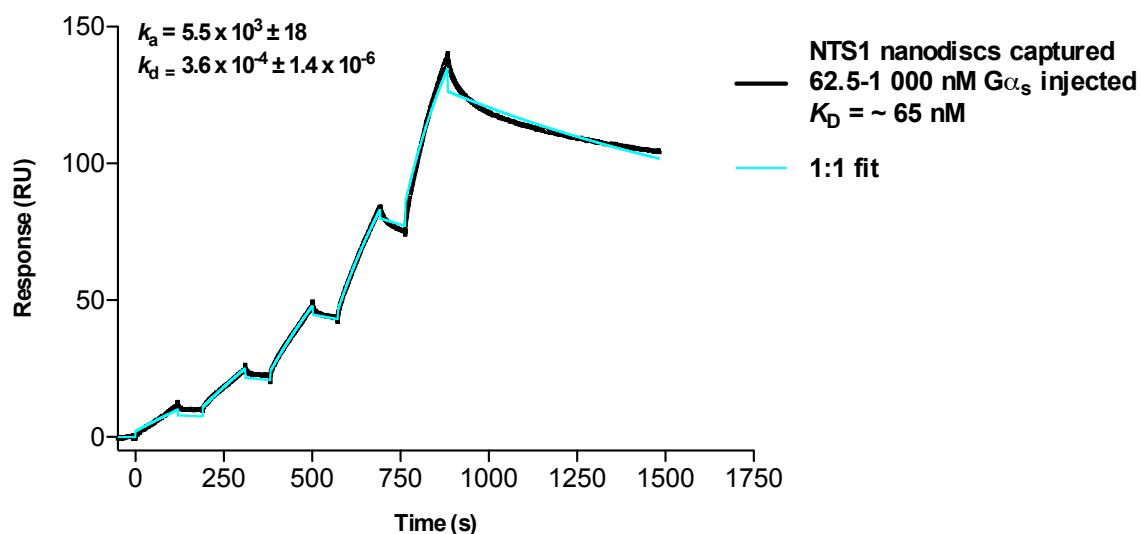


Figure 5.16. His₆-Gα_s coupling to FLAG-NTS1-PC:PG nanodiscs captured on an L1 chip.

FLAG-NTS1-PC:PG nanodiscs (2 500 RU) and empty PC:PG nanodiscs (2 000 RU) were captured in FC 4 and 3, respectively, of an L1 chip by an 800-s injection at 5 µl/min. The chip was thoroughly washed in running buffer at 50 µl/min for 30-60 min. Serial dilutions of 1 000 nM (62.5, 125, 250, 500, 1 000 nM) His₆-Gα_s were injected across the flow cells for 150 s per concentration at 50 µl/min. The data was fitted with a 1:1 Langmuir binding model as well as a heterogeneous ligand binding model, giving K_D values of 65 nM for the 1:1 fit and 0.5 and 80 nM for K_{D1} and K_{D2} respectively. The χ^2 values for the fits were 4.4 and 3.3, respectively.

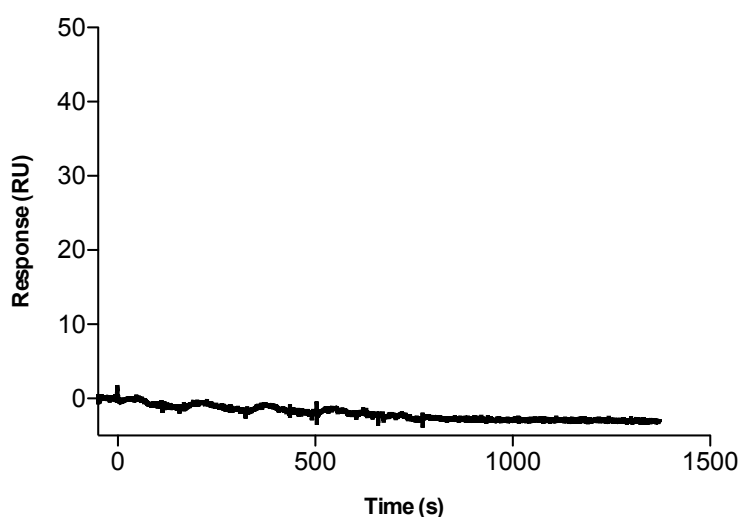


Figure 5.17. Control flow cell.

Sensorgram showing there is no non-specific binding to the sensor chip surface. One flow cell on the same chip as that used for the experiments in Figure 5.14 was left open and the same nanodisc sample was passed over all four flow cells. After double referencing, this trace and the traces in Figure 5.14 were obtained.

Table 1. Raw data showing kinetic parameters obtained for each of 22 different experiments coupling His₆-Gα_{ii} or His₆-Gα_s to NTS1-PC:PG nanodiscs for which reasonable fits were obtained.

	Conc. range (nM)	$k_a1 \pm SE$ (M ⁻¹ s ⁻¹)	$k_d1 \pm SE$ (s ⁻¹)	K _D 1 (nM)	$k_a2 \pm SE$ (M ⁻¹ s ⁻¹)	$k_d2 \pm SE$ (s ⁻¹)	K _D 2 (nM)	R _{max} 1	R _{max} 2	Chi ²
Gα_s	41.25-660	5.2 × 10 ⁴ ± 2.6 × 10 ²	6.1 × 10 ⁻⁴ ± 6.2 × 10 ⁻⁶	11.7	3.9 × 10 ⁴ ± 5.0 × 10 ²	3.6 × 10 ⁻² ± 2.1 × 10 ⁻⁴	922	23	80	1.35
Gα_s	41.25-660	1.6 × 10 ⁴ ± 1.5 × 10 ²	1.4 × 10 ⁻⁴ ± 6.1 × 10 ⁻⁶	9.0	4.1 × 10 ⁵ ± 7.4 × 10 ³	1.6 × 10 ⁻² ± 2.5 × 10 ⁻⁴	39	20	14	0.551
Gα_s	25-400	7.4 × 10 ⁵ ± 8.4 × 10 ³	3.0 × 10 ⁻³ ± 1.5 × 10 ⁻⁴	43	1.1 × 10 ⁵ ± 1.1 × 10 ⁴	7.0 × 10 ⁻² ± 1.8 × 10 ⁻³	635	1.9	7.4	0.009
Gα_s	25-400	5.6 × 10 ⁵ ± 4.0 × 10 ³	1.3 × 10 ⁻³ ± 1.1 × 10 ⁻⁴	2.4	2.0 × 10 ⁵ ± 6.2 × 10 ³	5.6 × 10 ⁻² ± 1.0 × 10 ⁻³	288	2.1	5.6	0.009
Gα_s	18.75-300	2.0 × 10 ⁴ ± 7.8 × 10 ²	4.5 × 10 ⁻³ ± 1.2 × 10 ⁻⁴	226	7.2 × 10 ⁴ ± 9.6 × 10 ²	4.9 × 10 ⁻² ± 2.9 × 10 ⁻⁴	672	7.3	41	0.038
Gα_s	18.75-300	4.4 × 10 ⁴ ± 1.1 × 10 ²	5.7 × 10 ⁻⁶ ± 8.9 × 10 ⁻⁶	0.13	3.0 × 10 ⁵ ± 2.3 × 10 ²	1.7 × 10 ⁻² ± 9.7 × 10 ⁻⁶	57	1.7	29	0.031
Gα_s over nanodiscs	62.5-1000 nM Gα _s	1.7 × 10 ³ ± 3.7	1.7 × 10 ⁻⁷ ± 8.4 × 10 ⁻⁷	0.54	1.1 × 10 ⁴ ± 17	9.1 × 10 ⁻⁴ ± 9.7 × 10 ⁻⁷	81	212	69	3.34
Gα_s anti-His single ref.	25-400	1.0 × 10 ⁴ ± 1.0 × 10 ²	4.5 × 10 ⁻⁴ ± 3.0 × 10 ⁻⁶	43	—	—		26		0.312
Gα_s anti-His single ref.	25-400	1.7 × 10 ⁵ ± 1.7 × 10 ³	1.5 × 10 ⁻³ ± 9.1 × 10 ⁻⁶	8.9	—	—		9.4		0.295
Gα_s anti-His single ref.	25-400	6.8 × 10 ⁵ ± 6.9 × 10 ³	1.7 × 10 ⁻² ± 9.3 × 10 ⁻⁵	26	3.3 × 10 ⁶ ± 2.7 × 10 ⁵	4.2 ± 7.1 × 10 ⁻²	1250	5.2	91	0.088
Gα_s	31.25-500	2.1 × 10 ⁴ ± 1.5 × 10 ²	8.2 × 10 ⁻⁷ ± 2.3 × 10 ⁻⁸	0.04	5.0 × 10 ⁴ ± 1.9 × 10 ³	2.2 × 10 ⁻² ± 5.9 × 10 ⁻⁵	438	20	12	0.378
Gα_s	31.25-500	2.2 × 10 ⁴ ± 1.6 × 10 ²	2.8 × 10 ⁻⁸ ± 1.6 × 10 ⁻⁷	0.0013	7.6 × 10 ⁴ ± 2.8 × 10 ³	2.2 × 10 ⁻² ± 1.2 × 10 ⁻⁴	284	17	8.2	0.322

	Conc. range (nM)	$k_a1 \pm SE$ ($M^{-1}s^{-1}$)	$k_d1 \pm SE$ (s^{-1})	K_D1 (nM)	$k_a2 \pm SE$ ($M^{-1}s^{-1}$)	$k_d2 \pm SE$ (s^{-1})	K_D2 (nM)	R_{max1}	R_{max2}	χ^2
Gα_s w/GTPyS	18.75-300	$2.1 \times 10^5 \pm 3.9 \times 10^2$	$1.6 \times 10^{-3} \pm 5.3 \times 10^{-5}$	74	$6.7 \times 10^4 \pm 1.4 \times 10^3$	$6.7 \times 10^{-2} \pm 3.9 \times 10^{-4}$	1020	3.2	22	0.0098
Gα_s w/GTPyS	18.75-300	$1.6 \times 10^2 \pm 0.29$	$2.0 \times 10^{-5} \pm 6.7 \times 10^{-5}$	128	$8.2 \times 10^4 \pm 1.5 \times 10^2$	$6.1 \times 10^{-2} \pm 8.6 \times 10^{-5}$	744	24	33	0.0612
Gα_s w/GTPyS	18.75-300	$1.7 \times 10^2 \pm 19$	$1.2 \times 10^{-5} \pm 2.1 \times 10^{-6}$	71	$1.3 \times 10^5 \pm 1.7 \times 10^3$	$6.6 \times 10^{-2} \pm 2.5 \times 10^{-4}$	507	93	17	0.023
Gα_s w/GTPyS	18.75-300	3.3×10^5	$5.0 \times 10^{-3} \pm 9.5 \times 10^{-5}$	15	$7.7 \times 10^4 \pm 4.1 \times 10^3$	$9.6 \times 10^{-2} \pm 1.3 \times 10^{-3}$	1250	1.3	11	0.0043
Gα_{il}	41.25-660	1.1×10^5	3.0×10^{-3}	27	3.4×10^4	2.7×10^{-2}	770	16	8.2	0.356
Gα_{il}	25-400	$1.2 \times 10^5 \pm 7.1 \times 10^2$	$2.0 \times 10^{-3} \pm 2.1 \times 10^{-5}$	17	$3.3 \times 10^4 \pm 5.4 \times 10^2$	$3.1 \times 10^{-2} \pm 1.4 \times 10^{-4}$	960	9.4	76	0.241
Gα_{il}	41.25-660	$7.8 \times 10^2 \pm 34$	$7.2 \times 10^{-6} \pm 4.3 \times 10^{-7}$	9.3	$9.6 \times 10^4 \pm 5.3 \times 10^2$	$1.4 \times 10^{-2} \pm 4.3 \times 10^{-5}$	150	102	48	1.48
Gα_{il}	25-400	$2.2 \times 10^3 \pm 5.4 \times 10^2$	$2.7 \times 10^{-6} \pm 1.1 \times 10^{-5}$	1.2	$4.3 \times 10^5 \pm 6.4 \times 10^3$	$1.5 \times 10^{-2} \pm 1.4 \times 10^{-4}$	35	21	5.7	0.122
Gα_{il} anti-His single ref.	12.5-200	1.7×10^6	6.0×10^{-2}	36	5.9×10^4	2.3×10^{-3}	40	3.1	5.1	0.129
Gα_{il}	31.25-500	$1.3 \times 10^4 \pm 71$	$4.1 \times 10^{-7} \pm 1.2 \times 10^{-6}$	0.03	$1.9 \times 10^5 \pm 3.6 \times 10^3$	$8.7 \times 10^{-3} \pm 1.1 \times 10^{-4}$	46	25	3.0	0.1

Table 2. Averaged kinetic parameters for G α coupling to FLAG-NTS1-PC:PG nanodiscs.

	His ₆ -G α_s			His ₆ -G α_s with GTP γ S			His ₆ -G α_{i1}		
	Mean	SEM ^a	N ^b	Mean	SEM	N ^b	Mean	SEM	N ^b
<i>k_{a1}</i> (M⁻¹s⁻¹)	1.9 x 10 ⁵	1.9 x 10 ³	12	1.4 x 10 ⁵	680	4	3.2 x 10 ⁵	340	6
<i>k_{d1}</i> (s ⁻¹)	2.4 x 10 ⁻³	4.2 x 10 ⁻⁵	12	1.7 x 10 ⁻³	5.4 x 10 ⁻⁵	4	1.1 x 10 ⁻²	8.4 x 10 ⁻⁶	6
K_{D1} (nM)	31	18	12	72	23	4	15	6	6
<i>k_{a2}</i> (M⁻¹s⁻¹)	4.6 x 10 ⁵	3.0 x 10 ⁴	10	8.9 x 10 ⁴	1.8 x 10 ³	4	1.4 x 10 ⁵	2.8 x 10 ³	6
<i>k_{d2}</i> (s ⁻¹)	4.4 x 10 ⁻¹	7.5 x 10 ⁻³	10	7.3 x 10 ⁻²	5.1 x 10 ⁻⁴	4	1.6 x 10 ⁻²	1.1 x 10 ⁻⁴	6
K_{D2} (nM)	470	130	10	880	160	4	330	170	6
R_{max1}	29	16	12	30	22	4	29	15	6
R_{max2}	33	10	10	21	4.6	4	37	15	6

^a standard error of the mean^b number of experiments

A one-tailed t-test comparing His₆-G α_s with GTP γ S and His₆-G α_{i1} with His₆-G α_s in pairs established that there were no significant differences between them ($p > 0.05$).

Remarkably, kinetic data were even obtained for His₆-G α_s coupling to NTS1 in nanodiscs captured on a hydrophobic L1 chip (Figure 5.16). The values (K_D s and association and dissociation rates) are very similar to those obtained for the other methods of tagging or immobilisation (Table 1). However, heterogeneous ligand binding models had to be applied to the data. Is this because the orientation of the nanodisc bound to the hydrophobic surface was random? The G protein needs to be able to access the C terminus of the receptor. If the nanodisc is captured “upside-down” on the chip, this is unlikely, particularly if the nanodiscs are packed closely on the surface. In this sense, one of the huge advantages of SPR, the ability to capture and couple ligands to the chip surface using with a choice of a wide array of potential

coupling chemistries and methods, is in some ways a drawback, in that coupling a ligand to a surface immediately makes the part of it facing the surface inaccessible to the analyte. Nevertheless, all of the data obtained indicates a relatively high affinity of His₆-Gα_s and His₆-Gα_{i1} for NTS1 (31 ± 18 nM and 15 ± 6 nM, respectively). What was interesting was that GTPγS did not appear to affect this affinity in His₆-Gα_s. When His₆-Gα_s was pre-incubated with GTPγS and then coupled to the chip, the binding affinity for NTS1 was only slightly lowered from 31 to 72 nM, but not significantly. This may be due to the amine coupling somehow affecting the GTPγS, or potentially not all of the His₆-Gα_s bound GTPγS and the high affinity signal arising from unbound G protein.

In summary, having presented kinetic binding parameters for the NTS1-nanodisc-Gα interaction that are not statistically different from one another, obtained using three different ligand tagging methods, this section has shown for the first time ever that it is possible to obtain clean, robust, reproducible binding data for one step in the critical cell-signalling system modulated by NT. There is little data in the literature for direct detection of G protein binding to GPCRs, the vast majority of assays using secondary messengers as a detection system. The method presented here opens the way for a whole new line of drug-development enquiry.

Chapter 6 - Discussion

6.1. (Cryo-)electron microscopy of small complexes

The EM studies undertaken in this thesis demonstrated that the technique has great applicability even to small particles and complexes, and showed the binding of both $G\alpha_s$ and $G\alpha_{i1}$ to NTS1, in detergent and in a lipid bilayer, using this method for the first time. The initial aim had been to show GPCR-G protein coupling using EM, and potentially to obtain a 3D cryo-structure for the interaction. The first aim was achieved, as was shown in Chapter 4. The second will require more optimisation of the system. Low resolution structures of NTS1 and $G\alpha_{i1}$ were obtained, and a negative stain structure of a GPCR-G protein complex has been solved by the Kobilka group ⁽²¹²⁾. Given this, the use in this thesis of the DNA lattice and of nanodiscs is certain to ensure the solution of a structure of the ternary complex in the near future.

The use in this thesis of the DNA lattice removes the problem of heterogeneity, concentrates particles without aggregation, keeps all particles in the active state, maintains all particles within a narrow plane, and is instantly recognizable under the EM. Because the receptor was bound to the lattice via its ligand, all particles were in the active state. Also, particles could be rapidly located on the grid simply by looking for patches of lattice, easily identifiable by a quick Fourier transform. The fact that the particles were restricted to a narrow two-dimensional plane within a few nanometers of the lattice adsorbed to the carbon meant that there was much less variation in defocus of particles within one hole of the grid or field of view. And, as mentioned

previously, tethering receptor particles to the lattice meant that thousands of particles that did not overlap or aggregate were present in each micrograph, allowing for rapid collection of large datasets, and furthermore, enabled the direct, visual demonstration of G protein-coupling to a receptor for the first time ⁽¹⁷⁹⁾. The use of 2D crystals and/or tagged monolayers for tethering proteins to EM grids have received some attention over the years as a means to decrease heterogeneity of samples, to increase throughput, and to immunopurify complexes directly from cell lysate ⁽²²⁸⁻²³⁰⁾. The grids, however, are relatively time and cost intensive to prepare, and suffer from some limitations, such as sensitivity to detergents and some buffer components, and clustering of tagged proteins due to lipid movement in the monolayer. The DNA lattice is relatively cheap and simple to prepare and proteins are tagged down in an orientationally free manner in ordered arrays.

The datasets of the separate receptor and G protein in this thesis were relatively small, due to more focus being placed on taking the work forward with the complex. However, the fact that data could be collected and structures aligned, and independently solved density maps reproduced with high correlation to one another, is a marked step forward for EM of small particles. This is one of the main findings of this thesis. The resolutions obtained for each of the proteins were high for the size of the particles. A cryo structure of the G protein processed with stricter FSC cross correlation requirements was resolved to 21 Å (personal communication, Daniele N. Selmi, formerly University of Oxford). Nevertheless, until very recently it was believed not possible to solve the structure of a particle so small. Along with the use

of the lattice, other modifications to the sample itself seemed likely to produce even better resolution improvements.

With this in mind, and considering also that cryo-specimen quality and thus resolution is degraded by the presence of detergents, reconstitution into nanodiscs seemed a logical step for a number of reasons: a) this would greatly increase the size of the particle, b) the blurring effect of detergent could be eliminated, and c) the receptor would be in its preferred lipid environment. The structures of some large membrane proteins and complexes reconstituted into nanodiscs have been solved using cryo-EM ^(78, 231, 232). The size of these complexes for EM was not an issue, but these papers nicely illustrate the cryo-EM structure of a nanodisc, and that the samples formed monodisperse specimens in vitreous ice. Samples used in this thesis for negative stain EM were vitrified for cryo-EM. The same samples that appeared far too concentrated under negative stain, and filled entire fields of view densely, were sparse in ice, with only a few discs per hole in the grid. Evidently there is some clustering of nanodiscs as a result of the negative staining, something that has been observed before, but usually with anionic, not cationic stains ^(233, 234). The nanodiscs were easily located under cryo-EM however, and the production of a stable complex of the nanodisc with G protein, coupled to the lattice and optimized for vitrification, is likely to be able to produce large data sets of the required quality for image processing and 3D structure resolution.

The work presented here has shown that not only can NTS1 be reconstituted functionally in nanodiscs, but G protein coupling with NTS1 in nanodiscs was demonstrated for the first time using gold-labelled $G\alpha$ subunits. This is a major finding. NTS1 in nanodiscs was also shown to be able to bind to the DNA lattice. This implies that the NTS1-nanodisc-G protein complex in an activated state should be able to be purified and imaged under EM, and the structures resolved here show that cryo-EM structures of the complex should be able to be resolved to low nanometer or even sub-nanometer resolution. A low-resolution negative stain structure of the detergent-solubilised β_2 -adrenergic receptor- G_s complex with stabilizing lysozyme and nanobody has already been resolved ⁽²¹²⁾, the first GPCR-G protein complex to be studied this way; and a high resolution (3.4 Å) ~100 kDa four-fold symmetric ion channel solubilised in amphipols has been solved using cryo-EM and motion correcting direct detection ⁽¹²²⁾. Another means of increasing the size of the NTS1-nanodisc-G protein complex was explored in the form of adding in streptavidin along with biotinylated NT (Figure 6.1), and a model of how this might look is shown in Figure 6.2. The experiment needs optimisation in that the complex must be purified from free streptavidin prior to EM, but essentially it would enable three things: firstly, the increased size mentioned, secondly, it would provide a structural feature for alignment, on the assumption that it was relatively rigidly bound to the receptor (although NT is easily shortened to limit spinning of a label on a bond if that were a problem), and thirdly, it would allow for the picking of ligand-bound particles, since inactive receptor would not bind the bioNT-streptavidin. Thus, the groundwork for cryo-EM of NTS1-G protein coupling presented in this thesis should allow rapid progress toward structural resolution of the interaction of these proteins in a close-to-native state.

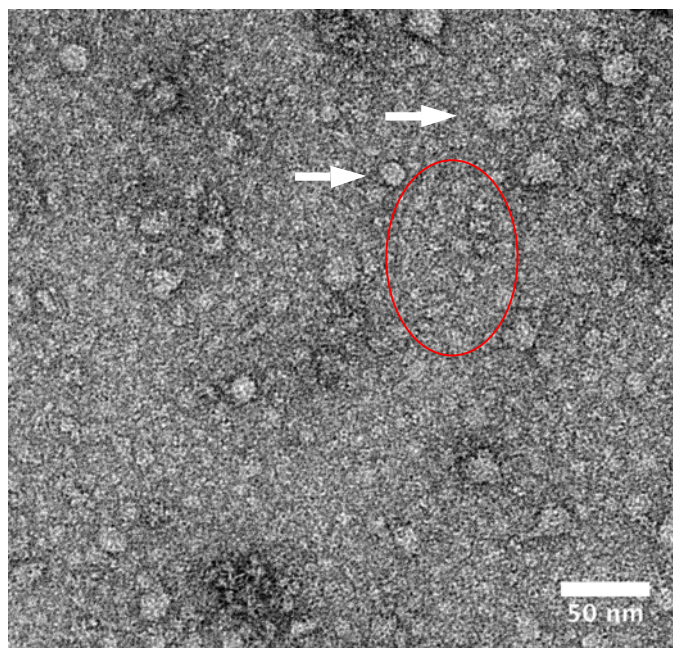


Figure 6.1. Negative stain micrograph of FLAG-NTS1-PC:PG nanodiscs incubated with bioNT and Nanogold®-labelled streptavidin.

In order to increase the size of the target particle, NTS1 nanodiscs were incubated with bioNT and Nanogold®-labelled streptavidin to test if a complex would form. No purification of the complex was performed prior to EM work. The sample was too concentrated to ascertain clearly if a complex had formed, and the need for purification is clear. The nanodiscs are marked with white arrows, and the red ring surrounds streptavidin particles. The sample was stained with 0.5 % UAc.

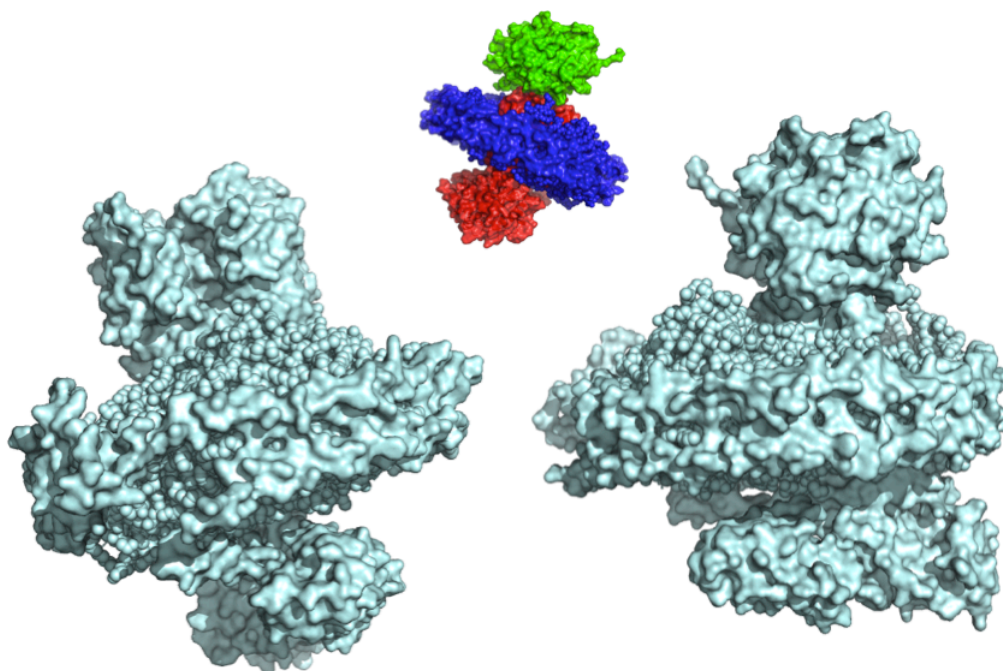


Figure 6.2. Schematic depiction of a $G\alpha$ -coupled GPCR in a nanodisc with streptavidin bound.

The likelihood of being able to see clearly and align projections of a particle from EM images increases with increasing size of the particle, as well as the presence some kind of recognisable structural feature or fiducial marker. Reconstituting NTS1 into nanodiscs bound to bioNT, coupling it with the $G\alpha$ subunit of a G protein, or the whole G protein, and then binding streptavidin to the bioNT would increase the size of the complex to ~280 kDa, as well as providing a symmetric object to act as an alignment marker in the form of streptavidin. This image gives some idea of the relative sizes and positionings of the molecules relative to each other as they would be in such a complex. The molecules are coloured as shown: streptavidin – green, PDB 3RY1⁽²³⁵⁾, β_2 G_s complex with nanobody, lysozyme and $G\beta\gamma$ removed – red, PDB 3SN6⁽⁹³⁾, the SecYE ribosome complex with everything but nanodisc removed – blue, PDB 3J00⁽⁷⁸⁾.

6.2. Nanostructures in structural and functional studies of protein-protein interactions

Of much interest is the kinetics of the interaction between GPCRs and G proteins, and the affinity of binding. These are aspects of G protein coupling that have rarely been assayed directly. Typical assays for G protein-GPCR coupling follow activation of the G protein via radioactive assays using [^{35}S]GTP γ S, or by assaying cAMP or Ca^{2+} levels. Knowing the affinity of a G protein for a GPCR, and the differential affinities of the various G proteins for the same GPCR, and then isolating the residues involved in the interaction and potentially studying how different $\beta\gamma$ subunits influenced the interaction, would be of immense use for the development of drugs targeting specific signalling pathways. An additional level of complexity that needs to be unravelled would be how different agonists affect the affinities and rates of binding of G proteins to GPCRs, and whether the type of lipid environment of the receptor has any influence on these parameters.

GPCR structure and function are most ideally assayed in a membrane environment. However, as discussed throughout this thesis and in much literature on the subject, lipid membranes and membrane-mimetic environments do not lend themselves readily to most biophysical methods. SPR is by now a well-established real-time, label-free means of robustly determining the binding constants and affinities of proteins for antibodies, ligands or other binding partners, and in fact, the binding of NTS1 to NT in detergent has already been demonstrated ^(151, 153), and a number of other studies have investigated GPCR-ligand or drug interactions, reconstitution of

GPCRs on SPR chips, or GPCR-G protein interactions in detergent^(145, 146, 148-150, 152, 155, 156, 236). Initially, the method of Harding *et al.* mentioned above, of tagging the receptor to the immobilised ligand on the chip surface was used to try to show G protein coupling. However, as has also been mentioned, SPR is very sensitive to small changes in refractive index in the buffer or sample, temperature changes and pH changes, which affect the swelling of the dextran matrix as well as influence the signal directly. There are a number of other effects to be aware of, including drift and mass transport, which affect the quality of the data obtained. Tagging NTS1 via the ligand and injecting $G\alpha_{i1}$ showed that coupling was taking place, but the data could not be analysed due to bulk effects. This was the case with all of the G protein coupling data obtained with the system in detergent. Additionally, most initial experiments were carried out with $G\alpha_{i1}$ as the analyte, which showed a very small binding signal. $G\alpha_s$, on the other hand, gave a much larger signal for the same concentrations used, and this was also apparent in some of the experiments with NTS1-nanodiscs, such as when the G proteins were captured by anti-His Abs on the chip surface. The $G\alpha_{i1}$ signal was too small and noisy to be analysed. On the other hand, the experiments with tagging NTS1 via bioNT to streptavidin amine-coupled to the chip surface, where no G protein binding signal was obtained, vs tagging NTS1 to thiolated NT coupled directly to the chip surface with an immediate detection of signal, show that the means of capturing or immobilising the ligand to the SPR chip can have a critical influence on the binding signal obtained. Essentially it is important to try a variety of immobilisation methods, and also to reverse the order of the ligand and analyte prior to concluding that no binding is occurring. Clearly some kind of steric clash or occlusion was occurring with the streptavidin-bound NT-NTS1. Did the streptavidin force the NT, and thus the receptor, into some inaccessible orientation?

This is entirely possible, given that thiol coupling the NT enabled a signal to be recorded.

On-chip reconstitution seemed like a promising means of obtaining the desired data, since a number of studies of a GPCR have been undertaken in a bilayer, showing G protein coupling ^(127, 160, 161), and rhodopsin has been reconstituted on an SPR chip, as have a number of other membrane receptors, using various methods ^(133, 143, 145, 148, 150). Tagging the receptor down to the chip via its ligand and within a lipid membrane and flowing the G α over it seemed the most logical organisation of the system, since this way all receptor molecules would be active, reducing heterogeneity, and the set-up would mimic the presentation of the receptor at the surface of a membrane, even though the G protein would not be tethered to the membrane via a lipid linker, as it would in a cell. However, the requirements of NTS1 in terms of the specific lipids and detergents in which it is active, and the sensor surface in terms of the level of complexity/hydrophobicity of lipid:detergent mixtures that are required in order to adhere to the surface, could not be balanced, and persistent drift was intractable. The only detergent:lipid mixture that appeared to be most stable, the same mixture that Karlsson and Löfås used ⁽¹⁴³⁾, was POPC:OG, in neither of which NTS1 is active. Other methods of on-chip reconstitution could have been explored, again highlighting the flexibility and broad applicability of SPR as a tool for examining protein-protein interactions. As tested in this thesis, proteoliposomes can be used to tag the receptor to the chip. In this case the liposomes were filled with NT on the assumption that the G α would bind the “intracellular” side of the receptor, which when reconstituted in liposomes would only be accessible from the outside. Using proteoliposomes,

however, immediately discards at least half of the potential signal due to symmetric insertion of the receptor into the membrane. Capturing proteoliposomes and then fusing them on the chip using 5 mM CaCl_2 was also tested, although not discussed, since G protein binding signals were not obtained this way. Modified lipids, such as thiolated or biotinylated lipids, can be used on the chip surface to act as nucleation points for tethering bilayers or proteoliposomes, and these may possibly have been a good option.

Nevertheless, the option ultimately used was successful. Reconstituting NTS1 into nanodiscs immediately eliminated the confounding factors of the previous experiments, a major finding for this thesis: bulk signals caused by detergent and/or glycerol, which are required for receptor function/stability but whose concentrations could not be perfectly matched to the running buffer because the large micelle size of DDM (70 kDa) precludes dialysis; and drift from the chip, because the receptor itself could be used as the analyte rather than ligand, and G protein could be coupled to the chip covalently. Further advantages were that NTS1 was in a bilayer, the nanodiscs could be dialysed and concentrated, and the NTS1-nanodiscs could be used as the ligand as well, simply by capturing them on an L1 chip. Using the empty nanodiscs as the reference “blank” ensured that the most authentic blank possible was being used to subtract any non-specific binding signal, unlike for example, using just buffer alone as the blank when injecting an analyte, since the protein solution alone has a refractive index slightly different from that of buffer, and this was seen in some of the experiments with on-chip reconstituted NTS1.

Most of the data obtained for the NTS1-nanodisc-G protein-coupling experiments could be fitted relatively well with a heterogeneous ligand binding model. The χ^2 values were low and the fits, by eye, were good. The standard errors and statistical tests for parameter significance were within the acceptable ranges, and the residuals for the fits were also within acceptable ranges for a good fit. The kinetic data was reproducible between experiments, within error, and changing the roles of the binding partners did not alter the outcome. The fraction of data with the best fits, representing possibly one third to one half of the total data was presented here. The heterogeneous ligand binding model assumes two equivalent and independent sites on the ligand, and is frequently used when the method of immobilisation is amine coupling, due to its non-specific nature. The ligand may be immobilised in many different orientations depending on the number and location of Lys residues, and binding sites may be occluded. This effect is illustrated in Figure 6.3. An examination of the Lys residues in $G\alpha_{i1}$ and $G\alpha_s$ shows some differences (Figure 6.4) between the two, potentially accounting for some of the differences seen in the immobilisation efficiency of the proteins and the variations in signal obtained for the two. No GDP-bound crystal structure of $G\alpha_s$ is available, but it is clear from looking at Figure 6.4 that the GTPase domain of $G\alpha_s$ has a patch that is clear of Lys residues, unlike the same area in $G\alpha_{i1}$, and this is where the C-terminal α -helix that binds the receptor is located. The possibility that receptor binding would be occluded by this portion of the molecule being covalently coupled to the chip are smaller than those for $G\alpha_{i1}$, which has Lys

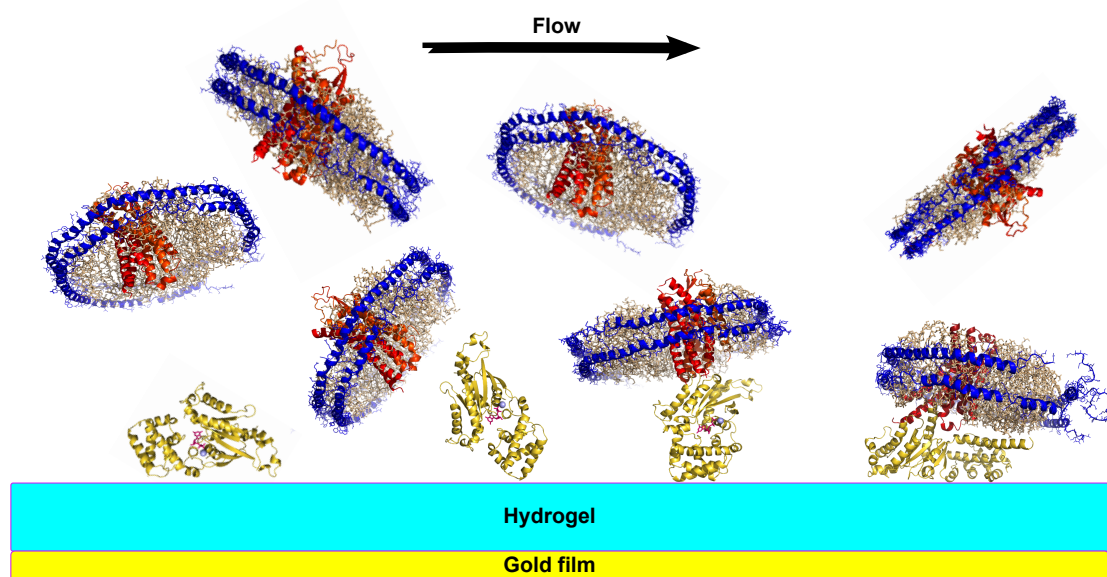


Figure 6.3. Schematic depiction of NTS1 nanodisc-G α coupling in an SPR flow cell.

A G α subunit (yellow) (PDB 1BOF⁽²¹⁵⁾) is amine-coupled to the chip surface, and NTS1-nanodiscs injected across the flow cell (PDBs 4GRV⁽¹⁰⁰⁾ and 3J00⁽⁷⁸⁾). The C-terminal α -helix of the G α involved in binding NTS1 is in the GTPase domain (the upper domain in the second from left G α). This binding site on the left hand G α would not be as accessible to the receptor, lowering the binding affinity. The G protein-coupled receptor-nanodisc on the right is represented by the β_2 -G $_s$ complex with nanobody, lysozyme and G $\beta\gamma$ removed (PDB 3SN6⁽⁹³⁾). As in that structure, the α -helical domain of the G α subunit would swing around relative to the GTPase domain upon receptor binding/activation. If both domains were covalently fixed to the chip surface, this would not be possible and binding may not take place.

residues clustered in both domains. In absolute numbers, G α_s has 5 fewer Lys residues (25) than G α_{i1} (30). However, within the system studied, ligand immobilisation is not the only potential source of heterogeneity. Other possible sources are: not all of the receptor may be ligand-bound; not all of the G α may be GDP-bound, since the G α storage buffer was not supplemented with GDP; and some of the nanodiscs could contain NTS1 dimers. GPCRs and G proteins are known to be able to form a pre-coupled complex prior to ligand-binding, which increases affinity for the ligand^(237, 238). Is it possible that non-ligand-bound NTS1 pre-coupled to G α

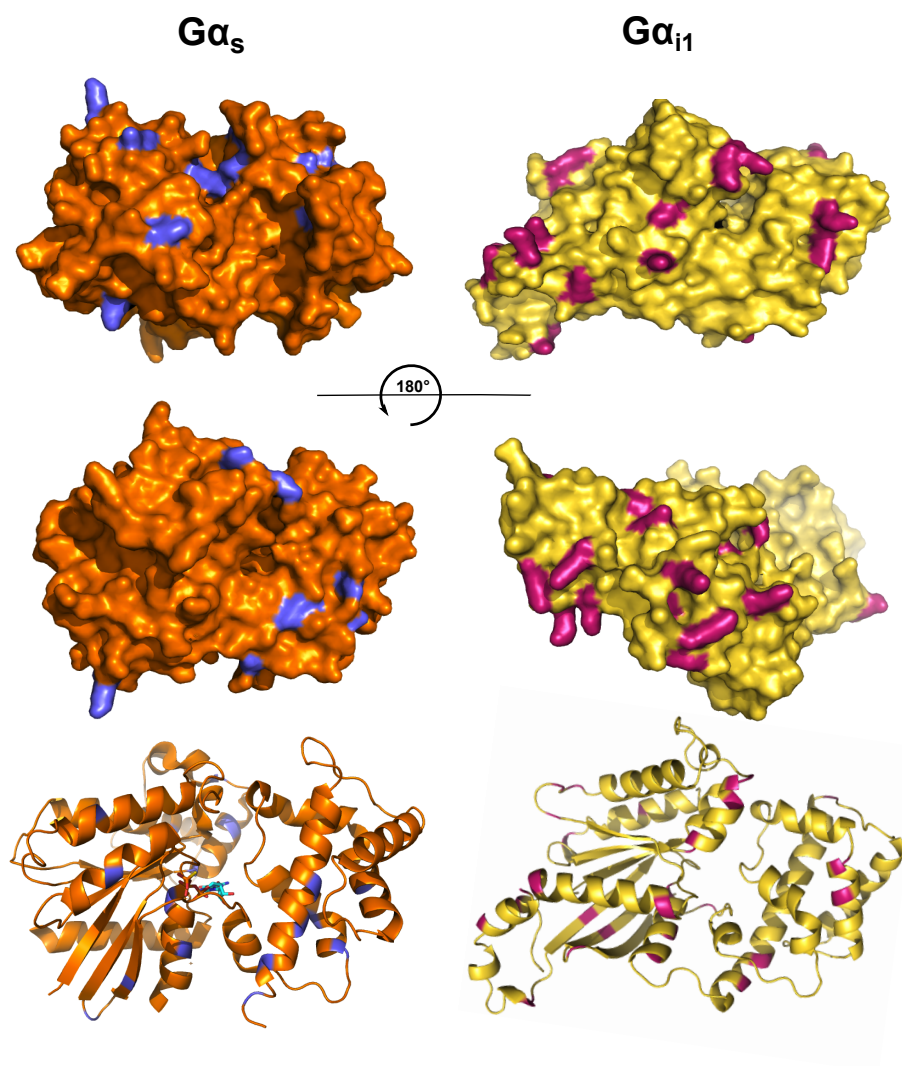


Figure 6.4. Comparison of accessible Lys residues in $G\alpha_s$ and $G\alpha_{i1}$.

Surface (top and middle) and ribbon representations of GTP-bound $G\alpha_s$ (left) (PDB 1AZT⁽²³⁹⁾) and GDP-bound $G\alpha_{i1}$ (right) (PDB 1BOF⁽²¹⁵⁾), showing the location of the Lys residues in purple and pink, respectively. The left-hand side of the molecules shown is the GTPase domain. Some of the differences in amine coupling efficiency are likely due to differences in number, coverage, and accessibility of Lys residues in the proteins. GTP-bound $G\alpha_s$ (left; PDB) and GDP-bound $G\alpha_{i1}$ (right)

on the chip surface with a lower binding affinity? If so, this would affect the data fit.

There is a small chance that some of the discs contain dimers. Reconstitution of target protein into nanodiscs follows a Poisson distribution⁽¹⁷¹⁾, such that at the 1:50 MSP:NTS1 ratio used for reconstitution here, 96 % of nanodiscs would be empty,

close to 3.8 % would contain one receptor and a tiny fraction would contain two receptors. After enrichment, this fraction would still constitute a negligible proportion, although the tendency for NTS1 to form dimers or not may skew this distribution. This could give differential binding parameters.

The affinity constants determined for both $G\alpha_{i1}$ and $G\alpha_s$ were in the low nanomolar range, implying high affinity for the receptor. There was statistically no difference in the affinities, or incidentally, in the affinity of GTP γ S-bound $G\alpha_s$ for the receptor. If a more specific tagging method can be found for the G protein in order to reduce heterogeneity in the system, this may prove not to be the case, but stable receptor-G protein-GTP γ S complexes have been observed ⁽²⁴⁰⁾. The EM data in this thesis also shows that addition of GTP γ S does not completely abolish G protein coupling.

Alves *et al.* used plasmon waveguide resonance, a variant of SPR, to study the affinities of various $G\alpha_i$ and $G\alpha_o$ proteins for the δ -opioid receptor. The affinities were found to be ligand- and $\beta\gamma$ -subunit-dependent ^(127, 160). For example, the affinity of $G\alpha_{i1}$ was ~300 nM for agonist-bound receptor, but only about 70 nM for unliganded receptor. The affinity of GTP γ S for the G proteins also differed, depending upon which molecule the receptor was bound to. What this means within the setting of the cell is that the receptor is able to broaden its scope of function greatly. With every additional parameter, sensitivity and exquisite subtlety of function grows. GPCRs are able to bind many different ligands, and many different G proteins. If the affinity of each different G protein for the receptor is modulated by the type and

presence or absence of ligand, the type and presence or absence of $\beta\gamma$ subunit, and the affinity of GTP(γ S), which activates the G protein, for the G protein alters according to the above parameters, the scope for function is huge. Add to this the potential for homo- and hetero-dimerisation of the receptor, and the question of whether a single ligand can activate a GPCR dimer, and it becomes increasingly clear why GPCRs are responsible for, and so very capable of controlling, so many of the most essential and critical cell functions, and why any defect of function anywhere along the signalling pathway can have such a profound influence on the health of the organism.

The work presented here is not the first time that nanodiscs have been used as the analyte in SPR studies. A few other instances were found ^(138, 139, 241), but to date no other SPR study has used nanodiscs to investigate either ligand binding to GPCRs, or GPCR-G protein coupling; and even though there are examples of on-chip reconstitution of GPCRs in the field, none of them demonstrates GPCR-G protein-coupling in a bilayer. This said, the affinities of G proteins for their receptors only tell a tiny fraction of the story of GPCR function, as indicated above. A high affinity may not necessarily indicate efficient function. It may be that G proteins with lower affinities, in other words, rapid dissociation rates, more effectively activate their signalling cascades, since they would more quickly dissociate from the receptor to move on to the next signalling partner in the cascade. This may be the significance of the increased affinity of the inhibitory G_i for the unliganded δ -opioid receptor. Does the lower affinity of G_i in the presence of ligand more efficiently activate the inhibition of adenylyl cyclase and cAMP levels? This would, of course, depend on the relative concentrations of G proteins in the cell, and there is no data on the extent to

which receptors discriminate between different G proteins in the cell, but is an interesting hypothesis to consider. The affinities of $G\alpha_{i1}$ and $G\alpha_s$ for NTS1 presented in this thesis have been determined in a completely *in vitro* setting, without any of the regulatory proteins or $\beta\gamma$ subunits that would normally be present within a cell context, that have the potential to influence the binding affinities of G proteins. Thus, the extent to which these numbers have meaning for the function of NTS1 can only be hypothesised, but the receptor is known to signal agonist-selectively through both G_s and G_i ^(99, 242, 243). Further work investigating the influence of regulatory proteins on the interaction is sure to elucidate these effects. The ability to find out, relatively rapidly, the affinities of various G proteins for their cognate receptors, and to test the effects of mutations to conserved residues within the C-terminal α -helix of the G protein; or within the residues of a GPCR that are expected to bind the G protein; or the effects of different lipid environments on the coupling affinity and rate of binding of a GPCR to G proteins; or the effect of the $\beta\gamma$ -subunit on the coupling, is immensely useful for later clinical research for drug-targeting of signalling pathways.

6.3. Conclusion

The major findings of this thesis are:

- that the use of a ligand-functionalised DNA lattice improves resolution and allows the structural resolution of small asymmetric proteins from cryo-EM data

- that GPCR-G protein coupling can be demonstrated on the DNA lattice under EM and by using SPR in detergent and in a soluble, nanoscale synthetic lipid bilayer termed a nanodisc
- that the reconstitution of NTS1 into nanodiscs immediately removes all confounding bulk effects from data signals in SPR
- that the affinity of NTSI in a lipid bilayer for $G\alpha$ subunits can be determined using SPR, implying that future studies of this interaction can employ multiple approaches for determining the residues and lipid types crucial for the interaction

Chapter 7 - Summary and future work

7.1. Summary

Chapter 1 introduced the areas of biological membranes, the field of membrane protein study, the structure and function of GPCRs, G proteins and the neurotensin receptor. The biophysical techniques used in this thesis were presented, and the scope and nature of the research were defined. The primary aims of the thesis were outlined: to investigate the interactions of NTS1 with G proteins structurally and functionally using the methods of electron microscopy and surface plasmon resonance.

Chapter 2 described all of the experimental methods and protocols used in order to produce functionalised self-assembling DNA lattices for the EM study of arrays of orientationally disordered NTS1, $G\alpha_{i1}$, and a complex of the two; as well as the methods used to produce all of the proteins used in the study, proteoliposomes, the methods for on-chip reconstitution and study of G protein coupling in a bilayer as well as in detergents, and the methods used to form nanodiscs into which NTS1 was reconstituted and studied using SPR. Image and data-processing were also described.

Chapter 3 described the characterisation of all of the components used in the study: the purification and activity assaying of NTS1, FLAG-NTS1, NTS1- $G\alpha_{i1}$, TEV protease, His₆- $G\alpha_{i1}$, His₆- $G\alpha_s$, and MSP1D1; the preparation of lipid:detergent mixtures, liposomes, proteoliposomes and nanodiscs; the preparation and negative stain and electron microscopy of DNA lattices and the structure of the lattice determined by 2D electron crystallography. The low-resolution negative stain structure of the large lattice shows the over-under three-way weave pattern of the

Kagome lattice. The optimal ratios of scaffold protein to lipid to detergent and NTS1 for successful nanodisc formation were discussed, and negative stain electron microscopy showed that populations of homogeneously-sized nanodiscs formed under the correct conditions.

Chapter 4 described the EM of the DNA-protein arrays, as well as the imaging of the NTS1-G protein complex on the arrays and in nanodiscs. Arrays of Nanogold®-labelled G protein were shown, with the Fourier transforms of the images indicating the presence of the lattice underlying the receptor-G protein complex. The 3D structures of NTS1 and $G\alpha_{i1}$, determined from single particle analysis processing of the EM data demonstrated how the protein structures determined through the use of tagging the targets to the DNA lattice represent a resolution breakthrough for SPA of small molecules. The density maps of NTS1 solved by different people independently were highly correlated.

Chapter 5 showed the means used to determine appropriate lipid:detergent ratios for on-chip reconstitution of NTS1, and the interactions of NTS1 with NT and with $G\alpha$ subunits in detergent, bilayers and in nanodiscs, using SPR to measure association and dissociation rates and the affinity constants. Kinetic data were extracted from NTS1-NT interactions in detergent and in nanodiscs, and from NTS1- $G\alpha$ interactions in nanodiscs, the latter two demonstrated for the first time ever.

Chapter 6 discussed the implications of the work presented in the thesis within the wider field in general, and considered some of the means and approaches that could be employed to improve the data. The advancement of cryo-EM resolution limits with improved instruments and strategies to enable the solution of low-molecular weight

proteins were discussed in relation to the advancements presented here, and how strategies could be combined to enable the cryo-EM solution of the NTS1-nanodisc-G protein structure. The methods used to extract kinetic data from the binding of G protein α subunits to NTS1 were covered, describing how the experiments built upon each other to develop a system that enabled clean data to be collected and fitted. The implications for the binding parameters within the context of signalling within the cell were considered, and how these are likely to be influenced by the presence or absence of ligand, $\beta\gamma$ subunits, and other regulatory proteins.

7.2. Future work

Future work will concentrate on forming and purifying an NTS1-nanodisc-G protein complex with a fiducial marker, such as the streptavidin already discussed, complexed to it that also increases the size of the complex. The $\beta\gamma$ subunits will be obtained and incorporated into the complex if possible. Further tests will be performed to ensure that the complex is able to bind to the DNA lattice for improved data collection. Tests that were attempted for this thesis that were not successful due to low gold-labelling efficiency will be performed again, including the use of Nanogold®-labelled CysNT to assess whether one or two NTS1 molecules are incorporated into nanodiscs under conditions that would allow for more of the discs to contain dimers, such as higher target protein amounts and the use of a longer scaffold protein. If dimeric NTS1-containing nanodiscs are able to be separated from those containing monomers, a most useful experiment would be to determine the structure of dimeric NTS1 with G protein. This would answer one of the perennial questions in the GPCR field, do

dimeric GPCRs couple to one or two G proteins? Cryo-EM data will preferably be collected on an instrument with a direct detector with motion-correcting software.

A more specific method of coupling the G protein to the SPR chip will be explored. NTS1 will be reconstituted into nanodiscs using different types of lipids, including BPL, in order to assess the lipid-dependence of G protein coupling. The $\beta\gamma$ subunits will be obtained and the effect of their presence tested on the affinities of the receptor $G\alpha$ interaction. The effect of the antagonist, SR 48692, on the affinity of G protein coupling, will also be tested.

References

1. Hunte, C., and Richers, S. (2008) Lipids and membrane protein structures, *Current opinion in structural biology* 18, 406-411.
2. Lee, A. G. (2005) How lipids and proteins interact in a membrane: a molecular approach, *Molecular bioSystems* 1, 203-212.
3. Shevchenko, A., and Simons, K. (2010) Lipidomics: coming to grips with lipid diversity, *Nature reviews. Molecular cell biology* 11, 593-598.
4. Singer, S. J., and Nicolson, G. L. (1972) The fluid mosaic model of the structure of cell membranes, *Science* 175, 720-731.
5. Day, C. A., and Kenworthy, A. K. (2009) Tracking microdomain dynamics in cell membranes, *Biochimica et Biophysica Acta (BBA) - Biomembranes* 1788, 245-253.
6. Meyer, B. H., Segura, J. M., Martinez, K. L., Hovius, R., George, N., Johnsson, K., and Vogel, H. (2006) FRET imaging reveals that functional neurokinin-1 receptors are monomeric and reside in membrane microdomains of live cells, *Proceedings of the National Academy of Sciences of the United States of America* 103, 2138-2143.
7. Lagerholm, B. C., Weinreb, G. E., Jacobson, K., and Thompson, N. L. (2005) Detecting microdomains in intact cell membranes, *Annual review of physical chemistry* 56, 309-336.
8. Vyas, N., Goswami, D., Manonmani, A., Sharma, P., Ranganath, H. A., VijayRaghavan, K., Shashidhara, L. S., Sowdhamini, R., and Mayor, S. (2008)

-
- Nanoscale organization of hedgehog is essential for long-range signaling, *Cell* 133, 1214-1227.
9. Kusumi, A., Koyama-Honda, I., and Suzuki, K. (2004) Molecular dynamics and interactions for creation of stimulation-induced stabilized rafts from small unstable steady-state rafts, *Traffic* 5, 213-230.
10. Wallin, E., and Heijne, G. V. (1998) Genome-wide analysis of integral membrane proteins from eubacterial, archaean, and eukaryotic organisms, *Protein Science* 7, 1029-1038.
11. Krogh, A., Larsson, B., von Heijne, G., and Sonnhammer, E. L. L. (2001) Predicting transmembrane protein topology with a hidden markov model: application to complete genomes, *Journal of molecular biology* 305, 567-580.
12. Davey, J. (2004) G-protein-coupled receptors: new approaches to maximise the impact of GPCRS in drug discovery, *Expert opinion on therapeutic targets* 8, 165-170.
13. Terstappen, G. C., and Reggiani, A. (2001) In silico research in drug discovery, *Trends in pharmacological sciences* 22, 23-26.
14. Arinaminpathy, Y., Khurana, E., Engelman, D. M., and Gerstein, M. B. (2009) Computational analysis of membrane proteins: the largest class of drug targets, *Drug discovery today* 14, 1130-1135.
15. Widom, B., Bhimalapuram, P., and Koga, K. (2003) The hydrophobic effect, *Physical Chemistry Chemical Physics* 5, 3085-3093.
16. Tanford, C. (1978) The hydrophobic effect and the organization of living matter, *Science* 200, 1012-1018.

-
17. Tanford, C. (1980) *The hydrophobic effect: Formation of micelles and biological membranes*, 2nd ed., John Wiley and Sons, Inc., Canada.
 18. Quinn, P. J. (1976) *The molecular biology of cell membranes*, Macmillan Press, London, UK.
 19. Vaz, W. L., Nisksch, A., and Jahnig, F. (1978) Electrostatic interactions at charged lipid membranes. Measurement of surface pH with fluorescent lipid pH indicators, *European journal of biochemistry / FEBS* 83, 299-305.
 20. Prats, M., Teissie, J., and Tocanne, J.-F. (1986) Lateral proton conduction at lipid-water interfaces and its implications for the chemiosmotic-coupling hypothesis, *Nature* 322, 756-758.
 21. van der Goot, F. G., Gonzalez-Manas, J. M., Lakey, J. H., and Pattus, F. (1991) A 'molten-globule' membrane-insertion intermediate of the pore-forming domain of colicin A, *Nature* 354, 408-410.
 22. McLaughlin, S. (1989) The electrostatic properties of membranes, *Annual review of biophysics and biophysical chemistry* 18, 113-136.
 23. Menestrina, G., Forti, S., and Gambale, F. (1989) Interaction of tetanus toxin with lipid vesicles. Effects of pH, surface charge, and transmembrane potential on the kinetics of channel formation, *Biophysical journal* 55, 393-405.
 24. Murray, D., Arbuzova, A., Hangyas-Mihalyne, G., Gambhir, A., Ben-Tal, N., Honig, B., and McLaughlin, S. (1999) Electrostatic properties of membranes containing acidic lipids and adsorbed basic peptides: theory and experiment, *Biophysical journal* 77, 3176-3188.

-
25. Kraayenhof, R., Sterk, G. J., and Sang, H. W. (1993) Probing biomembrane interfacial potential and pH profiles with a new type of float-like fluorophores positioned at varying distance from the membrane surface, *Biochemistry* 32, 10057-10066.
 26. Bortoletto, R. K., and Ward, R. J. (1999) A stability transition at mildly acidic pH in the alpha-hemolysin (alpha-toxin) from *Staphylococcus aureus*, *FEBS letters* 459, 438-442.
 27. Bretscher, M. S. (1972) Asymmetrical lipid bilayer structure for biological membranes, *Nature: New biology* 236, 11-12.
 28. Zachowski, A. (1993) Phospholipids in animal eukaryotic membranes: transverse asymmetry and movement, *The Biochemical journal* 294 (Pt 1), 1-14.
 29. Balasubramanian, K., and Schroit, A. J. (2003) Aminophospholipid asymmetry: A matter of life and death, *Annual review of physiology* 65, 701-734.
 30. Kyte, J. (1995) *Structure in protein chemistry.*, Garland Publishing, New York.
 31. Marsh, D. (2013) *Handbook of lipid bilayers.*, Second Edition ed., CRC Press, FL, USA.
 32. London, E. (2002) Insights into lipid raft structure and formation from experiments in model membranes, *Current opinion in structural biology* 12, 480-486.
 33. Simons, K., and Gerl, M. J. (2010) Revitalizing membrane rafts: new tools and insights, *Nature reviews. Molecular cell biology* 11, 688-699.

-
34. Heller, H., Schaefer, M., and Schulten, K. (1993) Molecular dynamics simulation of a bilayer of 200 lipids in the gel and in the liquid crystal phase, *The Journal of Physical Chemistry* 97, 8343-8360.
35. Landau, E. M., and Rosenbusch, J. P. (1996) Lipidic cubic phases: a novel concept for the crystallization of membrane proteins, *Proceedings of the National Academy of Sciences of the United States of America* 93, 14532-14535.
36. Garavito, R. M., and Ferguson-Miller, S. (2001) Detergents as tools in membrane biochemistry, *The Journal of biological chemistry* 276, 32403-32406.
37. Wennerström, H., and Lindman, B. (1979) Micelles. Physical chemistry of surfactant association, *Physics Reports* 52, 1-86.
38. Mitchell, D. J., Tiddy, G. J. T., Waring, L., Bostock, T., and McDonald, M. P. (1983) Phase behaviour of polyoxyethylene surfactants with water. Mesophase structures and partial miscibility (cloud points), *Journal of the Chemical Society, Faraday Transactions 1: Physical Chemistry in Condensed Phases* 79, 975-1000.
39. Seddon, A. M., Curnow, P., and Booth, P. J. (2004) Membrane proteins, lipids and detergents: not just a soap opera, *Biochimica et biophysica acta* 1666, 105-117.
40. Jelinek, R., and Kolusheva, S. (2005) Membrane interactions of host-defense peptides studied in model systems, *Current protein & peptide science* 6, 103-114.
41. Sanders, C. R., and Prosser, R. S. (1998) Bicelles: a model membrane system for all seasons?, *Structure* 6, 1227-1234.

-
42. Sanders, C. R., 2nd, and Schwonek, J. P. (1992) Characterization of magnetically orientable bilayers in mixtures of dihexanoylphosphatidylcholine and dimyristoylphosphatidylcholine by solid-state NMR, *Biochemistry* 31, 8898-8905.
43. Sanders, C. R., 2nd, and Prestegard, J. H. (1990) Magnetically orientable phospholipid bilayers containing small amounts of a bile salt analogue, CHAPSO, *Biophysical journal* 58, 447-460.
44. Sanders, C. R., 2nd, and Landis, G. C. (1995) Reconstitution of membrane proteins into lipid-rich bilayered mixed micelles for NMR studies, *Biochemistry* 34, 4030-4040.
45. Greenhall, M. H., Yarwood, J., Brown, R., and Swart, R. M. (1998) Spectroscopic Studies of Model Biological Membranes in Vesicles and Langmuir–Blodgett Films, *Langmuir : the ACS journal of surfaces and colloids* 14, 2619-2626.
46. Chen, H. M., Leung, K. W., Thakur, N. N., Tan, A., and Jack, R. W. (2003) Distinguishing between different pathways of bilayer disruption by the related antimicrobial peptides cecropin B, B1 and B3, *European journal of biochemistry / FEBS* 270, 911-920.
47. Harrop, S. J., DeMaere, M. Z., Fairlie, W. D., Reztsova, T., Valenzuela, S. M., Mazzanti, M., Tonini, R., Qiu, M. R., Jankova, L., Warton, K., Bauskin, A. R., Wu, W. M., Pankhurst, S., Campbell, T. J., Breit, S. N., and Curmi, P. M. (2001) Crystal structure of a soluble form of the intracellular chloride ion channel CLIC1 (NCC27) at 1.4-Å resolution, *The Journal of biological chemistry* 276, 44993-45000.
48. Warton, K., Tonini, R., Fairlie, W. D., Matthews, J. M., Valenzuela, S. M., Qiu, M. R., Wu, W. M., Pankhurst, S., Bauskin, A. R., Harrop, S. J., Campbell, T. J.,

-
- Curmi, P. M., Breit, S. N., and Mazzanti, M. (2002) Recombinant CLIC1 (NCC27) assembles in lipid bilayers via a pH-dependent two-state process to form chloride ion channels with identical characteristics to those observed in Chinese hamster ovary cells expressing CLIC1, *The Journal of biological chemistry* 277, 26003-26011.
49. Winterhalter, M. (2000) Black lipid membranes, *Current Opinion in Colloid & Interface Science* 5, 250-255.
50. Papahadjopoulos, D., and Miller, N. (1967) Phospholipid model membranes. I. Structural characteristics of hydrated liquid crystals, *Biochimica et biophysica acta* 135, 624-638.
51. Lasch, J., Weissig, V., and Brandl, M. (2003) Preparation of liposomes., In *Liposomes*. (Torchilin, V. P., and Weissig, V., Eds.) 2nd ed., Oxford University Press, Oxford, UK.
52. Szoka, F., Jr., and Papahadjopoulos, D. (1978) Procedure for preparation of liposomes with large internal aqueous space and high capture by reverse-phase evaporation, *Proceedings of the National Academy of Sciences of the United States of America* 75, 4194-4198.
53. Olson, F., Hunt, C. A., Szoka, F. C., Vail, W. J., and Papahadjopoulos, D. (1979) Preparation of liposomes of defined size distribution by extrusion through polycarbonate membranes, *Biochimica et biophysica acta* 557, 9-23.
54. MacDonald, R. C., MacDonald, R. I., Menco, B. P., Takeshita, K., Subbarao, N. K., and Hu, L. R. (1991) Small-volume extrusion apparatus for preparation of large, unilamellar vesicles, *Biochimica et biophysica acta* 1061, 297-303.

-
55. Hope, M. J., Bally, M. B., Webb, G., and Cullis, P. R. (1985) Production of large unilamellar vesicles by a rapid extrusion procedure: characterization of size distribution, trapped volume and ability to maintain a membrane potential, *Biochimica et biophysica acta* 812, 55-65.
56. Mimms, L. T., Zampighi, G., Nozaki, Y., Tanford, C., and Reynolds, J. A. (1981) Phospholipid vesicle formation and transmembrane protein incorporation using octyl glucoside, *Biochemistry* 20, 833-840.
57. Angelova, M. I., and Dimitrov, D. S. (1986) Liposome electroformation, *Faraday Discussions of the Chemical Society* 81, 303-311.
58. Jones, M. N. (1995) The surface properties of phospholipid liposome systems and their characterisation, *Advances in colloid and interface science* 54, 93-128.
59. Leyland-Jones, B. (1993) Targeted drug delivery, *Seminars in oncology* 20, 12-17.
60. Philips, N. C. (1992) *Liposomal carriers for the treatment of acquired immune deficiency syndromes*, Vol. 90, Masson, Paris, FRANCE.
61. Škalko, N., Čajkovac, M., and Jalšenjak, I. (1992) Liposomes with clindamycin hydrochloride in the therapy of acne vulgaris, *International Journal of Pharmaceutics* 85, 97-101.
62. Li, S. D., and Huang, L. (2006) Gene therapy progress and prospects: non-viral gene therapy by systemic delivery, *Gene therapy* 13, 1313-1319.
63. Karmali, P. P., and Chaudhuri, A. (2007) Cationic liposomes as non-viral carriers of gene medicines: resolved issues, open questions, and future promises, *Medicinal research reviews* 27, 696-722.

-
64. Puglia, C., Trombetta, D., Venuti, V., Saija, A., and Bonina, F. (2004) Evaluation of in-vivo topical anti-inflammatory activity of indometacin from liposomal vesicles, *The Journal of pharmacy and pharmacology* 56, 1225-1232.
65. Betz, G., Aeppli, A., Menshutina, N., and Leuenberger, H. (2005) In vivo comparison of various liposome formulations for cosmetic application, *Int J Pharm* 296, 44-54.
66. Nasr, M., Mansour, S., Mortada, N. D., and El Shamy, A. A. (2008) Lipospheres as carriers for topical delivery of aceclofenac: preparation, characterization and in vivo evaluation, *AAPS PharmSciTech* 9, 154-162.
67. Matsuda, R., Kaneko, N., and Horikawa, Y. (1997) Presence and comparison of Ca^{2+} transport activity of annexins I, II, V, and VI in large unilamellar vesicles, *Biochemical and biophysical research communications* 237, 499-503.
68. Kahya, N., Pecheur, E. I., de Boeij, W. P., Wiersma, D. A., and Hoekstra, D. (2001) Reconstitution of membrane proteins into giant unilamellar vesicles via peptide-induced fusion, *Biophysical journal* 81, 1464-1474.
69. Leitz, A. J., Bayburt, T. H., Barnakov, A. N., Springer, B. A., and Sligar, S. G. (2006) Functional reconstitution of Beta2-adrenergic receptors utilizing self-assembling Nanodisc technology, *BioTechniques* 40, 601-602, 604, 606, passim.
70. Bayburt, T. H., Leitz, A. J., Xie, G., Oprian, D. D., and Sligar, S. G. (2007) Transducin activation by nanoscale lipid bilayers containing one and two rhodopsins, *The Journal of biological chemistry* 282, 14875-14881.
71. Whorton, M. R., Bokoch, M. P., Rasmussen, S. G., Huang, B., Zare, R. N., Kobilka, B., and Sunahara, R. K. (2007) A monomeric G protein-coupled receptor

-
- isolated in a high-density lipoprotein particle efficiently activates its G protein, *Proceedings of the National Academy of Sciences of the United States of America* 104, 7682-7687.
72. Kuszak, A. J., Pitchiaya, S., Anand, J. P., Mosberg, H. I., Walter, N. G., and Sunahara, R. K. (2009) Purification and functional reconstitution of monomeric mu-opioid receptors: allosteric modulation of agonist binding by Gi2, *The Journal of biological chemistry* 284, 26732-26741.
73. Velez-Ruiz, G. A., and Sunahara, R. K. (2011) Reconstitution of G protein-coupled receptors into a model bilayer system: reconstituted high-density lipoprotein particles, *Methods in molecular biology* 756, 167-182.
74. Inagaki, S., Ghirlando, R., White, J. F., Gvozdenovic-Jeremic, J., Northup, J. K., and Grisshammer, R. (2012) Modulation of the interaction between neurotensin receptor NTS1 and Gq protein by lipid, *Journal of molecular biology* 417, 95-111.
75. Bayburt, T. H. G., Y. V.; Sligar, S. G. (2002) Self-assembly of discoidal phospholipid bilayer nanoparticles with membrane scaffold proteins, *Nano letters* 2, 853-856.
76. Denisov, I. G., Grinkova, Y. V., Lazarides, A. A., and Sligar, S. G. (2004) Directed self-assembly of monodisperse phospholipid bilayer Nanodiscs with controlled size, *Journal of the American Chemical Society* 126, 3477-3487.
77. Shih, A. Y., Arkhipov, A., Freddolino, P. L., Sligar, S. G., and Schulten, K. (2007) Assembly of lipids and proteins into lipoprotein particles, *The journal of physical chemistry. B* 111, 11095-11104.

-
78. Frauenfeld, J., Gumbart, J., Sluis, E. O., Funes, S., Gartmann, M., Beatrix, B., Mielke, T., Berninghausen, O., Becker, T., Schulten, K., and Beckmann, R. (2011) Cryo-EM structure of the ribosome-SecYE complex in the membrane environment, *Nature structural & molecular biology* 18, 614-621.
79. Flower, D. R. (1999) Modelling G-protein-coupled receptors for drug design, *Biochimica et biophysica acta* 1422, 207-234.
80. Bridges, T. M., and Lindsley, C. W. (2008) G-Protein-Coupled Receptors: From Classical Modes of Modulation to Allosteric Mechanisms, *ACS chemical biology* 3, 530-541.
81. Fredriksson, R., Lagerstrom, M. C., Lundin, L. G., and Schioth, H. B. (2003) The G-protein-coupled receptors in the human genome form five main families. Phylogenetic analysis, paralogon groups, and fingerprints, *Molecular pharmacology* 63, 1256-1272.
82. Palczewski, K., Kumasaka, T., Hori, T., Behnke, C. A., Motoshima, H., Fox, B. A., Le Trong, I., Teller, D. C., Okada, T., Stenkamp, R. E., Yamamoto, M., and Miyano, M. (2000) Crystal structure of rhodopsin: A G protein-coupled receptor, *Science* 289, 739-745.
83. Cherezov, V., Rosenbaum, D. M., Hanson, M. A., Rasmussen, S. G., Thian, F. S., Kobilka, T. S., Choi, H. J., Kuhn, P., Weis, W. I., Kobilka, B. K., and Stevens, R. C. (2007) High-resolution crystal structure of an engineered human beta2-adrenergic G protein-coupled receptor, *Science* 318, 1258-1265.
84. Serrano-Vega, M. J., Magnani, F., Shibata, Y., and Tate, C. G. (2008) Conformational thermostabilization of the beta1-adrenergic receptor in a

- detergent-resistant form, *Proceedings of the National Academy of Sciences of the United States of America* 105, 877-882.
85. Topiol, S., and Sabio, M. (2009) X-ray structure breakthroughs in the GPCR transmembrane region, *Biochemical pharmacology* 78, 11-20.
86. Lebon, G., Bennett, K., Jazayeri, A., and Tate, C. G. (2011) Thermostabilisation of an agonist-bound conformation of the human adenosine A(2A) receptor, *Journal of molecular biology* 409, 298-310.
87. Rasmussen, S. G., Choi, H. J., Fung, J. J., Pardon, E., Casarosa, P., Chae, P. S., Devree, B. T., Rosenbaum, D. M., Thian, F. S., Kobilka, T. S., Schnapp, A., Konetzki, I., Sunahara, R. K., Gellman, S. H., Pautsch, A., Steyaert, J., Weis, W. I., and Kobilka, B. K. (2011) Structure of a nanobody-stabilized active state of the beta(2) adrenoceptor, *Nature* 469, 175-180.
88. Granier, S., and Kobilka, B. (2012) A new era of GPCR structural and chemical biology, *Nature chemical biology* 8, 670-673.
89. Latek, D., Modzelewska, A., Trzaskowski, B., Palczewski, K., and Filipek, S. (2012) G protein-coupled receptors--recent advances, *Acta biochimica Polonica* 59, 515-529.
90. Zhao, Q., and Wu, B. L. (2012) Ice breaking in GPCR structural biology, *Acta pharmacologica Sinica* 33, 324-334.
91. Bertheleme, N., Chae, P. S., Singh, S., Mossakowska, D., Hann, M. M., Smith, K. J., Hubbard, J. A., Dowell, S. J., and Byrne, B. (2013) Unlocking the secrets of the gatekeeper: Methods for stabilizing and crystallizing GPCRs, *Biochimica et biophysica acta* 1828, 2583-2591.

-
92. Maeda, S., and Schertler, G. F. (2013) Production of GPCR and GPCR complexes for structure determination, *Current opinion in structural biology* 23, 381-392.
93. Rasmussen, S. G., DeVree, B. T., Zou, Y., Kruse, A. C., Chung, K. Y., Kobilka, T. S., Thian, F. S., Chae, P. S., Pardon, E., Calinski, D., Mathiesen, J. M., Shah, S. T., Lyons, J. A., Caffrey, M., Gellman, S. H., Steyaert, J., Skinotitis, G., Weis, W. I., Sunahara, R. K., and Kobilka, B. K. (2011) Crystal structure of the beta2 adrenergic receptor-Gs protein complex, *Nature* 477, 549-555.
94. Vincent, J. P., Mazella, J., and Kitabgi, P. (1999) Neurotensin and neurotensin receptors, *Trends in pharmacological sciences* 20, 302-309.
95. Nielsen, M. S., Jacobsen, C., Olivecrona, G., Gliemann, J., and Petersen, C. M. (1999) Sortilin/Neurotensin Receptor-3 Binds and Mediates Degradation of Lipoprotein Lipase, *Journal of Biological Chemistry* 274, 8832-8836.
96. Katada, T., Amano, T., and Ui, M. (1982) Modulation by islet-activating protein of adenylate cyclase activity in C6 glioma cells, *The Journal of biological chemistry* 257, 3739-3746.
97. Katada, T., and Ui, M. (1982) Direct modification of the membrane adenylate cyclase system by islet-activating protein due to ADP-ribosylation of a membrane protein, *Proceedings of the National Academy of Sciences of the United States of America* 79, 3129-3133.
98. Dobner, P. R. (2005) Multitasking with neurotensin in the central nervous system, *Cellular and molecular life sciences : CMLS* 62, 1946-1963.
99. Kitabgi, P. (2006) Functional domains of the subtype 1 neurotensin receptor (NTS1), *Peptides* 27, 2461-2468.

-
100. White, J. F., Noinaj, N., Shibata, Y., Love, J., Kloss, B., Xu, F., Gvozdenovic-Jeremic, J., Shah, P., Shiloach, J., Tate, C. G., and Grishammer, R. (2012) Structure of the agonist-bound neurotensin receptor, *Nature* 490, 508-513.
101. Chiu, W. (2005) Electron cryomicroscopy of cellular machines at subnanometer resolution, *Microscopy and microanalysis : the official journal of Microscopy Society of America, Microbeam Analysis Society, Microscopical Society of Canada 11 Suppl 2*, 1086-1087.
102. Jiang, W., and Ludtke, S. J. (2005) Electron cryomicroscopy of single particles at subnanometer resolution, *Current opinion in structural biology* 15, 571-577.
103. Frank, J. (2006) *Three-Dimensional Electron Microscopy of Macro-molecular Assemblies: Visualization of Biological Molecules in Their Native State.*, Oxford University Press, New York.
104. Glaeser, R. M. (2008) Cryo-electron microscopy of biological nanostructures, *Physics Today* 61.
105. Cheng, Y., and Walz, T. (2009) The advent of near-atomic resolution in single-particle electron microscopy, *Annual review of biochemistry* 78, 723-742.
106. Chang, W. H., Chiu, M. T., Chen, C. Y., Yen, C. F., Lin, Y. C., Weng, Y. P., Chang, J. C., Wu, Y. M., Cheng, H., Fu, J., and Tu, I. P. (2010) Zernike phase plate cryoelectron microscopy facilitates single particle analysis of unstained asymmetric protein complexes, *Structure* 18, 17-27.

-
107. Glaeser, Robert M., and Hall, Richard J. (2011) Reaching the Information Limit in Cryo-EM of Biological Macromolecules: Experimental Aspects, *Biophysical journal* 100, 2331-2337.
108. Bammes, B. E., Rochat, R. H., Jakana, J., Chen, D. H., and Chiu, W. (2012) Direct electron detection yields cryo-EM reconstructions at resolutions beyond 3/4 Nyquist frequency, *Journal of structural biology* 177, 589-601.
109. Kourkoutis, L. F., Plitzko, J. M., and Baumeister, W. (2012) Electron Microscopy of Biological Materials at the Nanometer Scale, *Annual Review of Materials Research* 42, 33-58.
110. Ludtke, S. J., Lawson, C. L., Kleywegt, G. J., Berman, H., and Chiu, W. (2012) The 2010 cryo-EM modeling challenge, *Biopolymers* 97, 651-654.
111. Henderson, R. (1995) The potential and limitations of neutrons, electrons and X-rays for atomic resolution microscopy of unstained biological molecules, *Quarterly reviews of biophysics* 28, 171-193.
112. Glaeser, R. M. (2008) Retrospective: Radiation damage and its associated “Information Limitations”, *Journal of structural biology* 163, 271-276.
113. Zhang, X., and Zhou, Z. H. (2011) Limiting factors in atomic resolution cryo electron microscopy: no simple tricks, *Journal of structural biology* 175, 253-263.
114. Chen, J. Z., Settembre, E. C., Aoki, S. T., Zhang, X., Bellamy, A. R., Dormitzer, P. R., Harrison, S. C., and Grigorieff, N. (2009) Molecular interactions in rotavirus assembly and uncoating seen by high-resolution cryo-EM, *Proceedings of the National Academy of Sciences of the United States of America* 106, 10644-10648.

-
115. Grigorieff, N., and Harrison, S. C. (2011) Near-atomic resolution reconstructions of icosahedral viruses from electron cryo-microscopy, *Current opinion in structural biology* 21, 265-273.
116. Wolf, M., Garcea, R. L., Grigorieff, N., and Harrison, S. C. (2010) Subunit interactions in bovine papillomavirus, *Proceedings of the National Academy of Sciences of the United States of America* 107, 6298-6303.
117. Zhang, X., Jin, L., Fang, Q., Hui, W. H., and Zhou, Z. H. (2010) 3.3 Å cryo-EM structure of a nonenveloped virus reveals a priming mechanism for cell entry, *Cell* 141, 472-482.
118. Cong, Y., Baker, M. L., Jakana, J., Woolford, D., Miller, E. J., Reissmann, S., Kumar, R. N., Redding-Johanson, A. M., Batth, T. S., Mukhopadhyay, A., Ludtke, S. J., Frydman, J., and Chiu, W. (2010) 4.0-Å resolution cryo-EM structure of the mammalian chaperonin TRiC/CCT reveals its unique subunit arrangement, *Proceedings of the National Academy of Sciences of the United States of America* 107, 4967-4972.
119. Armache, J. P., Jarasch, A., Anger, A. M., Villa, E., Becker, T., Bhushan, S., Jossinet, F., Habeck, M., Dindar, G., Franckenberg, S., Marquez, V., Mielke, T., Thomm, M., Berninghausen, O., Beatrix, B., Soding, J., Westhof, E., Wilson, D. N., and Beckmann, R. (2010) Cryo-EM structure and rRNA model of a translating eukaryotic 80S ribosome at 5.5-Å resolution, *Proceedings of the National Academy of Sciences of the United States of America* 107, 19748-19753.
120. Penczek, P. A., Kimmel, M., and Spahn, C. M. (2011) Identifying conformational states of macromolecules by eigen-analysis of resampled cryo-EM images, *Structure* 19, 1582-1590.

-
121. Li, X., Mooney, P., Zheng, S., Booth, C. R., Braunfeld, M. B., Gubbens, S., Agard, D. A., and Cheng, Y. (2013) Electron counting and beam-induced motion correction enable near-atomic-resolution single-particle cryo-EM, *Nat Meth* 10, 584-590.
122. Liao, M., Cao, E., Julius, D., and Cheng, Y. (2013) Structure of the TRPV1 ion channel determined by electron cryo-microscopy, *Nature* 504, 107-112.
123. Wu, S., Avila-Sakar, A., Kim, J., Booth, D. S., Greenberg, C. H., Rossi, A., Liao, M., Li, X., Alian, A., Griner, S. L., Juge, N., Yu, Y., Mergel, C. M., Chaparro-Riggers, J., Strop, P., Tampe, R., Edwards, R. H., Stroud, R. M., Craik, C. S., and Cheng, Y. (2012) Fabs enable single particle cryoEM studies of small proteins, *Structure* 20, 582-592.
124. Cheng, Y. (2009) Toward an atomic model of the 26S proteasome, *Current opinion in structural biology* 19, 203-208.
125. Shatsky, M., Hall, R. J., Brenner, S. E., and Glaeser, R. M. (2009) A method for the alignment of heterogeneous macromolecules from electron microscopy, *Journal of structural biology* 166, 67-78.
126. Homola, J., Yee, S. S., and Gauglitz, G. (1999) Surface plasmon resonance sensors: review, *Sensors and Actuators B: Chemical* 54, 3-15.
127. Alves, I. D., Salamon, Z., Varga, E., Yamamura, H. I., Tollin, G., and Hruby, V. J. (2003) Direct observation of G-protein binding to the human delta-opioid receptor using plasmon-waveguide resonance spectroscopy, *The Journal of biological chemistry* 278, 48890-48897.

-
128. de Mol, N. J., and Fischer, M. J. (2010) Surface plasmon resonance: a general introduction, *Methods in molecular biology* 627, 1-14.
129. Cooper, M. A. (2002) Optical biosensors in drug discovery, *Nature reviews. Drug discovery* 1, 515-528.
130. Myszka, D. G., Morton, T. A., Doyle, M. L., and Chaiken, I. M. (1997) Kinetic analysis of a protein antigen-antibody interaction limited by mass transport on an optical biosensor, *Biophys Chem* 64, 127-137.
131. Cooper, M. A., Try, A. C., Carroll, J., Ellar, D. J., and Williams, D. H. (1998) Surface plasmon resonance analysis at a supported lipid monolayer, *Biochimica et biophysica acta* 1373, 101-111.
132. Cooper, M. A., Hansson, A., Lofas, S., and Williams, D. H. (2000) A vesicle capture sensor chip for kinetic analysis of interactions with membrane-bound receptors, *Analytical biochemistry* 277, 196-205.
133. Sevin-Landais, A., Rigler, P., Tzartos, S., Hucho, F., Hovius, R., and Vogel, H. (2000) Functional immobilisation of the nicotinic acetylcholine receptor in tethered lipid membranes, *Biophys Chem* 85, 141-152.
134. Papo, N., and Shai, Y. (2003) Exploring peptide membrane interaction using surface plasmon resonance: differentiation between pore formation versus membrane disruption by lytic peptides, *Biochemistry* 42, 458-466.
135. Besenicar, M., Macek, P., Lakey, J. H., and Anderluh, G. (2006) Surface plasmon resonance in protein-membrane interactions, *Chemistry and physics of lipids* 141, 169-178.

-
136. Bousquet, C., Guillermet-Guibert, J., Saint-Laurent, N., Archer-Lahlou, E., Lopez, F., Fanjul, M., Ferrand, A., Fourmy, D., Pichereaux, C., Monsarrat, B., Pradayrol, L., Esteve, J. P., and Susini, C. (2006) Direct binding of p85 to sst2 somatostatin receptor reveals a novel mechanism for inhibiting PI3K pathway, *The EMBO journal* 25, 3943-3954.
137. Vatinel, S., Ferrand, A., Lopez, F., Kowalski-Chauvel, A., Esteve, J. P., Fourmy, D., Dufresne, M., and Seva, C. (2006) An ITIM-like motif within the CCK2 receptor sequence required for interaction with SHP-2 and the activation of the AKT pathway, *Biochimica et biophysica acta* 1763, 1098-1107.
138. Borch, J., Torta, F., Sligar, S. G., and Roepstorff, P. (2008) Nanodiscs for immobilization of lipid bilayers and membrane receptors: kinetic analysis of cholera toxin binding to a glycolipid receptor, *Analytical chemistry* 80, 6245-6252.
139. Gluck, J. M., Koenig, B. W., and Willbold, D. (2011) Nanodiscs allow the use of integral membrane proteins as analytes in surface plasmon resonance studies, *Analytical biochemistry* 408, 46-52.
140. Smith, E., Vekaria, R., Brown, K. A., and Longstaff, C. (2013) Kinetic regulation of the binding of prothrombin to phospholipid membranes, *Molecular and cellular biochemistry* 382, 193-201.
141. Beaumont, K., and Negulescu, P. (1999) Chipping away at GPCR function, *Nature biotechnology* 17, 1060.
142. Duchene, J., Schanstra, J. P., Pecher, C., Pizard, A., Susini, C., Esteve, J. P., Bascands, J. L., and Girolami, J. P. (2002) A novel protein-protein interaction between a G protein-coupled receptor and the phosphatase SHP-2 is involved in

-
- bradykinin-induced inhibition of cell proliferation, *The Journal of biological chemistry* 277, 40375-40383.
143. Karlsson, O. P., and Lofas, S. (2002) Flow-mediated on-surface reconstitution of G-protein coupled receptors for applications in surface plasmon resonance biosensors, *Analytical biochemistry* 300, 132-138.
144. Neumann, L., Wohland, T., Whelan, R. J., Zare, R. N., and Kobilka, B. K. (2002) Functional immobilization of a ligand-activated G-protein-coupled receptor, *Chembiochem : a European journal of chemical biology* 3, 993-998.
145. Stenlund, P., Babcock, G. J., Sodroski, J., and Myszka, D. G. (2003) Capture and reconstitution of G protein-coupled receptors on a biosensor surface, *Analytical biochemistry* 316, 243-250.
146. Northup, J. (2004) Measuring rhodopsin-G-protein interactions by surface plasmon resonance, *Methods in molecular biology* 261, 93-112.
147. Kang, H., Lee, W. K., Choi, Y. H., Vukoti, K. M., Bang, W. G., and Yu, Y. G. (2005) Molecular analysis of the interaction between the intracellular loops of the human serotonin receptor type 6 (5-HT6) and the alpha subunit of GS protein, *Biochemical and biophysical research communications* 329, 684-692.
148. Minic, J., Grosclaude, J., Aioun, J., Persuy, M. A., Gorojankina, T., Salesse, R., Pajot-Augy, E., Hou, Y., Helali, S., Jaffrezic-Renault, N., Bessueille, F., Errachid, A., Gomila, G., Ruiz, O., and Samitier, J. (2005) Immobilization of native membrane-bound rhodopsin on biosensor surfaces, *Biochimica et biophysica acta* 1724, 324-332.

-
149. Navratilova, I., Sodroski, J., and Myszka, D. G. (2005) Solubilization, stabilization, and purification of chemokine receptors using biosensor technology, *Analytical biochemistry* 339, 271-281.
150. Sen, S., Jaakola, V. P., Pirila, P., Finel, M., and Goldman, A. (2005) Functional studies with membrane-bound and detergent-solubilized alpha2-adrenergic receptors expressed in Sf9 cells, *Biochimica et biophysica acta* 1712, 62-70.
151. Harding, P. J., Hadingham, T. C., McDonnell, J. M., and Watts, A. (2006) Direct analysis of a GPCR-agonist interaction by surface plasmon resonance, *European biophysics journal : EBJ* 35, 709-712.
152. Komolov, K. E., Senin, II, Philippov, P. P., and Koch, K. W. (2006) Surface plasmon resonance study of g protein/receptor coupling in a lipid bilayer-free system, *Analytical chemistry* 78, 1228-1234.
153. Harding, P. J., Attrill, H., Ross, S., Koeppe, J. R., Kapanidis, A. N., and Watts, A. (2007) Neurotensin receptor type 1: Escherichia coli expression, purification, characterization and biophysical study, *Biochemical Society transactions* 35, 760-763.
154. Nehme, R., Joubert, O., Bidet, M., Lacombe, B., Polidori, A., Pucci, B., and Mus-Veteau, I. (2010) Stability study of the human G-protein coupled receptor, Smoothed, *Biochimica et biophysica acta* 1798, 1100-1110.
155. Langelan, D. N., Ngweniform, P., and Rainey, J. K. (2011) Biophysical characterization of G-protein coupled receptor-peptide ligand binding, *Biochemistry and cell biology = Biochimie et biologie cellulaire* 89, 98-105.

-
156. Navratilova, I., Besnard, J., and Hopkins, A. L. (2011) Screening for GPCR Ligands Using Surface Plasmon Resonance, *ACS medicinal chemistry letters* 2, 549-554.
157. Rich, R. L., Errey, J., Marshall, F., and Myszk, D. G. (2011) Biacore analysis with stabilized G-protein-coupled receptors, *Analytical biochemistry* 409, 267-272.
158. Christopher, J. A., Brown, J., Dore, A. S., Errey, J. C., Koglin, M., Marshall, F. H., Myszk, D. G., Rich, R. L., Tate, C. G., Tehan, B., Warne, T., and Congreve, M. (2013) Biophysical fragment screening of the beta1-adrenergic receptor: identification of high affinity arylpiperazine leads using structure-based drug design, *Journal of medicinal chemistry* 56, 3446-3455.
159. Tollin, G., Salamon, Z., and Hruby, V. J. (2003) Techniques: plasmon-waveguide resonance (PWR) spectroscopy as a tool to study ligand-GPCR interactions, *Trends in pharmacological sciences* 24, 655-659.
160. Alves, I. D., Ciano, K. A., Boguslavski, V., Varga, E., Salamon, Z., Yamamura, H. I., Hruby, V. J., and Tollin, G. (2004) Selectivity, cooperativity, and reciprocity in the interactions between the delta-opioid receptor, its ligands, and G-proteins, *The Journal of biological chemistry* 279, 44673-44682.
161. Alves, I. D., Park, C. K., and Hruby, V. J. (2005) Plasmon resonance methods in GPCR signaling and other membrane events, *Current protein & peptide science* 6, 293-312.
162. Grisshammer, R., Averbek, P., and Sohal, A. K. (1999) Improved purification of a rat neurotensin receptor expressed in Escherichia coli, *Biochemical Society transactions* 27, 899-903.

-
163. White, J. F., Trinh, L. B., Shiloach, J., and Grisshammer, R. (2004) Automated large-scale purification of a G protein-coupled receptor for neurotensin, *FEBS letters* 564, 289-293.
164. Sambrook, J., Fritsch, E. F., and Maniatis, T. (1989) *Molecular cloning*, Vol. 2, Cold spring harbor laboratory press New York.
165. Birnboim, H. C., and Doly, J. (1979) A rapid alkaline extraction procedure for screening recombinant plasmid DNA, *Nucleic acids research* 7, 1513-1523.
166. Attrill, H., Harding, P. J., Smith, E., Ross, S., and Watts, A. (2009) Improved yield of a ligand-binding GPCR expressed in E. coli for structural studies, *Protein expression and purification* 64, 32-38.
167. Grisshammer, R., White, J. F., Trinh, L. B., and Shiloach, J. (2005) Large-scale expression and purification of a G-protein-coupled receptor for structure determination -- an overview, *Journal of structural and functional genomics* 6, 159-163.
168. Liu, H., and Naismith, J. H. (2009) A simple and efficient expression and purification system using two newly constructed vectors, *Protein expression and purification* 63, 102-111.
169. Greentree, W. K., and Linder, M. E. (2004) Purification of recombinant G protein alpha subunits from Escherichia coli, *Methods in molecular biology* 237, 3-20.
170. Tanaka, M., Dhanasekaran, P., Nguyen, D., Ohta, S., Lund-Katz, S., Phillips, M. C., and Saito, H. (2006) Contributions of the N- and C-Terminal Helical

-
- Segments to the Lipid-Free Structure and Lipid Interaction of Apolipoprotein A-I†, *Biochemistry* 45, 10351-10358.
171. Ritchie, T. K., Grinkova, Y. V., Bayburt, T. H., Denisov, I. G., Zolnericiks, J. K., Atkins, W. M., and Sligar, S. G. (2009) Chapter 11 - Reconstitution of membrane proteins in phospholipid bilayer nanodiscs, *Methods in enzymology* 464, 211-231.
172. Goedert, M. (1989) Radioligand-binding assays for study of neurotensin receptors, *Methods in enzymology* 168, 462-481.
173. Tucker, J., and Grisshammer, R. (1996) Purification of a rat neurotensin receptor expressed in *Escherichia coli*, *The Biochemical journal* 317 (Pt 3), 891-899.
174. Sun, W.-C., Gee, K. R., Klaubert, D. H., and Haugland, R. P. (1997) Synthesis of Fluorinated Fluoresceins, *The Journal of organic chemistry* 62, 6469-6475.
175. Malo, J., Mitchell, J. C., Venien-Bryan, C., Harris, J. R., Wille, H., Sherratt, D. J., and Turberfield, A. J. (2005) Engineering a 2D protein-DNA crystal, *Angewandte Chemie* 44, 3057-3061.
176. Syôzi, I. (1951) Statistics of Kagomé Lattice, *Progress of Theoretical Physics* 6, 306-308.
177. Seeman, N. C. (1990) De novo design of sequences for nucleic acid structural engineering, *Journal of biomolecular structure & dynamics* 8, 573-581.
178. Goodman, R. P. (2005) NANEV: A program employing evolutionary methods for the design of nucleic acid nanostructures., *BioTechniques* 38, 548-550.

-
179. Selmi, D. N., Adamson, R. J., Attrill, H., Goddard, A. D., Gilbert, R. J., Watts, A., and Turberfield, A. J. (2011) DNA-templated protein arrays for single-molecule imaging, *Nano letters* 11, 657-660.
180. Goodman, R. P., Erben, C. M., Malo, J., Ho, W. M., McKee, M. L., Kapanidis, A. N., and Turberfield, A. J. (2009) A facile method for reversibly linking a recombinant protein to DNA, *Chembiochem : a European journal of chemical biology* 10, 1551-1557.
181. Goddard, A. D., Dijkman, P. M., Adamson, R. J., and Watts, A. (2013) Chapter 18 - Lipid-Dependent GPCR Dimerization, In *Methods in cell biology* (Conn, P. M., Ed.), pp 341-357, Academic Press.
182. Harding, P. J., Attrill, H., Boehringer, J., Ross, S., Wadhams, G. H., Smith, E., Armitage, J. P., and Watts, A. (2009) Constitutive dimerization of the G-protein coupled receptor, neurotensin receptor 1, reconstituted into phospholipid bilayers, *Biophysical journal* 96, 964-973.
183. Rigaud, J. L., Mosser, G., Lacapere, J. J., Olofsson, A., Levy, D., and Ranck, J. L. (1997) Bio-Beads: an efficient strategy for two-dimensional crystallization of membrane proteins, *Journal of structural biology* 118, 226-235.
184. Paternostre, M. T., Roux, M., and Rigaud, J. L. (1988) Mechanisms of membrane protein insertion into liposomes during reconstitution procedures involving the use of detergents. 1. Solubilization of large unilamellar liposomes (prepared by reverse-phase evaporation) by triton X-100, octyl glucoside, and sodium cholate, *Biochemistry* 27, 2668-2677.
185. Knol, J., Sjollem, K., and Poolman, B. (1998) Detergent-mediated reconstitution of membrane proteins, *Biochemistry* 37, 16410-16415.

-
186. Rigaud, J. L., and Levy, D. (2003) Reconstitution of membrane proteins into liposomes, *Methods in enzymology* 372, 65-86.
187. Chen, P. S., Toribara, T. Y., and Warner, H. (1956) Microdetermination of Phosphorus, *Analytical chemistry* 28, 1756-1758.
188. Bayburt, T. H., Grinkova, Y. V., and Sligar, S. G. (2006) Assembly of single bacteriorhodopsin trimers in bilayer nanodiscs, *Archives of biochemistry and biophysics* 450, 215-222.
189. Ludtke, S. J., Baldwin, P. R., and Chiu, W. (1999) EMAN: semiautomated software for high-resolution single-particle reconstructions, *Journal of structural biology* 128, 82-97.
190. Crowther, R. A., Henderson, R., and Smith, J. M. (1996) MRC image processing programs, *Journal of structural biology* 116, 9-16.
191. Shaikh, T. R., Gao, H., Baxter, W. T., Asturias, F. J., Boisset, N., Leith, A., and Frank, J. (2008) SPIDER image processing for single-particle reconstruction of biological macromolecules from electron micrographs, *Nat Protoc* 3, 1941-1974.
192. Gasteiger, E., Hoogland, C., Gattiker, A., Duvaud, S., Wilkins, M. R., Appel, R. D., and Bairoch, A. (2005) Protein identification and analysis tools on the ExPasy server., In *The Proteomics Protocols Handbook* (Walker, J. M., Ed.), pp 571-607, Humana Press.
193. Haendler, B., Hechler, U., Becker, A., and Schleuning, W. D. (1993) Expression of human endothelin receptor ET(B) by Escherichia coli

-
- transformants, *Biochemical and biophysical research communications* 191, 633-638.
194. Grisshammer, R., Little, J., and Aharony, D. (1994) Expression of rat NK-2 (neurokinin A) receptor in *E. coli*, *Receptors & channels* 2, 295-302.
195. Stanasila, L., Massotte, D., Kieffer, B. L., and Pattus, F. (1999) Expression of δ , κ and μ human opioid receptors in *Escherichia coli* and reconstitution of the high-affinity state for agonist with heterotrimeric G proteins, *European Journal of Biochemistry* 260, 430-438.
196. Weiss, H. M., and Grisshammer, R. (2002) Purification and characterization of the human adenosine A(2a) receptor functionally expressed in *Escherichia coli*, *European journal of biochemistry / FEBS* 269, 82-92.
197. Song, H. S., Lee, S. H., Oh, E. H., and Park, T. H. (2009) Expression, solubilization and purification of a human olfactory receptor from *Escherichia coli*, *Current microbiology* 59, 309-314.
198. Locatelli-Hoops, S. C., Gorshkova, I., Gawrisch, K., and Yeliseev, A. A. (2013) Expression, surface immobilization, and characterization of functional recombinant cannabinoid receptor CB, *Biochimica et biophysica acta* 1834, 2045-2056.
199. Ma, Y., Kubicek, J., and Labahn, J. (2013) Expression and Purification of Functional Human Mu Opioid Receptor from *E.coli*, *PloS one* 8, e56500.

-
200. Grisshammer, R., Duckworth, R., and Henderson, R. (1993) Expression of a rat neurotensin receptor in *Escherichia coli*, *The Biochemical journal* 295 (Pt 2), 571-576.
201. Hanninen, A. L., Bamford, D. H., and Grisshammer, R. (1994) Expression in *Escherichia coli* of rat neurotensin receptor fused to membrane proteins from the membrane-containing bacteriophage PRD1, *Biological chemistry Hoppe-Seyler* 375, 833-836.
202. Yeliseev, A. A., Wong, K. K., Soubias, O., and Gawrisch, K. (2005) Expression of human peripheral cannabinoid receptor for structural studies, *Protein Science* 14, 2638-2653.
203. Mohanty, A. K., Simmons, C. R., and Wiener, M. C. (2003) Inhibition of tobacco etch virus protease activity by detergents, *Protein expression and purification* 27, 109-114.
204. Fang, L., Jia, K.-Z., Tang, Y.-L., Ma, D.-Y., Yu, M., and Hua, Z.-C. (2007) An improved strategy for high-level production of TEV protease in *Escherichia coli* and its purification and characterization, *Protein expression and purification* 51, 102-109.
205. van den Berg, S., Löfdahl, P.-Å., Härd, T., and Berglund, H. (2006) Improved solubility of TEV protease by directed evolution, *Journal of Biotechnology* 121, 291-298.
206. McEwen, D. P., Gee, K. R., Kang, H. C., and Neubig, R. R. (2001) Fluorescent BODIPY-GTP analogs: real-time measurement of nucleotide binding to G proteins, *Analytical biochemistry* 291, 109-117.

-
207. Stark, H. (2010) Chapter Five - GraFix: Stabilization of Fragile Macromolecular Complexes for Single Particle Cryo-EM, In *Methods in enzymology* (Grant, J. J., Ed.), pp 109-126, Academic Press.
208. Malo, J., Mitchell, J. C., and Turberfield, A. J. (2009) A two-dimensional DNA array: the three-layer logpile, *Journal of the American Chemical Society* *131*, 13574-13575.
209. Gipson, B., Zeng, X., Zhang, Z. Y., and Stahlberg, H. (2007) 2dx--user-friendly image processing for 2D crystals, *Journal of structural biology* *157*, 64-72.
210. Dickey, A., and Faller, R. (2008) Examining the contributions of lipid shape and headgroup charge on bilayer behavior, *Biophysical journal* *95*, 2636-2646.
211. Kuszak, A. J., Pitchiaya, S., Anand, J. P., Mosberg, H. I., Walter, N. G., and Sunahara, R. K. (2009) Purification and Functional Reconstitution of Monomeric μ -Opioid Receptors: ALLOSTERIC MODULATION OF AGONIST BINDING BY Gi2, *Journal of Biological Chemistry* *284*, 26732-26741.
212. Westfield, G. H., Rasmussen, S. G., Su, M., Dutta, S., DeVree, B. T., Chung, K. Y., Calinski, D., Velez-Ruiz, G., Oleskie, A. N., Pardon, E., Chae, P. S., Liu, T., Li, S., Woods, V. L., Jr., Steyaert, J., Kobilka, B. K., Sunahara, R. K., and Skiniotis, G. (2011) Structural flexibility of the G α s α -helical domain in the beta2-adrenoceptor Gs complex, *Proceedings of the National Academy of Sciences of the United States of America* *108*, 16086-16091.
213. Pettersen, E. F., Goddard, T. D., Huang, C. C., Couch, G. S., Greenblatt, D. M., Meng, E. C., and Ferrin, T. E. (2004) UCSF Chimera--a visualization system

-
- for exploratory research and analysis, *Journal of computational chemistry* 25, 1605-1612.
214. Raw, A. S., Coleman, D. E., Gilman, A. G., and Sprang, S. R. (1997) Structural and biochemical characterization of the GTPgammaS-, GDP.Pi-, and GDP-bound forms of a GTPase-deficient Gly42 --> Val mutant of Gialpha1, *Biochemistry* 36, 15660-15669.
215. Coleman, D. E., and Sprang, S. R. (1998) Crystal structures of the G protein Gi alpha 1 complexed with GDP and Mg²⁺: a crystallographic titration experiment, *Biochemistry* 37, 14376-14385.
216. Yao, X. J., Velez Ruiz, G., Whorton, M. R., Rasmussen, S. G., DeVree, B. T., Deupi, X., Sunahara, R. K., and Kobilka, B. (2009) The effect of ligand efficacy on the formation and stability of a GPCR-G protein complex, *Proceedings of the National Academy of Sciences of the United States of America* 106, 9501-9506.
217. Traut, T. W. (1994) Physiological concentrations of purines and pyrimidines, *Molecular and cellular biochemistry* 140, 1-22.
218. Blagova, E. V., Levnikov, V. M., Tachikawa, K., Sonenshein, A. L., and Wilkinson, A. J. (2003) Crystallization of the GTP-dependent transcriptional regulator CodY from *Bacillus subtilis*, *Acta crystallographica. Section D, Biological crystallography* 59, 155-157.
219. Guex, N., and Peitsch, M. C. (1997) SWISS-MODEL and the Swiss-PdbViewer: an environment for comparative protein modeling, *Electrophoresis* 18, 2714-2723.

-
220. Patching, S. G. (2014) Surface plasmon resonance spectroscopy for characterisation of membrane protein–ligand interactions and its potential for drug discovery, *Biochimica et Biophysica Acta (BBA) - Biomembranes* 1838, 43-55.
221. Salamon, Z., Tollin, G., Alves, I., and Hruby, V. (2009) Chapter 6. Plasmon resonance methods in membrane protein biology applications to GPCR signaling, *Methods in enzymology* 461, 123-146.
222. Bieri, C., Ernst, O. P., Heyse, S., Hofmann, K. P., and Vogel, H. (1999) Micropatterned immobilization of a G protein-coupled receptor and direct detection of G protein activation, *Nature biotechnology* 17, 1105-1108.
223. Hruby, V. J., and Tollin, G. (2007) Plasmon-waveguide resonance (PWR) spectroscopy for directly viewing rates of GPCR/G-protein interactions and quantifying affinities, *Current opinion in pharmacology* 7, 507-514.
224. Tanaka, K., Masu, M., and Nakanishi, S. (1990) Structure and functional expression of the cloned rat neurotensin receptor, *Neuron* 4, 847-854.
225. Grisshammer, R., and Tucker, J. (1997) Quantitative evaluation of neurotensin receptor purification by immobilized metal affinity chromatography, *Protein expression and purification* 11, 53-60.
226. Civjan, N. R., Bayburt, T. H., Schuler, M. A., and Sligar, S. G. (2003) Direct solubilization of heterologously expressed membrane proteins by incorporation into nanoscale lipid bilayers, *BioTechniques* 35, 556-560, 562-553.
227. Shaw, A. W., McLean, M. A., and Sligar, S. G. (2004) Phospholipid phase transitions in homogeneous nanometer scale bilayer discs, *FEBS letters* 556, 260-264.

-
228. Kelly, D. F., Dukovski, D., and Walz, T. (2008) Monolayer purification: a rapid method for isolating protein complexes for single-particle electron microscopy, *Proceedings of the National Academy of Sciences of the United States of America* 105, 4703-4708.
229. Kelly, D. F., Dukovski, D., and Walz, T. (2010) A practical guide to the use of monolayer purification and affinity grids, *Methods in enzymology* 481, 83-107.
230. Wang, L., and Sigworth, F. J. (2009) Structure of the BK potassium channel in a lipid membrane from electron cryomicroscopy, *Nature* 461, 292-295.
231. Akkaladevi, N., Hinton-Chollet, L., Katayama, H., Mitchell, J., Szerszen, L., Mukherjee, S., Gogol, E. P., Pentelute, B. L., Collier, R. J., and Fisher, M. T. (2013) Assembly of anthrax toxin pore: lethal-factor complexes into lipid nanodiscs, *Protein science : a publication of the Protein Society* 22, 492-501.
232. Gogol, E. P., Akkaladevi, N., Szerszen, L., Mukherjee, S., Chollet-Hinton, L., Katayama, H., Pentelute, B. L., Collier, R. J., and Fisher, M. T. (2013) Three dimensional structure of the anthrax toxin translocon-lethal factor complex by cryo-electron microscopy, *Protein science : a publication of the Protein Society* 22, 586-594.
233. Zhang, L., Song, J., Newhouse, Y., Zhang, S., Weisgraber, K. H., and Ren, G. (2010) An optimized negative-staining protocol of electron microscopy for apoE4 POPC lipoprotein, *Journal of lipid research* 51, 1228-1236.
234. Zhang, L., Tong, H., Garewal, M., and Ren, G. (2013) Optimized negative-staining electron microscopy for lipoprotein studies, *Biochimica et biophysica acta* 1830, 2150-2159.

-
235. Le Trong, I., Wang, Z., Hyre, D. E., Lybrand, T. P., Stayton, P. S., and Stenkamp, R. E. (2011) Streptavidin and its biotin complex at atomic resolution, *Acta crystallographica. Section D, Biological crystallography* 67, 813-821.
236. Navratilova, I., Dioszegi, M., and Myszka, D. G. (2006) Analyzing ligand and small molecule binding activity of solubilized GPCRs using biosensor technology, *Analytical biochemistry* 355, 132-139.
237. Nobles, M., Benians, A., and Tinker, A. (2005) Heterotrimeric G proteins precouple with G protein-coupled receptors in living cells, *Proceedings of the National Academy of Sciences of the United States of America* 102, 18706-18711.
238. Gales, C., Van Durm, J. J., Schaak, S., Pontier, S., Percherancier, Y., Audet, M., Paris, H., and Bouvier, M. (2006) Probing the activation-promoted structural rearrangements in preassembled receptor-G protein complexes, *Nature structural & molecular biology* 13, 778-786.
239. Sunahara, R. K., Tesmer, J. J., Gilman, A. G., and Sprang, S. R. (1997) Crystal structure of the adenylyl cyclase activator G α , *Science* 278, 1943-1947.
240. Strange, P. G. (2010) Use of the GTP γ S ([³⁵S]GTP γ S and Eu-GTP γ S) binding assay for analysis of ligand potency and efficacy at G protein-coupled receptors, *British journal of pharmacology* 161, 1238-1249.
241. Justesen, B. H., Hansen, R. W., Martens, H. J., Theorin, L., Palmgren, M. G., Martinez, K. L., Pomorski, T. G., and Fuglsang, A. T. (2013) Active plasma membrane P-type H⁺-ATPase reconstituted into nanodiscs is a monomer, *The Journal of biological chemistry* 288, 26419-26429.

242. Skrzydelski, D., Lhiaubet, A. M., Lebeau, A., Forgez, P., Yamada, M., Hermans, E., Rostene, W., and Pelaprat, D. (2003) Differential involvement of intracellular domains of the rat NTS1 neurotensin receptor in coupling to G proteins: a molecular basis for agonist-directed trafficking of receptor stimulus, *Molecular pharmacology* 64, 421-429.
243. Pelaprat, D. (2006) Interactions between neurotensin receptors and G proteins, *Peptides* 27, 2476-2487.

Appendix

DNA oligonucleotide sequences

The sticky ends are shown in italics. The sequences are as follows:

Small lattice

1 - Yellow

TGT TCC GTC CTG CTC ATC GC *GATACT*

2 - Red

CTA ACT CAA TGC CTT CTG GA *TATGGC*

3 - Blue

GCG ATG AGC AGG AGA GTT AG *AGTATC*

4 - Green

TCC AGA AGG CAT TCG GAA CA *GCCATA*

Large lattice

1 – Large Yellow

TGTCATGTTCCGTCCTGCTCATCGCTCGCAC *GATACT*

2 – Large Red

GTAATCTAACTCAATGCCTTCTGGACCTTAC *TATGGC*

3 – Large Blue

GTGCGAGCGATGAGCAGGAGAGTTAGATTAC *AGTATC*

4 – Large Green

GTAAGGTCCAGAAGGCATTCGGAACATGACA *GCCATA*